Summer 2021

Improving the data quality in gravitation-wave detectors by mitigating transient noise artifacts

Kentaro Mogushi

Department: Physics

IMPROVING THE DATA QUALITY IN GRAVITATION-WAVE DETECTORS BY MITIGATING TRANSIENT NOISE ARTIFACTS

by

KENTARO MOGUSHI

A DISSERTATION

Presented to the Graduate Faculty of the

MISSOURI UNIVERSITY OF SCIENCE AND TECHNOLOGY

In Partial Fulfillment of the Requirements for the Degree

DOCTOR OF PHILOSOPHY

in

PHYSICS

2021

Approved by:

Dr. Marco Cavaglià, Advisor
Dr. Thomas Vojta
Dr. Shun Saito
Dr. Alexey Yamilov
Dr. Sergei Kopeikin

PUBLICATION DISSERTATION OPTION

This dissertation consists of the following two articles which have been submitted for publication, or will be submitted for publication as follows:

Paper I: Pages 48-70 have been accepted by Classical and Quantum Gravity Journal. This work is documented as K. Mogushi, 2021, *Application of a new transient-noise analysis tool for an unmodeled gravitational-wave search pipeline* (Mogushi, 2021a) and has been reviewed by LIGO scientific collaboration (LSC) and has been published by the journal.

Paper II: Pages 71-129 are intended for submission to Classical and Quantum Gravity Journal. This work is documented as K. Mogushi, 2021, *Reduction of transient noise artifacts in gravitational-wave data using deep learning* Mogushi (2021b).

Disclaimer: The content of this dissertation work does not reflect the scientific opinion of the LSC.

ABSTRACT

The existence of gravitational waves (GWs), small perturbations in spacetime produced by accelerating massive objects was first predicted in 1916 as solutions of Einstein's Theory of General Relativity (Einstein, 1916). Detecting and analyzing GWs produced by sources allows us to probe astrophysical phenomena.

The era of GW astronomy began from the first direct detection of the coalescence of a binary black hole in 2015 by the collaboration of the advanced Laser Interferometer Gravitational-wave Observatory (LIGO) (Aasi *et al.*, 2015) and advanced Virgo (Abbott *et al.*, 2016a). Since 2015, LIGO-Virgo detected about 50 confident transient events of GW signals (Abbott *et al.*, 2019d, 2021b).

To detect GW signals, the detectors must be extremely sensitive, causing them to be susceptible to instrumental and environmental noise. Particularly, excess transient noise artifacts, or *glitches* significantly impair the quality of detector data. Identification of the source of these glitches is a crucial point for the improvement of GW signal detectability and a better estimate of source parameters. However, glitches are the product of short-lived linear and non-linear couplings among the interrelated detector-control systems that include optic alignment systems and mitigation systems of ground motions, generally making it difficult to find their origin. We present a new software called PyChChoo (Mogushi, 2021a) which uses time series recorded in the instrumental control systems and environmental sensors around times when glitches are present in the detector's output read-out to reveal essential clues about their origin. Using these time series, we subtract glitches using a machine learning algorithm. We find that our method reduces 20-70% of excess power due to the presence of glitches. For low-latency operations, we present another machine-learning based algorithm called NNETFIX (Mogushi *et al.*, 2021) to estimate the data containing a GW signal that is partially removed due to the presence of an overlapping glitch.

ACKNOWLEDGMENTS

I have been very fortunate to meet many great people in my life. I wish to express my sincere gratitude to those people without whom it would not be possible to write my dissertation.

First and foremost, I would like to thank my supervisor Dr. Marco Cavaglià. I thank him for training me and giving useful comments to me. Most importantly, I thank him for financially supporting me as a research assistant such that I had food on my table.

Next, I would like to thank Dr. Adriana Edwards Wurzinger who trained me and opened my career in academia. I can still remember the practice for the Drama Workshop directed by her as a fresh memory and never forget her great support when I was at the Saitama University.

Also, I would like to thank Dr. Rick Savage for his ultimate kind support. I enjoyed working with him during the fellowship at the LIGO-Hanford site in 2017. I was greatly influenced by how he likes physics.

I have to thank the whole members of the LIGO-MST group. I also thank all members of the LIGO and Virgo collaborations for helping me quickly when I asked.

Thank all my committee members, Dr. Thomas Vojta, Dr. Shun Saito, Dr. Alexey Yamilov, and Dr. Sergei Kopeikin for reading my dissertation and nice suggestions.

Finally, I would like to thank my family and friends for supporting me through all my life.

TABLE OF CONTENTS

Page

LIST OF ILLUSTRATIONS

Figure Page

SECTION

PAPER I

PAPER II

SECTION

LIST OF TABLES

NOMENCLATURE

Symbol	Description
ANN	Artificial Neural Network: a type of machine-learning algorithms that uses interconnected artificial neurons (mathematical functions) to process user-provided data. For example, ANNs are used for classifying vehicle images and estimating the trend of the stock market in near future.
ASD	Amplitude Spectrum Density: the square root of **PSD**.
Auxiliary channels	On-site auxiliary sensors or control systems that monitor instrumental and environmental disturbances in **GW** detectors. Auxiliary channels can be potential witnesses for **glitches** present in the detector's output readout.
BBH	Binary Black Hole: a binary system of two black holes.
BNS	Binary Neutron Star: a binary system of two neutron stars.
CBC	Compact Binary Coalescence: for example, a binary system of two black holes, two neutron stars, or a neutron star and a black hole.
CCSN	Core-Collapse Supernovae.
CLE	Contour Level Enhancement: the ratio of the one minus the contour level in the sky map obtained from the **NNETFIX** reconstructed data to one minus the contour level of the sky map obtained from the **gated** data.
CNN	Convolutional neural network: a type of **MLP** consisting of a series of layers, where small groups of neurons in each layer are convoluted with window functions to learn local features in the input data. For example, CNNs are generally used for image processing.
Contour level	The sum of probability densities of pixels with their values greater than the value of the pixel containing the sky location of the injected signal. Smaller values of the contour level imply that the estimates of the source sky location are more accurate.
CQT	Constant Q-transform: a type of wavelet-transformation that uses logarithm-spacing frequency bins. Values of Q are defined as the ratio of the characteristic frequency to the variance in frequency. Wavelet bases are generally sinusoidal or Gaussian-modulated sinusoid functions.

cWB Coherent WaveBurst: an unmodeled **GW** search algorithm used in **LIGO** and **Virgo**. cWB identifies candidate **GW** events by calculating coherent excess power in the time-frequency representations via wavelet-basis between multiple **GW** detectors maximized over all potential sky locations.

EM Electromagnetic.

ETG Event Trigger Generator: ETGs identify excess-power events by generally characterizing these events with a characteristic time, frequency, and measure of loudness compared to the corresponding loudness measure of stationary Gaussian noise.

FAR False Alarm Rate: FAR is the rate of terrestrial-noise events with their significance equal to or higher than the significance of an astrophysical candidate event.

FFT Fast Fourier transform: a type of discrete Fourier transform.

FGT Fast Griffin-Lim: modified Griffin-Lin transform to converge faster.

FMG Fractional match gain: the ratio of the ***match*** gained due to the **NNET-FIX** reconstruction over the ***match*** lost due to a **gate** used to remove the presence of a **glitch** overlapping a detected **CBC** signal.

FNR Fraction of **SNR** reduction after subtracting glitches. In the context of this dissertation, an extracted glitch waveform and the data before or after glitch subtraction are used for calculating SNRs.

Gate Techniques to remove the data affected by a glitch. One of the gating techniques is to set the data affected by a glitch to be zero and smoothly connect the gated portion to the surrounding parts using a window function.

GL Griffin-Lim: the GL transform creates time series from **mSTFT** by estimating the phase

Glitch A transient noise artifact observed in ground-based gravitational-wave detectors.

GRB Gamma-ray burst: GRBs are extremely energetic astrophysical explosions.

GWs Gravitational waves: ripples of curved spacetime generated by accelerated massive objects.

H1 One of **LIGO** observatory sites located in Hanford, Washington in the United States.

hVETO hierarchical Veto: hVETO is an algorithm similar to **UPV** but finds witness channels hierarchically to minimize the vetoed time as much as possible.

iFAR Inverse false alarm rate

IMBBH Intermediate Binary Black Hole: black holes between stellar black holes and supermassive black holes which are believed to be at the center of general galaxies.

KS Kolmogorov-Smirnov: one-simple **KS** test is typically used to compare the similarity between an empirical set and an expected distribution while a two-sample **KS** test is used to compare the similarity between two empirical sets.

L1 One of **LIGO** observatory sites located in Livingston, Louisiana in the United States.

LHS Left-Hand Side.

LIGO Laser Interferometer Gravitational-wave Observatory: two ground-based **GW** interferometers with two 4-kilometer arms located in the United States.

LSC **LIGO** Scientific Collaboration.

Match The noise-weighted inner product of two time series, normalized to 1 for a perfect match.

MLP Multi-Layered Perceptron: a type of **ANN** consisting of layers of artificial neurons, where information from neurons is fed into the preceding layers.

MSE Mean Square Error: MSE is the average of the squared difference of the estimated and the true data.

mSTFT magnitude of **STFT**

NNETFIX A Neural NETwork to 'FIX' **GW** signal coincident with short-duration **glitches** in detector data: a machine learning-based software package to interpolate the data.

NSBH A binary system of a Neutron Star and a Black Hole.

O1 The first **LIGO-Virgo** observation run from September 12, 2015 to January 19, 2016.

O2 The second **LIGO-Virgo** observation run from November 30, 2016, to August 25, 2017.

O3a	The first half of the third **LIGO-Virgo** observation run from Apr 1, 2019 to September 30, 2019.
Omicron	The primary **ETG** used in **LIGO** and **Virgo**, intended to identify **glitches** using a generic sine-Gaussian time-frequency projection.
PCA	Principle Component Analysis.
PSD	Power Spectrum Density: PSD describes the distribution of power of the data into frequency bins.
PyChChoo	Python-based glitch Characterization tool: PyChChoo statistically identifies the auxiliary witness channels for **glitches** detected in the detector's output readout.
RHS	Right-Hand Side.
RS	Ranking Statistic: RS is the significance of candidate **GW** events.
sGRB	Short gamma-ray burst or short **GRB**: **sGRBs** are produced by **BNS** or **NSBH** mergers.
Sky localization error region	Posterior distribution of the source location in the sky given data. Numerically, the sky localization error region is provided as probabilities over pixelized solid angles in the sky (so-called sky map).
SNR	Signal-to-Noise-Ratio: SNR for a particular frequency range is the ratio of the amplitude associated with a known waveform or an identified waveform to the averaged amplitude over the analyzed time period.
SSR	Sum of Squares of Residuals: SSR is the sum of squares of the difference between the predicted and the true data over the data set.
STFT	discrete Short-Time Fourier transform: STFT is obtained by calculating discrete Fourier transforms in divided data portions.
SUT	Stationarity Upper Threshold: SUT represents the averaged upper threshold of noise fluctuations in an auxiliary channel with a given duration in a given frequency range during time periods when no glitches are present in the detector's output readout.
TFR	Time-Frequency Representation: a view of time series represented over both time and frequency.
TSS	Total Sum of Squares: TSS is the sum of squares of the difference between the true data and the mean of the true data over the data set.

UPV Use-Percentage Veto: UPV is an algorithm that finds the statistical correlation using the percentage of the number of transients in each **auxiliary channel** in coincidence with **glitches** in the detector's output readout, relative to the total number of transients to determine vetoed periods in LIGO and Virgo.

Virgo A ground-based **GW** interferometer with two 3-kilometer arms in Italy.

1. INTRODUCTION

This chapter presents a brief introduction of Einstein's special relativity (Einstein, 1905), general relativity (Einstein, 1915), the derivation of the field equations in the weak gravitational field regime, polarizations, and the quadrupole moment approximation based on Carroll (2003); Poisson and Will (2014); Saulson (1994). Also, the four primary classes of gravitational wave (GW) sources will be described.

1.1. GRAVITATIONAL WAVES

In 1905, Einstein formulated special relativity (Einstein, 1905) where space and time are interchangeable. The interval of two events described by a union of space and time, or *spacetime* is invariant under coordinate transformations. In the spacetime, an event is labeled with the spatial coordinates (x, y, z) and the time t. Using a unified coordinate $x^\mu = (ct, x, y, z)$ where c is the speed of light and the index μ runs over values $\{0, 1, 2, 3\}$ such that $x^0 = ct$, $x^1 = x$, $x^2 = y$, and $x^3 = z$, the spacetime interval ds^2 is defined as

$$ds^2 = \eta_{\mu\nu} dx^\mu dx^\nu , \tag{1.1}$$

where dx^μ are the coordinate displacements, and $\eta_{\mu\nu} = diag(-1, 1, 1, 1)$ is the metric tensor of the flat spacetime, or the Minkowski tensor. For more details, Appendix A shows the conventions used in Equation (1.1). More specifically, the spacetime interval defined above is invariant under Lorentz transformations as shown in Appendix A. Special relativity states that all the laws of classical physics must be invariant in inertial systems.

To include gravity into the relativistic laws of physics, Einstein generalized special relativity by introducing the notion of the curved spacetime in 1915 (Einstein, 1915). Using a generalized metric $g_{\mu\nu}$ for the curved spacetime instead of $\eta_{\mu\nu}$, the spacetime interval

$$ds^2 = g_{\mu\nu} dx^\mu dx^\nu \tag{1.2}$$

is invariant under general invertible coordinate transformations.

In the famous words from John A. Wheeler, the field equations tell "Spacetime tells matter how to move; matter tells spacetime how to curve" (Misner *et al.*, 1973). The field equations are written as

$$R_{\mu\nu} - \frac{1}{2} g_{\mu\nu} R = \frac{8\pi G}{c^4} T_{\mu\nu} \,, \tag{1.3}$$

where G is the gravitational constant, $T_{\mu\nu}$ is the energy-momentum tensor, $R_{\mu\nu}$ is the Ricci tensor:

$$R_{\mu\nu} = R^{\sigma}{}_{\mu\sigma\nu} \,, \tag{1.4}$$

where $R^{\mu}{}_{\alpha\mu\beta}$ is the Riemann curvature tensor:

$$R^{\alpha}{}_{\beta\gamma\delta} = \partial_\gamma \Gamma^{\alpha}{}_{\beta\delta} - \partial_\delta \Gamma^{\alpha}{}_{\beta\gamma} + \Gamma^{\alpha}{}_{\mu\gamma} \Gamma^{\mu}{}_{\beta\delta} - \Gamma^{\alpha}{}_{\mu\delta} \Gamma^{\mu}{}_{\beta\gamma} \,, \tag{1.5}$$

where $\Gamma^{\mu}{}_{\alpha\beta}$ are the Christoffel symbols:

$$\Gamma^{\mu}{}_{\alpha\beta} = \frac{1}{2} g^{\mu\nu} \left(\partial_\alpha g_{\nu\beta} + \partial_\beta g_{\nu\alpha} - \partial_\nu g_{\alpha\beta} \right) \,. \tag{1.6}$$

The Ricci scalar in Equation (1.3) is obtained by contracting the indices of the Ricci tensor as

$$R = g^{\alpha\beta} R_{\alpha\beta} \,. \tag{1.7}$$

Because the Ricci tensor and Ricci scalar are defined with derivatives of the metric up to second order, Equation (1.3) describes a set of second-order, partial differential equations. Importantly, Einstein's field equations are defined in covariant form, i.e., the form of equations is invariant under general invertible transformations.

One year later, in 1915, Einstein published an article on the linearized approximate solution of Einstein's field equations that suggested the existence of 'ripples' of the spacetime known as gravitational waves (Einstein, 1916).

1.1.1. Einstein's Equations in Weak Gravitational Field. In the linearized approximation, we consider a spacetime far enough from GW sources such that the metric $g_{\mu\nu}$ is 'nearly' flat. Comparing Equations (1.1) and (1.2), the metric of the curved spacetime is given as a small perturbation added to the metric of the flat spacetime:

$$g_{\mu\nu} = \eta_{\mu\nu} + h_{\mu\nu} \qquad \text{with} \quad |h_{\mu\nu}| \ll 1. \tag{1.8}$$

If we want to choose coordinates that satisfy several restrictions including (1) the metric in the transformed coordinates is also the sum of the metric of the flat spacetime plus a small perturbation; (2) the coordinate transformations include the Lorentz transformations; and (3) the coordinate transformations are limited to small changes with the order of $|h_{\mu\nu}|$, the coordinate transformations are formulated as

$$x'^{\alpha} = x^{\alpha} + \zeta^{\alpha}(x^{\alpha}) \qquad \text{with} \quad |\zeta^{\alpha}| \ll 1\,, \tag{1.9}$$

where ζ^{α} is a vector field. To the first order in ζ^{α}, the metric in the new coordinates is given as

$$g'_{\alpha\beta} = \eta_{\alpha\beta} + h_{\alpha\beta} - \partial_{\alpha}\eta_{\beta\mu}\zeta^{\mu} - \partial_{\beta}\eta_{\alpha\nu}\zeta^{\nu}\,. \tag{1.10}$$

For the first requirement to be satisfied, the perturbation must be

$$h'_{\alpha\beta} = h_{\alpha\beta} - \partial_{\alpha}\zeta_{\beta} - \partial_{\beta}\zeta_{\alpha}\,, \tag{1.11}$$

where $\zeta_\alpha := \eta_{\alpha\mu}\zeta^\mu$. Because the Minkowski tensor is the same before and after the Lorentz transformations, $h_{\mu\nu}$ is a tensor under any of the Lorentz transformations. This equation is referred to as a gauge transformation, meaning that any small coordinate transformations $|\zeta^\alpha| \ll 1$ can be chosen to get Equation (1.8) while preserving the law of physics unchanged.

Let us rewrite the Einstein field equations in terms of the linearized metric. To first order in $h_{\mu\nu}$, the Ricci tensor becomes

$$R_{\mu\nu} = -\frac{1}{2}\left(\Box h_{\mu\nu} + \partial_\mu\partial_\nu h - \partial_\mu\partial^\gamma h_{\gamma\nu} - \partial_\nu\partial^\gamma h_{\gamma\mu}\right) \tag{1.12}$$

and the Ricci scalar becomes

$$R = -\Box h + \partial^\mu\partial^\nu h_{\mu\nu}\,, \tag{1.13}$$

where $h = \eta^{\mu\nu}h_{\mu\nu}$, and $\Box := \eta^{\mu\nu}\partial_\mu\partial_\nu$ is the d'Alembert operator or the wave operator in the flat spacetime. Substituting Equations (1.12) and (1.13) into Equation (1.3), the Einstein field equations become

$$-\frac{1}{2}\left(\Box h_{\mu\nu} + \partial h - \partial_\mu\partial^\gamma h_{\gamma\nu} - \partial_\nu\partial^\gamma h_{\gamma\mu}\right) + \frac{1}{2}\eta_{\mu\nu}\left(\Box h - \partial^\gamma\partial^\delta h_{\gamma\delta}\right) = \frac{8\pi G}{c^4}T_{\mu\nu}\,. \tag{1.14}$$

These linearized equations can be further simplified by defining a new variable called "trace-reversed" perturbation:

$$\bar{h}_{\mu\nu} := h_{\mu\nu} - \frac{1}{2}\eta_{\mu\nu}h\,. \tag{1.15}$$

Using Equation (1.15), Equation (1.14) becomes

$$-\frac{1}{2}\left(\Box\bar{h}_{\mu\nu} - \partial_\mu\partial^\gamma\bar{h}_{\gamma\nu} - \partial_\nu\partial^\gamma\bar{h}_{\gamma\mu} + \eta_{\mu\nu}\partial^\gamma\partial^\delta\bar{h}_{\gamma\delta}\right) = \frac{8\pi G}{c^4}T_{\mu\nu}\,. \tag{1.16}$$

The small perturbation $\bar{h}_{\mu\nu}$ in the weak gravitational field should obey these field equations.

The above equations can be even further simplified by using the new coordinate freedom in Equation (1.9) and imposing the Lorenz gauge condition:

$$\partial^{\nu}\bar{h}_{\mu\nu} = 0\,. \tag{1.17}$$

This gauge condition is always achievable because one can find a coordinate transformation such that the perturbation in the new coordinates satisfies the Lorenz gauge condition when the perturbation in the old coordinates does not satisfy this gauge condition. Assuming that the metric perturbation does not satisfy the Lorenz gauge condition, one can find the perturbation in the new coordinates as

$$\bar{h}^{'}_{\mu\nu} = \bar{h}_{\mu\nu} - \partial_{\mu}\zeta_{\nu} - \partial_{\nu}\zeta_{\mu} + \eta_{\mu\nu}\partial_{\gamma}\zeta^{\gamma}\,, \tag{1.18}$$

where we have substituted Equation (1.15) into Equation (1.11). The metric perturbation in the new coordinates satisfies the Lorenz gauge condition if

$$0 = \partial^{\nu}\bar{h}^{'}_{\mu\nu} = \partial^{\nu}\bar{h}_{\mu\nu} - \Box\zeta_{\mu}\,, \tag{1.19}$$

i.e.,

$$\Box\zeta_{\mu} = \partial^{\nu}\bar{h}_{\mu\nu}\,. \tag{1.20}$$

Equation (1.20) can be solved if $\bar{h}_{\mu\nu}$ is differentiable, i.e., $\partial^{\nu}\bar{h}_{\mu\nu} = f_{\mu}(x^{\gamma})$, the solutions are

$$\zeta_{\mu} = \int d^4y G(x^{\gamma} - y^{\gamma}) f_{\mu}(x^{\gamma})\,, \tag{1.21}$$

where $G(x)$ is the Green's function for the d'Alembert operator.

Because of the Lorenz gauge condition, the last three terms in Equation (1.16) vanish, and finally, we get

$$\Box\bar{h}_{\mu\nu} = -\frac{16\pi G}{c^4}T_{\mu\nu}\,. \tag{1.22}$$

Equation (1.22) implies that the perturbation generated by the energy-momentum tensor propagates through the flat spacetime at the speed of light. Besides, substituting Equation (1.22) into Equation (1.17) leads to the energy and momentum conservation $\partial^{\nu} T_{\mu\nu} = 0$, i.e., the matter fields and non-gravitational radiation that produce $T_{\mu\nu}$ can exchange energy and momentum with themselves but not with the gravitational field. Physically, the dynamics of matter fields are dominated by non-gravitational fields rather than gravitational fields.

1.1.1.1. Propagation of gravitational waves in vacuum. Equation (1.22) shows how GWs are generated from the fields expressed by the energy-momentum tensor. Here, we focus on the properties of their propagation by studying the vacuum solutions of the linearized Einstein's field equations. In this case,

$$\Box \bar{h}_{\mu\nu} = 0\,. \tag{1.23}$$

To solve Equation (1.23) for $\bar{h}_{\mu\nu}$, we impose the additional constraints, $\Box \zeta_{\mu} = 0$, on the coordinate transformations in addition to the Lorenz gauge condition Equation (1.17). It follows that $\bar{h}_{\mu\nu}$ is purely spatial, traceless, and transverse:

$$h_{0\mu} = 0\,, \quad h^{i}{}_{i} = 0\,, \quad \partial^{i} h_{ij} = 0\,, \tag{1.24}$$

where the Roman indices run over the spatial components and the last two equations are due to the Lorenz gauge condition. The above condition is called *transverse-traceless* gauge, or TT gauge. Because the perturbation is now traceless, there is no difference between $\bar{h}_{\mu\nu}$ and $h_{\mu\nu}$. Importantly, the degrees of freedom in $h_{\mu\nu}$ are reduced to two from ten by imposing the above gauge condition.

Next, we present the matrix form of the surviving degrees of freedom. To do so, we assume the form of the solution in Equation (1.23) to be

$$h^{\mathrm{TT}}_{\mu\nu} = A_{\mu\nu} e^{ik^{\sigma} x_{\sigma}}\,, \tag{1.25}$$

where $k^\sigma = (\omega, \vec{k})$ is a wave vector and $A_{\mu\nu}$ is a symmetric tensor called *polarization tensor*. ω is the angular frequency of the GW with the dispersion relation of $\omega/c = |\vec{k}|$. For a plane wave propagating in the direction parallel to the wave-vector $\hat{n} = \vec{k}/|\vec{k}|$, the Lorenz-gauge condition implies $A_{\mu\nu}k^\nu = 0$, i.e., that the non-zero components of the GW are transverse to $\hat{n}$. In the special case where the GW is propagating in the z-direction, the wave solution takes the form:

$$h^{\mathrm{TT}}_{\mu\nu} = \begin{pmatrix} 0 & 0 & 0 & 0 \\ 0 & A_{11} & A_{12} & 0 \\ 0 & A_{12} & -A_{11} & 0 \\ 0 & 0 & 0 & 0 \end{pmatrix} e^{i(kz-\omega t)} . \tag{1.26}$$

We will show that A_{11} and A_{12} are the amplitudes of the 'plus' and 'cross' polarizations of the wave in TT gauge, respectively.

1.1.1.2. Slow-motion sources in linearized approximation. We now probe the wave solution in a region that includes the matter fields. In this context, we will compute the leading order contribution to the spatial components of the metric perturbation from a source whose internal matter moves slowly compared to the speed of light. In the following calculations, we use the Lorenz gauge and the energy-momentum conservation $\partial^\nu T_{\mu\nu} = 0$. Using the Green function of the d'Alembert operator that describes the field at $(ct, \vec{x})$ due to the source element at $(ct', \vec{x}')$, the solution of Equation (1.22) takes the form:

$$\bar{h}_{\mu\nu}(x^\sigma) = -\frac{16\pi G}{c^4} \int d^4x' G(x^\sigma, x'^\sigma) T_{\mu\nu}(x'^\sigma) , \tag{1.27}$$

where the Green function satisfies

$$\Box_x G(x^\sigma, x'^\sigma) = \delta^{(4)}(x^\sigma - x'^\sigma) , \tag{1.28}$$

and $\Box_x$ is the d'Alembert operator applied to the field at the point $(ct, \vec{x})$. The solution for this equation is the *retarded* Green function:

$$G(x^\sigma, x'^\sigma) = -\frac{1}{4\pi\,|\vec{x} - \vec{x}'|} \delta\left(t' - \left[t - \frac{|\vec{x} - \vec{x}'|}{c}\right]\right) . \tag{1.29}$$

Equation (1.27) becomes

$$\bar{h}_{\mu\nu} = \frac{4G}{c^4}\int d^3x' \frac{1}{|\vec{x}-\vec{x}'|} T_{\mu\nu}\left(t - \frac{|\vec{x}-\vec{x}'|}{c}, \vec{x}'\right). \tag{1.30}$$

We evaluate the perturbation $\bar{h}_{\mu\nu}$ at a distance far away from the source assuming that the radius d of the source is much smaller than the distance $r := |\vec{x}|$, i.e., $d \ll r$. In this case, we consider only the leading term in the expansion in $1/r$

$$|\vec{x}-\vec{x}'| = r - \hat{\vec{n}}\cdot\vec{x}' + O(1/r), \tag{1.31}$$

where $\hat{n} = \vec{x}/|\vec{x}|$. Assuming that the motion of the source is slow compared to the speed of light, we can replace $|\vec{x}-\vec{x}'|$ with r in the energy-momentum tensor. Equation (1.30) becomes

$$\bar{h}_{\mu\nu} = \frac{4G}{rc^4}\int d^3x' T_{\mu\nu}(t - r/c, \vec{x}'). \tag{1.32}$$

In the linearized theory, we keep only the leading order of $|\bar{h}_{\mu\nu}|$ so that the raising/lowering operator acting on $T_{\mu\nu}$ can be approximated with the Minkowski metric, leading to $T^{\mu\nu} = \eta^{\mu\rho}\eta^{\nu\sigma}T_{\rho\sigma}$.

The radiative degrees of freedom are fully contained in the spatial part of the perturbation, projected onto the transverse-traceless part. Therefore, we only focus on the spatial part T^{ij} in the following calculation. Taking a partial derivative of $\partial_\nu T^{i\nu} = 0$ with respect to x^0 and combining it with $\partial_\nu T^{0\nu} = 0$, we get

$$\partial_0\partial_0 T^{00} = \partial_k\partial_l T^{kl}. \tag{1.33}$$

Multiplying both sides by $x^i x^j$, the energy-momentum tensor becomes

$$T^{ij} = \frac{1}{2}\left[\partial_0\partial_0(T^{00}x^i x^j) - \partial_k\partial_l(T^{kl}x^i x^j) + 2\partial_k(T^{ik}x^j + T^{kj}x^i)\right]. \tag{1.34}$$

The right-hand side (RHS) of Equation (1.32) becomes

$$\begin{aligned}\frac{4\pi G}{rc^4}\int d^3x' T^{ij} &= \frac{2\pi G}{rc^4}\int d^3x' \left[\partial'_0\partial'_0(T^{00}x'^i x'^j) - \partial'_k\partial'_l(T^{kl}x'^i x'^j)\right. \\ &\qquad \left. + 2\partial'_k(T^{ik}x'^j + T^{kj}x'^i)\right] \\ &= \frac{2\pi G}{rc^4}\int d^3x' \partial'_0\partial'_0(T^{00}x'^i x'^j) \\ &= \frac{2\pi G}{rc^4}\partial_0\partial_0\int d^3x' T^{00}x'^i x'^j u\,. \end{aligned} \tag{1.35}$$

In the derivation of Equation (1.35), we have used the Gauss theorem to re-express the volume integral as the surface integral. Because the source is bounded within the radius d, the surface integrals become zero. Also, we take the time derivatives out of the integral and convert ∂'_0 to ∂_0 since $t' = t - r/c$.

Using the notation $T^{00} = \rho c^2$, where ρ is the mass density, Equation (1.32) becomes

$$\begin{aligned}\bar{h}_{ij} &= \frac{2G}{rc^4}\frac{\partial^2}{\partial t^2}\int d^3x' \rho(t - r/c, \vec{x}')x'^i x'^j \\ &= \frac{2G}{rc^4}\frac{\partial^2}{\partial t^2} I_{ij}(t - r/c)\,, \end{aligned} \tag{1.36}$$

where I_{ij} is the moment of inertia of the source defined as

$$I_{ij} = \int d^3x' \rho(t, \vec{x}')x'^i x'^j\,. \tag{1.37}$$

Because the non-vanishing components of GWs are contained in the traceless part, we take the traceless part of the inertia tensor or the quadrupole moment tensor

$$Q_{ij} := I_{ij} - \frac{1}{3}\delta_{ij} I\,, \tag{1.38}$$

where $I := I_{ii}$ is the trace of the moment of inertia. Thus, the perturbation becomes

$$\bar{h}_{ij} = \frac{2G}{rc^4}\frac{\partial^2}{\partial t^2}Q_{ij}(t - r/c)\,. \tag{1.39}$$

This equation suggests that GWs are generated by any accelerated time-varying quadrupole moment at the leading order $O(1/r)$ in the linearized theory.

1.1.2. Extraction of the Transverse-Traceless Part. Because of the gauge freedom, the perturbation $\bar{h}_{ij}$ can be further simplified by extracting only the gauge-invariant components of $\bar{h}_{ij}$. To get the gauge-invariant components, we formulate the transverse-traceless extraction approach for a generic tensor. By defining a TT projector $\Lambda_{ij}{}^{kl}$ for a generic tensor B^{kl} such as to be $B^{\rm TT}_{ij} = \Lambda_{ij}{}^{kl}B_{kl}$, the TT projector is constructed as

$$\Lambda_{ij}{}^{kl} := P_i{}^k P_j{}^l - \frac{1}{2}P_{ij}P^{kl}\,, \tag{1.40}$$

where $P_i{}^k$ is the transverse projector:

$$P_i{}^k := \delta_i{}^k - n_i n^k\,, \tag{1.41}$$

where $n^i = x^i/r$ is the unit vector. By setting the unit vector to be along the direction of the GW propagation, we get the transverse-traceless part of the metric perturbation as $h^{\rm TT}_{ij} = \Lambda_{ij}{}^{kl}\bar{h}_{kl}$. Note that vectors with identical upper and lower indices are the same in the linearized theory, i.e., $n_i = n^i$ because the raising/lowering operator is the Minkowski metric, but we keep the notation for readability.

If the GW propagates along the z direction, i.e., $\hat{n} = \hat{z}$, the transverse projector $P_j{}^k$ is a diagonal matrix, $diag(1,1,0)$. Then, the projected tensor will be in the x-y plane transverse to the z direction. Under this assumption, the transverse-traceless part of $\ddot{Q}_{ij}$, where the double dot denotes the second derivative with respect to t, is

$$\Lambda_{ij}{}^{kl}\ddot{Q}_{kl} = (P_i{}^k P_j{}^l - \frac{1}{2}P_{ij}P^{kl})\ddot{Q}_{kl} = (P\ddot{Q}P)_{ij} - \frac{1}{2}P_{ij}Tr(P\ddot{Q})\,, \tag{1.42}$$

and its matrix representation is

$$\Lambda_{ij}{}^{kl}\ddot{Q}_{kl} = \begin{pmatrix} (\ddot{Q}_{11} - \ddot{Q}_{22})/2 & \ddot{Q}_{12} & 0 \\ \ddot{Q}_{21} & -(\ddot{Q}_{11} - \ddot{Q}_{22})/2 & 0 \\ 0 & 0 & 0 \end{pmatrix}_{ij} . \tag{1.43}$$

Because of the definition of the moment of inertia in Equation (1.37), $\ddot{Q}_{ij}$ is symmetric, i.e., $\ddot{Q}_{12} = \ddot{Q}_{21}$. Applying the transverse-traceless projector to the left-hand side (LHS) of Equation (1.39) and comparing the components to the one in the RHS, we get the two degrees of freedom:

$$h_+ = \frac{G}{rc^4}(\ddot{Q}_{11} - \ddot{Q}_{22}), \tag{1.44a}$$

$$h_\times = \frac{2G}{rc^4}\ddot{Q}_{12} . \tag{1.44b}$$

The h_+ and $h_\times$ are amplitudes of polarizations perpendicular to the direction of propagation.

For a generic direction of propagation, we can use Equation (1.40) by choosing the unit vector $\hat{n}$ to be in a generic direction. In the spherical coordinates, where a direction is given by the polar angle θ and the azimuthal angle ϕ, the unit vector $\hat{n}$ is defined as

$$\hat{n} := [\sin\theta\cos\phi, \sin\theta\sin\phi, \cos\theta], \tag{1.45}$$

and the two orthogonal unit vectors are defined as

$$\hat{\vartheta} := [\cos\theta\cos\phi, \cos\theta\sin\phi, -\sin\theta], \tag{1.46a}$$

$$\hat{\varphi} := [-\sin\phi, \cos\phi, 0], \tag{1.46b}$$

where the vector $\hat{\vartheta}$ points in the direction of increasing colatitude and $\hat{\varphi}$ points in the direction of increasing longitude. Using these basis vectors, the transverse projector $P_j{}^k$ is written as

$$P_j{}^k = \vartheta_j\vartheta^k + \varphi_j\varphi^k . \tag{1.47}$$

The above equation is invariant under the rotation of the transverse vectors $\hat{\vartheta}$ and $\hat{\varphi}$ around the radial-directional unit vector $\hat{n}$ so that $P_j{}^k$ is uniquely defined. Substituting Equation (1.47) into Equation (1.40), the TT projector $\Lambda_{ij}{}^{kl}$ can be constructed for arbitrary directions of the GW propagation. Applying this TT projector to both sides of Equation (1.39), the TT part of the metric perturbation is obtained as

$$h_{ij}^{\mathrm{TT}}(t,\theta,\phi) = \frac{2G}{rc^4}\Lambda_{ij}{}^{kl}\ddot{Q}_{kl}(t-r/c)\,. \tag{1.48}$$

Once the second time derivative of the quadrupole moment evaluated at the retarded time $t - r/c$ is computed in the RHS, we obtain the GW with two polarizations perpendicular to the direction denoted with θ and ϕ in the spherical coordinates.

1.1.3. The Effect of Waves on Masses. We have presented that GWs are generated accelerated by a time-varying quadrupole moment. Here we look at the effect of GWs on masses, which is relevant to the measurement of GWs. We first consider a single isolated particle which is freely moving in the spacetime without the effect of any non-gravitational field. Because there is always a locally inertial Lorentz-invariant frame, the path of such a particle is *locally straight* everywhere. In other words, the path $x^\mu(\tau)$ of the particle, parameterized by the time τ measured by a clock moving along the path has its four-velocity $dx^\mu/d\tau$ that stays constant both in direction and magnitude. The equation the path obeys is called the *geodesic* equation, which is formulated as

$$\frac{d^2x^\mu}{d\tau^2} + \Gamma^\mu_{\alpha\beta}\frac{dx^\alpha}{d\tau}\frac{dx^\beta}{d\tau} = 0\,, \tag{1.49}$$

where $\Gamma^\mu_{\alpha\beta}$ are the Christoffel symbols defined in Equation (1.6). In the linearized theory, the coordinate time t for a particle at rest is approximately equal to τ because $|h_{\mu\nu}| \ll 1$. The four-velocity is $dx^\mu/d\tau = (c,0,0,0)$. Using Equation (1.8), the geodesic equation becomes

$$\frac{d^2x^\mu}{dt^2} = -c^2(\partial_0 h^\mu{}_0 - \frac{1}{2}\partial^\mu h_{00})\,. \tag{1.50}$$

Because of the TT-gauge condition in Equation (1.24), we get

$$\frac{d^2x^\mu}{dt^2} = 0\,. \tag{1.51}$$

Equation (1.51) is still valid for a particle slowly moving compared to the speed of light at leading order $O(h_{\mu\nu})$. We conclude that the effect of GWs on a static or slowly moving isolated particle is the same in the condition without GWs. Equation (1.51) is also valid for another particle parameterized by the time measured by a clock moving along the path.

To see the non-vanishing effect of GWs on particles, we must consider the separation $\xi^\mu(\tau)$ of a pair of particles, parameterized by the time of the first particle, where the first particle is at $x^\mu(\tau)$ and the second particle is at $x^\mu(\tau) + \xi^\mu(\tau)$ with $|\xi^\mu(\tau)|$ small compared to the GW's wavelength. The separation $\xi^\mu(\tau)$ follows the equation of *geodesic deviation* at leading order, formulated as

$$\frac{d^2\xi^\mu}{dt^2} = -R^\mu{}_{\beta\gamma\delta}\frac{dx^\beta}{d\tau}\xi^\gamma\frac{dx^\delta}{d\tau}\,, \tag{1.52}$$

where $R^\mu{}_{\beta\gamma\delta}$ is the Riemann tensor defined in Equation (1.5). The non-vanishing Riemann tensor can be shown to be $R^\mu{}_{0\gamma0} = -\partial_0\partial_0 h^\mu{}_\gamma/2$. Equation (1.52) becomes

$$\frac{d^2\xi^\mu}{dt^2} = \frac{1}{2}\xi^\gamma\frac{\partial^2}{\partial t^2}h_{\mathrm{TT}}{}^\mu{}_\gamma\,. \tag{1.53}$$

Because the gauge-invariant part of the metric perturbation is fully contained in the TT part h_{ij}^{TT}, the solution of the above equation at leading order is

$$\xi^j(t) = \xi^j(0) + \frac{1}{2}h^{jk}_{\mathrm{TT}}\xi_k(0)\,, \tag{1.54}$$

where $\xi_j(0)$ is the initial separation at $t = 0$.

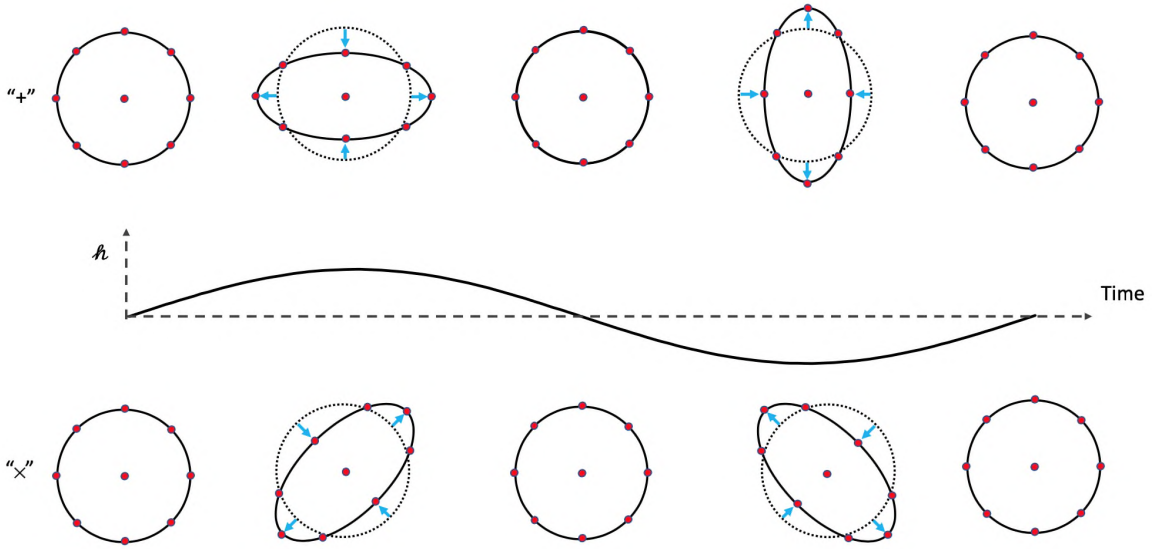

Figure 1.1. The effect of the two polarizations of a GW on a set of test masses arranged as a ring shape in a plane perpendicular to the direction of the GW propagation.

Equation (1.54) can be further simplified. Choosing the TT-gauge and assuming that the GW propagates in the z direction, only non-vanishing components of ξ^j are in the x^1 and x^2 directions. By renaming $A_{11} = h_+$ and $A_{12} = h_\times$ in Equation (6), $\xi^j(t)$ can be written as $\xi^j(t) = \xi^j(0) + \xi^j_+(t) + \xi^j_\times(t)$, where

$$\xi^1_+(t) := \frac{1}{2}h_+ e^{i(kz-\omega t)}\xi^1(0), \quad \xi^2_+(t) := -\frac{1}{2}h_+ e^{i(kz-\omega t)}\xi^2(0), \tag{1.55a}$$

$$\xi^1_\times(t) := \frac{1}{2}h_\times e^{i(kz-\omega t)}\xi^2(0), \quad \xi^2_\times(t) := \frac{1}{2}h_\times e^{i(kz-\omega t)}\xi^1(0). \tag{1.55b}$$

where k is the z-component of the wave vector and ω is the angular frequency of the wave. Thus, the length of the separation of a pair of particles expands and squeezes periodically over time due to two polarizations of GWs as shown in Figure 1.1.

1.1.4. Gravitational-Wave Sources. In the previous section, we have seen that the amplitude of a GW is proportional to the second time-derivative of the quadrupole moment in Equation (1.39). Physically, this implies that any accelerating bodies can generate a GW.

As a simple toy model following Saulson (1994), we consider a dumbbell which has two masses with each mass of M connected by a massless rod with a length of $2l_o$ orbiting with a frequency of f_o in the x-y plane. After calculating the quadrupole moment of the dumbbell and substituting it into Equation (1.44a), the cross and plus polarizations are obtained as

$$h_+ = \frac{32\pi^2 G}{rc^4} M l^2 f_o^2 \cos\{2(2\pi f_o)t\}\,, \tag{1.56a}$$

$$h_\times = -\frac{32\pi^2 G}{rc^4} M l^2 f_o^2 \sin\{2(2\pi f_o)t\}\,. \tag{1.56b}$$

These equations imply that the amplitude of the GW is proportional to the mass and the square of the orbital frequency of the source. Also, the amplitude is inversely proportional to the distance of the observer from the source. Heavier and faster-orbiting dumbbells produce louder amplitudes of the waves. As an analogy to astrophysical objects, let us calculate the amplitude of a GW produced by a dumbbell consisting of masses with $M = 1$ ton connected by a massless rod with 2-meter long in a lab, spinning at a frequency of $f_o = 1$ kHz around its middle. We find the amplitude of the GWs to be $h \sim 10^{-33} \times \frac{1}{r}$. To observe the metric perturbation as a GW in the linearized theory, the distance from the observer to the source needs to be equal to or larger than the GW wavelength. Accounting for this fact, the observer should be separated by the dumbbell at least by 300 km in this example. At this distance, the amplitude is given as $h \sim 10^{-39}$. Larger amplitudes can be achieved with more massive sources. Similar to the dumbbell example discussed above, a pair of massive stars such as black holes or neutron stars, orbit around each other and shrink their separation by losing the angular momentum as GW radiation, and then merge into a single object. For example, a pair of neutron stars with a mass of $M \sim 10^{30}$ kg with an orbital frequency of 30 Hz reduces its separation from $\sim$ 350 km to $\sim$ 60 km within 1 minute (Abbott *et al.*, 2017e). Let us consider a merging binary system of compact stars with a mass of $M \sim 10^{30}$ kg, separated by $\sim$ 60 km, orbiting at an orbital frequency of $f_o = 400$ Hz, and located in the Virgo Cluster, at $r \sim 15$ Mpc. The amplitude of GWs

would be $h \sim 10^{-21}$. The existence of binary systems of compact stars that emit GW was supported by the discovery of the first binary pulsar named PSR 1913+16 by Hulse and Taylor (1975). The orbital frequency of this binary pulsar gradually reduces over time by emitting GWs. The observation of the orbital frequency evolution matches the prediction based on general relativity with an accuracy of $\sim 1\%$. Following the indirect measurement of GWs, the ground-based GW detectors detected GWs from a binary black hole merger in 2015 (Abbott *et al.*, 2016e) and then made about 50 confident detections (Abbott *et al.*, 2019d, 2021b). There are other GW sources in addition to binary mergers. We discuss the four major types of astronomical GW sources categorized based on their waveforms.

1.1.4.1. Compact binary coalescing stars. GW signals produced from compact binary coalescing objects have amplitude at $\sim 100 - 1000$ Hz at the end of the inspiral period, where the ground-based GW detectors are tuned to be most sensitive. This type of signal is well modeled compared to any other category. As the separation becomes smaller, the orbital frequency and the amplitude of GW increases. Finally, the two objects merge into a single massive object. The mass of the final object is related to the peak frequency and the observable length of the signal: GWs from lighter stars such as neutron stars have a peak frequency of ~ 1000 Hz and last about 1 minute in the most sensitive LIGO frequency band; the signal from a pair of stellar-mass black holes have a typical peak frequency of ~ 100 Hz and last about a few hundred milliseconds. Among others, probing these types of sources allows us to understand the age of the universe through the Hubble constant estimate (Abbott *et al.*, 2021a) and verify the validity of general relativity (Abbott *et al.*, 2021c).

1.1.4.2. Continuous GWs. Continuous GWs are expected to be emitted for a long time period at a nearly fixed frequency. One of the expected sources for this type of GWs is a single rapidly spinning neutron star with a rotational frequency of ~ 100 Hz. Because of its internal strong magnetic field, the neutron star could have a 'bump' of size ~ 10 centimeters and non-axisymmetric quadrupole moment. The spinning rate of such neutron

stars gradually slows down by emitting GWs. Because spinning neutron stars with a small bump have smaller quadrupole moments compared to compact binary coalescing stars, they produce GWs with smaller amplitude. Therefore, scientists have developed techniques that accumulate the SNR over a long stretch of data. Detecting this type of GWs will allow us to understand the equation of state in neutron stars (Abbott *et al.*, 2019a).

1.1.4.3. Stochastic background GWs. A superposition of many different GW events such as unresolved low SNR binary black hole mergers, cosmic strings, and GWs produced as early as $\sim 10^{-30}$ seconds after the Big Bang is expected to produce a stochastic background of GWs (Abbott *et al.*, 2016a). Because GWs interact weakly with matter, observing this type of GWs potentially allows us to understand the physics dominated at the beginning of the universe, which can not be achieved with the electromagnetic (EM) observations. These signals are expected to be stationary, anisotropic in the sky, and unpolarized.

1.1.4.4. Burst GWs. Burst GWs are signals lasting from a fraction of a second to $\sim$ 500 seconds with unknown waveforms or signals from unknown or unanticipated sources. The expected sources include core-collapse supernovae (CCSN) (Abbott *et al.*, 2016b; Burrows *et al.*, 1995; Couch and Ott, 2015; Herant, 1995; Ott, 2009) and long gamma-ray bursts (Abbott *et al.*, 2019e, 2020b; Modjaz, 2011) that have a complicated mechanism for generating GWs. Hence, predicting their theoretical waveforms is difficult. Detection of burst GWs uses excess power and cross-correlation methods that do not rely on known waveforms (Abbott *et al.*, 2019b; Klimenko *et al.*, 2016; Lynch *et al.*, 2017; Sutton *et al.*, 2010). Despite the detection efficiency lower than that for compact binary coalescence (CBC) signals, burst GW events would allow us to discover new physics.

1.2. GRAVITATIONAL DETECTORS

Any accelerating massive object produces GWs. As seen in the previous section, there are various types of astrophysical sources that can generate potentially detectable GWs by ground-based detectors. We first discuss the Michelson interferometer as a GW detector and how it measures GWs from arbitrary directions in the sky. Then, we discuss the modern techniques involved in the detectors to enhance their sensitivities to detect GW signals with amplitude of $h \sim 10^{-21}$ in the condition having various instrumental and environmental noise disturbances.

1.2.1. Michelson Interferometer. Michelson and Morley (1887) experimented to prove the existence of a hypothetical *wind* for light, or 'aether' in the space using an interferometer. The Michelson-Morley interferometer consisted of an input light injected into a beam splitter and two identical perpendicular arms to measure the interference of the light bounced back from the mirrors at the end of each arm. If aether existed, the light travel time in one arm is expected to be longer than the time in the other arm, leading to the relative phase shift would be measured as interference fringes. The Michelson-Morley did not show any evidence of the existence of aether. Laser Interferometer Gravitational-wave Observatory (LIGO) interferometers located in Livingston, Louisiana and Hanford, Washington, USA (Aasi *et al.*, 2015) uses the concept of a Michelson-Morley interferometer to detect GWs.

1.2.2. Interferometer as a GW Detector and Antenna Pattern. GWs stretch and squeeze the space perpendicularly to their direction of propagation as seen in Equation (1.54). When GWs pass through the interferometer, the distance between the beam splitter and the mirrors at the end of each arm varies. The phase difference of the laser at the beam splitter after bouncing back in each arm is

$$\Delta\Phi = \frac{2\pi}{\lambda}(2L_1 - 2L_2), \tag{1.57}$$

where λ is the GW wavelength, and L_1 and L_2 are the arm lengths. To calculate the variation of the interferometer's arm lengths in the presence of a GW, we choose a coordinate system S adapted to the detector in which the two orthogonal unit vectors $\hat{e}_x$ and $\hat{e}_y$ are aligned to each arm, as seen in Figure 1.2. Assuming the GW wavelength to be much longer than the arm lengths, i.e., $L_1, L_2 \ll \lambda$, the separation vectors between the beam splitter and the mirrors in the arms are obtained from Equation (1.54) as

$$\xi_x^j = L_o(e_x^j + \frac{1}{2}h_{jk}^{\mathrm{TT}} e_x^k), \tag{1.58a}$$

$$\xi_y^j = L_o(e_y^j + \frac{1}{2}h_{jk}^{\mathrm{TT}} e_y^k), \tag{1.58b}$$

where L_o is the length of each arm when the GW is absent. The arm lengths are obtained by projecting the separation vector onto the unit vectors, i.e., taking the inner product with the unit vectors as

$$L_1 = \xi_x^j e_x^j = L_o(1 + \frac{1}{2}h_{jk}^{\mathrm{TT}} e_x^j e_x^k), \tag{1.59a}$$

$$L_2 = \xi_y^j e_x^j = L_o(1 + \frac{1}{2}h_{jk}^{\mathrm{TT}} e_y^j e_y^k). \tag{1.59b}$$

Substituting Equation (1.59) into Equation (1.57), the phase difference becomes

$$\Delta\Phi = \frac{4\pi}{\lambda}\frac{1}{2}(e_x^j e_x^k - e_y^j e_y^k)h_{jk}^{\mathrm{TT}}. \tag{1.60}$$

By rewriting $\Delta\Phi = (4\pi/\lambda)h$, h is defined as $h(t) := \frac{1}{2}(e_x^j e_x^k - e_y^j e_y^k)h_{jk}^{\mathrm{TT}}$. It is convenient to define $h(t)$ in terms of the detector antenna response factors F_+ and $F_\times$ as

$$h(t) := h'_+ F_+(\theta, \phi) + h'_\times F_\times(\theta, \phi). \tag{1.61}$$

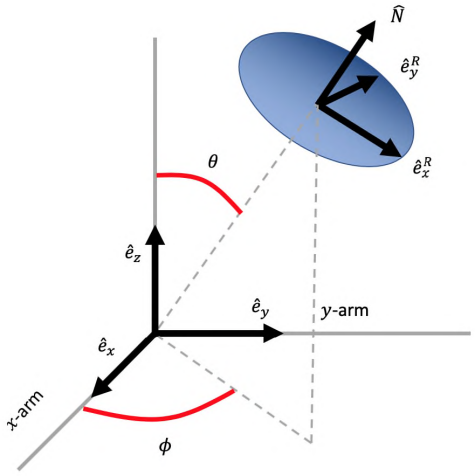

Figure 1.2. Geometric representation of the transformation from the source frame S' to the detector frame S described in Equation (1.63).

The antenna factors F_+ and $F_\times$ represent the projection of the relative lengths between the arms due to the GW propagating from the direction (θ, ϕ) in the detector frame S. We will discuss F_+ and $F_\times$ in more detail later in Equation (1.61). By choosing the basis vector to be $\hat{e}_x = (1,0,0)$ and $\hat{e}_y = (0,1,0)$, Equation (1.61) becomes $h = (h_{11}^{\mathrm{TT}} - h_{22}^{\mathrm{TT}})/2$ in the frame S. We can relate the two terms to the simpler expression of the GW polarizations:

$$h_{ij}^{\prime\mathrm{TT}} = \begin{pmatrix} h'_+ & h'_\times & 0 \\ h'_\times & -h'_+ & 0 \\ 0 & 0 & 0 \end{pmatrix}_{ij} , \tag{1.62}$$

by defining the source frame S' such that the unit vector $-\hat{N}$ points to the direction of the wave propagation and the two transverse vectors $\hat{e}_x^{\mathrm{R}}, \hat{e}_y^{\mathrm{R}}$ are in the plane orthogonal to $\hat{N}$, as shown in Figure 1.2. The relation is given as

$$h_{ij}^{\mathrm{TT}} = R_i{}^k R_j{}^l h_{kl}^{\prime\mathrm{TT}} , \tag{1.63}$$

where

$$R = \begin{pmatrix} \cos\phi & \sin\phi & 0 \\ -\sin\phi & \cos\phi & 0 \\ 0 & 0 & 1 \end{pmatrix} \begin{pmatrix} \cos\theta & 0 & \sin\theta \\ 0 & 1 & 0 \\ -\sin\theta & 0 & \cos\theta \end{pmatrix} \tag{1.64}$$

is an operator that rotates around the $\hat{e}_y^R$ with $-\theta$ and then rotates around the new z-axis with $-\phi$. Substituting Equations (1.62) and (1.64) into Equation (1.63), we obtain

$$h_{11}^{\mathrm{TT}} = h'_+(\cos^2\theta\cos^2\phi - \sin^2\phi) + 2h'_\times(\cos\theta\cos\phi\sin\phi)\,, \tag{1.65a}$$

$$h_{22}^{\mathrm{TT}} = h'_+(\cos^2\theta\sin^2\phi - \cos^2\phi) - 2h_\times(\cos\theta\cos\phi\sin\phi)\,. \tag{1.65b}$$

Therefore, Equation (1.61) becomes

$$h(t) = h_+\frac{1}{2}(1+\cos^2\theta)\cos 2\phi + h_\times(\cos\theta\sin 2\phi)\,. \tag{1.66}$$

Equations (1.61) and (1.66) imply

$$F_+ = \frac{1}{2}(1+\cos^2\theta)\cos 2\phi\,, \tag{1.67a}$$

$$F_\times = \cos\theta\sin 2\phi\,. \tag{1.67b}$$

Figure 1.3 shows the antenna response factors where the detector arms are aligned to the x- and y-directions, respectively. The detector has the maximum response for incoming GWs in the direction orthogonal to the detector plane. The detector has four blind spots at $\theta = \pi/2, \phi = \pm\pi/4$ or $\phi = \pm 3\pi/4$ where the GW causes no relative length difference between the two arms.

Except for the four blind spots mentioned above, the detector is sensitive to GWs coming from any direction. Therefore, the detector can observe the entire sky without pointing in a particular direction. However, this comes at the cost of directional dependency of the sensitivity.

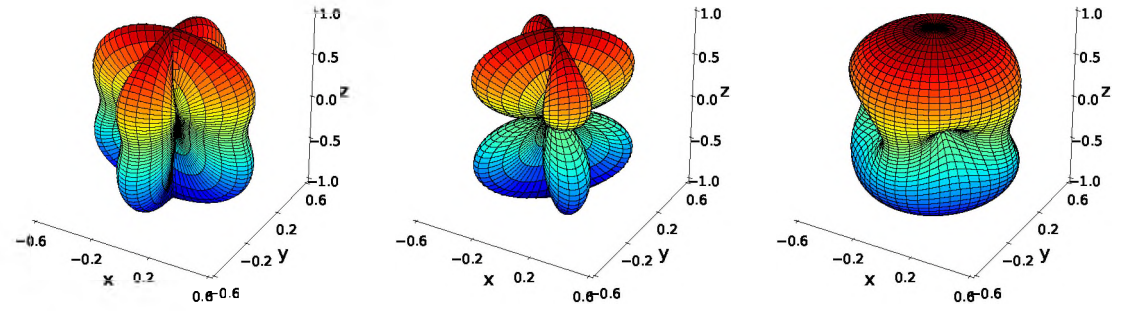

Figure 1.3. Antenna response patterns F_+ (left), $F_\times$ (middle), and the quadrature sum $(F_+^2 + F_\times^2)^{1/2}$ (right) for an interferometer with the two arms aligned to x- and y-axis. The absolute value of the antenna response is shown as the radius with given values of polar and azimuthal angles in the spherical coordinates. The colors are shown for visibility.

1.2.3. Modern Ground-Based GW Detectors. Having multiple GW detectors is useful to increase the observable sky area which may cover blind spots of a detector and useful for triangulation and the sky localization of sources. Currently, the global network of ground-based GW detectors consists of two identical LIGO interferometers with 4-kilometer arm length, located in Livingston, Louisiana, and Hanford, Washington, USA (Aasi *et al.*, 2015), operated together with the 3-kilometer arm-length Virgo detector (Acernese *et al.*, 2015) in Pisa, Italy. After the end of the third observation run in 2019-2020, the 3-kilometer arm length interferometer KAGRA (Akutsu *et al.*, 2020) consisting of a cryogenically cooling system mounted in the interferometer under the ground in Gifu, Japan joined the global network. The 600-meter long detector called GEO (Luck *et al.*, 2010) is located in Hannover, Germany. Another identical LIGO detector in India is under construction and expected to join in 2025 (Iyer *et al.*, 2011).

To detect the small-amplitude $h \sim 10^{21}$ of GWs, corresponding $\sim 10^{-18}$ meters in the kilometer-scale GW interferometers, GW detectors use various techniques in addition to the configuration of a Michelson interferometer.

The LIGO detectors have several modifications from the configuration of a Michelson interferometer including 1) a partially transmissive cavity called *power-recycling* cavity located in the input port to resonantly buildup the laser power from 20 Watts to 700 Watts (Abbott *et al.*, 2016e); 2) a Fabry-Perot cavity in each arm made by two test mass mirrors to further increase the power to 100 kilowatts, resulting in an increase of the effect of GWs by a factor of ~ 300 (Bond *et al.*, 2016); and 3) a signal-recycling cavity at the output port to improve the extraction of GWs in the frequency range of interest (Meers, 1988). Since the first half of the third observation run (O3a), LIGO and Virgo began using a technique so-called "quantum squeezer" located between and the signal recycling cavity and the photodetector at the end of the interferometer to reduce the "quantum noise" coupled with the laser (Abadie *et al.*, 2011; Schnabel *et al.*, 2010; Yu *et al.*, 2020). The quantum noise is caused by 1) the statistical fluctuations in the arrival time of photons at the photodetector at the end of the interferometer and 2) the fluctuations in the photon flux to push the mirror. The quantum squeezer improves the detectable distance for hypothetical binary neutron stars (BNSs) by $\sim 15\%$ by tuning the fluctuations in the arrival time and the intensity of the photons created from the vacuum coupled with the laser (Tse *et al.*, 2019). Figure 1.4 shows the schematic layout of the LIGO detector configuration.

1.2.4. Interferometer Noise. The main factor of the sensitivity of GW detectors is determined by the physics related to their design, the laser light, the mirror coatings, and the optic suspension systems (Aasi *et al.*, 2015). Above ~ 1000 Hz, the fluctuations of the photon arrival time, or *shot noise* at the output-port photodiode or harmonic couplings of fibers in the optic suspensions dominate the detector noise budget. In the frequency range of $100 - 1000$ Hz, the fluctuating laser intensity in the arm cavities and the thermal fluctuations of the mirror coatings are major noise sources. At low frequencies below ~ 100 Hz, the dominating noise sources are due to the residual gas molecules in the vacuum system and environmental disturbances such as wind and earthquakes shaking the buildings (Abbott *et al.*, 2017a).

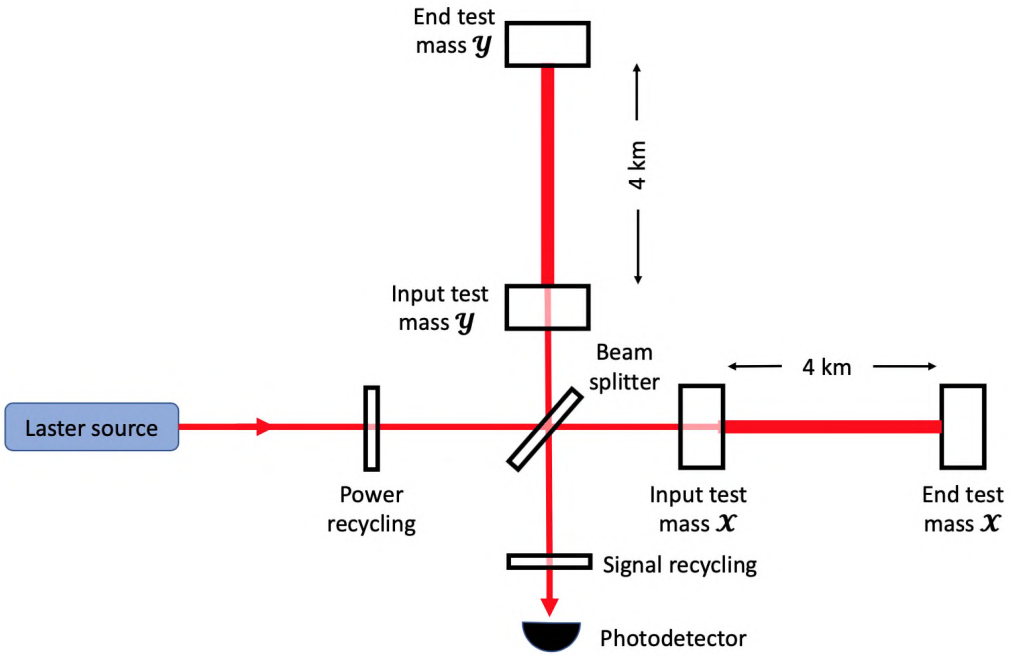

Figure 1.4. Schematic diagram of a 4-kilometer arm-length LIGO detector with three resonance cavities: the power-recycling cavity at the input port, a Fabry-Perot cavity in each arm, and a signal recycling cavity at the output port. The relative arm length difference induced by a GW is measured with the photodetector at the end port.

GW detectors use numerous subsystems including optic alignment systems and mitigation of seismic disturbances. For instance, the misalignment of the laser beam pointing at the test mass mirrors due to vibrations of the laser cooling system cause broadband noise, or *jitter* noise, in the frequency band $\sim 100 - 1000$ Hz. By studying auxiliary sensors/control-systems monitoring instrumental and environmental disturbances, the physical couplings among instruments or environmental-noise sources can be understood or statistical couplings among the noise recorded in these sensors/control-systems and the detector's output readout can be found. As a result, the noise in the detector's output readout can be mitigated. By finding the linearly coupled witness sensor with the detector's output, the *jitter* noise can be subtracted (Davis *et al.*, 2019). The noise sources discussed above typically last longer than ~ 4 seconds.

Other than the noise sources discussed above, excess-power transient noise artifacts, *glitches* with a duration of $\sim 0.01 \sim 1$ seconds impact the quality of the detector data and the detection of astrophysical GW signals. Because glitches are the product of short-lived linear and non-linear couplings of interrelated instruments, identifying their causes and modeling their noise couplings are typically difficult. In particular, unmodeled GW search pipelines are susceptible to the presence of glitches. Therefore, scientists veto periods of data containing glitches with known causes or statistically verified to be of terrestrial origin. For CBC searches, the significance of GW signal candidates detected with a single GW detector is reduced using the probability of the presence of glitches estimated with the data from auxiliary sensors/control-systems (Biswas *et al.*, 2013) to reduce the false identification of GW signals. The Bayesian inference method to model a signal and glitches is available for a signal from the CBC sources (Chatziioannou *et al.*, 2021; Cornish, 2021).

1.3. NOTORIOUS GLITCHES

As mentioned in the previous section, glitches are present in the detector's output readout and adversely affect the detections of astrophysical signals. We briefly discuss what kinds of glitches exist. Also, we discuss the characteristic frequencies and SNRs of three glitch classes mainly focused on in this dissertation.

In O3a with the calendar time period of $\sim$ 183 days, the duty cycle factors of each detector are 71%, 76%, and 76% for the LIGO-Hanford (H1), LIGO-Livingston (L1), and Virgo detectors, respectively (Abbott *et al.*, 2021b). According to glitches with SNR above 7.5 in the glitch database created by a machine-learning classification algorithm called *Gravity Spy* (Zevin *et al.*, 2017), each detector had about 1 glitch per 2 minutes during their observing times. Figure 1.5 shows the total number of events of 24 different glitch classes from three detectors during O3a. A class of glitches called *Scattered light* was the most frequently observed with $\sim$ 14% out of all 24 glitch classes and have a peak frequency of $\sim$ 30 Hz with SNR of $\sim$ 17 on average, where the peak frequency is the frequency of a pixel

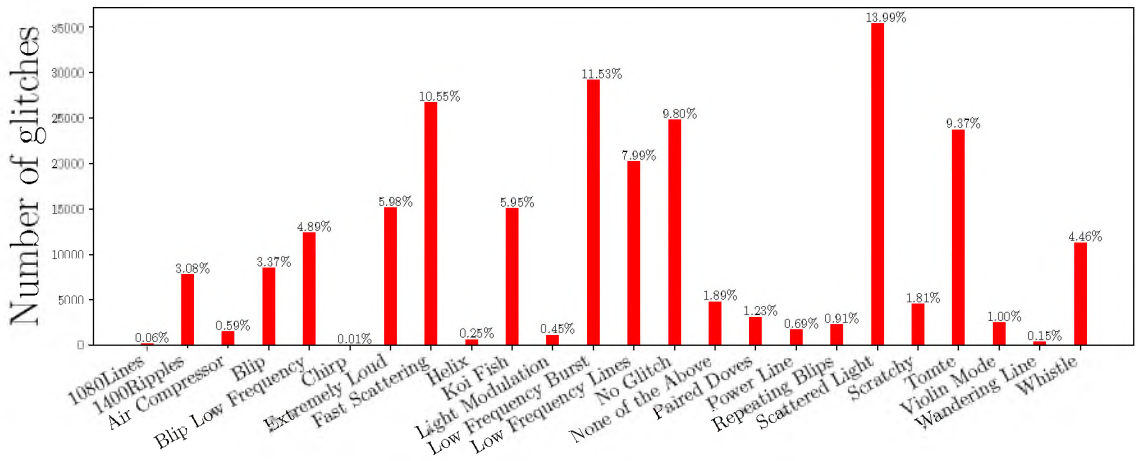

Figure 1.5. Number of glitches with SNR above 7.5 in O3a. The Gravity Spy (Zevin *et al.*, 2017) data set for the LIGO-L1, LIGO-H1 and Virgo detectors is used.

with the highest energy in the time-frequency representation using Q-transform (Robinet *et al.*, 2020). The second most frequently observed glitch class is called *Low frequency burst* with a peak frequency of $\sim$ 18 Hz and SNR of $\sim$ 19 on average. *Low frequency burst* glitches are typically eliminated with a high-pass filter at 20 Hz applied to the data in searches for GW signals.

Besides *Scattered light* glitches, another glitch class called *Extremely loud* also adversely affect GW searches because they have extremely high SNRs with SNR $\sim$ 1500 on average, and the power is distributed widely in bandwidth from 2 - 2048 Hz with the peak frequency is at 110 Hz on average, where the detector is most sensitive. *Scattered light* and *Extremely loud* glitches typically have witness channels so that scientists can veto time periods where these glitches are present. However, there are glitches with no witnesses. for example, *Blip* glitches. *Blip* glitches generally last $\sim$ 0.2 seconds and have a peak frequency of $\sim$ 220 Hz.

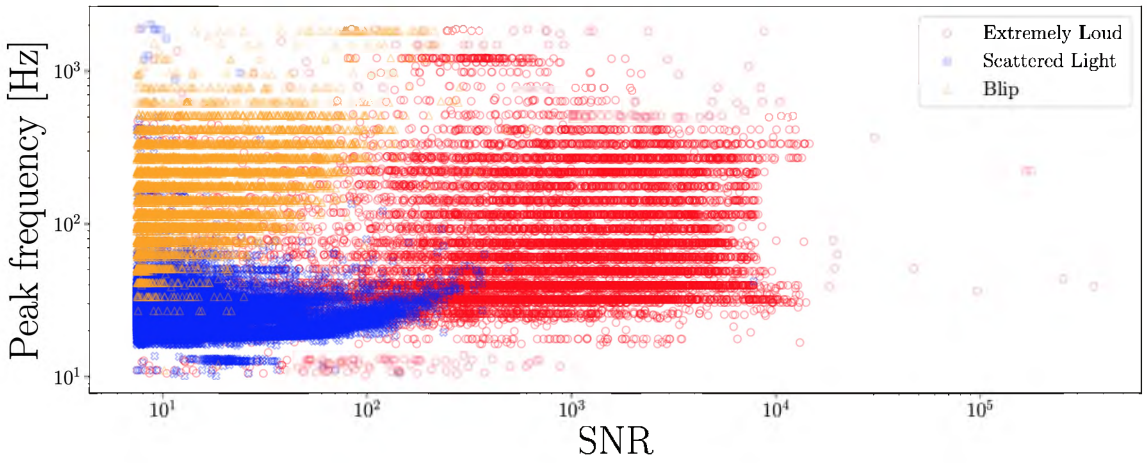

Figure 1.6. Distributions of peak frequency and SNR about three notorious glitch classes with SNR above 7.5. The Gravity Spy (Zevin *et al.*, 2017) data set for the LIGO-L1, LIGO-H1 and Virgo detectors in O3a is used.

Figure 1.6 shows the distributions of SNRs and peak frequencies about three major notorious glitch classes discussed above. Figure 1.7 shows the time-frequency representations of these three classes of glitches. In this dissertation, we mainly focus on *Scattered light*, *Extremely loud*, and *Blip* glitches.

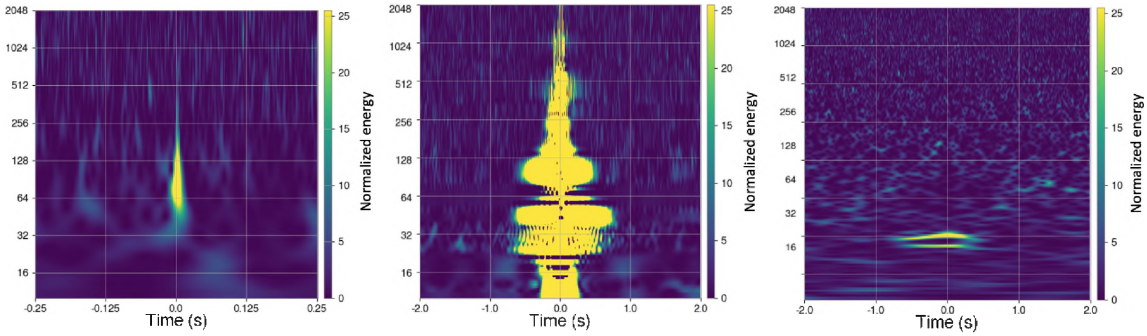

Figure 1.7. Time-frequency representations of three notorious glitch classes. Time-frequency representations of *Blip* (left), *Extremely loud* (middle), and *Scattered light* (right) glitches are created using the Q-transform (Robinet *et al.*, 2020).

1.4. DETECTION PIPELINES FOR GRAVITATIONAL WAVES

Assuming the noise in the detector's output readout is stationary and Gaussian and there are no couplings between the noise and a signal, the detector's output data stream when a signal is present can be expressed as

$$s(t) = h(\vec{\lambda}; t) + n(t), \tag{1.68}$$

where $h(\vec{\lambda}; t)$ is the time series of a signal with a set of parameters $\vec{\lambda}$ depending on a source and an observer (e.g., masses, spins, the direction of the source and the source orientation, peak time, polarization angle, etc) and $n(t)$ is the time series of noise. The ensemble average of the noise time series is

$$< n(t) >= \lim_{N\to\infty} \frac{1}{N} \sum_{i=1}^{N} n^{(i)}(t) = 0, \tag{1.69}$$

where $n^{(i)}(t)$ is a realization of the noise at the time t and N is the total number of different noise realizations. The ensemble average of the Fourier transform $\tilde{n}(f)$ is

$$\langle \tilde{n}(f) \rangle = \left\langle \int_{-\infty}^{\infty} n(t) e^{-2\pi i f t} \right\rangle = \int_{-\infty}^{\infty} \langle n(t) \rangle \, e^{-2\pi i f t} = 0, \tag{1.70}$$

because $e^{-2\pi i f t}$ is the same for all noise realizations. According to the Wiener-Khinchine theorem (Kittel, 2004), the covariance of the noise is related to its one-sided power spectral density (PSD) $S_n(|f|)$ (Finn, 1992) as

$$\langle n(f) \tilde{n}^*(f') \rangle = \frac{1}{2} S_n(|f|) \delta(f - f'), \tag{1.71}$$

where $S_n(|f|)$ is a real non-zero even function and $\delta(f - f')$ is the Dirac delta function. The probability density of obtaining the data in the presence of a signal (Finn, 1992) is

$$p(s|0) = C \exp\left[-\frac{1}{2}(\tilde{n}|\tilde{n})\right], \tag{1.72}$$

where C is a normalization constant which depends only on the noise PSD and the inner product $(\cdot|\cdot)$ is defined (Brown, 2004; Finn, 1992) as

$$(\tilde{a}|\tilde{b}) = \int_{-\infty}^{\infty} df \frac{\tilde{a}^*(f)\tilde{b}(f) + \tilde{a}(f)\tilde{b}^*(f)}{S_n(|f|)}, \tag{1.73}$$

where $\tilde{a}$ and $\tilde{b}$ are the Fourier transform of the time series $a(t)$ and $b(t)$, respectively. If $a(t)$ and $b(t)$ are real, Equation (1.73) can be written as

$$(\tilde{a}|\tilde{b}) = 2\int_{-\infty}^{\infty} df \frac{\tilde{a}^*(f)\tilde{b}(f)}{S_n(|f|)}, \tag{1.74}$$

where Appendix E shows details of the derivation. The probability density of obtaining the data when a signal is present is

$$p(s|h) = C \exp\left[-\frac{1}{2}(\tilde{s} - \tilde{h}|\tilde{s} - \tilde{h})\right]. \tag{1.75}$$

Hence, the likelihood ratio is given as

$$\Lambda := \frac{p(s|h)}{p(s|0)} = \frac{e^{-(\tilde{s}-\tilde{h}|\tilde{s}-\tilde{h})/2}}{e^{-(\tilde{s}|\tilde{s})/2}}, \tag{1.76}$$

and the log-likelihood ratio is written as

$$\ln \Lambda = (\tilde{s}|\tilde{h}) - \frac{1}{2}(\tilde{h}|\tilde{h}) \ . \tag{1.77}$$

Detecting GW signals, there are two classes of errors, namely, false alarm and false dismissal. The false alarm is to identify the noise as a signal while the false dismissal is to identify a signal as the noise. According to the Neyman-Pearson criterion (Neyman and Pearson, 1933), the likelihood ratio in Equation (1.76) should be maximized for a given rate of false alarms to reduce the false dismissal.

1.4.1. Matched-filter Pipeline. The matched-filter technique is the optimal linear filter to search for a signal when signals are theoretically modeled in priori. In particular, the matched-filter technique has been used to search for CBC signals by maximizing the likelihood ratio over the constant amplitude scaling factor, merger time, and coalescence phase analytically, as well as over the other parameters such as masses and spins using a template bank. We present a brief introduction about this technique based on (Allen, 2005; Brown, 2004; Finn, 1992).

Suppose we know the waveform of a signal in priori except a constant amplitude scaling factor A_0 such that $h = A_0\hat{h}$, Equation (1.77) becomes

$$\ln \Lambda = A_0(\tilde{s}|\tilde{\hat{h}}) - \frac{1}{2}A_0^2(\tilde{\hat{h}}|\tilde{\hat{h}})\,. \tag{1.78}$$

We want to maximize the likelihood ratio (equivalently log-likelihood ratio) with respect to A_0. The log-likelihood ratio is maximized in the condition $\partial \ln \Lambda/\partial A_0 = 0$. The maximized log-likelihood ratio is given as

$$\ln \Lambda|_{\max} = \frac{(\tilde{s}|\tilde{\hat{h}})^2}{2(\tilde{\hat{h}}|\tilde{\hat{h}})} \quad \text{at} \quad A_0 = \frac{(\tilde{s}|\tilde{\hat{h}})}{(\tilde{\hat{h}}|\tilde{\hat{h}})}\,. \tag{1.79}$$

We show the physical meaning of $\ln \Lambda|_{\max}$ in Equation (1.79) by considering the cross-correlation between a linear filter $Q(t)$ and the data containing a signal:

$$h(t) = A_0\hat{h}(t - t_0)\,, \tag{1.80}$$

where t_0 is the merger time. We have explicitly showed the merger time in Equation (1.80). However, we typically do not know the merger time before applying the filter $Q(t)$ to the data. We will discuss this point later.

We want to find the optimal linear filter $Q(t)$ to search for a signal from the data using the zero-lag cross-correlation:

$$\begin{aligned} z(t_0) &= \int_{-\infty}^{\infty} dt Q(t) s(t), \\ &= \int_{-\infty}^{\infty} dt \int_{-\infty}^{\infty} df \tilde{Q}(f) e^{2\pi i f t} \int_{-\infty}^{\infty} df' \tilde{s}(f'), \\ &= \int_{-\infty}^{\infty} df \int_{-\infty}^{\infty} df' \tilde{Q}(f) \tilde{s}(f') \int_{-\infty}^{\infty} dt e^{2\pi i t (f+f')}, \\ &= \int_{-\infty}^{\infty} df \tilde{Q}(f) \tilde{s}(-f), \\ &= \int_{-\infty}^{\infty} df \tilde{Q}^*(f) \tilde{s}(f), \\ &= (\tilde{Q} S_n, \tilde{s})/2 . \end{aligned} \tag{1.81}$$

The ensemble average of z is

$$\begin{aligned} \langle z \rangle &= (\tilde{Q} S_n, \langle \tilde{n} \rangle + \tilde{h})/2, \\ &= (\tilde{Q} S_n, \tilde{h})/2, \\ &= (\tilde{Q} S_n, A_0 \tilde{\tilde{h}} e^{-2\pi i f t})/2 . \end{aligned} \tag{1.82}$$

Let us consider the first term $\langle z^2 \rangle$ of the variance of $z = \langle z^2 \rangle - \langle z \rangle^2$:

$$\begin{aligned} \langle z^2 \rangle &= \left\langle \int_{-\infty}^{\infty} df \int_{-\infty}^{\infty} df' \tilde{Q}^*(f) \tilde{Q}^*(f') \left[\tilde{n}(f) + \tilde{h}(f) \right] \left[\tilde{n}(f') + \tilde{h}(f') \right] \right\rangle , \\ &= \int_{-\infty}^{\infty} df \int_{-\infty}^{\infty} df' \tilde{Q}^*(f) \tilde{Q}^*(f') \left[\langle \tilde{n}(f) \tilde{n}(f') \rangle + \tilde{h}^*(f) \tilde{h}^*(f') \right] , \\ &= (\tilde{Q} S_n, \tilde{Q} S_n)/4 + (\tilde{Q} S_n, \tilde{h})^2/4 . \end{aligned} \tag{1.83}$$

Hence, the variance of z is

$$\left\langle z^2 \right\rangle - \langle z \rangle^2 = (\tilde{Q}S_n, \tilde{Q}S_n)/4\,. \tag{1.84}$$

The optimal choice of the linear filter Q is obtained by maximizing the ratio of the *expected* value of z to the standard deviation of z with respect to Q, equivalently maximizing the square of the ratio. According to the variation principle:

$$\begin{aligned}
0 &= \delta\left[\frac{\langle z \rangle^2}{\left\langle z^2 \right\rangle - \langle z \rangle^2}\right]_Q, \\
&= \delta\left[\frac{(\tilde{Q}S_n, \tilde{h})^2}{(\tilde{Q}S_n, \tilde{Q}S_n)}\right]_Q, \\
&= \frac{2(\tilde{Q}S_n, \tilde{h})(\delta\tilde{Q}S_n, \tilde{h})(\tilde{Q}S_n, \tilde{Q}S_n) - 2(\tilde{Q}S_n, \tilde{h})^2(\delta\tilde{Q}S_n, \tilde{Q}S_n)}{(\tilde{Q}S_n, \tilde{Q}S_n)^2}, \\
&= (\delta\tilde{Q}S_n, \tilde{h})(\tilde{Q}S_n, \tilde{Q}S_n) - (\tilde{Q}S_n, \tilde{h})(\delta\tilde{Q}S_n, \tilde{Q}S_n), \\
&= (\delta\tilde{Q}S_n, (\tilde{Q}S_n, \tilde{Q}S_n)\tilde{h} - (\tilde{Q}S_n, \tilde{h})\tilde{Q}S_n)\,.
\end{aligned} \tag{1.85}$$

Hence, the optimal filter which satisfies Equation (1.85) is

$$\begin{aligned}
\tilde{Q}_{\mathrm{opt}}(f) &= \frac{\tilde{h}(f)}{S_n(f)}, \\
&= A_0 \frac{\tilde{\hat{h}}(f)}{S_n(f)} e^{-2\pi i f t_0}\,.
\end{aligned} \tag{1.86}$$

Hence, the optimal filter is the noise-weighted signal. To see the meaning of this optimal filter in a sense of cross-correlation, let us substitute Equation (1.86) into Equation (1.81). We get

$$\begin{aligned}
z &= \int_{-\infty}^{\infty} df A_0 \tilde{\hat{h}}^*(f) e^{2\pi i f t_0} \tilde{d}(f), \\
&= A_0 \int_{-\infty}^{\infty} df \int_{-\infty}^{\infty} dt \int_{-\infty}^{\infty} dt' \hat{h}(t) d(t') e^{2\pi i f (t - t' + t_0)}, \\
&= A_0 \int_{-\infty}^{\infty} dt \hat{h}(t - t_0) d(t)\,.
\end{aligned} \tag{1.87}$$

Equation (1.87) shows that the optimal filter is cross-correlation with the lag of t_0. As mentioned above, the true merger time is not known in real cases. To estimate the merger time, we find a value of t_0 which corresponds to the largest value of $z(t_0)$, as shown in Figure 1.8.

The signal-to-noise ratio SNR is conventionally defined as the *observed* filter output z to its expected standard deviation (Allen, 2005; Brown, 2004) as

$$\begin{aligned} \mathrm{SNR} &= \frac{(\tilde{Q}_{\mathrm{opt}}, d)}{\sqrt{(\tilde{Q}_{\mathrm{opt}}, \tilde{h}_{\mathrm{opt}})}}, \\ &= \frac{(\tilde{\tilde{h}}, \tilde{s}e^{2\pi i f t_0})}{\sqrt{(\tilde{\tilde{h}}, \tilde{\tilde{h}})}} \end{aligned} \tag{1.88}$$

which does not depend on the constant amplitude A_0. Suppose we know the merger time such that $t_0 = 0$, we get

$$\mathrm{SNR}^2 = 2 \ln \Lambda|_{\mathrm{max}} \tag{1.89}$$

by comparing Equations (1.88) and (1.78). Hence, the square of matched-filter SNR is the maximized log-likelihood ratio with a factor of 2.

In addition to A_0 and t_0, we can analytically maximize the matched-filter SNR over the coalescence phase. The Fourier transform of an amplitude-normalized signal can be written (Allen *et al.*, 2012) as

$$\tilde{\tilde{h}}(f) = \tilde{\tilde{h}}_0(f) e^{-2i\phi_0}, \tag{1.90}$$

where ϕ_0 is the termination phase and $\hat{\tilde{h}}_0$ is the waveform when $t_0 = 0$ and $\phi_0 = 0$. The termination phase is related to the coalescence phase ϕ_c by

$$2\phi_0 = 2\phi_c - \arctan\left(\frac{F_\times}{F_+} \frac{2\cos\iota}{1 + \cos^2\iota}\right), \tag{1.91}$$

where $F_\times$ and F_+ are the antenna response factors in Equation (1.67) and ι is the inclination angle, i.e., the angle between the orbital angular momentum and the observer's line of sight. Because maximizing SNR over the coalescence phase is equivalent to maximizing SNR over the termination phase, we focus on the termination phase in the following. Also, the denominator in Equation (1.88) does not depend on ϕ_0 so that we consider the nominator $(\hat{h}, se^{2\pi i f t_0})$. Using Equation (1.90), we get

$$\begin{aligned}
(\tilde{\hat{h}}, \tilde{s}e^{2\pi i f t_0}) &= 2\int_{-\infty}^{\infty} df \frac{\tilde{\hat{h}}^*(f)\tilde{s}(f)e^{2\pi i f t_0}}{S_n(|f|)}, \\
&= 4\Re \int_0^{\infty} df \frac{\hat{\tilde{h}}_0^*(f)e^{2i\phi_0}\tilde{s}(f)e^{2\pi i f t_0}}{S_n(f)}, \\
&= z_{\rm re}\cos 2\pi + z_{\rm im}\sin 2\pi, \qquad (1.92)
\end{aligned}$$

where we define $z_{\rm re}$ and $z_{\rm im}$ as

$$\begin{aligned}
z_{\rm re} &= 4\Re \int_0^{\infty} df \frac{\hat{\tilde{h}}_0^*(f)\tilde{s}(f)e^{2\pi i f t_0}}{S_n(f)}, \\
z_{\rm im} &= 4\Im \int_0^{\infty} df \frac{\hat{\tilde{h}}_0^*(f)\tilde{s}(f)e^{2\pi i f t_0}}{S_n(f)}, \qquad (1.93)
\end{aligned}$$

Setting the derivative of Equation (1.92) with respect to ϕ_0, we get the maximum:

$$(\tilde{\hat{h}}_0, \tilde{s}e^{2\pi i f t_0})^2 = z_{\rm re}^2 + z_{\rm im}^2 \quad \text{at} \quad \phi_0 = \frac{1}{2}\arg(z_{\rm re} + i z_{\rm im}). \qquad (1.94)$$

Hence, the SNR time series maximized over the coalescence phase is obtained as

$$\mathrm{SNR}(t_0) = \left| 4\int_0^{\infty} df \frac{\tilde{\hat{h}}_0^*(f)\tilde{s}(f)e^{2\pi i f t_0}}{S_n(f)} \right| \left\{ 4\int_0^{\infty} df \frac{|\tilde{\hat{h}}_0(f)|^2}{S_n(f)} \right\}^{-1/2}. \qquad (1.95)$$

Equation (1.95) is the optimal SNR analytically maximized over the constant amplitude A_0, the merger time t_0, and the termination phase ϕ_0 (equivalently the coalescence phase ϕ_c).

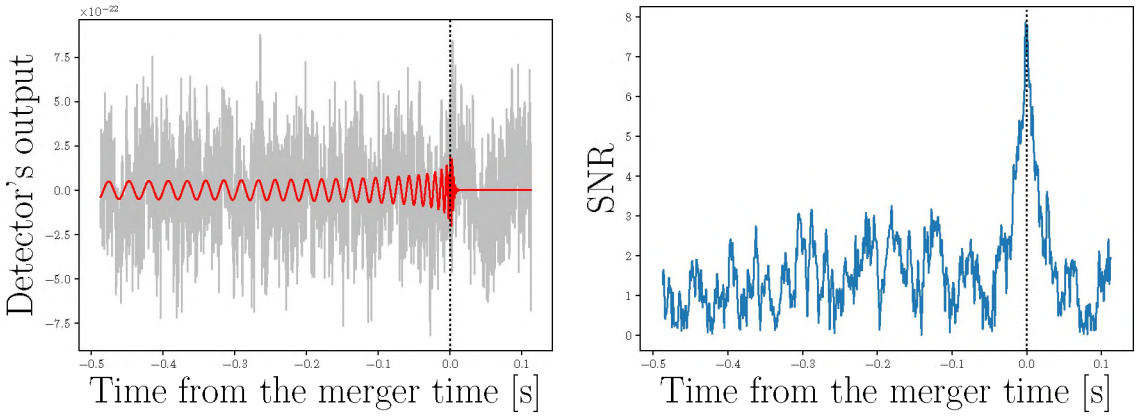

Figure 1.8. Left: waveform of a simulated binary black hole (BBH) signal with the component masses $(m_1, m_2) = (20, 15)\ M_\odot$ and no spins injected into the colored simulated Gaussian noise data (gray) with LIGO's design sensitivity. Right: the corresponding SNR time series. The dotted lines denote the merger time.

In real cases, the data has a finite sample rate so that the upper cutoff frequency in Equation (1.95) should be less than the Nyquist frequency of the data. The lower-cutoff frequency can be chosen to focus on the frequency range where a signal is expected to be dominated in the data. Also, we do not know a true signal contained in the data. Hence, scientists use a bank of templates generated with a set of source-specific parameters, or *intrinsic* parameters such as masses and spins of CBCs. For example, a bank used for the first detected BBH called GW150914 had $\sim 250,000$ template waveforms (Abbott *et al.*, 2016d). The combined SNR, or network SNR among different detectors is defined as a quadrature sum of SNRs in each detector. The network SNR of GW150914 was ~ 24.

In the above, we present the derivation of SNR under the hypothesis that the noise in the data is Gaussian and stationary. However, the noise in the actual GW detector data contains non-stationary noise and/or glitches that might generate triggers with high values of SNR. To account for these factors, one of the matched-filter pipelines called PyCBC (Usman *et al.*, 2016) uses a chi-square statistic to down-weight SNR for triggers with terrestrial origin. If a trigger is a CBC signal, the time-frequency distribution of power in the data is consistent with the expected power distribution of the matched template

waveform (Allen *et al.*, 2012). Therefore, the reduced chi-square statistic $\chi_r^2 = \chi^2/(2n-2)$, where χ^2 is the chi-square statistic and n is the number of frequency bins, is closed to one. On the other hand, triggers with terrestrial origin have higher values of χ_r^2. Hence, the chi-square weighted SNR is defined (Usman *et al.*, 2016) as

$$\mathrm{SNR}_{\chi^2} = \begin{cases} \mathrm{SNR}\left[\frac{1+(\chi_r^2)^3}{2}\right]^{-\frac{1}{6}} & \text{if} \quad \chi_r^2 > 1\,, \\ \mathrm{SNR} & \text{if} \quad \chi_r^2 \leq 1\,. \end{cases} \tag{1.96}$$

PyCBC uses SNR_{χ^2} as a ranking statistic for signal candidates.

1.4.2. Pipelines for Unmodeled Transient GW Signals. There are astrophysical sources that are expected to generate GW signals with their waveforms are difficult to be modeled. In this case, techniques which do not rely on waveforms are better to be used than the matched-filter technique discussed in the previous section. The LIGO-Virgo collaboration has been using various unmodeled GW search pipelines including cWB (Klimenko *et al.*, 2008, 2016), Omicron-LIB (Lynch *et al.*, 2017), BayesWave (Cornish and Littenberg, 2015), and X-pipeline (Sutton *et al.*, 2010) for short-lived transient GW signals with a duration from milliseconds to a few seconds (Abbott *et al.*, 2019c) as well as cWB (Klimenko *et al.*, 2008, 2016), STAMP-AS (Abbott *et al.*, 2016c), X-SphRad (Cannon, 2007) for long-lived transient GW signals with a duration from 10 to 500 seconds (Abbott *et al.*, 2018). We focus on techniques used for short-lived transient GW searches and present the theoretical framework based on Sutton *et al.* (2010) and show example output of a cWB run (Klimenko *et al.*, 2008, 2016).

Unlike the matched-filter technique which maximizes the likelihood ratio over the constant amplitude factor as shown in Equation (1.78), we want to maximize the likelihood ratio over an unknown GW signal for a given source direction in the sky. Unmodeled search pipelines use the time-frequency representations of the data from multiple detectors. The sampling rate and the duration of the data are finite so that the time-frequency representations are pixelized. Hence, we present the framework with discretized data.

Let us consider the data of the α^{th} detector, where $\alpha \in [1,\ldots,D]$ with D denoting the total number of detectors in the network, to be the linear combination of a signal and the noise as

$$s_\alpha(t + \Delta t_\alpha(\hat{\Omega})) = h(t;\hat{\Omega}) + n(t + \Delta t_\alpha(\hat{\Omega}))\,, \tag{1.97}$$

where $\hat{\Omega}$ is a particular direction in the sky, $\Delta t_\alpha(\hat{\Omega})$ is the time delay between the position $\vec{r}_\alpha$ of the α^{th} detector from a reference position $\vec{r}_0$ which is typically chosen to be the geocenter of the earth:

$$\Delta t_\alpha(\hat{\Omega}) = \frac{1}{c}(\vec{r}_\alpha - \vec{r}_0)\cdot\hat{\Omega}. \tag{1.98}$$

Using Equation (1.61), the signal $h(t;\hat{\Omega})$ recorded in the α^{th} detector can be written as

$$h(t;\hat{\Omega}) = F_\alpha^{+}(\hat{\Omega})h_{+}(t) + F_\alpha^{\times}h_{\times}(t)\,, \tag{1.99}$$

where h_+ and $h_\times$ are the plus and cross polarizations of a GW signal. In Equation (1.99), we have assumed the different data streams $d_\alpha(t)$ to be time-shifted within possible arrival-time differences of a signal between $\vec{r}_\alpha$ and $\vec{r}_0$. With this assumption, we have written $h_+ := h_+(t,\vec{r}_\alpha,t)$ and $h_\times := h_\times(t,\vec{r}_\alpha,t)$ in Equation (1.99).

Let us write the discrete Fourier transforms $\tilde{s}(k)$ of the time series $s[j]$ as

$$\tilde{s}[k] = \sum j = 0^{N-1} s[j]e^{-2i\pi jk/N}\,, \tag{1.100}$$

$$\tilde{s}[j] = \frac{1}{N}\sum_{k=0}^{N-1}\tilde{s}[k]e^{-2i\pi jk/N}\,, \tag{1.101}$$

where N is the number of data points in the time series. Using the discretized noise data, Equation (1.71) under the assumption that the noise in different detectors are uncorrelated, is written (Sutton *et al.*, 2010) as

$$\left\langle \tilde{n}_\alpha^{*}[k]\tilde{n}_\beta[k']\right\rangle = \frac{N}{2}\delta_{\alpha\beta}\delta_{kk'}S_\alpha[k]\,, \tag{1.102}$$

where $S_\alpha[k]$ is the one-sided PSD. As we have seen in the previous section, the data is whitened to calculate the likelihood ratio. For convenience, we define the whitened data, noise, and antenna response function as

$$\tilde{s}_{\mathrm{w}\alpha}[k] = \frac{\tilde{s}_\alpha[k]}{\sqrt{\frac{N}{2}S_\alpha[k]}}, \tag{1.103}$$

$$\tilde{n}_{\mathrm{w}\alpha}[k] = \frac{\tilde{n}_\alpha[k]}{\sqrt{\frac{N}{2}S_\alpha[k]}}, \tag{1.104}$$

$$F^{+,\times}_{\mathrm{w}\alpha}(k,\hat{\Omega}) = \frac{F^{+\times}_\alpha(\hat{\Omega})}{\sqrt{\frac{N}{2}S_\alpha[k]}}, \tag{1.105}$$

where $F^{+,\times}_\alpha$ denotes F^+_α or $F^\times_\alpha$. The factor N in the denominator is due to the discretization of the Fourier transform that can been seen in Equation (1.102) and the factor $1/2$ in the denominator is for the convenience such that the inner product defined in Equation (1.74) is written simpler with the discrete Fourier transforms.

With these notations, Equation (1.97) can be written as a vector form including all detectors in the network as

$$\tilde{\boldsymbol{s}} = \boldsymbol{F}\tilde{\boldsymbol{h}} + \tilde{\boldsymbol{n}}, \tag{1.106}$$

where

$$\tilde{\boldsymbol{s}} := \begin{pmatrix} \tilde{s}_{\mathrm{w}1} \\ \tilde{s}_{\mathrm{w}2} \\ \vdots \\ \tilde{s}_{\mathrm{w}D} \end{pmatrix}, \quad \tilde{\boldsymbol{h}} := \begin{pmatrix} \tilde{h}_+ \\ \tilde{h}_\times \end{pmatrix}, \quad \tilde{\boldsymbol{n}} := \begin{pmatrix} \tilde{n}_{\mathrm{w}1} \\ \tilde{n}_{\mathrm{w}2} \\ \vdots \\ \tilde{n}_{\mathrm{w}D} \end{pmatrix}, \tag{1.107}$$

and

$$\boldsymbol{F} := \begin{pmatrix} \boldsymbol{F}^+ & \boldsymbol{F}^\times \end{pmatrix} = \begin{pmatrix} F^+_{\mathrm{w}}1 & F^\times_\times 1 \\ F^+_{\mathrm{w}}2 & F^\times_\times 2 \\ \vdots & \vdots \\ F^+_{\mathrm{w}}D & F^\times_\times D \end{pmatrix}, \tag{1.108}$$

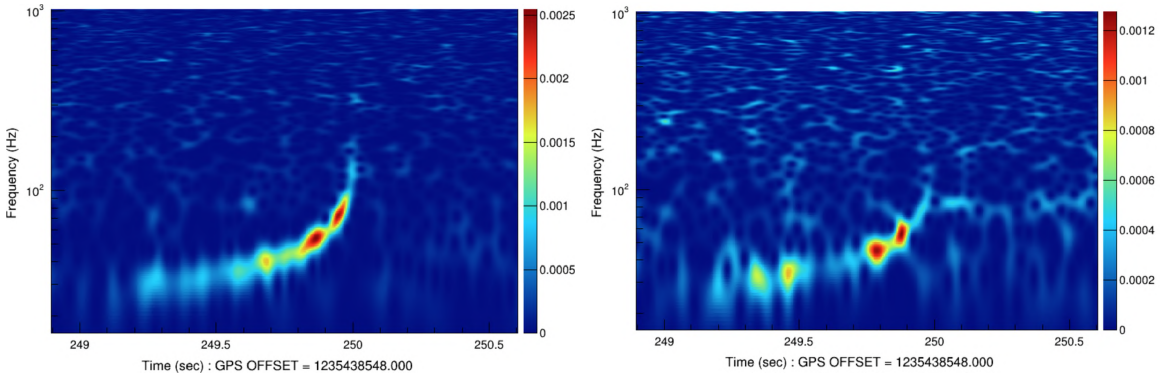

Figure 1.9. Spectrograms of simulated BBH signals with the component masses $(m_1, m_2) = (20, 15)\, M_\odot$, no spins and an injected network SNR of 28.2 added into the simulated colored Gaussian-noise data in the two-detector network with the LIGO's design sensitivity. The color scale denotes the normalized energy.

and the log-likelihood ratio in Equation (1.77) is written as

$$\ln \Lambda = \sum_k \left[\tilde{\boldsymbol{s}}^\dagger \boldsymbol{F} \tilde{\boldsymbol{h}} - \frac{1}{2} \left| \boldsymbol{F} \tilde{\boldsymbol{h}} \right|^2 \right], \tag{1.109}$$

where † denotes the conjugate transpose and we now assume that the discrete Fourier transforms are taken in each divided segment of the time series so that we let k run over pixel indices of the time-frequency representation. Figure 1.9 shows example spectrograms of simulated BBH signals injected into the simulated colored Gaussian-noise data in the two-detector network with the LIGO's design sensitivity.

We want to maximize the log-likelihood ratio over an unknown signal $\tilde{\boldsymbol{h}}$. Mathematically it is written as

$$0 = \left. \frac{\partial \ln \Lambda}{\partial \tilde{\boldsymbol{h}}} \right|_{\tilde{\boldsymbol{h}} = \tilde{\boldsymbol{h}}_{\rm max}}. \tag{1.110}$$

The $\tilde{\boldsymbol{h}}_{\rm max}$ is

$$\tilde{\boldsymbol{h}}_{\rm max} = (\boldsymbol{F}^\dagger \boldsymbol{F})^{-1} \boldsymbol{F}^\dagger \tilde{\boldsymbol{s}}, \tag{1.111}$$

and when $\tilde{\boldsymbol{h}} = \tilde{\boldsymbol{h}}_{\rm max}$, Equation (1.109) becomes

$$\ln \Lambda_{\rm max} = \frac{1}{2} \sum_k \tilde{\boldsymbol{s}}^\dagger \boldsymbol{P} \tilde{\boldsymbol{s}} , \tag{1.112}$$

where

$$\boldsymbol{P} := \boldsymbol{F}(\boldsymbol{F}^\dagger \boldsymbol{F})^{-1} \boldsymbol{F}^\dagger , \tag{1.113}$$

is a projection operator that projects the data onto the subspace of the vectors $\boldsymbol{F}^+$ and $\boldsymbol{F}^\times$. The $\ln \Lambda_{\rm max}$ is the so-called *standard likelihood.*

Similar to Equation (1.89), the maximum amount of normalized energy (so-called *standard-likelihood energy*) which is consistent with a GW for a given sky position can be defined using $\ln \Lambda_{\rm max}$ with a factor of 2 as

$$E_{\rm SL} = 2 \ln \Lambda_{\rm max} . \tag{1.114}$$

The square root of $E_{\rm SL}$ is the network SNR. Using the total energy:

$$E_{\rm tot} = \sum_k |\tilde{\boldsymbol{s}}|^2 , \tag{1.115}$$

which contains only auto-correlation terms without cross-correlation terms, the *null* energy is defined as

$$E_{\rm null} := E_{\rm tot} - E_{\rm SL} = \sum_k \tilde{\boldsymbol{s}}^\dagger (\boldsymbol{I} - \boldsymbol{P}) \tilde{\boldsymbol{s}} , \tag{1.116}$$

where $\boldsymbol{I}$ is the identity matrix with a dimension of D, and $\boldsymbol{P}^{\rm null} := \boldsymbol{I} - \boldsymbol{P}$ is orthogonal to $\boldsymbol{P}$. $E_{\rm null}$ is the minimum amount of energy in the data inconsistent with a hypothetical signal from a given sky position.

We can simplify Equation (1.114) with particular basis vectors constructed with $\boldsymbol{F}_+$ and $\boldsymbol{F}_\times$ by rotating the original basis in the direction of the GW polarization angle. Equation (1.99) is invariant with a rotation with an arbitrary polarization angle ψ because

$\tilde{\boldsymbol{h}}$ and $\boldsymbol{F}$ are rotated in the opposite directions (Klimenko *et al.*, 2005, 2006) as

$$\tilde{\boldsymbol{h}}' = R^{(2)}(\psi)\tilde{\boldsymbol{h}}\,, \tag{1.117}$$

$$\boldsymbol{F}'^{\dagger} = R^{(2)}(-\psi)\boldsymbol{F}^{\dagger}\,, \tag{1.118}$$

where $R^{(2)}(\psi)$ is the 2-dimensional rotation operator and its matrix representation is

$$R^{(2)}(\psi) = \begin{pmatrix} \cos\psi & -\sin\psi \\ -\sin\psi & \cos\psi \end{pmatrix}. \tag{1.119}$$

The most convenient choice of the frame is the so-called dominant polarization frame (Klimenko *et al.*, 2005, 2006), where the first basis is aligned with $\boldsymbol{F}^{+}$, the second basis vector is aligned with $\boldsymbol{F}^{\times}$, and these two basis vectors are orthogonal to each other. In the dominant polarization frame, the detector network has the maximum antenna response in the direction projected by $\boldsymbol{P}$, and the minimum response in the direction projected by $\boldsymbol{P}^{\mathrm{null}}$. To find the rotation angle ψ, we write the new vectors $\boldsymbol{f}^{+}$ and $\boldsymbol{f}^{\times}$ as a rotation applied to old basis vectors $\boldsymbol{F}^{+}$ and $\boldsymbol{F}^{\times}$ as

$$\boldsymbol{f}^{+} = \cos\psi\boldsymbol{F}^{+} + \sin\psi\boldsymbol{F}^{\times}\,, \tag{1.120}$$

$$\boldsymbol{f}^{+} = -\sin\psi\boldsymbol{F}^{+} + \cos\psi\boldsymbol{F}^{\times}\,. \tag{1.121}$$

By requiring $\boldsymbol{f}^{+}\cdot\boldsymbol{f}^{\times} = 0$, the solution ψ for Equation (1.120) is

$$\psi = \frac{1}{2}\arctan\left(\frac{2\boldsymbol{F}^{+}\cdot\boldsymbol{F}^{\times}}{|\boldsymbol{F}^{+}|^2 + |\boldsymbol{F}^{+}|^2}\right). \tag{1.122}$$

In the dominant polarization frame, the projection operator becomes $\boldsymbol{P} = \boldsymbol{e}^{+}\boldsymbol{e}^{+\dagger} + \boldsymbol{e}^{\times}\boldsymbol{e}^{\times\dagger}$, where $\boldsymbol{e}^{+} := \boldsymbol{f}^{+}/|\boldsymbol{f}^{+}|$ and $\boldsymbol{e}^{+} := \boldsymbol{f}^{\times}/|\boldsymbol{f}^{\times}|$. Therefore, the standard-likelihood energy becomes

$$E_{\mathrm{SL}} = \sum_{k}\left[\left|\boldsymbol{e}^{+}\cdot\tilde{\boldsymbol{s}}\right|^2 + \left|\boldsymbol{e}^{\times}\cdot\tilde{\boldsymbol{s}}\right|^2\right], \tag{1.123}$$

and Equation (1.111) becomes

$$\tilde{\boldsymbol{h}}_{\max} = \begin{pmatrix} \boldsymbol{e}^{+} \cdot \tilde{\boldsymbol{s}}/|\boldsymbol{f}^{+}| \\ \boldsymbol{e}^{\times} \cdot \tilde{\boldsymbol{s}}/|\boldsymbol{f}|^{\times}. \end{pmatrix} \tag{1.124}$$

Hence, the whitened reconstructed GW signal received in the α^{th} detector is

$$\begin{aligned} \tilde{h}_{\alpha}^{\text{rec}} &= \tilde{h}_{\max}^{+} f_{\alpha}^{+} + \tilde{h}_{\max}^{\times} f_{\alpha}^{\times}, \\ &= \frac{\boldsymbol{e}^{+} \cdot \tilde{\boldsymbol{s}}}{|\boldsymbol{f}^{+}|} f_{\alpha}^{+} + \frac{\boldsymbol{e}^{\times} \cdot \tilde{\boldsymbol{s}}}{|\boldsymbol{f}|^{\times}} f_{\alpha}^{\times}. \end{aligned} \tag{1.125}$$

The algorithm of the cWB pipeline creates the time-frequency pixels using a wavelet transformation, in particular, *fast Wilson-Daubechies* basis (Necula *et al.*, 2012) to obtain E_{SL} and obtain the reconstructed waveform in Equation (1.125) using the inverse transform. As a ranking statistic, cWB constructs the *coherent energy* E_{c} from E_{SL} and uses E_{null} as a penalty factor because E_{c} contains larger energy and E_{null} contains smaller energy when a signal is present in the data of the detector network.

By rewriting E_{SL} explicitly with indices of the projection operator $\boldsymbol{P}$ in Equation (1.113) and the data vector $\tilde{\boldsymbol{s}}$ in Equation (1.106):

$$\begin{aligned} E_{\text{SL}} &= \sum_{k} \sum_{\alpha,\beta} \tilde{s}_{\alpha}^{*} P_{\alpha\beta} \tilde{s}_{\beta}, \\ &:= \sum_{k} \sum_{\alpha,\beta} E_{\alpha\beta} \end{aligned} \tag{1.126}$$

where α and β run over the detector's indices $[1, \ldots, D]$, we can get the coherent energy by taking only cross-correlation terms (i.e., off-diagonal terms):

$$E_{\text{c}} = \sum_{k} \sum_{\alpha \neq \beta} E_{\alpha\beta}. \tag{1.127}$$

The network correlation coefficient is defined (Drago, 2010) as

$$\mathrm{cc} = \frac{E_\mathrm{c}}{E_\mathrm{c} + E_\mathrm{null}}, \tag{1.128}$$

where cc $\sim$ 1 for a signal. To make the ranking statistic more robust, let us consider the incoherent energy which is constructed by taking only auto-correlation terms (i.e., diagonal terms) in Equation (1.126):

$$E_\mathrm{a} = \sum_k \sum_\alpha E_{\alpha\alpha}\,. \tag{1.129}$$

In the physically allowed situation, where $0 \leq E_\mathrm{c} \leq E_\mathrm{a}$, we expect $E_\mathrm{c} \sim E_\mathrm{a}$ for signals and $E_\mathrm{c} \ll E_\mathrm{a}$ for glitches. Using the Pearson's correlation coefficient:

$$r_{\alpha\beta} = \frac{E_{\alpha\beta}}{2\sqrt{E_{\alpha\alpha}E_{\beta\beta}}}, \tag{1.130}$$

the reduced correlated energy is defined as

$$e_\mathrm{c} = \sum_k \sum_{\alpha\neq\beta} E_{\alpha\beta}|r_{\alpha\beta}|\,. \tag{1.131}$$

With e_c, cc and the total number of detectors D, cWB uses the *effective correlated* SNR:

$$\rho = \sqrt{\frac{e_\mathrm{c}}{D}\mathrm{cc}}, \tag{1.132}$$

as a ranking statistic. When a signal is fully coherent between detectors, the reduced correlated energy becomes $e_\mathrm{c} = E_\mathrm{SL}/2$ and cc = 1, leading to $\rho = \mathrm{SNR}_\mathrm{net}/\sqrt{2D}$, where $\mathrm{SNR}_\mathrm{net}$ is the network SNR. Figure 1.10 shows E_SL and E_null of a simulated BBH signal shown in Figure 1.9. This trigger has $\rho = 15.9$. Appendix F shows the comparison of the accuracy between the sky maps obtained with a modeled search and cWB.

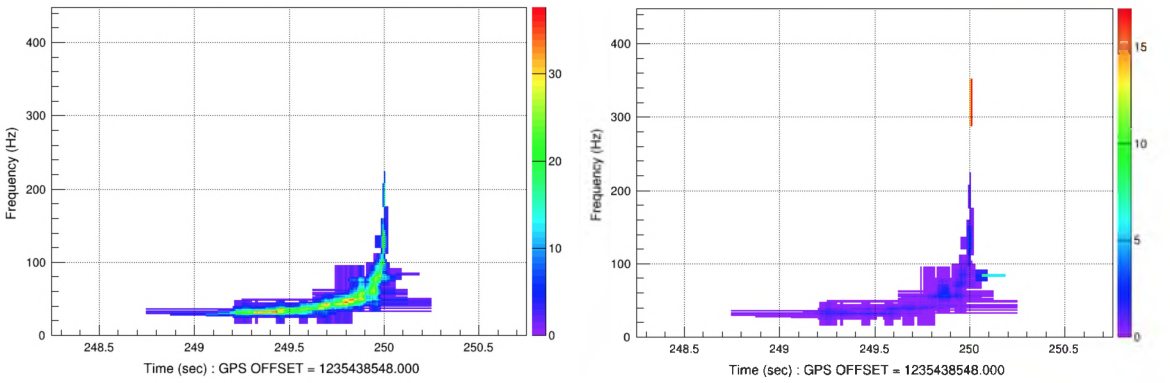

Figure 1.10. Scalograms of standard energy (left) and corresponding null energy (right) of a simulated BBH signal shown in Figure 1.9.

1.4.3. Confidence in Signal Detections. The real noise in the detector's output readout is neither stationary nor Gaussian. Triggers might be generated due to noise in chance coincidence between detectors. To quantify how rare signal-candidate triggers are generated due to the noise, LIGO-Virgo collaboration uses the rate of triggers due to the noise with their ranking statistics equal or greater than the ranking statistic of a signal candidate, or false alarm rate (FAR):

$$\mathrm{FAR} = \frac{N(r \geq r_h)}{T_{\mathrm{bkg}}} \tag{1.133}$$

where r is the ranking statistic of a trigger due to the noise, r_h is the ranking statistic of a signal candidate, and T_{bkg} is the total time period of the analysis time to obtain noise triggers. Smaller values of FAR imply that the signal candidate is due to astrophysical origin with high confidence.

The duration of the actual data is finite and not sufficiently long for calculating FARs. To compensate for this limitation, scientists apply time shifts to either of the detectors to enlarge the duration of the data (Abbott *et al.*, 2005), as shown in Figure 1.11.

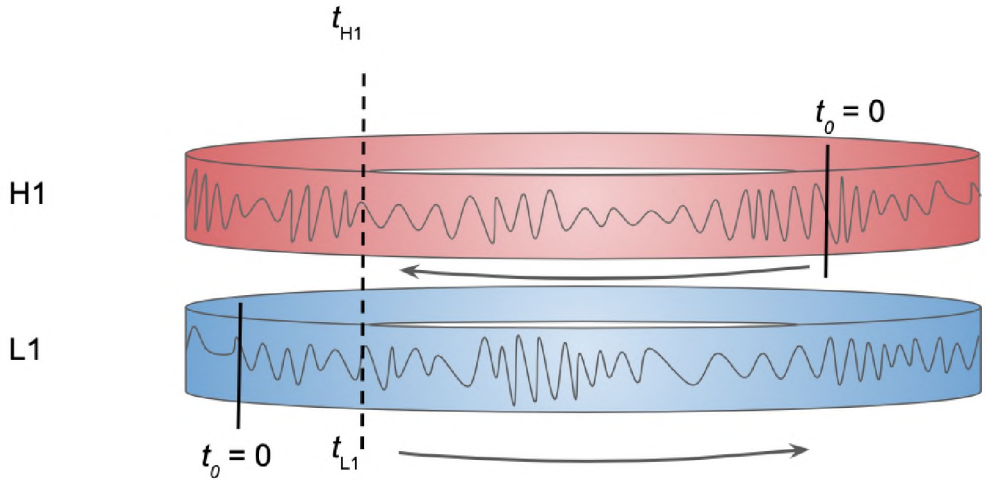

Figure 1.11. Schematic picture of time shifts applied to either of the detectors.

For example, the FAR of GW150914 was 1 event per 203,000 years (Abbott *et al.*, 2016e), implying that the ranking statistic of GW150914 could be obtained only by the noise if the detectors were operated over 203,000 years.

2. BACKGROUND TO PAPER I

Because glitches may resemble astrophysical signals, the presence of glitches also reduces the significance of GW signal candidates. Hence, the identification of the glitch origin is the crucial point to improve the detectability of GW signals. However, it is generally difficult to find their origin. GW detectors employ approximately two hundred thousand auxiliary *channels* such as sensors/control-systems reading-out environmental or instrumental conditions inside and around detectors in parallel to the detector's output readout in the time domain. Those channels can be potential witnesses of coupling mechanisms of glitches and their output can be used to mitigate the effect of glitches on the detector's output. In the next chapter, we present a software package that statistically identifies witness channels for glitches observed in the detector's output. Starting with the software architecture, we validate the software using a class of glitches observed during the second observation run (O2). Also, we show its application to triggers of the noise events generated by one of the burst GW search pipelines called cWB (Klimenko *et al.*, 2008, 2016), and compare our results with the LIGO's current infrastructure. With PyChChoo, we can find that triggers with high ranking statistics due to glitches can be vetoed. Hence, FAR can be smaller for signal candidates as seen in Equation (1.133). The next chapter is a reprint of an article (Mogushi, 2021a) that has been submitted to arXiv.org and has been published by Classical and Quantum Gravity Journal for publication.

3. BACKGROUND TO PAPER II

After the identification of witness channels for glitches, removing glitches from the data of the detector's output is desirable. One of the techniques to remove the effect of glitches on searches for astrophysical signals is to veto time present where glitches are present because glitches are the product of short-lived linear and non-linear couplings in the detector and their coupling mechanisms are generally difficult to be understood. The LIGO-Virgo collaboration has been adapting the veto technique at the cost of reducing the analyzable data and use another technique that reduces the significance of signal candidates based on the probability of the presence of glitches (Abbott *et al.*, 2021b) (discussed in more detail in the next section). To increase the significance of signal candidates without reducing the analyzable data, we present a machine learning-based algorithm to subtract glitches using auxiliary channels. We apply two classes of glitches that adversely affect cWB (Klimenko *et al.*, 2008, 2016) trigger with high values of significance and quantify the performance of our tool. Adding simulated astrophysical signals before subtraction and then comparing the recovered signal before and after subtraction, as well as the recovered signal added into a clean time period, we assess the robustness of our method not to manipulate or introduce any biases to those astrophysical signals. The next chapter is a reformatted version of an article (Mogushi, 2021b) that has been submitted to arXiv.org.

PAPER

I. APPLICATION OF A NEW TRANSIENT-NOISE ANALYSIS TOOL FOR AN UNMODELED GRAVITATIONAL-WAVE SEARCH PIPELINE

Kentaro Mogushi
Institute of Multi-messenger Astrophysics and Cosmology
Missouri University of Science and Technology
Physics Building, 1315 N. Pine St.
Rolla, MO 65409, USA
mogus261@gmail.com

ABSTRACT

Excess transient noise events, or "glitches", impact the data quality of ground-based GW detectors and impair the detection of signals produced by astrophysical sources. Identification of the causes of these glitches is a crucial starting point for the improvement of GW signal detectability. However, glitches are the product of linear and non-linear couplings among the interrelated detector-control systems that include mitigation of ground motion and regulation of optic motion, which generally makes it difficult to find their origin. We present a new software called PyChChoo which uses time series recorded in the instrumental control systems and environmental sensors around times when glitches are present in the detector's output to reveal essential clues about their origin. Applying PyChChoo to the most adversely affecting glitches on *background* triggers generated by one of unmodeled GW detection pipelines called coherent WaveBurst (cWB) operated in the data from the LIGO detectors between January 1st, 2020 and February 3rd, 2020, we find that 80% of triggers are marked as either being vetoed or unvetoed in common between our analysis and the current LIGO infrastructure.

Keywords: gravitational waves, glitch, statistics

1. INTRODUCTION

The dawn of gravitational-wave (GW) astronomy was opened with the first direct detection of a GW signal produced from a BBH merger (Abbott *et al.*, 2016) on September 14^{th}, 2015.

During the first and second observing runs of LIGO (Aasi *et al.*, 2015) and Virgo (Acernese *et al.*, 2015), nine additional BBH mergers and a BNS merger were detected with high confidence (Abbott *et al.*, 2019). Furthermore, 39 events were observed with high confidence during the first half of the third observation run (Abbott *et al.*, 2021). The detection rate was approximately 1 per week.

In order to detect GW signals, the ground-based GW detectors must be extremely sensitive, causing them to become susceptible to instrumental and environmental artifacts (Abbott *et al.*, 2019). In particular, transient noise artifacts, or *glitches* may mimic GW signals in their morphology so that it is crucial to differentiate if trigger events identified by GW detection pipelines are astrophysical or terrestrial in origin to reduce false detections.

The initial and essential task to identify an event trigger as a glitch is to understand the origin of the glitch. Glitches are, however, the product of linear and non-linear coupling among the interrelated detector-control systems that include mitigation of ground motion and regulation of optical motion, which typically makes it difficult to find their origin. Clues of the origin may be recorded in some of around fifty thousand auxiliary *channels* such as instrumental sensors and environmental monitors. Because the number of channels is numerous, the task to find the clues is typically made by automated software packages.

LIGO-Virgo collaboration has been using software engines that find the statistical correlation between the excess power recorded in the auxiliary channels and glitches present in the detector's output. An algorithm called use-percentage veto (UPV) (Isogai, 2010) finds the statistical correlation using the percentage of the number of the excess power events identified in each of the auxiliary channels in coincidence with glitches in the detector's output, relative to the total number of excess power events. As a consequence, UPV vetoes

time periods that have a high correlation factor. Similarly, hierarchical Veto (hVETO) (Smith *et al.*, 2011) uses a coincidence statistic to find the correlation while minimizing the vetoed time as much as possible. For finding the correlation for a single glitch, Pointy Poisson (Essick *et al.*, 2021) uses a statistical confidence level that can reject the chance-coincidence hypothesis estimated from the excess power events in the longer time window. iDQ (Biswas *et al.*, 2013) calculates the probability that glitches are present in the detector's output as a function of time, inferred from excess power in the auxiliary channels.

In this paper, we present a new software (publicly accessible in `https://git.ligo.org/kentaro.mogushi/origli`) called PyChChoo ("Python-based glitCh Characterization tool") designed to identify the clue of the origin of glitches in GW detectors and remove the effect in the detector's output. Using a set of glitches, PyChChoo conditions the time series recorded in the auxiliary channels around the glitch-time and then counts the fraction of frequency bins above a threshold in a given frequency band in order to quantify the excess power in coincidence with the glitch. To identify highly correlated channels (so-called *witness* channels), PyChChoo uses the probability showing the loudness of the excess-power measure in the glitch set compared with the measure in another set which is created with randomly selected timestamps when the detector's output is quiet. After witness channels are identified, removable glitches are determined by the probability that the excess-power measure for a glitch belongs to the glitch set.

The most novel feature of this algorithm is that it can be used as a "targeted" approach. To understand the origin of a particular population of glitches having their specific characteristics denoted such as the peak frequency, SNR and/or time-frequency morphology, a user can choose the list of those glitches for running PyChChoo. Instead of providing a single channel that is the most significantly correlated, the algorithm can find multiple channels to help a thorough understanding of potential unknown physical couplings inside instruments. Besides, the ultimate goal of GW searches is to detect more signals. Not all glitches are adversely affecting GW detection pipelines. Therefore,

studying all glitches present in the detector's output that typically is made with UPV and hVETO might introduce redundant removal time periods. To compensate for this issue, only adversely affecting glitches for a GW pipeline can be chosen for running this algorithm. We demonstrate the "targeted" approach using triggers with high-ranking statistics that are generated by one of unmodeled GW detection pipelines. Finding the witness channels is particularly beneficial for unmodeled GW detection pipelines (Klimenko *et al.*, 2008, 2016; Sutton *et al.*, 2010) because they are more susceptible to glitches than matched-filter pipelines (Nitz *et al.*, 2017; Sachdev *et al.*, 2019) by their design. Conversely, they have potential capabilities to detect GW signals with unknown waveforms or signals empowered by unknown sources.

2. SOFTWARE ARCHITECTURE

PyChChoo aims to identify the essential clues of the origin of glitches in the detector's output and remove the effect of those glitches. A set of glitches can be selected from any event trigger generators (ETGs) or glitch databases, e.g., Omicron (Robinet *et al.*, 2020), pyCBC-live (Nitz *et al.*, 2018), the database created based on Gravity Spy (Zevin *et al.*, 2017), or user-defined glitches on demand. Those glitches can be further down-selected based on their characteristics such as peak frequencies, SNRs, and/or particular glitch-class, etc.

2.1. QUANTIFY EXCESS POWER

In order to identify the origin of glitches driven from terrestrial disturbances, a set of system control sensors and environmental monitors that do not causally follow from the detector's output (so-called *safe* auxiliary channels) is used. To identify safe channels, LIGO uses hVETO (Smith *et al.*, 2011) and Pointy Poison (Essick *et al.*, 2021).

Witness channels are expected to show excess power in coincidence with a glitch detected in the detector's output. Those channels might record excess power in different frequency bands. Also, a measure quantifying the excess power depends on a provided time window used to calculate itself. To account for these dependencies on excess-power values, PyChChoo uses the one-sided amplitude spectrum density (ASD) that indicates the noise amplitude. The one-sided ASD is a square root of the one-sided PSD $S(f)$ defined as

$$\frac{1}{2}\delta(f - f')S(f) = \langle \tilde{n}(f)\tilde{n}(f') \rangle \ , \tag{1}$$

where the brackets $\langle \cdots \rangle$ denote an ensemble average over noise realizations (Cutler and Flanagan, 1994), and $\tilde{n}(f)$ and $\tilde{n}(f')$ are the Fourier transforms of the time series $n(t)$ at the frequencies f and f', respectively. Using the ASD of the time series recorded in a set of safe channels in the *quiet* time, we define the *stationarity* upper threshold (SUT) as follows.

The SUT is obtained from the time series when no glitches are present in the detector's output. We consider Omicron triggers (Robinet *et al.*, 2020) with SNR ≤ 5.5 to be the absence of glitches. To calculate values of SUT, PyChChoo first selects random timestamps during the quiet period and then chooses time windows for each of the timestamps by randomly selecting durations ($t_{d,s}$) which are log-uniformly distributed between the minimum duration ($t_{d,min}$) and the maximum duration ($t_{d,max}$). The value of $t_{d,min}$ is chosen to be 0.02 seconds because of the computational requirement for the ASD calculation in GWpy (Virtanen *et al.*, 2020). The value of $t_{d,max}$ is typically chosen to be 35 seconds where the majority of glitches (82% of glitches in the Gravity Spy glitch database in the O2) have durations less than this value. After setting the time window for each of the timestamps, the ASD is calculated using the time series in this time window. This ASD is subsequently normalized with the median value of ASDs of overlapping periodograms with a single fast Fourier transform (FFT) duration of $t_{d,s}$ in the time window of 128 seconds spanning around the timestamp.

Using a set of timestamps, the value of SUT is defined as a 3-σ standard deviation above the mean value of the normalized ASD for each channel in a given frequency band with a given duration. To obtain values of SUT for any durations, PyChChoo interpolates SUT as a function of duration for each channel in a given frequency band. We find that the polynomial best fit with the degree of 10 while removing the outliers outside of the median absolute error with a 6-σ is suitable. Figure 1 shows the interpolated SUT as a function of duration for the two representative channels in particular frequency bands. The interpolated SUT are saved and to be used to evaluate glitches like the following.

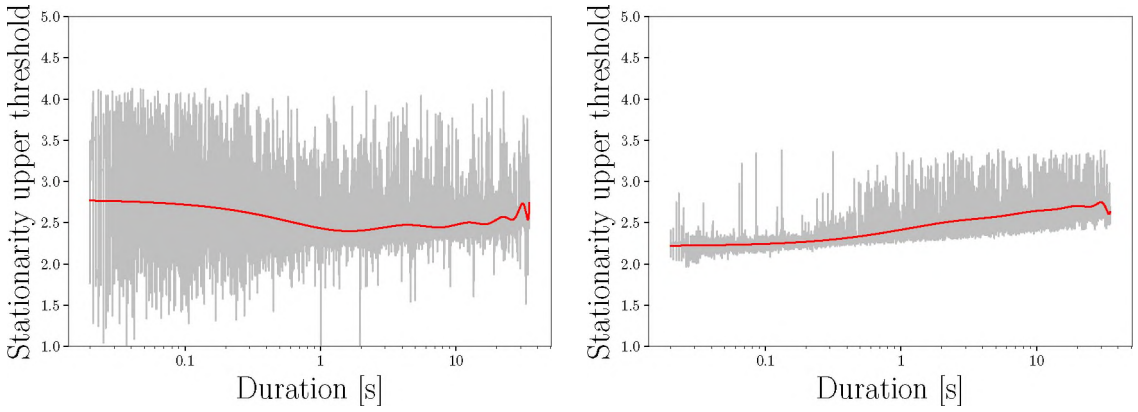

Figure 1. SUT of two representative channels: L1:ASC-SRC2_Y_OUT_DQ in 1-128 Hz (left) and L1:PEMEX_MAG_VEA_FLOOR_Y_DQ in 2048-4096 Hz (right) as a function of duration. The red curves are the polynomial best fits with the degree of 10 obtained from the gray curves that denote the values SUT for 8010 different random samples. Outlying values of SUT outside of the median absolute error with a 6-σ are removed.

For each glitch, PyChChoo conditions the time series recorded in each of the safe channels in the time window:

$$W = \left[t_g - \alpha t_d \, , t_g + (1-\alpha) t_d\right] \, , \tag{2}$$

where t_g is the time of a glitch, t_d is its duration, and α is a fraction of the duration before t_g. A value of $\alpha = 0.5$ sets the window to be evenly spanned around the glitch time t_g. A value of t_d can be chosen to be the duration provided by an ETG or manually selected if needed. Witness channels are expected to record excess power in particular frequency bands in this window when the glitch is present in the detector's output.

To quantify the excess power for a glitch, PyChChoo firstly calculates the ASD of the time series in the window W, secondly normalize the ASD with the median value of ASDs which are obtained from the time series in the 128-second window spanning evenly around t_g, finally counts the fraction (q) of the frequency bins above the value of SUT in a given frequency band. Because the sampling frequencies differ between channels (from 256 Hz to 16384 Hz), the lower and/or upper bounds of a chosen frequency band can be greater than the Nyquist frequency of some channels. When only the upper bound is above the Nyquist frequency, we use the frequency bins up to the Nyquist frequency for calculating q. When the lower bound is above the Nyquist frequency, we define the value of q to be zero.

2.2. PROBABILISTIC INSIGHT

After a set of glitches (hereafter called target set) is quantified with values of q from each of the safe auxiliary channels in different frequency bands, the probabilistic measure is used to identify witness channels. Channels with large values of q in the target set could have large values of q during the absence of glitches as well. Channels that record excess power regardless of the presence of glitches indicate no or mild correlation with the glitches. The probabilistic measure accounts for this factor to identify witness channels.

To identify witness channels, PyChChoo compares the target set with another data set (null set). The null set is created by randomly generating time periods with durations being distributed as that of the target set, and then selecting only the subset of these time periods that do not overlap with any glitches being present in the detector's output. We

typically consider Omicron triggers with SNR ≤ 5.5 to be the absence of glitches. Because the null set represents the data set when the detector's output is quiet, channels with large values of q in the null set imply no or mild correlation with the targeted glitches.

Witness channels are expected to show a larger number of samples with greater values of q in the target set than the null set. To formulate this manifestation, we consider the distributions $t(q)$ and $n(q)$ of q in the target and null sets, respectively. The probability that the target set has values in the small interval $(q, q + \Delta q)$ is $t(q)\Delta q$, while the probability that the null set has values less than q is $\mathcal{N}(q) = \int_0^q n(q')dq'$, which is known as the cumulative distribution. Multiplying $t(q)\Delta q$ and $\mathcal{N}(q)$ gives the probability of the pair of the above two situations occur in unison. Summing $t(q)\Delta q\mathcal{N}(q)$ over the range of all possible values of q, formulated as

$$p_g = \int_0^1 t(q)\mathcal{N}(q)dq\,, \tag{3}$$

is the probability that arbitrary values of q in the target set are greater than values in the null set. Channels with $p_g \lesssim 0.5$ imply chance coincidences. Channels with $p_g \sim 1$ indicate evidence of being the witness for the glitches. Therefore, PyChChoo uses p_g to identify the witness channels. In experiments, only a finite number of samples can be obtained. To compensate for this experimental limit, a continuous distribution is preferred to make a robust measure for Equation (3). Because values of q are bounded between 0 and 1, a candidate distribution for q is a Beta distribution. The shape of the Beta distribution is obtained with the first and second moments estimated from the measured samples.

After witness channels are identified, the effect of the glitches on the GW detection pipelines can be mitigated. The simple and standard procedure is to veto the time periods of glitches that are correlated with witness channels. For a glitch, a value of q obtained from the witness channel implies either of two mutually exclusive situations: a value of q follows the target set with being greater than values in the null set, or a value of q follows

the null set with being greater than values in the target set. Thus, the probability that q belongs to the target set is given as

$$p_v = \frac{t(q)\mathcal{N}(q)}{t(q)\mathcal{N}(q) + \mathcal{T}(q)n(q)}, \tag{4}$$

where $\mathcal{T}(q)$ is the cumulative distribution of q in the target set. A value of $p_v \sim 1$ indicates evidence of a strong correlation between excess power in the witness channel and the glitch. PyChChoo uses p_v as a veto criterion.

3. SOFTWARE VALIDATION

For validating PyChChoo's performance to identify witness channels, we use a class of glitches with the known instrumental origin that was identified during O2. The L1 detector was contaminated with a new class of glitches between February 9th, 2017 and April 10th, 2019 due to the magnetic coupling between the magnetic field produced from electronics racks and the detector's internal components such as cables, connectors, and actuators (Cavaglia *et al.*, 2019). These glitches were short-lived spikes with a duration of $\sim$ 0.3 seconds and appeared in the frequency band of $\sim$ 50-60 Hz in the detector's output. hVETO (Smith *et al.*, 2011) identified a series of coincident excess power in auxiliary channels in the Physical Environmental Monitor (PEM) mains voltage monitor (MAINSMON) of the Electronics Bay (EBay) in the X-arm end station (EX) as well as in the EX magnetometers. The follow-up study conducted by Cavaglia *et al.* (2019) using the machine-learning-based tools called Karoo GP (Staats *et al.*, 2017) and Random Forest (Breiman, 2001), identified a physically coupled channel called ISI-ETMX_ST1_BLND_Z_T240_CUR_ IN1_DQ in the active seismic isolation internal to the vacuum system (ISI) in addition to the EX magnetometer channels.

As the target set, we choose 595 glitch samples with SNR $\geq$ 7.5 from this *magnetometer* set. Also, we create the null set with a sample size of 477 by analyzing the randomly chosen timestamps when no Omicron triggers with SNR $\geq$ 5.5 are present in the detector's output. We analyze 700 safe auxiliary channels with 8 different frequency bands. Figure 2 shows values of q for the target and null sets. One of the EX magnetometer channels called PEM-EX_MAG_VEA_FLOOR_X_DQ in the PEM sub-system has values of $q \geq 0.6$ for 93% of the target set and 0% of the null set. The Alignment Sensing and Control (ASC) channels show random fluctuating values of q both in the target and null sets.

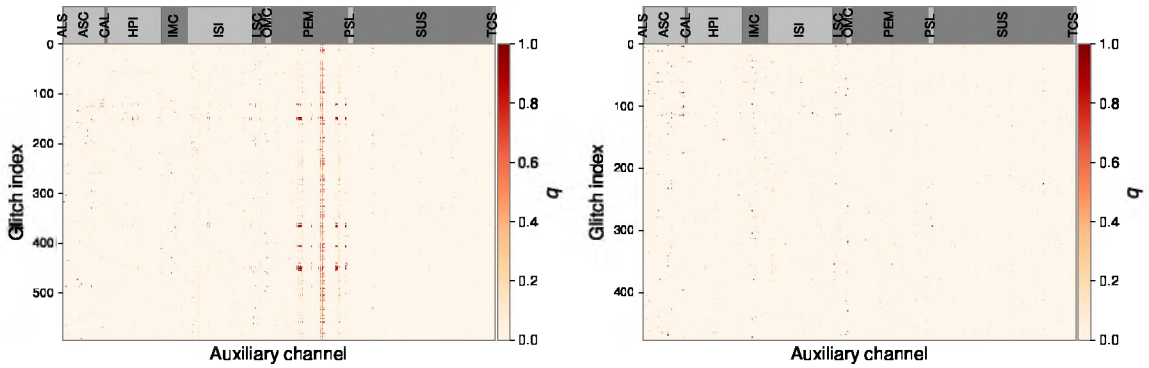

Figure 2. Left: Values of the excess power measure q for 700 safe auxiliary channels with 8 different frequency bands in coincidence with 595 magnetometer glitch set with SNR $\geq$ 7.5. Right: values of q for the null set with a sample size of 477. The channels in the 8 different frequency bands are shown side by side from left to right where the chosen frequency bands are 1-128 Hz, 128-256 Hz, 256-512 Hz, 512-1024 Hz, 1024-2048 Hz, 2048-4096 Hz, 4096-8192 Hz, and the range from 1 Hz to the Nyquist frequency. The dark and light gray bars in the top denote each of the channel groups in the common sub-instrumental sensor or environmental monitor.

Using the target and null sets in Figure 2, we calculate the probability p_g in Equation (4) for channels in each frequency band. Figure 3 shows values of p_g for the magnetometer set. PyChChoo successfully identifies the witness channels including the EX magnetometer channels as well as ISI-ETMX_ST1_BLND_Z_T240_CUR_ IN1_DQ channel in 1-128 Hz with $p_g = 0.95$, in agreement with Cavaglia *et al.* (2019).

rank	Channel	Band [Hz]	p_g	Threshold 0.9
1	PEM-EX_MAG_VEA_FLOOR_X_DQ	1-128	0.99969	pass
2	PEM-EX_MAG_VEA_FLOOR_Y_DQ	1-128	0.99939	pass
3	PEM-EX_MAG_VEA_FLOOR_Y_DQ	128-256	0.9989	pass
4	PEM-EX_MAG_VEA_FLOOR_X_DQ	128-256	0.9983	pass
5	PEM-EX_MAG_VEA_FLOOR_Z_DQ	256-512	0.99163	pass

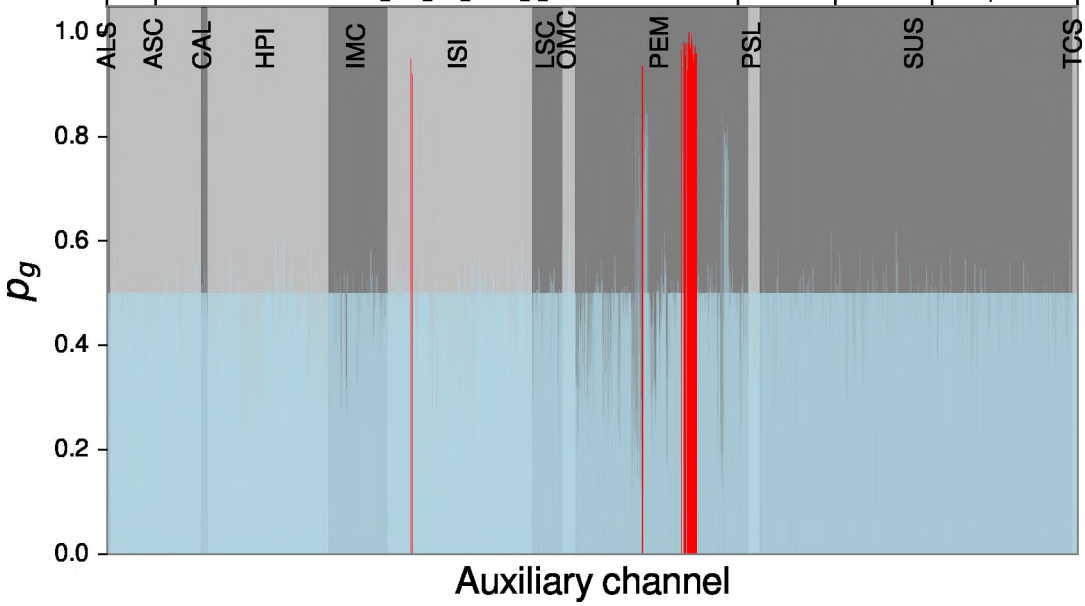

Figure 3. p_g obtained from the 700 safe auxiliary channels in 8 different frequency bands for the magnetometer set. The red (cyan) bars denote channels with a given frequency band with $p_g \geq 0.9\,(< 0.9)$. The channels in the 8 different frequency bands are shown side by side from left to right where the chosen frequency bands are 1-128 Hz, 128-256 Hz, 256-512 Hz, 512-1024 Hz, 1024-2048 Hz, 2048-4096 Hz, 4096-8192 Hz, and the range from 1 Hz to the Nyquist frequency. The dark and light gray background colors denote each of the channel groups in the common sub-instrumental sensor or environmental monitor. The table shows the top five channels in different frequency bands. *Pass* (*fail*) in the last column in the table shows whether values of p_g are above (below) 0.9.

4. APPLICATION TO AN UNMODELED GW DETECTION PIPELINE

In GW signal searches, the detection pipelines generate triggers with ranking statistics (RSs) (e.g., SNR). Typically, triggers from astrophysical signals have SNR $\gtrsim$ 8. The confidence in detecting astrophysical signals is characterized by a FAR, which is the rate of terrestrial-noise triggers with RSs equal or higher than the RS of an astrophysical candidate event. The FAR is typically required to be smaller than 2.0 per year (Abbott *et al.*, 2021).

For increasing confidence in GW detections, it is crucial to reduce outlying noise triggers with large values of RS. As mentioned earlier, unmodeled detection pipelines are typically susceptible to glitches, causing a large number of noise triggers with high values of RS. Hence, we focus on noise triggers generated with one of the unmodeled pipelines called cWB (Klimenko *et al.*, 2008, 2016) in the analysis.

We use a set of *background-mode* cWB triggers created from the data of the L1 and H1 detectors between January 1st, 2020 and February 3rd, 2020. Because the background-mode cWB applies some time shifts much longer than the light-travel time between detectors, these triggers represent noise artifacts. In our analysis, there is *no* trigger of astrophysical signals in origin. In this period, the detector's output was significantly contaminated with glitches, resulting in 40 cWB triggers with the RS of $\rho > 9$ being generated. Around the trigger time in the L1 detector, we analyze the data from auxiliary channels with PyChChoo.

Because more than one trigger representing a same glitch could be generated in the proximity of trigger times in a detector, we cluster the cWB triggers by keeping the subset of triggers with the largest value of ρ in the window of 0.5 seconds to avoid double-counting glitches. For the target set, we choose the 39 clustered outlying trigger with $\rho > 9$. We consider the clustered trigger times as the center times for the target samples. Also, we manually choose the duration of 1 second for these samples because the durations provided by cWB are found to be too small (typically ~ 0.01 seconds) to represent the durations of glitches. For the null set, we create 200 samples with a duration of 1 second during the quiet period when there is no Omicron trigger with SNR ≥ 5.5. We use the 759 safe channels in the L1 detector and 9 different frequency bands for each of the channels. In this analysis, we have a band of 1-50 Hz in addition to a list of bands used in the previous section because the peak frequency of some cWB triggers is around 20 Hz and the witness of those triggers are expected to have excess power only in the low-frequency (below ~ 40 Hz) region.

Figure 4 shows three witness channels with values of $p_g \geq 0.9$. The first-ranked channel (ASC-CSOFT) monitors the motions of mirrors in the arm in the GW detector. The second-ranked channel (LSC-REFL) typically monitors the laser intensity dips. The third-ranked channel (SUS-ETMX) monitors the displacement in the suspension system in the end station in the X-arm.

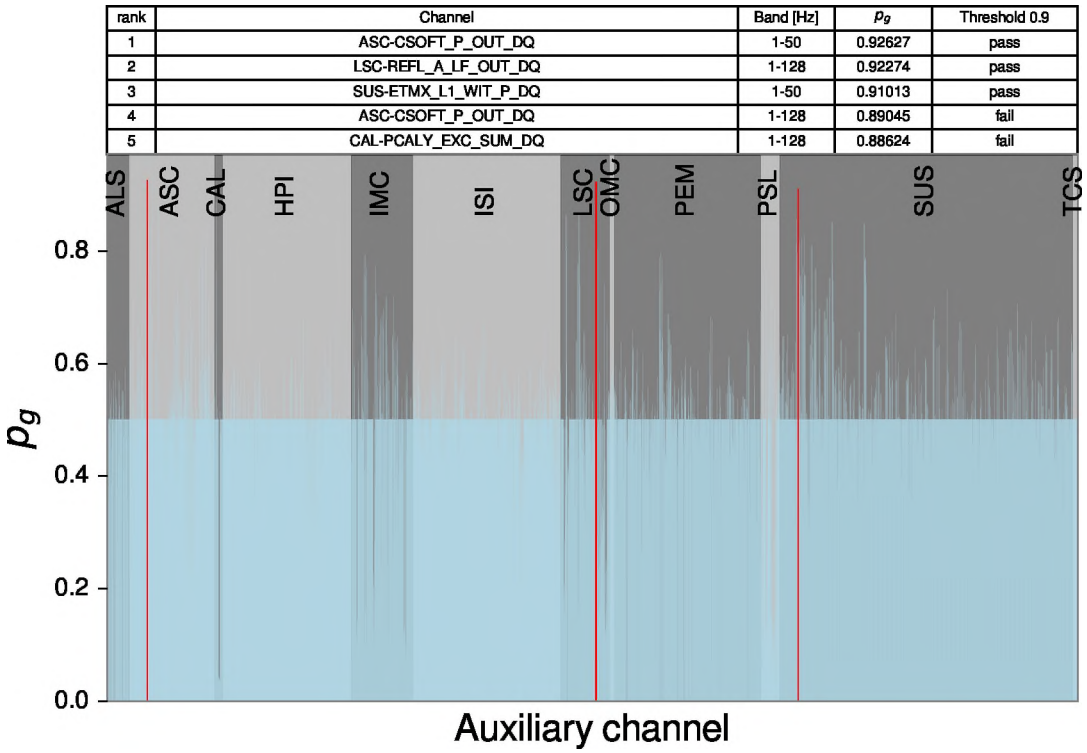

Figure 4. p_g obtained from the 759 safe auxiliary channels in 8 different frequency bands for the clustered outlying cWB triggers with $\rho > 9$ from January 1st to February 3rd, 2020. The red (cyan) bars denote channels with a given frequency band with $p_g \geq 0.9\,(< 0.9)$. The channels in the 9 different frequency bands are shown side by side from left to right where the chosen frequency bands are 1-50 Hz, 1-128 Hz, 128-256 Hz, 256-512 Hz, 512-1024 Hz, 1024-2048 Hz, 2048-4096 Hz, 4096-8192 Hz, and the range from 1 Hz to the Nyquist frequency. The dark and light gray background colors denote each of the channel groups in the common sub-instrumental sensor or environmental monitor. The table shows the top five channels in different frequency bands. *Pass* (*fail*) in the last column in the table shows whether values of p_g are above (below) 0.9.

Using values of p_v obtained with the top two channels in the frequency band in Figure 4, we consider triggers to be vetoed using the 1-second window around the trigger. We find that the channels up to the second-ranked are sufficient because no additional triggers can be removed by adding the third-ranked channel. For vetoing triggers, we choose a conservative criterion of $p_v > 0.95$. The left panel in Figure 5 shows the cWB outlying triggers which can be vetoed. The triggers with a central frequency less than 80 Hz are typically vetoed with the ASC-CSOFT channel because the mirror motion produces low-frequency glitches shown in the left panels in Figure 6. Because the glitches produced by the laser power intensity dips typically have a large bandwidth ranging from ~10 to ~ 2000 Hz, vetoed triggers with the LSC-REFL have the central frequencies of either less than ~ 110 Hz or greater than ~ 800 Hz. Figure 6 shows two representative glitches witnessed with either the ASC-CSOFT or LSC-REFL channels. Overall, 72.5% of 40 outlying triggers in this search period can be vetoed with our analysis. The right panel in Figure 5 shows that the rates of ρ in the cWB triggers before and after the veto.

As a complementary check, we compare our veto performance with that obtained by the current LIGO infrastructure. Using a set of veto periods obtained from three different flag categories indicating: 1) a critical issue with an abnormally operating detector (CAT1) ; 2) times of glitches with understood physical coupling between auxiliary channels and the detector's output (CAT2); and 3) times of glitches with unknown causes but statistical correlation (CAT3), 35 out of the cWB outliers can be vetoed. Because the periods of the CAT1 flag are already removed commonly for the analyses, we compare unvetoed triggers between our analysis and the union of the CAT2 and CAT3 flags. There are 4 commonly unvetoed triggers. We veto a single trigger that is not vetoed with the CAT2 and CAT3 flags because of the chance-coincident excess power witnessed with the LSC-LEFT channel. Seven triggers are vetoed with the CAT2 and CAT3 flags but not vetoed with our analysis. This discrepancy can be explained for two reasons. Because our veto window is 1 second around the trigger time, the quantity for the excess power outside this window is not large

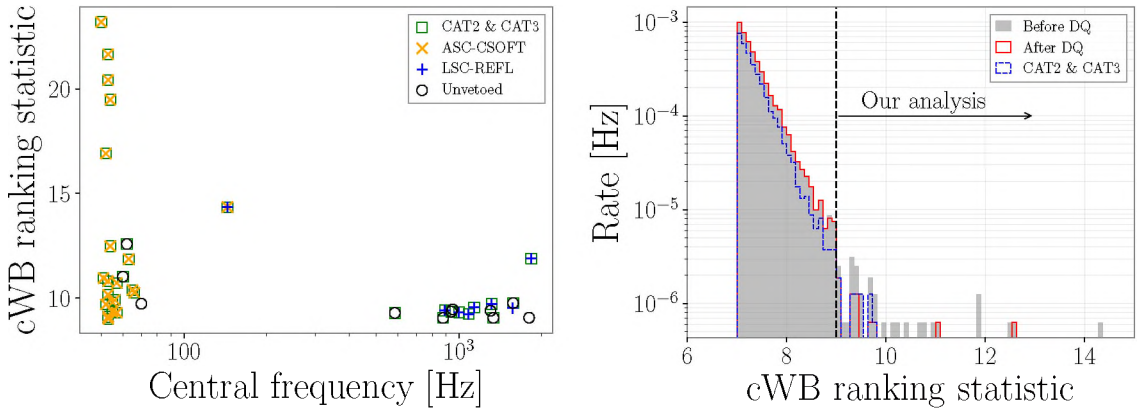

Figure 5. Left: 40 outlying *background* cWB triggers with the ranking statistic of $\rho > 9$. Right: Rate of all the *background* cWB triggers between January 1st, 2020 and February 3rd, 2020. The orange-× (blue-+) markers denote the triggers vetoed with ASC-CSOFT (LSC-REFL) channels based on the criterion of $p_v > 0.95$. The black circles denote the remaining triggers in our analysis. The green squares denote the triggers vetoed with the CAT2 and CAT3 flags. The grey and red histograms denote the rates with cWB triggers before and after our veto, respectively. The blue-dashed histogram is the rate after the CAT and CAT3 flags applied.

enough to pass our veto criterion. Otherwise, channels other than the two high-ranked witness channels selected in our analysis might witness coincident excess power. Table 1 summarizes details about these triggers. In conclusion, we have 80% of 40 triggers are in common between our analysis and the CAT2 and CAT3 flags.

5. CONCLUSION

In this paper, we have presented a new software, PyChChoo, designed to identify the origin of glitches and remove the effect of glitches.

Using a set of time series recorded in the instrumental and environmental monitors which do not causally follow from the detector's output, PyChChoo queries the time series from each of the sensors around the times of glitches and then counts the fraction (q) of frequency bins above the stationarity upper threshold to quantify excess power. Comparing with another data set when the detector's output is quiet that is analyzed in the same way, the

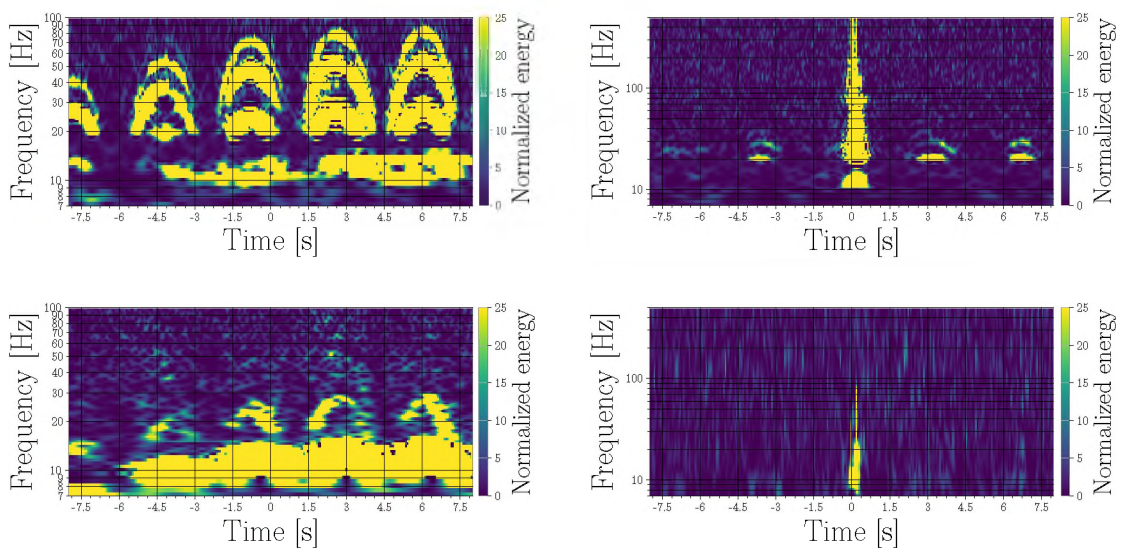

Figure 6. The time-frequency representation of the glitches in the detector's output (top) and the excess power in the witness auxiliary channels (bottom) using the Q-transform (Robinet *et al.*, 2020). The left and right panels show the glitches witnessed with the ASC-CSOFT and LSC-REFL channels, respectively. The trigger times are marked as zero on the maps. The ASC-CSOFT channel in 1-50 Hz and the LSC-REFL channel in 1-128 Hz have the values of $p_v = 0.999$ and $p_v = 0.954$ for each glitch, respectively.

witness sensors are probabilistically identified based on values of q. To remove the effect of the glitches in the detector's output, time periods when the witness sensors monitor excess power in coincidence with the glitches, are marked as a veto. The veto criterion is given as a probability that a value of q obtained with a witness channel belongs to the distribution of q in the glitch set.

To demonstrate the effect on GW searches, we have used the *background* triggers given by the cWB pipeline running on the L1 and H1 detectors from January 1st, 2020 to February 3rd, 2020. Because these triggers are generated by applying some time shifts longer than the light-travel time between detectors, there is *no* trigger of astrophysical signals in origin in our analysis. During this period, the detector's output was significantly contaminated with glitches. We analyze the data of the L1 auxiliary channels using the L1 trigger time of the outlying triggers with the ranking statistic of $\rho > 9$. We find at least

Table 1. List of 11 unvetoed outlying *background* cWB triggers with $\rho > 9$ in our analysis using a threshold of $p_v > 0.95$ for the first and second ranked witness channels with comments for triggers in the discrepancy between our analysis and the CAT2 and CAT3 flags. The trigger in the last row is vetoed because of the chance-coincident excess power witnessed by the LSC-REFL channel. The values in the columns of ASC-CSOFT and LSC-REFL denote values of p_v. The shaded rows denote the unvetoed triggers based on the CAT2 and CAT3 data quality flags of LIGO.

GPS time in L1	ASC-CSOFT in 1-50 Hz	LSC-REFL in 1-128 Hz	Comments
1262326892.30	0.874	0.905	Excess power in $(-2.0, -0.7)$ seconds in LSC-RELF
1262403661.68	0.824	0.936	Excess power in 1-50 Hz in LSC-REFL with $p_v = 0.953$
1262655787.22	0.785	0.942	Glitches in $(0.4, 1.0)$ seconds at $\sim$ 25 Hz
1262674230.37	0.874	0.930	A glitch at -1.4 seconds at $\sim$ 12 Hz
1262676098.05	0.785	0.938	Glitches below 9 Hz
1262758399.380	0.785	0.950	Quiet within (-8, 8) seconds
1262842889.30	0.824	0.899	-
1263363175.48	0.874	0.905	-
1263715708.16	0.941	0.903	-
1264327099.43	0.785	0.905	-
1264703139.12	0.785	0.905	A glitch in $(-2.5, 0)$ seconds
1262664659.84	0.824	0.960	Excess power in the LSC-REFL channel

two kinds of adversely affecting glitches to the pipeline, one of which seems to be due to the mirror-motions witnessed by the ASC-CSOFT channel and the other one seems to be typically caused by the laser intensity dips witnessed by the LSC-REFL channel with high confidence. Using these two witness channels, we consider that 72.5% of 40 outlying triggers to be vetoed. We find that none of the cWB triggers marked as being vetoed are in coincidence with super events reported in the database server of the candidate GW events (GraceDB) (Prestegard *et al.*, 2021).

As a complementary check, we compare our results with the current LIGO infrastructure; the CAT2 and CAT3 flags. We veto a single trigger that is not vetoed with the CAT2 and CAT2 flags because of the coincident excess power witness with the LSC-LEFT channel. Our analysis does not veto 7 triggers that are vetoed with the CAT2 and CAT3 flags because the excess power is present outside of the 1-second window used in our analysis or the coincident excess power is not witnessed with our selected two channels. Overall, 80% of the triggers are in common between our analysis and the LIGO infrastructure.

As mentioned, these 40 outlying triggers seem to have at least two distinct sources of glitches. In our analysis, we have used all triggers to calculate p_v. Values of p_v could be higher by grouping glitch samples based on q of all channels and calculate p_v for each group. To group samples, machine-learning clustering algorithms such as Gaussian Mixture Clustering (Ghosh and Sen, 1984; Hartigan, 1985) or Agglomerative Clustering (Gower and Ross, 1969) can be applied after using some dimensionality reduction algorithms including Principle Component Analysis (PCA) (F.R.S., 1901; Hotelling, 1933; Minka, 2000) in Scikit-Learn (Pedregosa *et al.*, 2011). PyChChoo has the in-progress implementation using Gaussian Mixture Clustering and PCA incorporating statistical tests such as a one-sided binomial test and a one-sided Welch's t-test (WELCH, 1947) to determine the number of clusters. Also, because the background cWB triggers are generated by applying some time shifts between detectors, our analysis might have a bias due to one realization of time shifts. To reduce the bias, a higher number of time shifts can be chosen to generate a larger number of background cWB triggers.

PyChChoo has several advantages. Firstly, it can work with any ETGs running only on the detector's output without the use of them running on auxiliary channels. Secondly, because a list of glitches can be chosen by a user, it can be used to help to understand the origin of glitches which are only adversely affecting a particular GW detection pipeline with specific parameters, e.g., high ranking statistic. The current existing veto infrastructure typically uses Omicron ETG. Omicron is intended to capture a wide variety of glitches

including those that are not similar to astrophysical GW signals. Analyzing only the data set obtained from a particular GW detection pipeline might make improvements in reducing veto times. Also, it takes less than 1 minute to analyze all the safe auxiliary channels and identify potentially witness channels for a given trigger. Therefore, it can be used for medium latency operations to assess if a trigger is due to astrophysical or terrestrial origin.

In addition to the purpose of vetoing glitches and the usage for the medium latency operations, PyChChoo has another crucial advantage. As discussed in Sec. 3, PyChChoo can find witness channels that hVETO might miss so that it can be used for the follow-up study about glitches identified by hVETO. This feature is beneficial for understanding more thoroughly about noise couplings inside the instruments. For glitches with the instrumental origin, noise couplings that cause glitches could be potentially mitigated by tuning the pieces of equipment setting or replacing them with improved ones. If mitigating of the cause is difficult to operate or the cause is of environmental origin, we envision that those glitches can be subtracted using the data recorded in witness channels based on a method similar to Ormiston *et al.* (2020) but adapted to transient noise artifacts. The Bayesian inference approach to subtract glitches is available for a signal from the compact binary merger (Chatziioannou *et al.*, 2021; Cornish, 2021). However, a subtraction method using auxiliary channels could have a significant impact on unmodeled search pipelines in the future.

As the detector's sensitivity increases, in particular, at the low-frequency region below $\sim$ 80 Hz, unmodeled GW detection pipelines play important roles in observing intermediate binary black hole (IMBBH) following the detection on May 21st, 2019 (Abbott *et al.*, 2020). Understanding the cause of glitches and mitigating those will be more crucial.

ACKNOWLEDGEMENTS

K.M. is supported by the U.S. National Science Foundation grant PHY-1921006. The author would like to thank their LIGO Scientific Collaboration and Virgo Collaboration colleagues for their help and useful comments, in particular Amber L. Stuver, Duncan MacLeod, Brennan Hughey, Marco Cavaglià, and Ryan Quitzow-James. The author is grateful for computational resources provided by the LIGO Laboratory and supported by the U.S. National Science Foundation Grants PHY-0757058 and PHY-0823459, as well as a service of the LIGO Laboratory, the LIGO Scientific Collaboration and the Virgo Collaboration. LIGO was constructed and is operated by the California Institute of Technology and Massachusetts Institute of Technology with funding from the U.S. National Science Foundation under grant PHY-0757058. Virgo is funded by the French Centre National de la Recherche Scientifique (CNRS), the Italian Istituto Nazionale di Fisica Nucleare (INFN) and the Dutch Nikhef, with contributions by Polish and Hungarian institutes. The publicly available source code in `https://git.ligo.org/kentaro.mogushi/origli` is made use of python packages including SciPy Virtanen *et al.* (2020), GWPy (Macleod *et al.*, 2020), Pandas (Reback *et al.*, 2021), GWTrigFind (Macleod and Nitz, 2019), Matplotlib (Hunter, 2007), nds2utils (Cahillane, 2020), and scikit-learn (Pedregosa *et al.*, 2011). This manuscript has been assigned LIGO Document Control Center number LIGO-P2100031.

REFERENCES

Aasi, J. *et al.*, 'Advanced LIGO,' Class. Quant. Grav., 2015, **32**, p. 074001, doi: 10.1088/0264-9381/32/7/074001.

Abbott, B. P. *et al.*, 'Observation of Gravitational Waves from a Binary Black Hole Merger,' Phys. Rev. Lett., 2016, **116**(6), p. 061102, doi: 10.1103/PhysRevLett.116.061102.

Abbott, B. P. *et al.*, 'Gwtc-1: A gravitational-wave transient catalog of compact binary mergers observed by ligo and virgo during the first and second observing runs,' Phys. Rev. X, 2019, **9**, p. 031040, doi: 10.1103/PhysRevX.9.031040.

Abbott, R. *et al.*, 'GW190521: A Binary Black Hole Merger with a Total Mass of 150 M⊙,' Phys. Rev. Lett., 2020, **125**(10), p. 101102, doi: 10.1103/PhysRevLett.125.101102.

Abbott, R. *et al.*, 'GWTC-2: Compact Binary Coalescences Observed by LIGO and Virgo During the First Half of the Third Observing Run,' Phys. Rev. X, 2021, **11**, p. 021053, doi: 10.1103/PhysRevX.11.021053.

Acernese, F. *et al.*, 'Advanced Virgo: a second-generation interferometric gravitational wave detector,' Class. Quant. Grav., 2015, **32**(2), p. 024001, doi: 10.1088/0264-9381/32/2/024001.

Biswas, R. *et al.*, 'Application of machine learning algorithms to the study of noise artifacts in gravitational-wave data,' Phys. Rev. D, 2013, **88**(6), p. 062003, doi: 10.1103/PhysRevD.88.062003.

Breiman, L., 'Random Forests,' Machine Learning, 2001, **45**(1), pp. 5–32, doi: 10.1023/A:1010933404324.

Cahillane, C., 'nds2utils,' 2020, https://pypi.org/project/nds2utils/.

Cavaglia, M., Staats, K., and Gill, T., 'Finding the origin of noise transients in LIGO data with machine learning,' Commun. Comput. Phys., 2019, **25**(4), pp. 963–987, doi: 10.4208/cicp.OA-2018-0092.

Chatziioannou, K., Cornish, N., Wijngaarden, M., and Littenberg, T. B., 'Modeling compact binary signals and instrumental glitches in gravitational wave data,' Phys. Rev. D, 2021, **103**(4), p. 044013, doi: 10.1103/PhysRevD.103.044013.

Cornish, N. J., 'Rapid and Robust Parameter Inference for Binary Mergers,' Phys. Rev. D, 2021, **103**(10), p. 104057, doi: 10.1103/PhysRevD.103.104057.

Cutler, C. and Flanagan, E. E., 'Gravitational waves from merging compact binaries: How accurately can one extract the binary's parameters from the inspiral wave form?' Phys. Rev. D, 1994, **49**, pp. 2658–2697, doi: 10.1103/PhysRevD.49.2658.

Essick, R., Mo, G., and Katsavounidis, E., 'A Coincidence Null Test for Poisson-Distributed Events,' Phys. Rev. D, 2021, **103**(4), p. 042003, doi: 10.1103/PhysRevD.103.042003.

F.R.S., K. P., 'Liii. on lines and planes of closest fit to systems of points in space,' The London, Edinburgh, and Dublin Philosophical Magazine and Journal of Science, 1901, **2**(11), pp. 559–572, doi: 10.1080/14786440109462720.

Ghosh, J. and Sen, P., 'On the asymptotic performance of the log likelihood ratio statistic for the mixture model and related results,' North Carolina State University. Dept. of Statistics, 1984 .

Gower, J. C. and Ross, G. J. S., 'Minimum spanning trees and single linkage cluster analysis,' Journal of the Royal Statistical Society. Series C (Applied Statistics), 1969, **18**(1), pp. 54–64, ISSN 00359254, 14679876.

Hartigan, J. A., 'A failure of likelihood asymptotics for normal mixtures,' Semantic Scholar, 1985 .

Hotelling, H., 'Analysis of a complex of statistical variables into principal components,' Journal of Educational Psychology, 1933, pp. 417–441.

Hunter, J. D., 'Matplotlib: A 2d graphics environment,' Computing in Science & Engineering, 2007, **9**(3), pp. 90–95, doi: 10.1109/MCSE.2007.55.

Isogai, T., 'Used percentage veto for LIGO and virgo binary inspiral searches,' J. Phys. Conf. Ser., 2010, **243**, p. 012005, doi: 10.1088/1742-6596/243/1/012005.

Klimenko, S., Yakushin, I., Mercer, A., and Mitselmakher, G., 'Coherent method for detection of gravitational wave bursts,' Class. Quant. Grav., 2008, **25**, p. 114029, doi: 10.1088/0264-9381/25/11/114029.

Klimenko, S. *et al.*, 'Method for detection and reconstruction of gravitational wave transients with networks of advanced detectors,' Phys. Rev. D, 2016, **93**(4), p. 042004, doi: 10.1103/PhysRevD.93.042004.

Macleod, D. and Nitz, A., 'gwtrigfind,' 2019, https://pypi.org/project/gwtrigfind/0.8.0/.

Macleod, D., Urban, A. L., Coughlin, S., Massinger, T., Pitkin, M., rngeorge, paulaltin, Areeda, J., Singer, L., Quintero, E., Leinweber, K., and Badger, T. G., 'gwpy/gwpy: 2.0.2,' 2020, doi: 10.5281/zenodo.4301851.

Minka, T. P., 'Automatic choice of dimensionality for pca,' NIPS, 2000, **13**, p. 514.

Nitz, A. H., Dal Canton, T., Davis, D., and Reyes, S., 'Rapid detection of gravitational waves from compact binary mergers with PyCBC Live,' Phys. Rev. D, 2018, **98**(2), p. 024050, doi: 10.1103/PhysRevD.98.024050.

Nitz, A. H., Dent, T., Dal Canton, T., Fairhurst, S., and Brown, D. A., 'Detecting binary compact-object mergers with gravitational waves: Understanding and Improving the sensitivity of the PyCBC search,' Astrophys. J., 2017, **849**(2), p. 118, doi: 10.3847/1538-4357/aa8f50.

Ormiston, R., Nguyen, T., Coughlin, M., Adhikari, R. X., and Katsavounidis, E., 'Noise Reduction in Gravitational-wave Data via Deep Learning,' Phys. Rev. Res., 2020, **2**(3), p. 033066, doi: 10.1103/PhysRevResearch.2.033066.

Pedregosa, F., Varoquaux, G., Gramfort, A., Michel, V., Thirion, B., Grisel, O., Blondel, M., Prettenhofer, P., Weiss, R., Dubourg, V., Vanderplas, J., Passos, A., Cournapeau, D., Brucher, M., Perrot, M., and Duchesnay, E., 'Scikit-learn: Machine learning in Python,' Journal of Machine Learning Research, 2011, **12**, pp. 2825–2830.

Prestegard, T., Pace, A., Stephens, B., Moe, B., and Brady, P., '"gracedb",' 2021, accessed: 2021-01-26.

Reback, J., jbrockmendel, McKinney, W., den Bossche, J. V., Augspurger, T., Cloud, P., Hawkins, S., gfyoung, Sinhrks, Roeschke, M., Klein, A., Petersen, T., Tratner, J., She, C., Ayd, W., Hoefler, P., Naveh, S., Garcia, M., Schendel, J., Hayden, A., Saxton, D., Gorelli, M. E., Shadrach, R., Jancauskas, V., McMaster, A., Battiston, P., Li, F., Seabold, S., Dong, K., and chris b1, 'pandas-dev/pandas: Pandas 1.3.0rc1,' 2021, doi: 10.5281/zenodo.4940217.

Robinet, F., Arnaud, N., Leroy, N., Lundgren, A., Macleod, D., and McIver, J., 'Omicron: A tool to characterize transient noise in gravitational-wave detectors,' SoftwareX, 2020, p. 100620, ISSN 2352-7110, doi: https://doi.org/10.1016/j.softx.2020.100620.

Sachdev, S. *et al.*, 'The GstLAL Search Analysis Methods for Compact Binary Mergers in Advanced LIGO's Second and Advanced Virgo's First Observing Runs,' 2019.

Smith, J. R., Abbott, T., Hirose, E., Leroy, N., Macleod, D., McIver, J., Saulson, P., and Shawhan, P., 'A Hierarchical method for vetoing noise transients in gravitational-wave detectors,' Class. Quant. Grav., 2011, **28**, p. 235005, doi: 10.1088/0264-9381/28/23/235005.

Staats, K., Pantridge, E. R., Cavaglia, M., Milovanov, I., and Aniyan, A., 'Tensorflow enabled genetic programming,' CoRR, 2017, **abs/1708.03157**.

Sutton, P. J. *et al.*, 'X-Pipeline: An Analysis package for autonomous gravitational-wave burst searches,' New J. Phys., 2010, **12**, p. 053034, doi: 10.1088/1367-2630/12/5/053034.

Virtanen, P. *et al.*, 'SciPy 1.0: Fundamental Algorithms for Scientific Computing in Python,' Nature Methods, 2020, **17**, pp. 261–272, doi: 10.1038/s41592-019-0686-2.

WELCH, B. L., 'THE GENERALIZATION OF 'STUDENT'S' PROBLEM WHEN SEVERAL DIFFERENT POPULATION VARLANCES ARE INVOLVED,' Biometrika, 1947, **34**(1-2), pp. 28–35, ISSN 0006-3444, doi: 10.1093/biomet/34.1-2.28.

Zevin, M. *et al.*, 'Gravity Spy: Integrating Advanced LIGO Detector Characterization, Machine Learning, and Citizen Science,' Class. Quant. Grav., 2017, **34**(6), p. 064003, doi: 10.1088/1361-6382/aa5cea.

II. REDUCTION OF TRANSIENT NOISE ARTIFACTS IN GRAVITATIONAL-WAVE DATA USING DEEP LEARNING

Kentaro Mogushi
Institute of Multi-messenger Astrophysics and Cosmology
Missouri University of Science and Technology
Physics Building, 1315 N. Pine St.
Rolla, MO 65409, USA
mogus261@gmail.com

ABSTRACT

Excess transient noise artifacts, or "glitches" impact the data quality of ground-based GW detectors and impair the detection of signals produced by astrophysical sources. Mitigation of glitches is crucial for improving GW signal detectability. However, glitches are the product of short-lived linear and non-linear couplings among the interrelated detector-control systems that include mitigation of ground motion and regulation of optic motion, generally making it difficult to model noise couplings. Hence, typically time periods containing glitches are vetoed to mitigate the effect of glitches in GW searches at the cost of reduction of the analyzable data. To increase the available data period and improve the detectability for both model and unmodeled GW signals, we present a new machine learning-based method which encompasses on-site sensors monitoring the instrumental and environmental disturbances to model noise couplings and subtract glitches in GW detector data. We find that our method reduces 20-70% of the glitch signal-to-noise ratio. By injecting software simulated signals into the data and recovering them with one of the unmodeled GW detection pipelines, we address the robustness of the glitch-reduction technique to efficiently remove glitches with no unintended effects on GW signals.

Keywords: gravitational-waves, glitch, statistics

1. INTRODUCTION

The first detection of a GW signal from a BBH merger (Abbott *et al.*, 2016b) on September 14th, 2019 was the breakthrough of GW astronomy. One of the dominating factors for the breakthrough in 2015 was the improvement of the detector sensitivity by a factor of $\sim$ 10 at the detector's most sensitive frequency compared to the initial LIGO (Aasi *et al.*, 2015a). Reducing transient and periodic noise sources in instrumental and environmental origin may enhance the identification of GW signals by increasing the significance of candidate events of astrophysical signals and avoiding classifying them as sub-threshold triggers (Abbott *et al.*, 2019; Riles, 2013).

The physical couplings due to the detector design are noise sources such as the fluctuating amplitude of laser light in the arm cavities, fluctuations of the photon arrival time at the output-port photodiode, thermal fluctuations of mirror coatings, and optic suspension (Aasi *et al.*, 2015b). Besides, during observation runs, environmental and instrumental noise sources including wind or ground motions as well as optic-controlling systems limit the detector sensitivity (Abbott *et al.*, 2016a). Reducing the effect of these noise sources on the detector's output, *strain* channel, is crucial to improve the detectability of any GW signals and better understand physics in the universe.

The Advanced LIGO (aLIGO) detector use approximately twenty hundred thousand auxiliary *channels*, or sensors/control-subsystems that monitor different aspects of environmental and instrumental conditions inside and around the detectors in parallel to the strain channel in the time domain. These auxiliary channels can be potential witnesses of couplings of noise sources and can be used to subtract the noise in the strain channel.

Long-lasting noise sources with a duration longer than $\sim$ 4 seconds have linear and/or non-linear non-stationary coupling mechanisms (Ormiston *et al.* (2020) set the analysis window to be 8 seconds for the long-lasting noise). Among others, the main technique to subtract linearly coupled long-lasting noise sources is to calculate coherence between the witness channels and the strain channel. For example, the main source in

$\sim 50 - 1000$ Hz frequency band coupled linearly with the jitter of the pre-stabilization laser beam in angle and size was subtracted (Davis *et al.*, 2019; Driggers *et al.*, 2019; Kwee *et al.*, 2012; Schofield, 2016). For non-linearly and non-stationary coupled noise sources in environmental and instrumental origin, techniques with machine learning algorithms show successful subtractions and improve the detector sensitivity (Meadors *et al.*, 2014; Mukund *et al.*, 2020; Ormiston *et al.*, 2020; Tiwari *et al.*, 2015; Vajente *et al.*, 2020).

Other than long-lasting noise, transient noise artifacts, or *glitches* significantly impair the quality of GW detector data and reduce confidence in the significance of candidate GW events because glitches may resemble astrophysical signals. Glitch removal is crucial for GW signal searches. However, glitches are the product of **short-lived** linear and non-linear couplings among interrelated detector subsystems, generally making it difficult to find their coupling mechanisms. To mitigate the effect of glitches on GW searches, LIGO-Virgo collaboration vetoes time periods where glitches are present (Abbott *et al.*, 2021; Davis *et al.*, 2021) or reduces the significance of GW candidates based on the probability of the glitch presence (Godwin *et al.*, 2020). Software engines such as UPV (Isogai, 2010), hVETO Smith *et al.* (2011), Pointy Poisson Essick *et al.* (2021), PyChChoo (Mogushi, 2021), and ıDQ (Biswas *et al.*, 2013; Essick *et al.*, 2020) find the statistical correlation of glitches between the detector's output and numerous auxiliary channels to identify the presence of glitches while avoiding the mitigation of astrophysical signals.

The above mitigation techniques have disadvantages: reduction of the analyzable data which might contain GW signals or remaining the effect of the glitch contamination on the data. Therefore, it is desirable to subtract glitches for overcoming the above disadvantages. The functional forms to model the coupling mechanisms of glitches can require detailed knowledge of instrumental subsystems and a large number of parameters (Was *et al.*, 2021). Also, there exist situations where functional forms can not be obtained because of unknown physical mechanisms about glitches. In addition to subtraction techniques for long-lasting noise sources noted above, other machine learning techniques have shown

promising applications to GW astronomy (Cuoco *et al.*, 2021). For instance, (Mukund *et al.*, 2017) present a method using various techniques including the wavelet decomposition to classify transient excess-power waveforms injected into the simulated Gaussian data and real data during the LIGO's sixth science run. Soni *et al.* (2021) show updated results of a glitch-classification software Gravity Spy (Zevin *et al.*, 2017) to the third observation run (O3) data with the help of citizen scientists. Biswas *et al.* (2013) show the comparison of various machine-learning algorithms to predict the presence of glitches based on auxiliary channels (Biswas *et al.*, 2013). (Mogushi *et al.*, 2021) introduce a method to estimate the data containing a CBC signal lost due to the presence of an overlapping glitch. These successes motivate us to develop a new machine learning-based method to subtract glitches using auxiliary channels with no dependency from any astrophysical-signal waveforms and no precise prior knowledge of all the system configurations, allowing the method to be easily adaptive to changes in the detector settings.

In this paper, we present a machine learning-based algorithm that subtracts glitches in the detector's output using auxiliary witness channels. Using two classes of glitches that are adversely affecting unmodeled GW detection searches, we characterize the performance of our subtraction technique. Adding simulated GW signals to the data before subtraction, we validate the algorithm not to manipulate or introduce biases to the resultant estimates of the astrophysical parameters.

2. GLITCH SUBTRACTION PIPELINE

We introduce the analysis pipeline applied to the ground-based GW data for glitch subtraction. The pipeline processes the spectrograms magnitude of time series recorded in the strain channel, $h(t)$, and a set of witness auxiliary channels for a class of glitches, $a_i(t)$. Those witness auxiliary channels do not causally follow from the detector's output where astrophysical signals are present. Choosing such channels allows the pipeline to only subtract glitches while preserving astrophysical signals. The algorithm uses a 2-dimensional

Convolutional Neural Network (CNN) which uses a user-chosen set of witness channels as the input and then outputs the predicted spectrogram magnitude of glitches in $h(t)$. The output of the CNN is then converted to time series using the Fast Griffin-Lim (FGL) transformation (Griffin and Jae Lim, 1984; Perraudin *et al.*, 2013) and conditioned before being subtracted from $h(t)$.

2.1. FORMALISM AND LOSS FUNCTION

The time series $h(t)$ in the strain channel can be formulated as

$$s(t) = h(t) + g(t) + n(t), \tag{1}$$

where $h(t)$ is the astrophysical signal that may be present in the data, $g(t)$ is a user-targeted glitch waveform that is coupled with witness channels, and $n(t)$ represents the sum of untargeted glitch waveforms and the noise that are not wanted to be subtracted. We design the pipeline to produce an estimate of $g(t)$ from a set of witness channels $a_i(t)$ and subtract it from $s(t)$.

Because the amplitude of a glitch waveform varies rapidly and differently in a given frequency bin over its duration, it is more efficient to build the frequency-dependent features before the data being fed into the neural network to learn the glitch-couplings. We create the discrete short-time Fourier transform (STFT) from the time series. The STFT divides the time series into small segments and calculates a discrete Fourier transform of each of divided segments. The STFT comprises the real and imaginary parts, which can be inverted to the corresponding time series. However, we find that the neural network more efficiently learns the wanted output with the magnitude of STFT (mSTFT) than using both real and imaginary parts together because the mSTFT has a simpler pattern than the real and imaginary parts individually have. The limitation of using the mSTFT is that it is not invertible. To compensate for this limitation, we use the FGL transformation (Griffin

and Jae Lim, 1984; Perraudin *et al.*, 2013) to invert the mSTFT to the corresponding time series by estimating the phase evolution. Because the phase is not fully recovered in this transformation, the phase of the estimated glitch waveform might slightly shift from the phase of the true waveform and the estimated waveform might have the opposite sign of the amplitude. Using the least square fitting method, we allow the amplitude of the estimated glitch waveform to change up to a factor of ±3 and allow the phase to shift up to ±0.02 seconds. We find that correcting the amplitude of the estimated waveform produces a better subtraction while preserving potential astrophysical signals. Also, changing the magnitude of the estimated waveform helps us avoid unwanted data manipulation because the amplitude correction factor tends to be zero when the estimated waveform mismatches the true glitch waveform.

Because of the complexity in estimating $g(t)$ directly, we design the neural network to uses the witness channels and produce an estimate of the mSTFT $G(t, f)$ of a glitch waveform, where f denotes the frequency. The neural network can be represented as a function $\mathcal{F}(A_i(t, f); \vec{\theta})$ which maps the magnitude mSTFTs $A_i(f, t)$ of the witness channels to $G(t, f)$ given a set of parameters $\vec{\theta}$. The parameters are obtained by minimizing a loss function J which denotes the difference between the real glitch mSTFT and the predicted counterpart. The operation in the network can be formulated as

$$\vec{\theta} = \text{argmin}_{\vec{\theta}'} J \left[G(t, f), \mathcal{F}(A_i(t, f); \vec{\theta}') \right] . \tag{2}$$

In the analysis, we choose the loss function to be the mean squared error (MSE) across each pixel of mSTFT as

$$J = \frac{1}{N} \sum_{k=1}^{N} (G[k] - \hat{G}[k; \vec{\theta}])^2 , \tag{3}$$

where k denotes each pixel, N is the total number of pixels, and $\hat{G}[k; \vec{\theta}] := \mathcal{F}(A_i(t, f), \vec{\theta})[k]$ is an estimate of mSTFT obtained with the neural network.

In practice, the dimension of mSTFT depends on the duration of $g(t)$, its sampling rate, and a user-chosen frequency resolution for mSTFT. Using an appropriate combination of the neural internal window function called *kernel* and the mSTFT dimension, the neural network can efficiently minimize the loss function.

2.2. DATA PRE-PROCESSING

The target class of glitches and its witness channels are chosen to create the data set for the neural network. We select a target glitch class that is labeled by a machine-learning classification tool called Gravity Spy (Zevin *et al.*, 2017) which classifies glitches based on their time-frequency representation (TFR) morphology using the Q-transform (Robinet *et al.*, 2020). Gravity Spy might misclassify some glitches by assigning inappropriate names. Also, some glitches are not loud enough to be worth to be subtracted. Because of the above two reasons, we select a set of glitches in the class with a relatively high SNR threshold (e.g., 10) and classification confidence level (e.g., 0.9) for the glitches.

To find the witness channels for these glitches, we use the software called PyChChoo which allows us to analyze safe auxiliary channels in the coincident windows for the glitches and discover witness channels statistically. Because of the computational efficiency for training the neural network and the achievement of an efficient prediction made by the network, using only witness channels without non-witness channels is sufficient. We use the auxiliary channels having the probability that the glitch set is louder than the quiet set greater than 0.9 as the witness channels. Because different noise couplings might produce a similar TFR morphology, not all of the glitches in the class have a strong correlation with excess power recorded in the witness channels. Therefore, we select the subset of glitches in a class with their top-ranked witness channel has the probability of an excess-power measure belonging to the glitch set, above 0.9 (Mogushi, 2021) to make sure that the subset of glitches has a strong correlation with the witness channel. Around the time of glitches, we use a set of time series of the strain and the witness channels with a duration of 36 seconds.

Glitches are excess power transients that are distinctively different from long-term varying noise sources. To filter out the long-term varying noise and magnify the characteristic of glitches, we whiten the time series by calculating the convolution between the time series and the time-domain *finite-impulse-response* filter created with the median value of ASDs, where each ASD is the square root of PSD obtained by calculating the ratio of the square of the FFT amplitude with the Hanning window (Essenwanger, 1986) of the divided time series with a duration of 2 seconds, to a given frequency-bin width (see details in Macleod *et al.* (2020)). The choice of 36-second duration for the time series is motivated such that the median value of ASD appropriately captures the long-term varying noise characteristic.

To have the same dimension for the mSTFTs of the glitch waveform and $a_i(t)$ and save the computational cost, we re-sample the whitened time series with the same sampling rate. For the glitch class used in the results in Sec. 3, we choose the sampling rate to be the lowest sampling rate of witness channels. This choice of sample rate has the Nyquist frequency ~ 2 times higher than the highest frequency of the glitch so that all the characteristics of glitches are captured. To subtracting a glitch waveform from $s(t)$, this choice also makes the resolution of the predicted glitch waveform small enough to apply a small time shift (~ 0.02 seconds) for the phase correction.

To extract a glitch waveform $g(t)$, we consider two distinct time-frequency regions. Glitches are expected to be present in one of the regions and not present in the other region. For example, for one of the glitch classes called *Scattered light* glitches in Sec. 3, we consider the two frequency regions above or below the highest frequency of the glitch (e.g., 100 Hz). We assume that the upper-frequency region represents the STFTs of $n(t)$ in Equation (1) and the lower-frequency region represents the STFT containing glitches (see Appendix F for the verification of this assumption). We keep pixels in both real and imaginary parts in the lower frequency region of the STFT with their magnitude values above 99 percentile (see the study regarding this threshold choice in Appendix F) of the mSTFT value in the upper-frequency region, otherwise, set the pixel values to be zero. Subsequently, we set the

pixel values in the upper region to be zero as well. After extracting the STFT of a glitch waveform, we invert the STFT to the time series to obtain the extracted glitch waveform. For *Scattered light* glitches, we find that the median value of the overlap O (defined in Equation (4)) between the predicted mSTFTs from the network and the mSTFTs of the extracted glitch waveform with the cutoff frequency of 100 Hz is 1% greater than the overlap with the cutoff frequency of 200 Hz. As Appendix F shows that the mSTFT does not contain excess power above the Gaussian fluctuations in the frequency region above 100 Hz in the data of *Scattered light* glitches, choosing the cutoff frequency of 200 Hz lets the data keep a few pixels of Gaussian fluctuations above 200 Hz. Therefore, the overlap with the cutoff frequency of 100 Hz is larger than that with the cutoff frequency of 200 Hz. We choose a different choice in splitting the time-frequency region in STFTs for the other class of glitches (see details in Sec. 3). To determine choices of splitting the time-frequency region in STFTs, one can use the method shown in Appendix F and/or use the peak times and peak frequencies of Omicron triggers (Robinet *et al.*, 2020) to find if glitches are isolated in the time domain (see details in Appendix F) or glitches have excess power in a particular frequency region (see details in Sec. 1.3).

To help the network learn the excess-power couplings more efficiently, we then divide each time series into smaller overlapping segments. Each training sample comprises segments from multiple witness channels. Larger overlap durations increase the data-set size so that the network can have more learnable resources and hence predict the output efficiently at the cost of computational time and memory.

Some of the segments might contain no glitches or only glitches that are not coupled with a set of chosen witness channels. Removing such segments from the data set helps the network learn the couplings more robustly. Using constant Q-transform (CQT) in nnAudio (Cheuk *et al.*, 2020), we only select segments with the peak pixel in the CQT of the strain channel being loud enough and being near the peak pixels of at least one of the witness channels within a coincidence window (e.g., less than 1 second). During the

above process, we further select the subset of segments with the peak frequency within an expected frequency range. As a criterion of the loudness of the pixel, we consider the peak pixel to be loud enough compared to be the Gaussian fluctuations when the peak pixel value is louder than the 90 percentile of the pixel values by a factor of 3.

After selecting the subset of segments, we finally create the mSTFTs of training sample segments and the corresponding mSTFT of a glitch waveform. To let the network learn efficiently, we normalize the mSTFTs of the strain and witness channels with their mean μ and standard deviation σ, then use these normalized mSTFTs as the input and the true output in Equation (2) to build the network model parameters.

2.3. NEURAL NETWORK ARCHITECTURE

As mentioned in the earlier section, the pipeline uses a 2-dimensional CNN that uses the witness channels and predicts the mSTFT of a glitch waveform in the detector's output. The input for the network is a multi-dimensional image with the width (height, depth) corresponding to time-bins (frequency-bins, channels). The CNN typically consists of a series of convolutional layers, where each layer uses discrete window functions, or kernel with trainable weight. After taking the input image, the layer slides its kernel through the input image and then computes the dot products between the kernels and the portion of the image inside of the kernel. Typically, the kernel's dimension is smaller than that of the image so that the CNN learns local features in the image, making the network suitable to process locally outstanding characteristics of excess-power transients in the image. The output of each layer is passed to a non-linear activation function and becomes the input for the subsequent layer. Because the output of each layer is down-sampled, the subsequent layer represents the input image with a fewer number of features. This sequence of layers is known as an *encoder* that can extract the glitch-coupled excess-power characteristics and suppress the slowly-varying noise in the image (Bank *et al.*, 2021). After the convolutional layer, the network consists of transposed convolutional layers known as a *decoder* (Baldi,

2012; Masci *et al.*, 2011; Rumelhart *et al.*, 1988; Vincent *et al.*, 2010). Each transposed convolution layer inserts pixels of zero between the pixels in the input image and then slides the kernel to computes the dot products of kernels and the modified input image within the kernel. As a consequence, transposed convolutional layers recast the encoded image to have a higher number of pixels by up-sampling. Comprising the encoding and decoding layers (so-called *autoencoder*) (Baldi, 2012; Masci *et al.*, 2011; Rumelhart *et al.*, 1988; Vincent *et al.*, 2010), the output of the network will have the same dimension as the glitch image with extracted glitch-coupled features.

The above considerations motivate us to use the fully connected convolutional autoencoder in our network that provides an estimate of the glitch image from the witness channels' counterpart. In addition to the autoencoder, we employ a convolutional layer before the encoder to normalize the input images, and use a convolution layer after the decoder to make the output-image dimension to be the same as that of the glitch image. More specifically, the input images of the witness channels are first passed to the input convolutional layer and then normalized with *Batch Normalization* (Ioffe and Szegedy, 2015). To make the dimension of the input and output images for the network, the input layer uses a stride of 1 and an appropriate zero padding arrangement. In the encoder, the width and height of the image are reduced by a factor of 2 while the depth (or the number of channels) is increased by a factor of 2. Instead of using pooling layers (e.g., Max Pooling (Yamaguchi *et al.*, 1990)), each layer makes use of a stride of 2 with an appropriate zero padding arrangement. The output of the encoding layer is passed to the decoding layer. In the decoding layer, the width and height of the image are increased by a factor of 2 while the depth is reduced by a factor of 2 by using a stride of 2 with an appropriate zero padding arrangement. The output of the decoding layer is fed into the output convolutional layer, in which an appropriate kernel with a stride of 1 is chosen to make the final output image has the same dimension as that of the glitch image. Except for the output layer, the output of each layer is passed to an activation function before being fed into the subsequent layer.

We adopt the symmetrical structure for the autoencoder similar to Ormiston *et al.* (2020) because each convolutional layer is commonly known to learn a different level of characteristics of the input images. An earlier (later) layer in the encoder tends to learn a lower (higher) level of characteristics. Hence, the first (last) layer in the encoder extracts a lower (higher) level of characteristics that are then recast by the last (first) layer in the decoder. Likewise, the intermediate levels of characteristics are also extracted and recast by a pair of layers in the encoder and decoder.

In our analysis, the network comprises four convolutional layers for both the encoder and decoder. We choose different sizes ($\sim$ 10) of a kernel for different classes of glitches. For the activation function, we the *ReLU* (Hahnloser *et al.*, 2000; Nair and Hinton, 2010) in the input and the autoencoder layers. We do not use any activation function after the output layer. Each encoding layer increases the number of channels from the value in the input image to 8, 16, 32, and 64, respectively. Each decoding layer decreases the number of channels in inverse order.

2.4. TRAINING AND VALIDATION

The analysis of the network can be divided to be two parts; training and validation. During training, the data set are divided into smaller chunks of data, or so-called *mini-batches* to reduce the computational memory. Data in each mini-batch are fed into the network and the loss function in Equation (3) is computed by averaging over each mini-batch. The network parameters $\vec{\theta}$ are updated according to the gradient of the loss function with respect to the parameters. For calculating the gradient, we use one of the first-order stochastic gradient descent methods, *ADAM* (Kingma and Ba, 2014). We iteratively update $\vec{\theta}$ by repeating the above calculations over a number of cycles, or *epochs*. After each epoch, the loss value and the coefficient of determination are calculated using the validation set to prevent over-fitting; the network parameters are tuned with the training set so that the network tends to represent the glitch couplings contained in the training set instead of

representing the couplings in a broader data set such as a validation set which is not used to turn the network parameters. To avoid over-fitting, the validation set is chosen not to be overlapping with any data in the training set. We stop the iteration if the network shows over-fitting according to the coefficient of determination of the validation set.

2.5. OUTPUT DATA POST-PROCESSING

The output of the network is conditioned before subtracting glitches in the detector's output data. Because the glitch mSTFT is normalized with the mean μ and the standard deviation σ of the pixel values across the training set before being fed into the network, we invert the normalization by multiplying the predicted mSTFT by σ and add μ. While the true mSTFT has no negative values by definition of mSTFT, the predicted mSTFT could have negative values due to the imperfection of the network prediction. We find that the negative values of the predicted mSTFT are typically anti-correlated with the values of the true mSTFT. The median values of the overlap O in 4 between negative pixels of the predicted mSTFTs and the corresponding pixels in the true mSTFTs are approximately -0.1 and -0.35 for *Scattered light* and *Extremely loud* glitches, respectively. Taking absolute values of the predicted mSTFTs makes these negative pixels have a positive effect on the overlap of all pixels though the effect is small because the average of the absolute values of the negative pixels is only $\sim$ 5% and $\sim$ 9% of the average value of the positive pixels for *Scattered light* and *Extremely loud* glitches, respectively. Using the FGL transformation (Griffin and Jae Lim, 1984; Perraudin *et al.*, 2013), we estimate the glitch waveform from the absolute value of mSTFT predicted by the network.

Because the estimated waveform has a slightly larger or smaller amplitude compared to the extracted glitch waveform and the phase of the estimated waveform is slightly shifted due to the network-prediction imperfection and the phase-estimation uncertainty in the FGL transformation, we let the estimated waveform change only its amplitude by a factor up to ± 3 and change the phase up to ± 0.04 seconds to subtract glitches efficiently and avoid

introducing unintended effects on astrophysical signals potentially present. To determine values of the amplitude and phase correction factors, we use the least square fitting method within the time periods where the glitch is present. To determine the portion of the glitch presence, we (1) calculate the absolute values of the estimated glitch waveform, (2) then smooth the curve with the convolution with the rectangular function, and (3) finally determine the time window where the absolute values are above a threshold.

Because the glitch waveforms (including both the estimate and extracted) are fluctuated instead of that their values are smoothly increased towards the peak of amplitude, taking the time window where the absolute values are above a threshold without smoothing the curves makes the time windows to be divided and to cover only sub-portions of glitches (corresponding to high thresholds) or the time window to cover wide portions including the region with no glitches (corresponding to low thresholds). Therefore, we employ the convolution with a rectangular function as one of the smoothing methods. We typically set this threshold to be the ~ 90 percentile of the absolutes values of a set of the estimated glitch waveforms (see details for each glitch class in Appendix F and Sec. 3). To subtract glitches even more efficiently, we divide this time portion and apply the least square fitting against the strain data within the divided portions (see details for each glitch class in Sec. 3). Smaller lengths of the divided portions allow us to subtract glitches more efficiently but less robustly preserve the waveform of astrophysical signals. To balance the above two factors, we divide the time portion finer around the center time of the glitch waveform because typically glitches have higher frequencies and larger amplitudes around the center time of the waveform. In the least square fitting, we find that the subtraction is better by separating the fitting with the bounds of the amplitude correction factor either in the range $(0,3)$ or $(-3,0)$ and then choose the better fitting result based on its coefficient of determination R^2.

3. PIPELINE PERFORMANCE ON LIGO DATA

We apply our glitch subtraction pipeline to the data of the L1 detector from January 1st, 2020 to February 3rd, 2020. We choose two district classes of glitches comprising different types of noise couplings that are dominant events for creating *background* cWB (Klimenko *et al.*, 2008, 2016) triggers with high-ranking statistics to study and quantify the performance of our pipeline.

To quantify the network-prediction accuracy, we use the overlap of the true mSTFT and the predicted mSTFT of the glitch given as

$$O = \frac{\sum_{i=1}^{N} G[i]\hat{G}[i]}{\sqrt{\sum_{j=1}^{N} G^2[j] \sum_{k=1}^{N} \hat{G}^2[k]}}, \tag{4}$$

where $G[i]$ and $\hat{G}[i]$ are the true and estimated mSTFTs of the glitch, respectively, and (i, j, k) run over pixel indices, and N is the total number of pixels. The overlap indicates the direct measure of the network prediction accuracy, ranging from 0 (mismatched) to 1 (perfect matched).

SNR is the dominant factor for the detection of GW signal searches. Lowering SNR of noise artifacts improves the detectability of GW signals. . We quantify the performance of the glitch reduction with our pipeline by calculating the fraction of glitch SNR reduction (FNR) after the subtraction as

$$\mathrm{FNR} = \frac{\mathrm{SNR}_b - \mathrm{SNR}_a}{\mathrm{SNR}_b}, \tag{5}$$

where SNR_b and SNR_a are the matched-filter SNRs (Usman *et al.*, 2016) obtained using the extracted glitch waveform as a template and the data before and after the subtraction, respectively (see how to obtain the extracted glitch waveform in Sec 2.2). Values of FNR close to 1 indicate efficient glitch reductions while negative values of FNR imply the increase of the glitch energy in the data.

3.1. SCATTERED LIGHT GLITCHES

We first apply our subtraction technique to a class of glitches called *Scattered light* glitches. Typically, winds and/or earthquakes shake the detector and move the test mass mirrors in the detector arms. The displacements of the mirrors in the longitudinal or rotational directions differ the relative arm lengths to produce arch-like glitches in the mSTFT in 10 – 90 Hz, with a duration of $\sim$ 2 seconds (Davis *et al.*, 2021; Soni *et al.*, 2020, 2021).

To identify the witness channels for this glitch class, we use PyChChoo (Mogushi, 2021) on the list of *Scattered light* glitches with SNR above 10 between January 1st, 2020 and February 3rd, 2020 in the L1 detector from the Gravity Spy catalog. We use two witness channels with high confidence: L1:ASC-CSOFT_P_OUT_DQ and L1:ASC-X_TR_B_NSUM_OUT_DQ which monitor the common length of the two arms and the transmitted light from the mirror at the end of the x-arm, respectively.

To check that the top two witness channels are sufficient, we train the network with various sets of channels with the confidence of being witnesses of this glitch class from $p_g = 0.93$ up to $p_g = 0.71$ (Mogushi, 2021). We consider 11 different channel sets, where i^{th} set contains up to i^{th} ranked channels. We train the network with a learning rate of 10^{-3} ($10^{-4}/10^{-5}$) for the 1-10 (11-30/31-60) epochs, where learning rates determine the gradient to update the network parameters and smaller learning rates correspond to smaller gradients. We terminate the training process if a value of R^2 in the validation set plateaus, i.e., a value of R^2 in the current epoch does not differ from the value in the previous epoch greater than $\pm 0.001\%$. Figure 1 shows losses in Equation (3) and overlaps in the validation sets, the validation sample size, and the GPU memories used to train the network for various channel sets. Overlaps at the termination for all channel sets range in $\sim 0.7 \sim 0.8$, where the GPU memory for the 11^{th} channel set is greater than the memory for the 1^{st} channel set by a factor of 2.5. Using a higher number of witness channels with high confidence provides a larger amount of glitch-coupling information to the network and let the performance

better whereas adding low confident witness channels only provides non-glitch-coupling information to the network and does not improve the performance because the network seems not to use those low confident channels. Furthermore, using low confident channels might add data samples that have chance coincident excess power between these channels and the strain channels and/or subdominant glitch-coupling information (see details for the coincident selection in Sec. 2.2), where the size of the validation set for the 11^{th} channel set is greater than the size for the 1^{st} channel set by a factor of 1.5. Therefore, the termination overlap tends to decrease with the use of redundant GPU memories by adding channels above the 5^{th} rank as shown in the top-right panel in Figure 1. Using the first two ranked channels is sufficient because the termination overlap for the 2^{nd} channel set is only less than 3% smaller than the largest value of the termination overlap (obtained by the 4^{th} channel set) and saves 18% GPU memory. In the following, we use the top-tow ranked channels for *Scattered light* glitches.

We pre-process the data as described in the previous section with the time series of the strain and the witness channels being re-sampled to a sampling rate of 512 Hz. During the pre-processing, we consider the frequency range above 100 Hz to be the background-noise region and use the 99 percentile pixel-value to extract the glitch waveform below 100 Hz. We also apply a high-pass filter to the strain channel at 10 Hz. We set the sample dimensions of the (training/validation/testing) sets to be (9131/2233/678) with the segment overlaps of (93.7/93.7/75)%, where the segment overlap is the fraction of the time-window overlap between segments created by sliding a time window to divide a larger segment into smaller segments (so-called *data augmentation* (Lemley *et al.*, 2017; Perez and Wang, 2017; Shorten and Khoshgoftaar, 2019)). We set that there is no overlapping time between the three sets and the testing set is later than the other sets. We create the mSTFT with a duration of 8 seconds, a frequency range up to 256 Hz, and (time/frequency) resolutions of 0.0625 seconds and 2 Hz, respectively. We use a square kernel with a size of $(8, 8)$ in the autoencoder in the network. During the post-processing, we consider the region where the

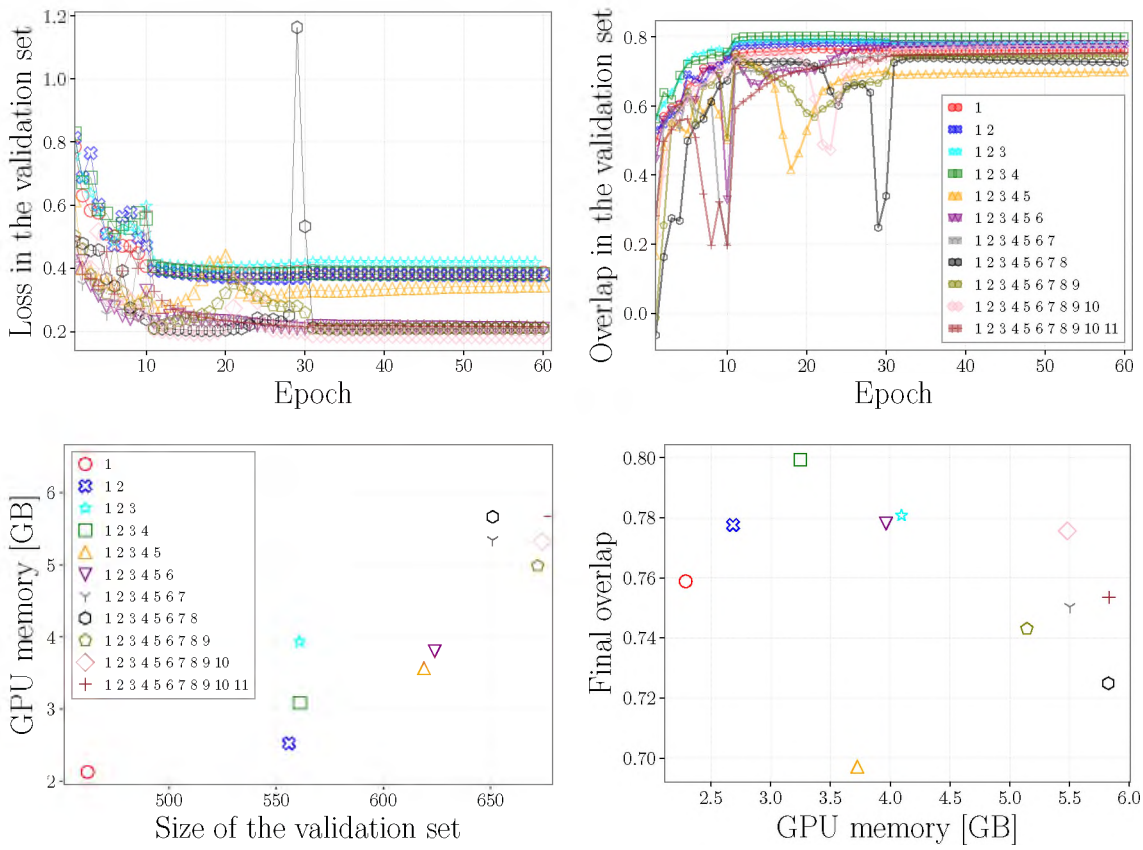

Figure 1. Losses defined in Equation (3) (top-left) and overlaps (top-right) over epochs in the validation sets using channel sets containing i^{th} ranked channels for *Scattered light* glitches. The bottom panels show sizes of the validation sets, overlaps at the end of the training, and used GPU memories.

glitches are present to be the time when the absolute value of the estimated glitch waveform is above the 75 percentile of the corresponding values across the testing set. We choose the divided window length for the least square fitting to be as small as 0.1 seconds and expand the window length from the center of the glitch by a factor of 1.1.

Figure 2 shows the distribution of the overlap of the mSTFT and the FNR of the testing set of *Scattered light* glitches. More similar mSTFTs correspond to more similar waveforms after the FGL transformation, resulting in more efficient reductions of glitch

SNRs. We find the overlap ranging from ~0.6-0.9 and the FNR ranging ~ 0.4 – 0.7 in 1-σ percentiles and no negative FNR, indicating no additional glitch energy added to the strain data.

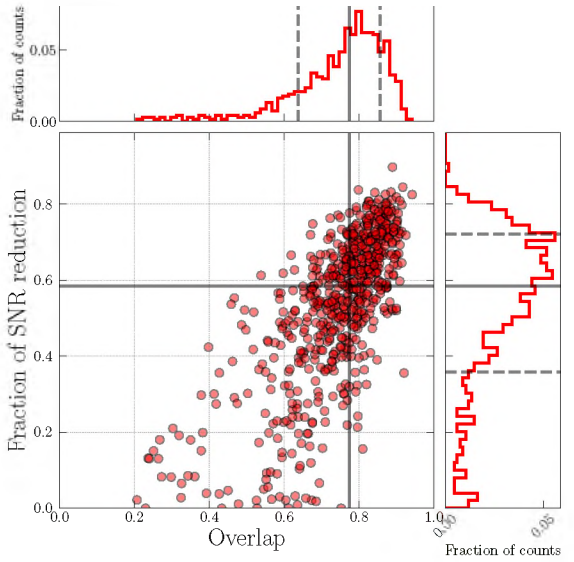

Figure 2. Distribution of the overlap of the extracted and estimated mSTFTs of *Scattered light* glitches in the testing set. The black solid and dashed lines denote the median and 1-σ percentiles.

Figures 3 (4/5) shows the mSTFT of a strain data down-sampled at 512 Hz and high-passed at 10 Hz in the testing set, the corresponding estimated mSTFT, and the time series used to subtract the glitches of the optimal (median/least) case, where the overlap between the mSTFT of the extracted glitch waveform and the estimated mSTFT is O = 0.92 (0.65/0.21) and FNR = 0.84 (0.58/0.02). In the least case, a short-lived arch-like glitch at ~ 6 seconds in the top-left panel in Figure 5 is estimated by the network. However, only the fractions of this glitch are subtracted due to our selection criterion about the glitch presence mentioned above. In this case, the small value of FNR = 0.02 is also due to the presence of a non-Scattered light glitch at ~ 0.5 seconds because this glitch contributes to SNR_b

dominantly. We note that we build the network for a particular class of glitches so that the glitch at ~ 0.5 seconds in the least case is consistent with the performance of our built network.

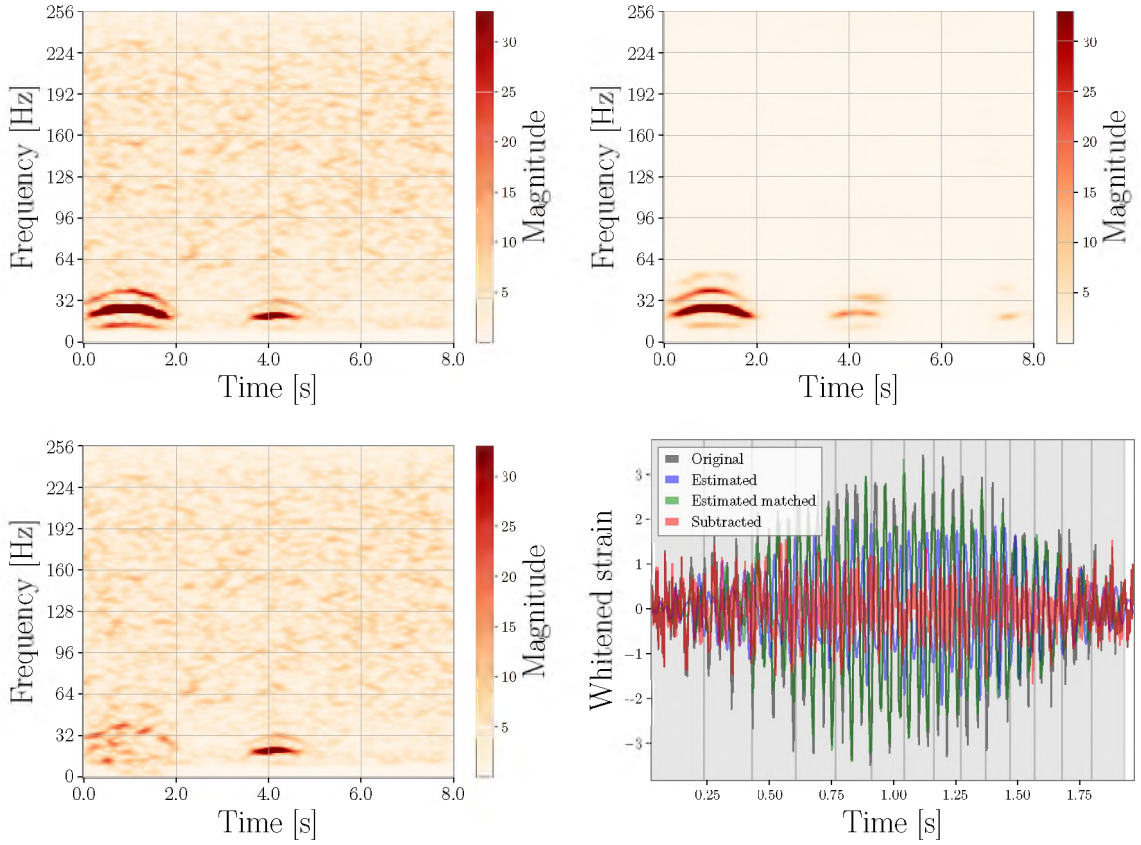

Figure 3. The mSTFT of the strain data (top-left), the network estimated mSTFT (top-right), and the mSTFT of the strain data after glitch subtraction (top-left) in the optimal testing sample of *Scattered light* glitches. In the bottom-right panel, the gray (blue/green/red) curves denote the original (estimated/estimated-matched/subtracted) whitened time series, where the estimated-matched time series is created after the amplitude and phase corrections with the least square fitting within divided segments shown as the gray bands. The overlap between mSTFT of the extracted glitch waveform and the estimated mSTFT is $O = 0.92$ and FNR $= 0.84$.

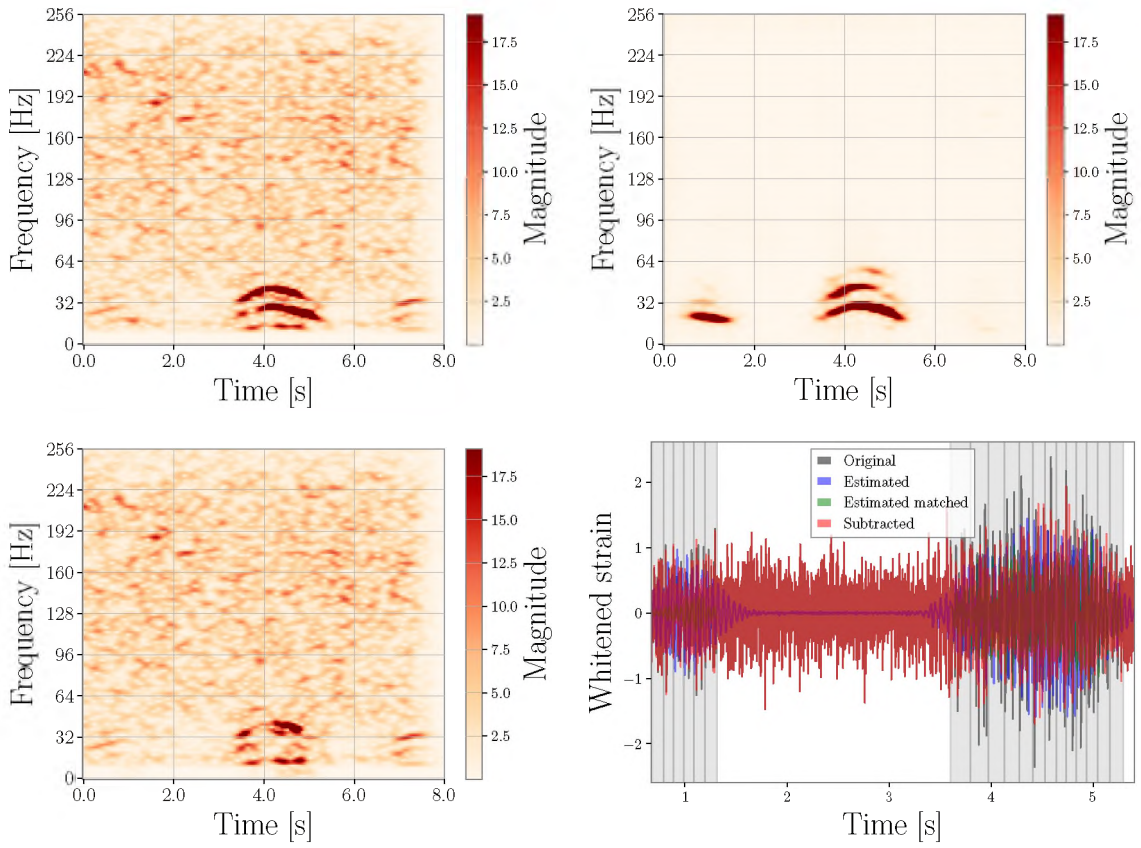

Figure 4. The mSTFT of a down-sampled strain data at 512 Hz with a high-pass filter at 10 Hz (top-left), the network estimated mSTFT (top-right), and the mSTFT of the strain data after glitch subtraction (top-left) in the median testing sample of *Scattered light* glitches. In the bottom-right panel, the gray (blue/green/red) curves denote the original (estimated/estimated-matched/subtracted) whitened time series, where the estimated-matched time series is created after the amplitude and phase corrections with the least square fitting within divided segments shown as the gray bands. The overlap between mSTFT of the extracted glitch waveform and the estimated mSTFT is $O = 0.65$ and FNR = 0.58.

3.2. EXTREMELY LOUD GLITCHES

Unlike *Scattered light* glitches where the waveforms in the strain can be analytically modeled with monitored mirror motions and the suspension systems (Was *et al.*, 2021), many other glitches are so far not modeled because of an incomplete understanding of their physical non-linear noise-coupling mechanisms. The non-linear activation function used in the network allows us to model non-linear noise couplings and subtract glitches. We apply

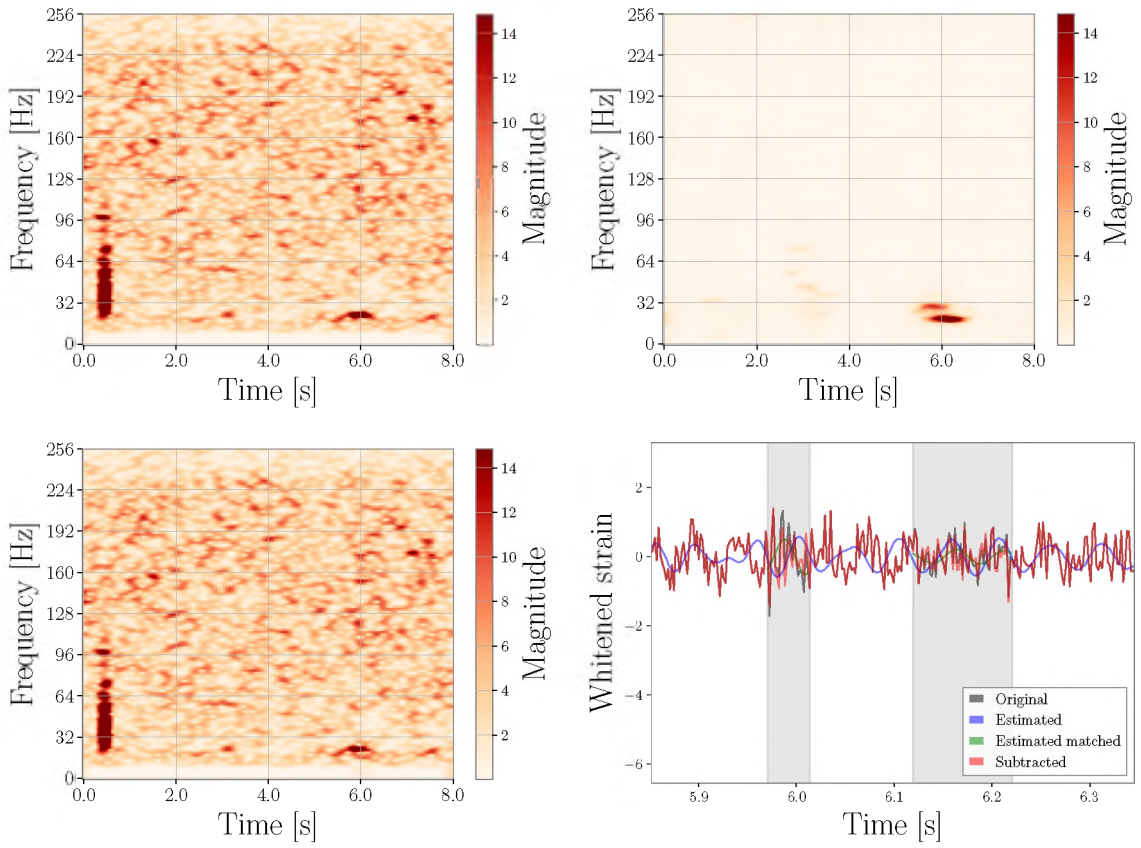

Figure 5. The mSTFT of a down-sampled strain data at 512 Hz with a high-pass filter at 10 Hz (top-left), the network estimated mSTFT (top-right), and the mSTFT of the strain data after glitch subtraction (top-left) in the least testing sample of *Scattered light* glitches. In the bottom-right panel, the gray (blue/green/red) curves denote the original (estimated/estimated-matched/subtracted) whitened time series, where the estimated-matched time series is created after the amplitude and phase corrections with the least square fitting within divided segments shown as the gray bands. The overlap between mSTFT of the extracted glitch waveform and the estimated mSTFT is $O = 0.21$ and FNR = 0.02.

our method to a class of *Extremely loud* glitches with SNR above 7.5 between January 1st, 2020 and February 3rd, 2020 in the L1 detector from the Gravity Spy catalog. We use 4 witness channels with high confidence: L1:LSC-POP_A_LF_OUT_DQ, L1:LSC-REFL_A_LF_OUT_DQ, L1:ASC-X_TR_A_NSUM_OUT_DQ, and L1:ASC-Y_TR_B_NSUM_OUT_DQ, identified by PyChChoo (Mogushi, 2021). This glitch class is expected to be produced by the laser intensity dips and have extremely high excess power in 10- 4096 Hz, lasting $\sim$ 0.2 seconds.

To check that the choice of witness channels noted above is sufficient, we train the network with various sets containing channels with $p_g = 0.99$ up to $p_g = 0.55$. We consider 11 different channel sets, where i^{th} set contains up to i^{th} ranked channels. Also, we consider the 12^{th} channel set containing the 1-3^{th} ranked channels and 5^{th} ranked channels because the 3^{rd} ranked channel (L1:ASC-Y_TR_B_NSUM_OUT_DQ) with $p_g = 0.98$ and the 4^{th} ranked channel (L1:ASC-Y_TR_A_NSUM_OUT_DQ) with $p_g = 0.97$ both record the transmitted light in yaw-direction in the alignment length control sub-system and have almost the same glitch-coupling information. The 5^{th} ranked channel (L1:LSC-POP_A_LF_OUT_DQ) records the transmitted light in low frequencies from the power recycling cavity. With the same procedure in Sec. 3.1, we compare losses, overlaps, GPU memories, and size of the validation sets for all channel sets as shown in Figure 6. The termination overlaps range from 0.77 obtained with the 10^{th} channel set to 0.84 obtained with the 3^{rd} channel set. The overlap decreases by adding channels 4-11^{th} ranked channels. In particular, 6-11 channels have values of $p_g < 0.57$, indicating no evidence of being witnesses so that the network obtain no significant glitch-coupling information from these low confidence channels with the use of redundant GPU memories up to 8.4 GB. In the following, we choose the 12^{th} channel set containing witness channels noted in the previous paragraph because its termination overlap is only less than 2% compared to the largest value obtained with the 3^{rd} channel set, and 0.5% increase of the data set.

During the data pre-processing, we re-sample the time series of the strain and the witness channels to a sampling rate of 2048 Hz and apply a high-pass filter at 10 Hz. We consider the time range outside of the 5-second window around the glitch time from the Gravity Spy catalog to be the background-noise region and use the 99 percentile pixel-value to extract the glitch waveform within the 5-second window because these glitches are isolated and not repeating, unlike *Scattered light* glitches. We set the sample dimensions of the (training/validation/testing) sets to be (3879/940/1233) with the segment overlaps of (96.8/96.8/87.5)%, where there is no overlapping time between the three sets and the

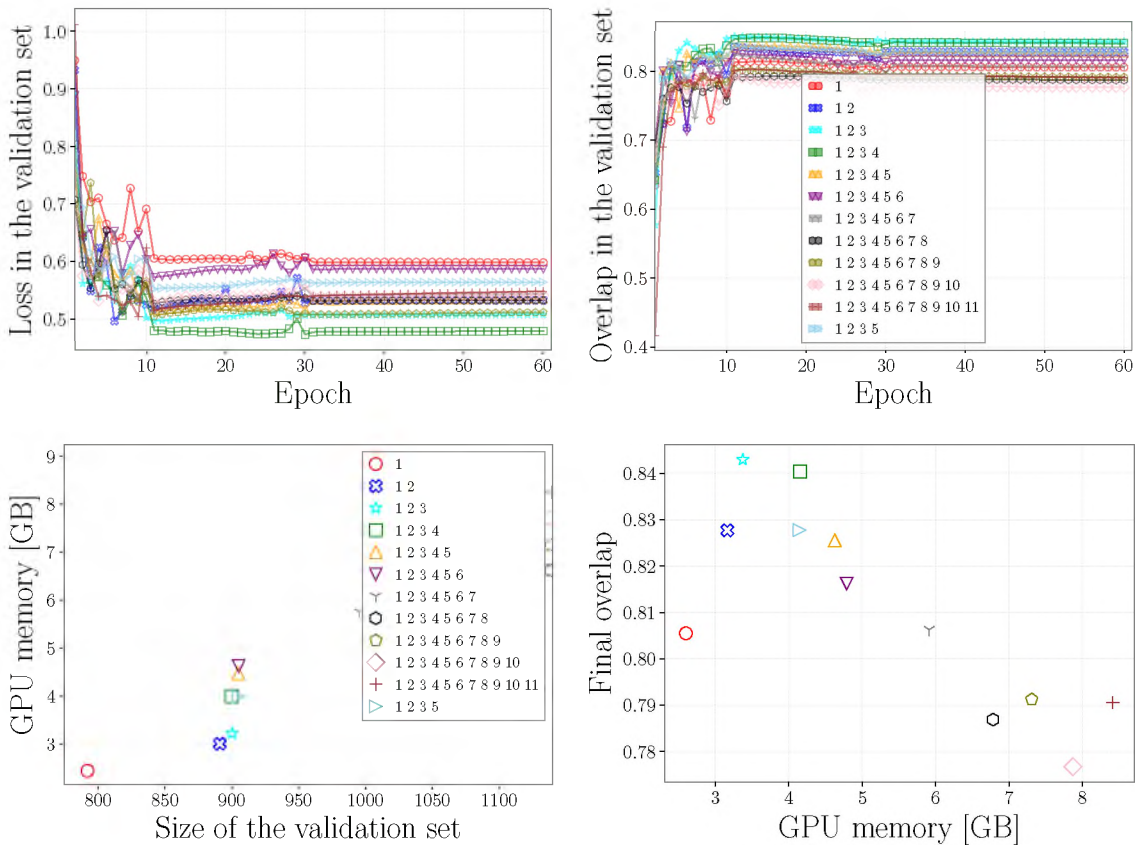

Figure 6. Losses defined in Equation (3) (top-left) and overlaps (top-right) over epochs in the validation sets using channel sets containing i^{th} ranked channels for *Extremely loud* glitches. The bottom panels show sizes of the validation sets, overlaps at the end of the training, and used GPU memories.

testing set is later than the other sets. We create the mSTFT with a duration of 2 seconds, a frequency range up to 1024 Hz, and (time/frequency) resolutions of 0.0156 seconds and 8 Hz, respectively. We use a rectangular kernel with a size of $(13, 4)$ in the autoencoder in the network. During the post-processing, we consider the region of the glitch presence to be the time when the absolute value of the estimated glitch waveform is above the 90 percentile of the corresponding values across the testing set. We choose the divided window length for the least square fitting to be as small as 0.02 seconds and expand the window length from the center of the glitch by a factor of 1.1.

Figure 7 shows the distribution of the overlap of the mSTFT and the FNR of the testing set of *Extremely loud* glitches. We find the overlap ranging from ~0.7-0.9 and the FNR ranging $\sim 0.1-0.6$ with 1-σ percentiles and no negative FNR indicating no additional glitch added to the strain data.

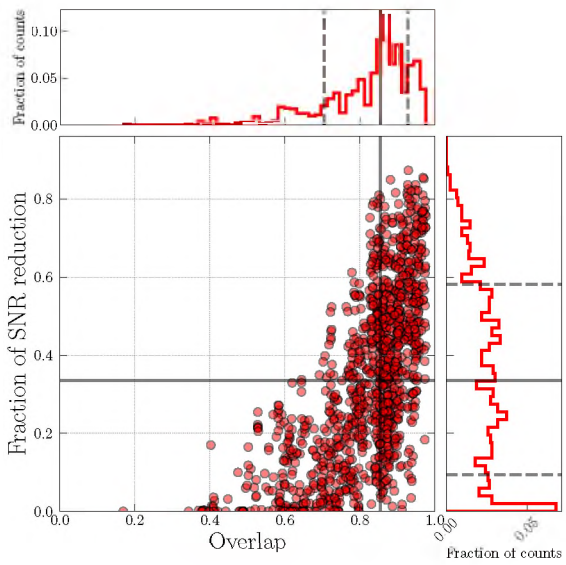

Figure 7. Distribution of the overlap of the extracted and estimated mSTFTs of *Extremely loud* glitches in the testing set. The black solid and dashed lines denote the median and 1-σ percentiles.

Figures 8 (9/10) shows the mSTFT of a strain data down-sampled at 2048 Hz and high-passed at 10 Hz in the testing set, the corresponding estimated mSTFT, and the time series used to subtract the glitches of the optimal (median/least) case, where the overlap between the mSTFT of the extracted glitch waveform and the estimated mSTFT is $O = 0.93$ (0.86/0.17) and FNR = 0.84 (0.33/0). In the least case, our chosen four witness channels seem not to witness no excess power coincident with the glitch so that the network estimates no glitches.

Our method subtracts *Scattered light* glitches more efficiently than *Extremely loud* glitches because the network finds it difficult to model short-lived (~ 0.2 seconds) non-linear couplings for *Extremely loud* glitches. In values of the overlap binned from 0.5 to 1.0

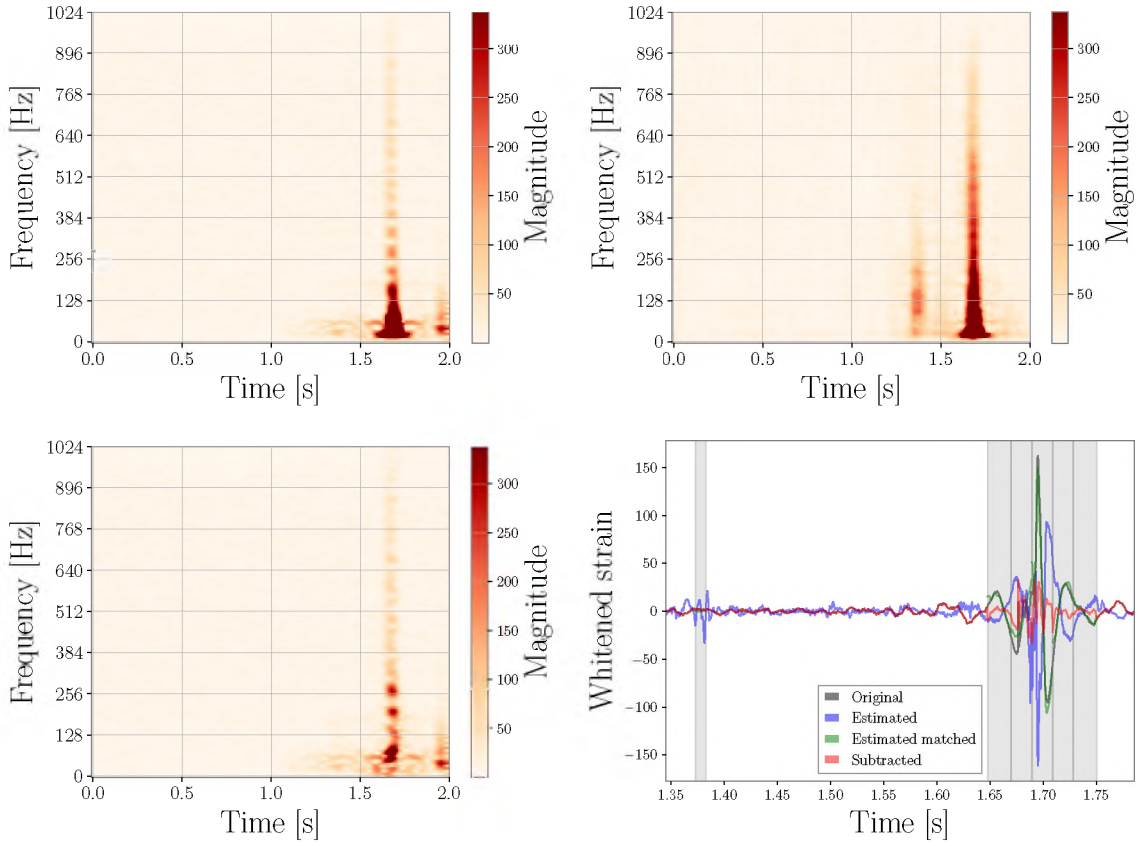

Figure 8. The mSTFT of a down-sampled strain data at 2048 Hz with a high-pass filter at 10 Hz (top-left), the network estimated mSTFT (top-right), and the mSTFT of the strain data after glitch subtraction (top-left) in the optimal testing sample of *Extremely loud* glitches. In the bottom-right panel, the gray (blue/green/red) curves denote the original (estimated/estimated-matched/subtracted) whitened time series, where the estimated-matched time series is created after the amplitude and phase corrections with the least square fitting within divided segments shown as the gray bands. The overlap between mSTFT of the extracted glitch waveform and the estimated mSTFT is $O = 0.93$ and FNR = 0.87.

with a bin width of 0.1, the averaged value of FNR for *Scattered light* glitches are greater than the corresponding values for *Extremely loud* glitches by a factor ranging from 1.3 for the bin $O = 0.9 - 1.0$ to 3.8 for the bin $O = 0.6 - 0.7$.

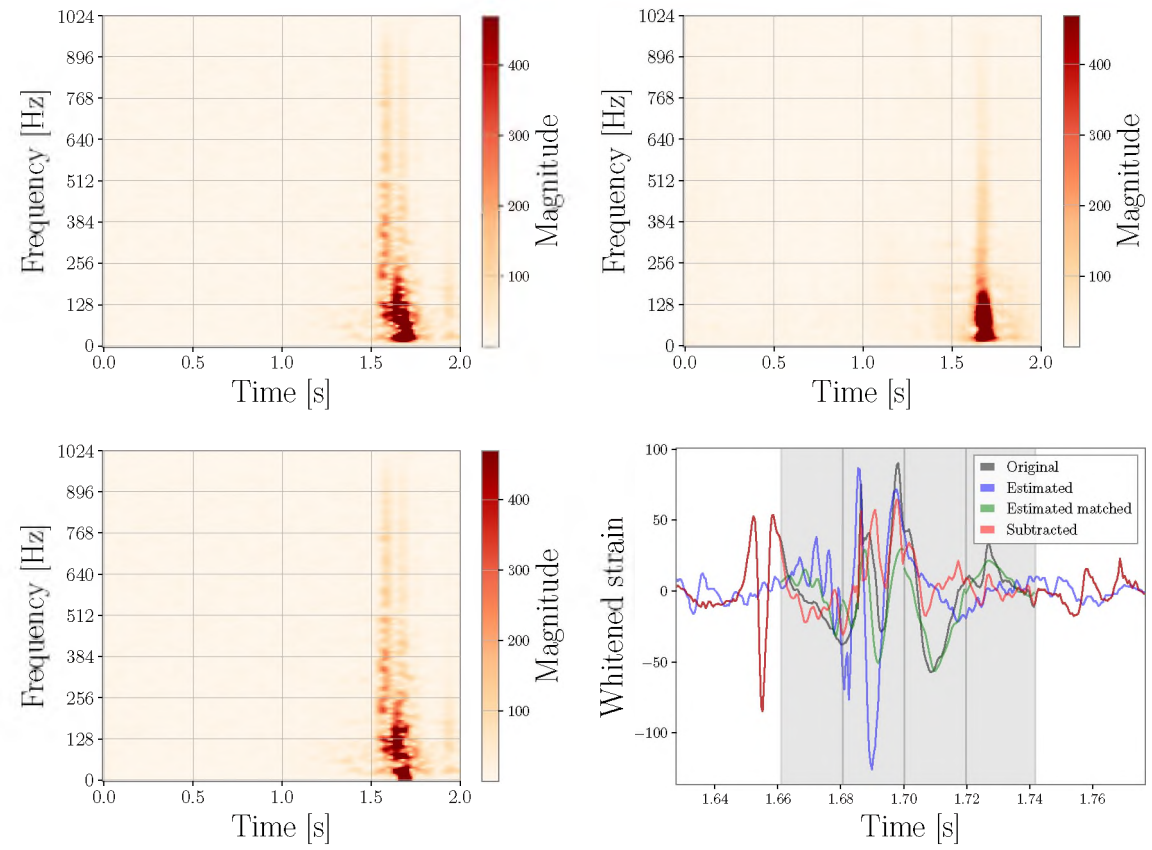

Figure 9. The mSTFT of a down-sampled strain data at 2048 Hz with a high-pass filter at 10 Hz (top-left), the network estimated mSTFT (top-right), and the mSTFT of the strain data after glitch subtraction (top-left) in the median testing sample of *Extremely loud* glitches. In the bottom-right panel, the gray (blue/green/red) curves denote the original (estimated/estimated-matched/subtracted) whitened time series, where the estimated-matched time series is created after the amplitude and phase corrections with the least square fitting within divided segments shown as the gray bands. The overlap between mSTFT of the extracted glitch waveform and the estimated mSTFT is $O = 0.86$ and FNR = 0.33.

3.3. INJECTION RECOVERY WITH COHERENT WAVEBURST

Subtracting glitches results in a new strain data which is expected to contain smaller energy due to the presence of glitches, leading to better detectability of astrophysical signals. One way of examining the robustness of our glitch-subtraction method is to add software-simulated signals with known astrophysical parameters into the strain data before subtraction and use GW detection pipelines to recover the injected signals. In this process,

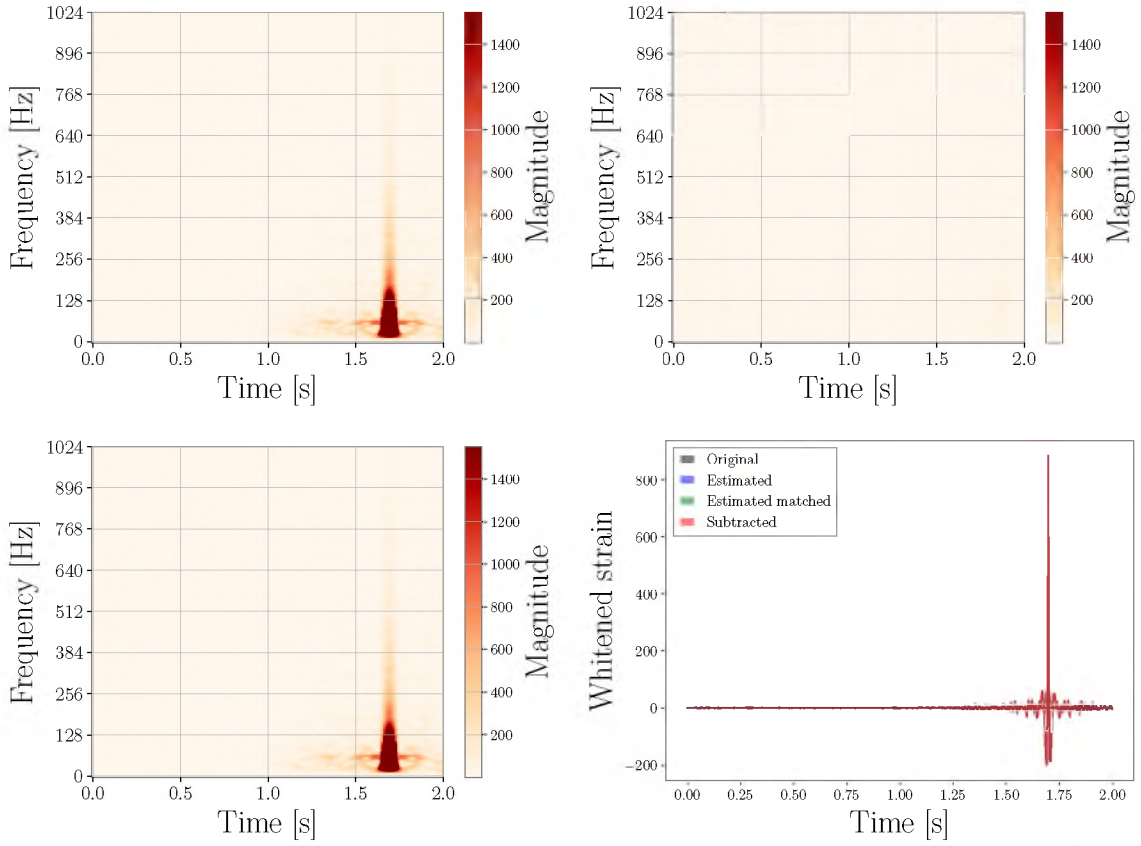

Figure 10. The mSTFT of a down-sampled strain data at 2048 Hz with a high-pass filter at 10 Hz (top-left), the network estimated mSTFT (top-right), and the mSTFT of the strain data after glitch subtraction (top-left) in the least testing sample of *Extremely loud* glitches. In the bottom-right panel, the gray (blue/green/red) curves denote the original (estimated/estimated-matched/subtracted) whitened time series, where the estimated-matched time series is created after the amplitude and phase corrections with the least square fitting within divided segments shown as the gray bands. The overlap between mSTFT of the extracted glitch waveform and the estimated mSTFT is $O = 0.17$ and FNR = 0.

we can assess whether the glitch subtraction technique reduces only the targeted glitches without manipulating the measured astrophysical signals. We use our glitch-subtraction method after injecting a signal in coincidence with a glitch.

The presence of glitches adversely affects the unmodeled GW signal searches that do not rely on known waveforms in priori. In O3a, the percentages of the single-detector observing time removed by the data-quality vetoes for the unmodeled searches are greater than the percentages for modeled searches by a factor of ~ 2.7 and ~ 7.9 for the H1-detector

and L1-detector, respectively (Abbott *et al.*, 2021). Therefore, it is more beneficial to apply glitch-subtraction techniques for unmodeled searches. We use cWB to recover injections before and after subtraction and compare these recovered signals as well as the recovered signal injected in a simulated colored Gaussian noise with the PSD of the L1 data when the glitch subtraction is applied.

To account for the performance of our glitch subtraction operated on only the L1 data, we create a simulated colored Gaussian noise for the H1 data with the same sensitivity as the L1 data and inject signals both in the L1 and H1 detectors where the signal coincides with a glitch in the L1 data. The ranking statistic ρ of cWB accounts for the correlation of a signal injected on the two-detector data so that higher-ranking statistics for a given injection imply that the recovered signal in the L1 data is more similar to the signal in the H1 data, indicating successful glitch subtraction and a better detectability.

3.3.1. Gaussian-modulated Sinusoid Injections. Following studies of unmodeled GW signal searches (Abadie *et al.*, 2012a,b; Abbott *et al.*, 2008, 2010; Adrian-Martinez *et al.*, 2013; Was *et al.*, 2012), we inject a circularly polarized Gaussian-modulated sinusoid signal:

$$\begin{bmatrix} h_+(t) \\ h_\times(t) \end{bmatrix} = \frac{A}{d} \begin{bmatrix} \cos\{2\pi f_c(t-t_0)\} \\ \sin\{2\pi f_c(t-t_0)\} \end{bmatrix} \exp\left[-\frac{2\pi f_c(t-t_0)}{2Q^2}\right], \tag{6}$$

where f_c is the central frequency, t_0 is the center time, d is the distance to the source, A is an arbitrary amplitude scaling factor, Q determines the length of the signal.

Motivated by studies (Abadie *et al.*, 2012a,b; Abbott *et al.*, 2008, 2010; Adrian-Martinez *et al.*, 2013; Was *et al.*, 2012) that use $f_c = 150$ Hz, we also choose $f_c = 150$ Hz. To validate the glitch subtraction technique successfully subtract glitches in the presence of signals with duration compatible glitches, we choose $Q = 30$, where the injected signal lasts ~ 1.5 seconds which is compatible with the duration of *Scattered light* glitches. In addition to the above motivation, we consider signals similar to the first detection of IMBBH (Abbott *et al.*, 2020a), where the detected signal has a peak frequency of ~ 50 Hz and ~ 3 wave

cycles. The improvement in the IMBBH detection by subtracting glitches might be useful to understand the mechanism of astrophysical populations (Abbott *et al.*, 2020b). Therefore, we choose $f_c = 50$ Hz and $Q = 5$ for the second choice.

Using the two representative signal waveforms with different sets of parameters: $f_c = 50$ Hz, $Q = 5$ and $f_c = 150$ Hz, $Q = 30$, and choosing the injected SNRs to be uniformly sampled from a set of SNRs, the source direction to be isotropically sampled in the sky, the injected time to be uniformly sampled in a given time window, we examine the pipeline performance on the testing samples with an optimal set of values of FNR = 0.84, $O = 0.92$ (shown in Figure 3) and a median value of FNR = 0.58, $O = 0.65$ (shown in Figure 4) for *Scattered light* glitches as well as an optimal set of values of FNR = 0.87, $O = 0.93$ (shown in Figure 8) and a median value of FNR = 0.33, $O = 0.86$ (shown in Figure 9) for *Extremely loud* glitches. To assess the effect of the injection time on the pipeline performance, we consider two different injection-time windows: the subtracted portion in the testing-sample data or the full length of the testing-sample data. Because we apply the glitch subtraction in the partial data with excess power detected from the estimated glitch waveform and keep the original data for the rest of the data portion, we inject signals in the subtracted portion to study if our technique can subtract glitches that are overlapping with signals. We also consider the full length of the testing-sample data as the injection-time window because subtracting glitches may affect detections of signals near to glitches but not overlapping with them. The injection times are uniformly sampled in the full window of 0.4-7.6 and 0.1-1.8 seconds, and the partial window of 0.1-1.8 (3.5-5.4) and 1.65-1.75 (1.65-1.75) seconds for the optimal (median) case of the *Scattered light* and *Extremely loud* glitches, respectively, with a time step of 5% of the window length. We use sets of injected SNRs of $\{2, 4, 8, 16, 30, 50, 100\}$ and $\{2, 4, 8, 16, 30, 50, 100, 200, 300, 400, 500\}$ *Scattered-light* and *Extremely-loud* glitch sets, respectively, where larger injected SNRs are chosen for *Extremely-loud* glitch set to assess the cWB detection performance for injections

overlapping with glitches with high excess power. We inject 500 (250) waveforms with either high or low f_c in the full (partial) injection-time window for each testing sample in each glitch class such that we have 16 injection-test sets.

Figure 11 shows the enhancement of ρ after glitch subtraction for Gaussian-modulated sinusoidal injections. With the typical setting in cWB, only a signal with a ranking statistic greater than 6 is reported. We set the statistic for those missed signals to be 6 to quantify the enhancement due to subtraction. The percentages of injections with values of ρ after glitch subtraction greater or equal to the corresponding values before glitch subtraction ranges from 67% (obtained from the set with high-frequency signals injected in the full window of the optimal testing samples of *Scattered light*) to 100% (obtained from the set with high-frequency signals injected in the partial window of the optimal testing sample of *Extremely loud* glitches). Similarly, values the enhancement $\langle \rho_{\rm a}/\rho_{\rm b} \rangle$, where $\rho_{\rm a}$ and $\rho_{\rm b}$ are ρ obtained from the data after and before the glitch subtraction, respectively, averaged over injections range from 1.2 (obtained from the set with high-frequency signals injected in the full window of the optimal testing samples of *Scattered light*) to 3.5 (obtained from the set with high-frequency signals injected in the partial window of the optimal testing sample of *Extremely loud* glitches).

Removing glitches with their characteristic frequencies close to that of signals typically improves values of ρ effectively because cWB reconstructs signals more effectively. Because *Scattered light* glitches have the largest power at a frequency of $\sim$ 30 Hz, the ρ enhancements for the low-frequency injection sets are larger than the enhancement for the high-frequency injection sets by a factor of up to $\sim$ 1.3. Similarly, *Extremely loud* glitches have a peak frequency of $\sim$ 110 Hz (see details in Sec. 1.3) so that values of the enhancement for the high-frequency injection sets are greater than values for the low-frequency injection sets by a factor of up to $\sim$ 1.8.

Higher values FNR indicate larger reductions of excess power due to glitches. Hence, values of ρ obtained from the optimal testing samples are larger than values obtained from the median samples. The ρ enhancements in optimal-sample sets are greater than the median-sample sets by a factor $\sim 1.15 \sim 1.23$ ($\sim 1.5 \sim 1.7$) and $\sim 1.8 \sim 2.2$ ($\sim 1.7 \sim 2.3$) for the full (partial) injected window for *Scattered light* and *Extremely loud* glitches. Because *Extremely loud* glitches typically have extremely loud SNR $\sim$ 1500 while *Scattered glitch* glitches have SNR $\sim$ 17 (see more details in Sec. 1.3), subtracting *Extremely loud* glitches improves ρ more than subtracting *Scattered light* glitches. Also, the partial injection-window sets, where signals are overlapping with glitches tend to correspond to larger ρ enhancements than the full injection-window sets. Values of ρ are typically improved after glitch subtraction for the majority of injections near to glitches but not overlapping with them because the incoherent energy between detectors is reduced and the cWB obtains higher correlations of signals between detectors. Table. 1 shows values of the ρ enhancement and percentages of injection with non-reduced ρ after glitch subtraction for all sets.

Injections with reduced ρ after glitch subtraction are mainly due to 1) the least square fitting process operated between estimated glitch waveforms and the data, or 2) the cWB reconstruct process. The first reason is typically observed when the amplitude of signals is significantly large so that the least-square fitting method dominantly reduces the difference between a signal and an estimated glitch waveform in these cases. Hence, the signal energy is reduced. for example, these cases are observed when signals with high values of ρ obtained from the no-glitch data are injected at the center of glitches. Figure 12 shows an example failure case due to this reason: when an injected signal has larger or comparable to the amplitude of the overlapping glitch, the least square fitting method dominantly minimizes the difference between the estimated glitch waveform and the injection. The second reason is observed when the amplitude of the remaining glitches after subtraction is comparable to the amplitude of the nearby non-overlapping injected signals so that cWB reconstructs the sum of the remaining glitch and the true signal as a

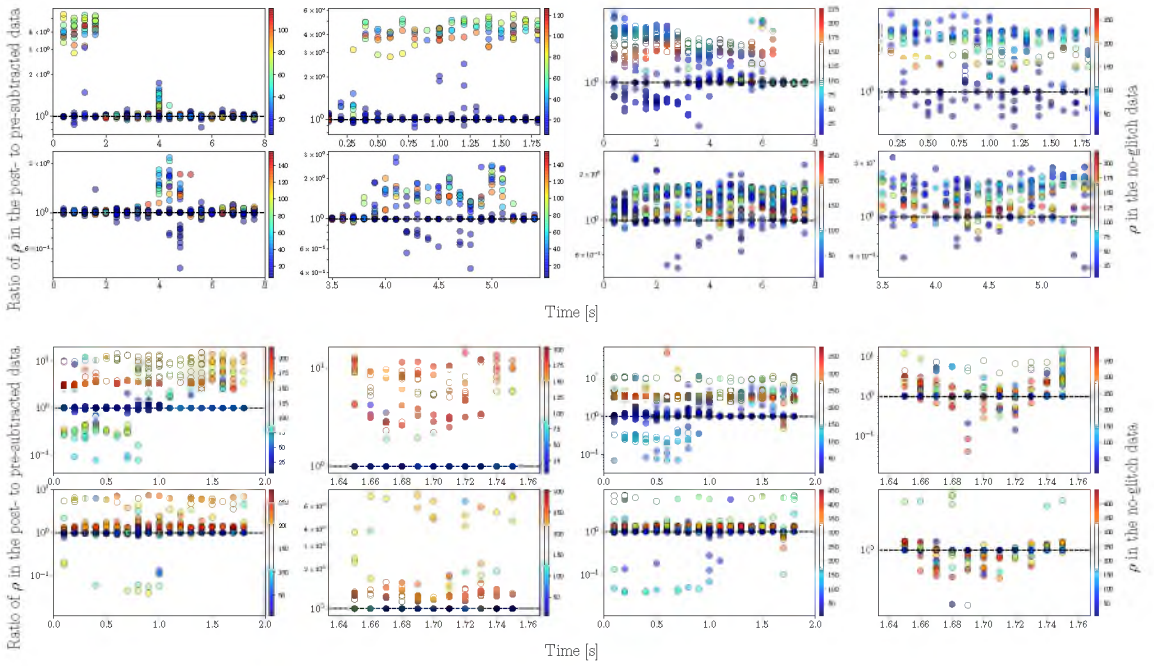

Figure 11. Enhancements of ρ after glitch subtraction for Gaussian-modulated sinusoidal injections. The panels show enhancements of ρ for high-frequency (1-2$^{\text{th}}$ columns) and low-frequency (3-4$^{\text{th}}$ columns) Gaussian-modulated sinusoidal waveforms injected in the full (1,3$^{\text{th}}$ columns) and partial (2,4$^{\text{th}}$ columns) windows of the optimal (1,3$^{\text{th}}$ rows) and median (2,4$^{\text{th}}$ rows) testing samples of *Scattered light* (1-2$^{\text{th}}$ rows) and *Extremely loud* (2-4$^{\text{th}}$ rows) glitches, respectively.

signal and the correlation of signals between detectors becomes smaller. The second reason can be seen in 0-1 seconds in the panels in the 3^{rd}-1,3$^{\text{th}}$ columns in Figure 11, where the original data without subtraction is used (see Figures 9 and 8 for the subtracted portions.) Figure 13 shows an example of unsuccessful cWB reconstruction for an injection nearby the remaining glitch after subtraction. In this case, the original data with injections is used around the injection time because no excess power is detected at the time of injections from the estimated glitch waveform. However, cWB reconstructs the injection differently before and after glitch subtraction. Before glitch subtraction, the cWB reconstruction process does not use the time portion containing the glitch because the amplitude of the glitch is not compatible with the signal amplitude. After glitch subtraction, the cWB used the data

portion containing the remaining glitch whose amplitude is compatible with the amplitude of the injection. As a result, the cWB network correlation coefficient in Equation (1.128) is reduced to 0.65 from 0.99 after glitch subtraction, leading to $\rho_a/\rho_b = 0.36$.

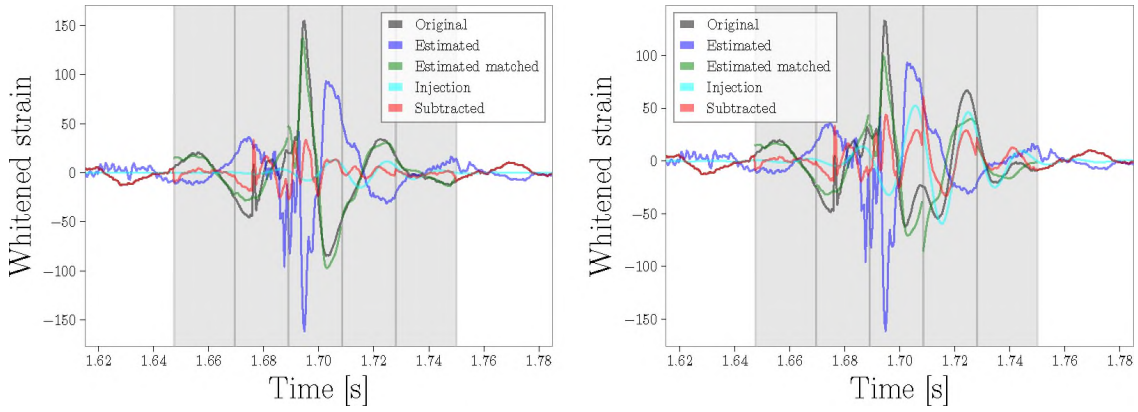

Figure 12. Successful glitch subtraction for a low-frequency (f_c = 50 Hz and Q = 5) Gaussian modulated sinusoidal injection with SNR of 50 (left) and failure subtraction for the same injection with SNR of 200 (right) in the optimal testing sample of *Extremely loud* glitches.

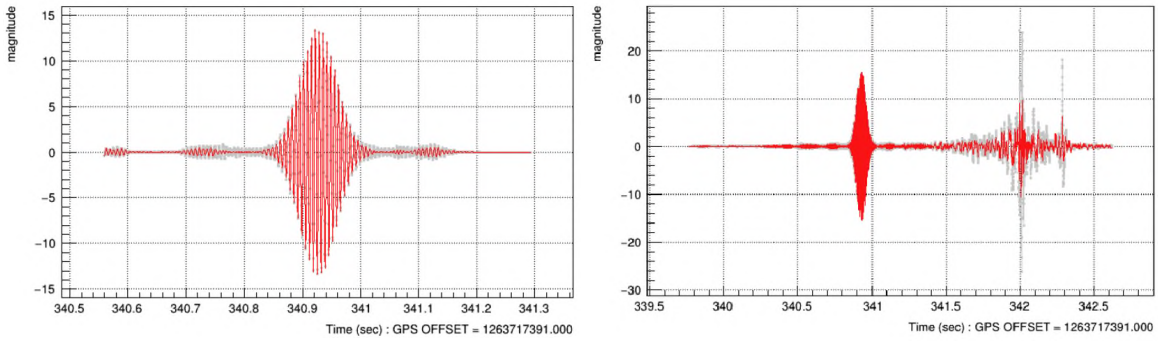

Figure 13. Successful cWB reconstruction for a high-frequency (f_c = 150 Hz and Q = 30) Gaussian modulated sinusoidal injection before glitch subtraction (left) and unsuccessful cWB reconstruction after glitch subtraction due to the nearby remaining glitch (right) in the optimal testing sample of *Extremely loud* glitches. The cWB correlation coefficients are 0.99 and 0.65 for the reconstructed signals before and after glitch subtraction, respectively. The ratio of ρ after and before subtraction is $\rho_a/\rho_b = 0.36$. Note that the time scales in the left and right panels are different due to the cWB automated reconstruction process, where the glitch is outside of the reconstruction time window before glitch subtraction.

More accurate signal reconstructions or higher values of the network correlation coefficient produce better estimates of the source direction. To assess the accuracy of the cWB source-direction estimates, we calculate the overlap of sky maps obtained with the no-glitch data and sky maps obtained with pre-subtracted data, where the sky map is provided as the probability distribution over pixelized solid angles and the sky-map overlap is calculated by taking the inner product between two sky maps similar to Equation (4). Also, we calculate the overlap of sky maps obtained with the no-glitch data and sky maps obtained with the post-subtracted data. For injection missed by cWB with no reported sky maps, we set sky maps to be uniform probability distributions over solid angles according to the maximum entropy principle (Ratnaparkhi, 1996; Reynar and Ratnaparkhi, 1997) for the least amount of knowledge about the source direction. We count percentages $P_{\rm sky}$ of injections with the sky-map overlap of the no-glitch-post-subtraction data greater or equal to the sky-map overlap of the no-glitch-pre-subtracted data. Values of $P_{\rm sky}$ greater 50% imply that estimates of the source direction become more accurate after glitch subtraction and $P_{\rm sky}$ 50% indicates that source-direction estimates are compatible before and after glitch subtraction.

Figure 14 shows ratios of sky-map overlaps between the no-glitch data and the post-subtracted data to sky-map overlaps with the former and the post-subtracted data for Gaussian modulated sinusoidal injections. Values of $P_{\rm sky}$ range from 60% (obtained with the set with high-frequency injections in the full window of the optimal testing sample of *Scattered light* glitches) to 94% (obtained with the set with high-frequency injections in the partial window of the optimal testing sample of *Extremely loud* glitches). Because better signal reconstructions correspond to more accurate source-direction estimates, Values of $P_{\rm sky}$ with optimal-testing-sample sets are greater than values with median-testing-sample sets by a factor of $\sim 0.86 \sim 1.2$ ($\sim 1.01 \sim 1.1$) for *Scattered light* and *Extremely loud* glitches. The exceptional sets with high-frequency injections in the full window for *Scattered light* glitches have $P_{\rm sky} = 60\%$ for the optimal-testing-sample set and $P_{\rm sky} = 69\%$ for the

median-testing-sample set, respectively. However, they are compatible. 90% of injections in the above two exceptional sets have the ratio of the sky-map overlap of the no-glitch-post-subtracted data to the sky-map overlap of the no-glitch-pre-subtracted data in 0.93-2.3 (0.94-1.2) for the optimal (median)-testing sample set because the central frequency $f_c = 150$ Hz is distinctively different from the peak frequency (~ 30 Hz) of *Scattered light* glitches. We find that the maximum value of the ratio of the sky-map overlaps to be 150 and 4.5 for the above optimal and median-testing-sample sets, respectively. Values of $P_{\rm sky}$ obtained with the low (high)-frequency sets are greater than values obtained with high (low)-frequency sets for *Scattered light* (*Extremely loud*) glitches by a factor of $\sim 1.08 \sim 1.35$ ($\sim 1.01 \sim 1.1$) because removing glitches with their characteristic frequencies compatible with central frequencies of injections improve the cWB reconstructions more effectively. Table. 1 shows percentages of injection with the non-reduced ratio of sky-map overlaps after glitch subtraction for all sets.

To assess the accuracy of the cWB estimated central frequency $\hat{f}_c$ across all injections, we calculate the normalized residual:

$$\Delta f_c = \frac{\hat{f}_c - f_c}{f_c}, \tag{7}$$

where f_c is the injected central frequency. To quantify the similarity between two distributions, we calculate the two-sided KS statistic $S_{\rm nb}$ (Massey, 1951) between values of Δf_c obtained with the no-glitch data and the data before glitch subtraction as well as the KS statistic $S_{\rm na}$ between values of Δf_c obtained with the former and the data after glitch subtraction. KS statistics are bounded between 0 and 1 and smaller values indicate two distributions are more similar. Values of the ratio $R^{\rm nb}_{\rm na} := S_{\rm nb}/S_{\rm na}$ greater 1 imply that the cWB estimated values of $\hat{f}_c$ in the post-subtracted data are more similar to corresponding values in the no-glitch data than the pre-subtracted data while smaller values indicate the

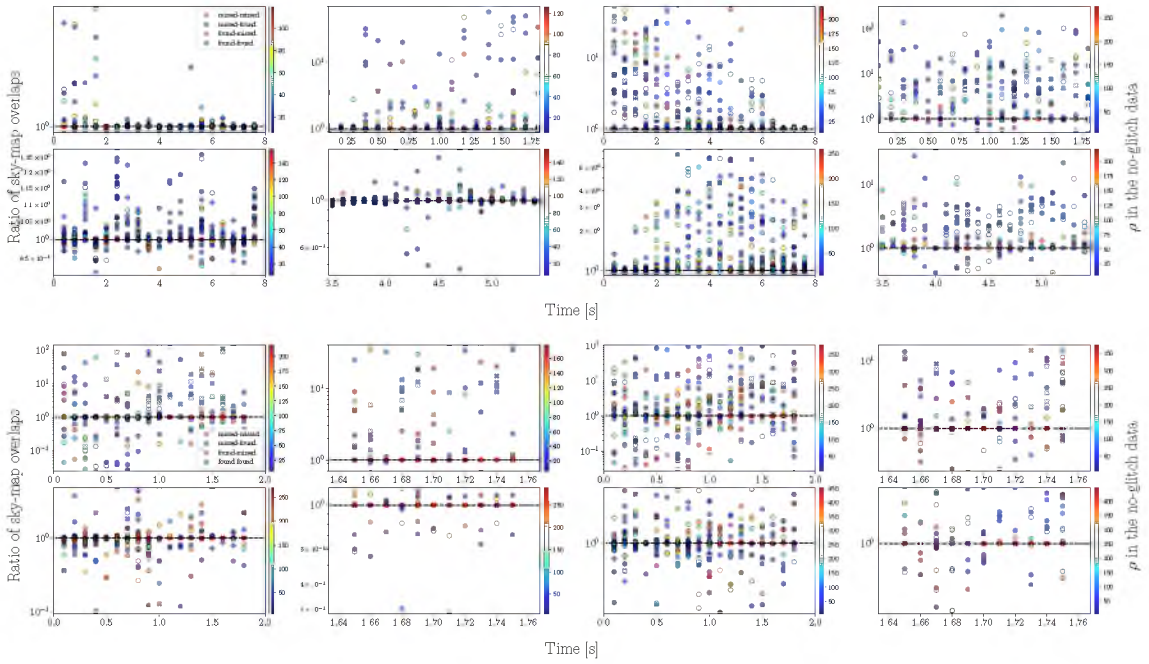

Figure 14. Ratio of sky-map overlaps for Gaussian-modulated sinusoidal injections. The panels show ratios of the sky-map overlap between the no-glitch data and the post-subtracted data to the sky-map overlap with the former and the post-subtracted data, as a function of the injection time for high-frequency (1-2$^{\text{th}}$ columns) and low-frequency (3-4$^{\text{th}}$ columns) Gaussian-modulated sinusoidal waveforms injected in the full (1,3$^{\text{th}}$ columns) and partial (2,4$^{\text{th}}$ columns) windows of the optimal (1,3$^{\text{th}}$ rows) and median (2,4$^{\text{th}}$ rows) testing samples of *Scattered light* (1-2$^{\text{th}}$ rows) and *Extremely loud* (2-4$^{\text{th}}$ rows) glitches, respectively.

cWB estimates in the post-subtracted data are less accurate than the pre-subtracted data. $R^{\text{nb}}_{\text{na}} \sim 1$ implies that the glitch-subtraction technique does not produce unintended effects on the data for the estimates of the central frequency.

Figure 15 shows distributions of Δf_c obtained with the no-glitch, the pre- and post-subtracted data. Values of $R^{\text{nb}}_{\text{na}}$ range from 0.41 (obtained from the set with low-frequency injections in the full window of the optimal testing sample of *Extremely loud* glitches) to 4.47 (obtained from the set with high-frequency injections in the partial window of the optimal testing sample of *Scattered light* glitches). When injections are overlapping with the remaining *Extremely* loud glitch after subtraction or the cWB reconstructs the sum of the injection and near non-overlapping glitches as a signal, the estimated central

frequency $\hat{f}_c$ deviates from the injected value f_c. For example, the set with the lowest $R^{\rm nb}_{\rm na} = 0.41$ has 9.6% of injections have values of $\Delta f_c = 0.28$-0.91 from the injected value $f_c = 50$ Hz (corresponding to $\hat{f}_c = 64$-95 Hz) for the post-subtracted data and no injection above $\hat{f}_c = 64$ Hz for the pre-subtracted data. For the set with the highest value $R^{\rm nb}_{\rm na} = 4.47$, distribution of Δf_c in the post-subtracted data differ from the distribution in the pre-subtracted data and compatible to the distribution in the no-glitch data (see the 1$^{\rm st}$ row-2$^{\rm nd}$ column in Figure 15). Values of $R^{\rm nb}_{\rm na}$ for the low (high)-frequency injection sets are greater than values for the high (low)-frequency injection sets by a factor of $\sim 1.04 \sim 1.68$ ($\sim 0.95 \sim 2.4$) because subtracting glitches with their characteristic frequency compatible with signal frequency improves the cWB reconstruction accuracy. For high-frequency injection sets, values of $R^{\rm nb}_{\rm na}$ obtained with optimal-testing-sample sets are greater than values obtained with corresponding median-testing-sample set by a factor $\sim 1.04 - 2.8$ across the two glitch classes. For low-frequency injection sets, values of $R^{\rm nb}_{\rm na}$ obtained with median-testing-sample sets are greater than values obtained with optimal-testing-sample sets by a factor of $\sim 1.05 \sim 2.43$ because of the contribution of high-frequency nearby remaining glitches to the cWB signal reconstruction, mentioned above for the set with the lowest value $R^{\rm nb}_{\rm na} = 0.41$. Table 2 shows percentages of found injections and values of $R^{\rm nb}_{\rm na}$.

3.3.2. Binary Black Hole Injections. In addition to tests with Gaussian-modulated sinusoid signals in Sec. 3.3.1, we also assess the performance of the cWB-signal recovery by injecting non-spinning IMRPHENOMD BBH merger waveforms (Khan *et al.*, 2016). Following the choice of injection parameters used in Ormiston *et al.* (2020), we choose the component masses to be uniformly distributed in [26, 64] $M_\odot$ with a constraint of the primary-mass m_1 to the secondary-mass m_2 ratio in $[0.125, 1]$, the source direction and binary orientation to be isotropically distributed, and the coalescence phase and the polarization angle to be uniformly distributed in $[0, 2\pi]$ and $[0, \pi]$, respectively. We choose

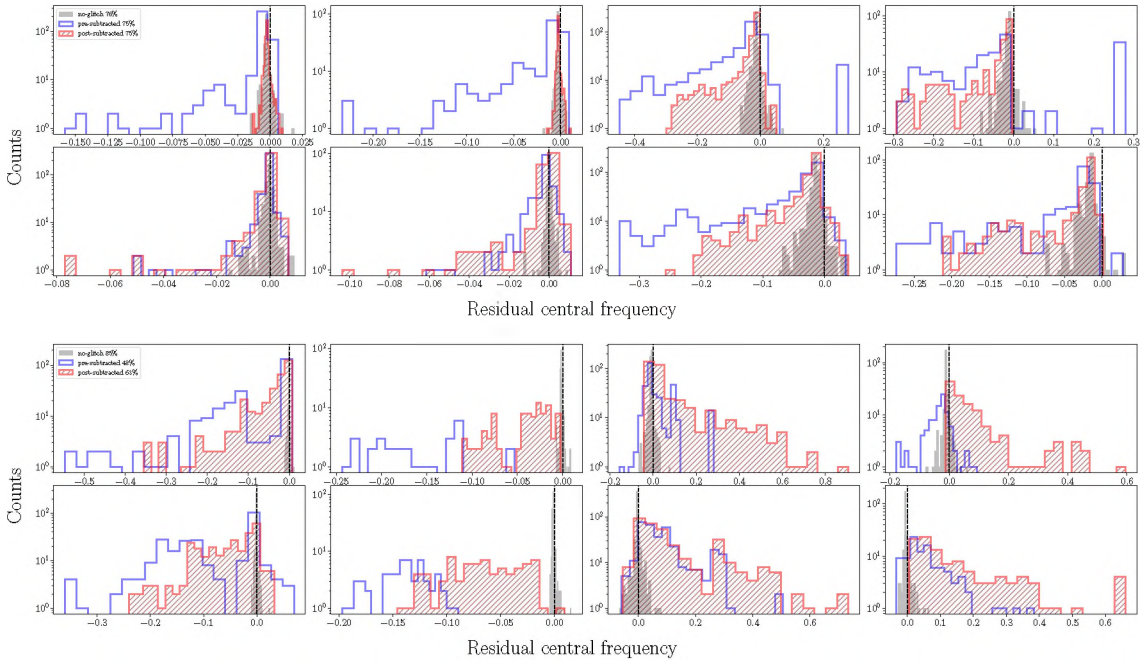

Figure 15. Distributions of the residual central frequency for Gaussian-modulated sinusoidal injections. The panels show distributions of the residual central frequency Δf_c for high-frequency (1-2$^{\text{th}}$ columns) and low-frequency (3-4$^{\text{th}}$ columns) Gaussian-modulated sinusoidal waveforms injected in the full (1,3$^{\text{th}}$ columns) and partial (2,4$^{\text{th}}$ columns) windows of the optimal (1,3$^{\text{th}}$ rows) and median (2,4$^{\text{th}}$ rows) testing samples of *Scattered light* (1-2$^{\text{th}}$ rows) and *Extremely loud* (2-4$^{\text{th}}$ rows) glitches, respectively.

the injected SNR sampled from a set of SNRs used in Sec. 3.3.1 and the injection time sampled in the full length of the testing sample data. We have 500 BBH injections for each set so that we have 4 BBH sets.

Figure 16 shows the ρ enhancement for BBH injections. Percentages P_ρ of injections with non-reduced ρ after glitch subtraction range from 76% (obtained with the median-testing-sample of *Scattered light* glitches) to 91% (obtained with the optimal-testing-sample of *Scattered light* glitches). Values of the enhancement $\langle \rho_a/\rho_b \rangle$ averaged over injections range from 1.2 (obtained with the median testing sample of *Scattered light* glitches) to 2.7 (obtained with the optimal testing sample of *Extremely loud* glitches). Subtracting significant energy due to glitches improves the cWB reconstruction so that values of the enhancement in *Extremely-loud* sets are greater than values in *Scattered-light* sets by a factor

of 1.25 and 1.8 for the optimal and median testing sample, respectively. In *Scattered-light* (*Extremely-loud*) sets, the value of the enhancement for the optimal test set is greater than the value of the median testing set by a factor of 1.25 (1.8). Table. 1 shows values the ρ enhancement and P_ρ for BBH injection sets.

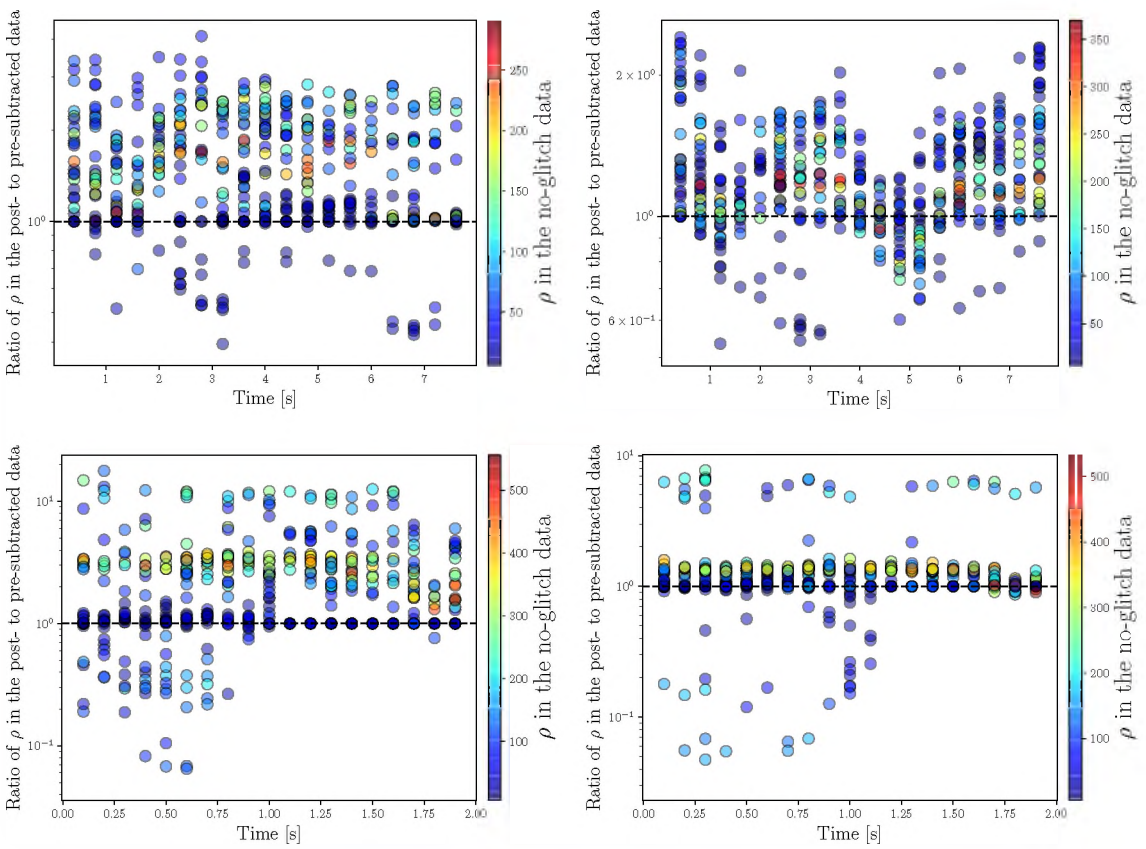

Figure 16. Enhancements of ρ after glitch subtraction as a function of the injection time for BBH waveforms injected in the optimal (left) and median testing (right) samples of *Scattered light* (top) and *Extremely loud* (bottom) glitches, respectively.

Similar to P_{sky} for Gaussian modulated sinusoidal injections, we compute P_{sky} for BBH injection set. Figure 17 shows ratios of sky-map overlaps between the no-glitch data and the post-subtracted data to sky-map overlaps with the former and the post-subtracted data for BBH injections. Values of P_{sky} range from 73% (obtained with the median testing sample of *Scattered light* glitches) to 80% (obtained with the optimal testing sample of

Extremely loud glitches). Values of $P_{\rm sky}$ in the optimal testing set are greater than values in the median testing sample set for *Scattered light* and *Extremely-loud* glitches by a factor of 1.06 and 1.14, respectively. Table. 1 shows values of $P_{\rm sky}$ for BBH injection sets.

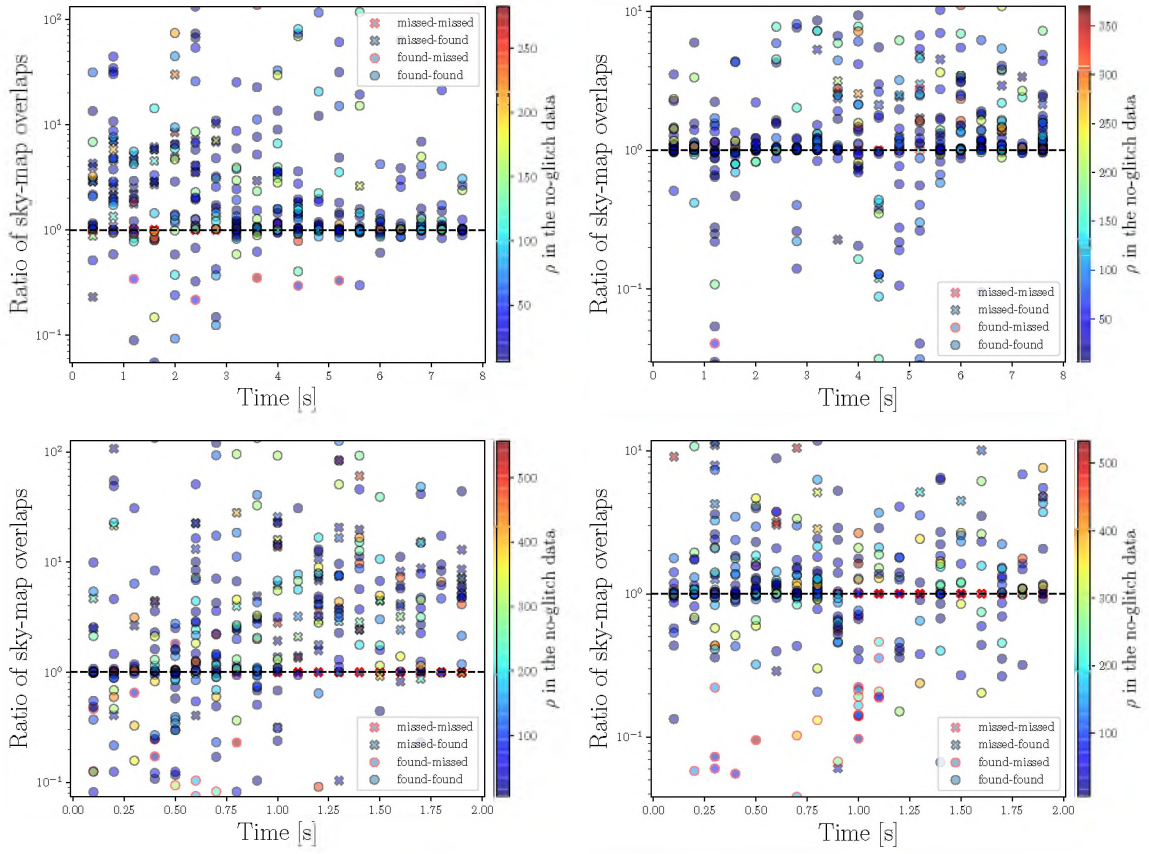

Figure 17. Ratio of sky-map overlaps for BBH injections. The panels show ratios of the sky-map overlap obtained with the no-glitch data and the pre-subtracted data to the sky-map overlap obtained with the former and the post-subtracted data as a function of the injection time for BBH waveforms injected in the optimal (left) and median testing (right) samples of *Scattered light* (top) and *Extremely loud* glitches, respectively. The first and second texts in labels in the legend denote that injections in the pre-subtracted and post-subtracted data are found or missed, respectively.

To assess the accuracy of the cWB estimated chirp mass across all injections, we calculate the normalized residual:

$$\Delta\mathcal{M} = \frac{\hat{\mathcal{M}} - \mathcal{M}}{\mathcal{M}}, \tag{8}$$

where $\hat{\mathcal{M}}$ and $\mathcal{M} = (m_1 m_2)^{3/5}/(m_1 + m_2)^{1/5}$ are the cWB estimated and injected chirp mass, respectively. Similar to the procedure in the previous section, we calculate the two-sided KS statistic $S_{\rm nb}$ (Massey, 1951) between $\Delta\mathcal{M}$ obtained with the no-glitch data and the pre-subtracted data as well as the KS statistic $S_{\rm na}$ obtained with the former and the post-subtracted data. We calculate values of the ratio $R_{\rm na}^{\rm nb} := S_{\rm nb}/S_{\rm na}$.

Figure 18 shows distributions of $\Delta\mathcal{M}$ obtained with the no-glitch, the pre- and post-subtracted data in the optimal testing sample sets. The distributions in the optimal testing sample sets are comparable with distributions in the median testing sample sets. As shown in Table 2, values of $R_{\rm na}^{\rm nb}$ range from 0.96 (obtained from the median testing sample of *Extremely loud* glitches) to 3.26 (obtained from the median testing sample of *Scattered light* glitches) as shown in Table 2. Values of $R_{\rm na}^{\rm nb}$ are close to or greater than 1, indicating the glitch subtraction technique produces no unintended effect on cWB estimates for the chirp mass or improves the estimates. As shown in Figure 19, $S_{\rm na}$ and $S_{\rm nb}$ are compatible for BBH sets so that the distribution of $\Delta\mathcal{M}$ in the post and pre-subtracted data are similar. Values of $S_{\rm na}$ and $S_{\rm nb}$ for BBH sets are typically smaller than values for Gaussian modulated sinusoidal sets because BBH waveforms distinctively differ from glitch waveforms and cWB reconstructs BBH injections more effectively than the Gaussian modulated sinusoidal injections.

3.3.3. False Alarm Rate. The confidence of a GW signal candidate is quantified by the FAR, or the rate of terrestrial noise events with their ranking statistics (e.g., ρ in cWB) equal or higher than the ranking statistic of an astrophysical candidate event. Lower values of FAR indicate that GW signal candidates are astrophysical in their origin with higher confidence. Similarly, higher values of the inverse FAR (iFAR) correspond to higher confidence. The glitch subtraction technique might reduce values ρ of the noise events and increase values of ρ for GW signal candidates when they near or overlap with glitches.

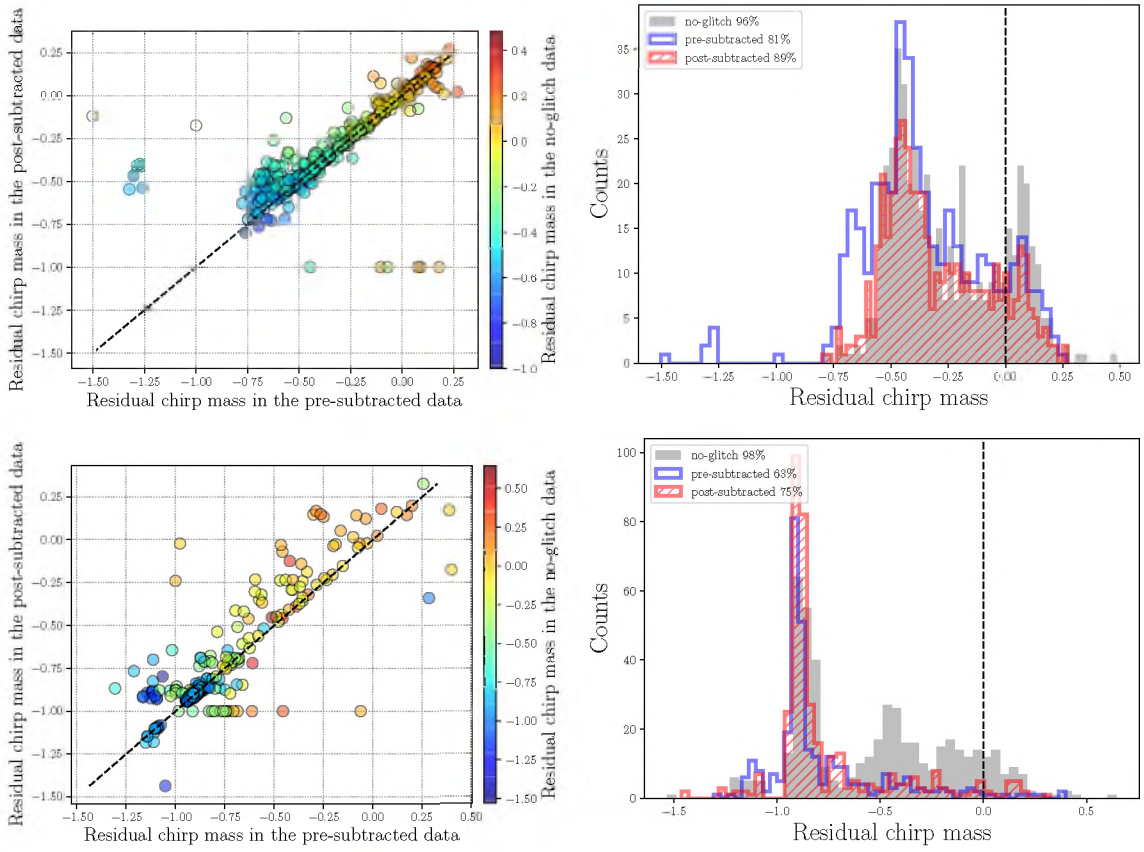

Figure 18. Residual of chirp mass estimated by cWB in the optimal testing sample of *Scattered light* (top) and *Extremely loud* (bottom) glitches. The dashed lines in the left panels denote the same value of residual chirp mass before and after glitch subtraction. The dashed lines in the right panels denote the injected values.

To assess the effect of the glitch subtraction technique on the FAR of injections used in the previous section, we use isolated samples in the testing sets with sample sizes of 237 and 156 for *Scattered light* and *Extremely loud* glitches from January 7th, 2020 3:00 UTC to February 2rd, 2020 03:55 UTC and January 15th, 2020 17:44 UTC to February 3rd, 2020 23:55 UTC, respectively. Because the testing sets used in the previous section have segment overlaps to account for statistical errors with larger sample sizes, we use the isolated testing samples from the sets to avoid double subtraction. We use the data containing the above testing samples during the detectors are observing, corresponding to the 20.4- and 20.5-day

Table 1. Enhancements of the cWB ranking statistic $\langle \rho_a/\rho_b \rangle$, i.e., ratios of the cWB ranking statistic ρ_a after and ρ_b before glitch subtraction averaged over injections, as well as percentages P_ρ of injections with non-reduced ranking statistics and percentages P_{sky} of non-reduced sky-map overlaps after glitch subtraction. The sky-map overlaps are calculated between sky maps obtained with the simulated colored Gaussian data and either of the data before or after glitch subtraction. Values of ρ are set to be 6 for injections missed. The sky-localization estimate is set to be uniformly distributed in solid angles.

Glitch class	Testing sample	Injection	Full window			Partial window		
			$\langle \rho_a/\rho_b \rangle$	P_ρ	P_{sky}	$\langle \rho_a/\rho_b \rangle$	P_ρ	P_{sky}
Scattered light	Optimal	High frequency	1.2	67%	60%	2.0	84%	79%
		Low frequency	1.6	69%	81%	2.0	89%	86%
		BBH	1.5	91%	78%	–	–	–
	Median	High frequency	1.03	75%	69%	1.2	86%	65%
		Low frequency	1.3	90%	81%	1.3	88%	84%
		BBH	1.2	76%	73%	–	–	–
Extremely loud	Optimal	High frequency	2.8	84%	74%	3.5	100%	94%
		Low frequency	2.8	87%	70%	2.0	88%	85%
		BBH	2.7	88%	80%	–	–	–
	Median	High frequency	1.5	83%	67%	1.5	100%	86%
		Low frequency	1.3	86%	66%	1.2	77%	84%
		BBH	1.5	85%	70%	–	–	–

data from the L1 and H1 detectors, respectively. The percentages of the total duration of the isolated testing samples are 0.07% and 0.026% of 20.4 days for *Scattered light* and *Extremely loud* glitches, respectively.

Using the L1 data before glitch subtraction with the original H1 data and applying time shifts to the L1 data, we get the *background* trigger set, where time shits are applied to get triggers representing the noise events coincident between detectors by chance and enlarge the analysis time. Similarly, we also use the L1 data after glitch subtraction with the original H1 data to get another background trigger set. With time shift applied to the

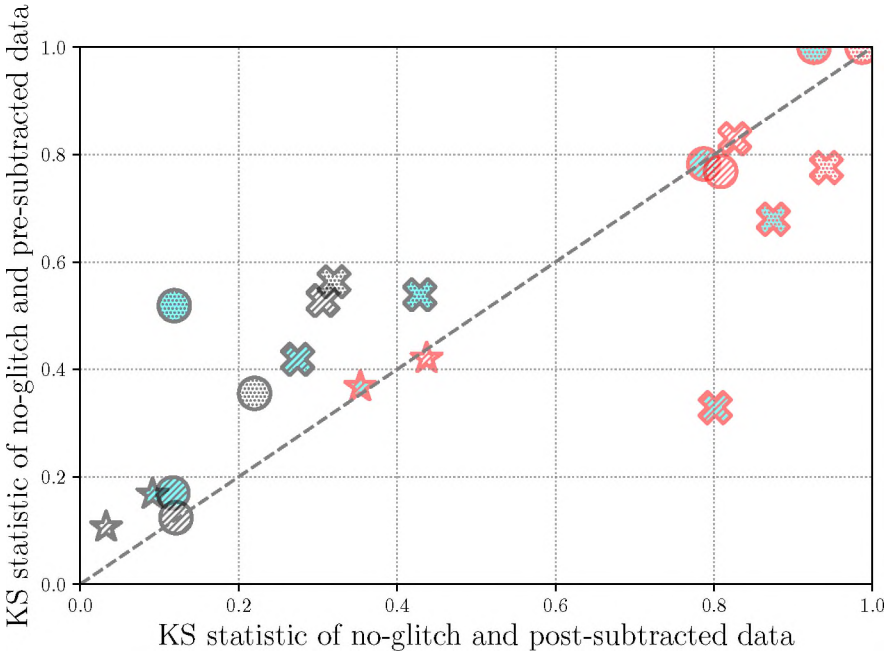

Figure 19. KS statistic obtained with the no-glitch data and the data before glitch subtraction VS. KS statistic obtained with the former and the data after glitch subtraction. The points denote KS statistics for residual peak frequency or chirp mass estimated by cWB in the cases of high-frequency (circle marker), low-frequency (cross marker) Gaussian-modulated sinusoidal waveforms and BBH waveforms (star marker) injected in the full (slashed hatch) and partial window (dotted hatch) in the optimal (cyan face color) and median (white face color) testing sample of *Scattered light* (black edge color) and *Extremely loud* (red edge color) glitches, respectively.

L1 data, we obtain 21.2-year equivalent background triggers both before and after glitch-subtracted data. Both trigger sets have the maximum values of $\rho = 53.8$ and the lowest FAR of 1.5×10^{-9} Hz (corresponding to iFAR of 21.2 years).

Figure 20 shows the FAR of background triggers before and after glitch subtraction. We find that the FAR is typically reduced in the interval from $\rho \sim 7$ to $\rho \sim 12$. The reduced FAR in this interval can be explained by the reduction of ρ in the subtracted part of the data. Figure 21 shows background triggers within the interval of the subtracted data portions. The distribution of these triggers is due to the quality of the L1 data. The average values of ρ are reduced by 13.2% and 1.9% for *Scattered light* and *Extremely loud* glitches. Because

Table 2. Percentages ($P_n/P_b/Pa$) of found injections in the (no-glitch data/data before subtraction/data after subtraction), as well as ratios $R^{nb}_{na} := S_{nb}/S_{na}$ of the KS statistic S_{nb} obtained with the no-glitch data and the data before glitch subtraction to the statistic S_{na} obtained with the former and the data after glitch subtraction for residual peak frequency and chirp mass.

Glitch class	Testing sample	Injection	Full window		Partial window	
			$(P_n/P_b/P_a)$	R^{nb}_{na}	$(P_n/P_b/P_a)$	R^{nb}_{na}
Scattered light	Optimal	High frequency	(76/75/75)%	1.45	(78/77/78)%	4.47
		Low frequency	(98/92/96)%	1.52	(97/74/88)%	1.26
		BBH	(96/81/89)%	1.84	–	–
	Median	High frequency	(75/75/75)%	1.02	(76/76/78)%	1.61
		Low frequency	(98/95/98)%	1.72	(99/81/93)%	1.76
		BBH	(98/93/96)%	3.26	–	–
Extremely loud	Optimal	High frequency	(85/48/63)%	0.99	(88/12/38)%	1.08
		Low frequency	(99/66/78)%	0.41	(99/39/49)%	0.78
		BBH	(98/63/75)%	1.04	–	–
	Median	High frequency	(88/52/55)%	0.95	(88/24/31)%	1.01
		Low frequency	(99/68/68)%	1.00	(99/40/42)%	0.82
		BBH	(97/66/67)%	0.96	–	–

Scattered light glitches are typically subtracted with our technique more effectively than *Extremely loud* glitches, the former has higher percentages than the latter. The FAR is increased in the interval from $\rho \sim 12$ to $\rho \sim 23$ in the glitch subtracted data because of two triggers with $\rho = 18.2$ and $\rho = 17.5$. However, the L1 times of these two triggers are not within the subtracted data portions so that it seems to be due to a realization of cWB trigger-generation process.

Using these two background sets, we first evaluate injections that are not nearby and overlap with glitches. Because we have created the no-glitch data sets in the previous section with the colored Gaussian noise using the PSD of the real L1 data at the time of

injections, we can consider injections in the no-glitch data to be those not nearby and overlap with glitches. As a lower limit, we set iFARs of injections with ρ greater than 53.8 to be iFAR = 21.2 years, which is the maximum length of our background.

Across high- and low frequency, and BBH injections, we find that $\sim$ 90% of injections in the no-glitch data have non-reduced iFARs after glitch subtraction. The iFARs after glitch subtraction is greater than the iFARs before glitch subtraction by a factor of $\sim$ 1.02 on average over injections because of the reduction of ρ in the background.

As mentioned above, the glitch subtraction technique may increase the ρ of injections near to or overlapping with glitches, causing higher iFARs. Figures 22 and 23 show iFAR distributions before and after glitch subtraction using corresponding backgrounds for Gaussian modulated sinusoidal and BBH injections, respectively. Percentages $P^{\mathrm{i}}_{\mathrm{ab}}$ of injections with non-reduced iFAR after glitch subtraction range from 88% (obtained from the set with the high-frequency injections in the full window of the median testing sample of *Scattered light* glitches) to 100% (obtained from the set with high-frequency injections in the partial window of the optimal testing sample of *Extremely loud* glitches). The sets with the lowest and highest values of $P^{\mathrm{i}}_{\mathrm{ab}}$ respectively correspond to the sets with the lowest and highest values P_ρ because the increases in ρ for injections correspond to the increases in iFAR.

The ratio $\langle R_{\mathrm{ab}} \rangle$ of iFAR values after glitch subtraction to iFAR values before glitch subtraction averaged over injections range from 1.03 (obtained from the set with high-frequency injections in the full window of the optimal testing sample of *Scattered light* glitches) to 1400 (obtained with high-frequency injections in the partial window of the optimal testing sample of *Extremely loud* glitches). Because high increases in ρ of injections correspond to higher increases in iFAR, values of $\langle R_{\mathrm{ab}} \rangle$ for sets with the optimal testing sample typically are greater than values for sets with the median testing sample by a factor of $\sim$ 0.7 $\sim$ 150 and $\sim$ 2.1 $\sim$ 4.3 for *Scattered light* and *Extremely loud* glitches. The sets with high-frequency injections in the full window for *Scattered light* glitches corresponding

to the lowest factor of ~ 0.7 have comparable values of $\langle R_{\rm ab}\rangle = 1.3$ and $\langle R_{\rm ab}\rangle = 1.9$ for the optimal- and median-testing-sample sets. Subtracting glitches with their peak frequencies close to the characteristic frequencies of injections lets cWB obtain higher values of ρ. Therefore, values of $\langle R_{\rm ab}\rangle$ for sets with (low/high)-frequency injections are greater than values of $\langle R_{ab}\rangle$ for sets with (high/low) frequency injections by a factor of ($\sim 3.1 \sim 74$ /$\sim 1.2 \sim 2.5$) for (*Scattered light/Extremely loud*) glitches.

Weak signals (so-called sub-threshold triggers) near or overlapping with glitches that are missed by cWB or are not confident enough to be classified as astrophysical signals can gain sufficient confidence after glitch subtraction. If we assume an iFAR threshold for weak signals to be a month, percentages $P^{\rm i}_{\rm w}$ of injections with iFAR above a month after glitch subtraction out of injections with iFAR below a month before glitch subtraction range from 1% (obtained from the set with high-frequency injections in the full window of the optimal testing sample of *Scattered light* glitches) to 57% (obtained with the set with low-frequency injections in the partial window of the optimal testing sample of *Scattered light* glitches). For *Scattered light* glitches, sets with low-frequency injections have values of $P^{\rm i}_{\rm w} \sim 40 \sim 57\%$ and sets with high-frequency and BBH injections have values of $P^{\rm i}_{\rm w} \sim 1 \sim 4\%$, where values for the optimal and median-testing-sample sets are compatible. For *Extremely loud* glitches, sets with the optima-testing sample have values of $P^{\rm i}_{\rm w} \sim 20 - 44\%$ and sets with the median-testing-sample have values of $P^{\rm i}_{\rm w} \sim 5 - 18\%$, where values for high-frequency sets are greater than values for the low-frequency sets by a factor of $\sim 0.7 \sim 1.8$. Table 3 shows values of ($P^{\rm i}_{\rm ab}/P^{\rm i}_{\rm n}/P^{\rm i}_{\rm w}$) and ($\langle R_{\rm ab}\rangle/\langle R_{\rm n}\rangle$).

4. CONCLUSION

In this paper, we have presented a new machine learning-based algorithm to subtract glitches using a set of auxiliary channels. Glitches are the product of short-live linear and non-linear couplings due to interrelated sub-systems in the detector including the optic alignment systems and mitigation systems of ground motions. Because of the character-

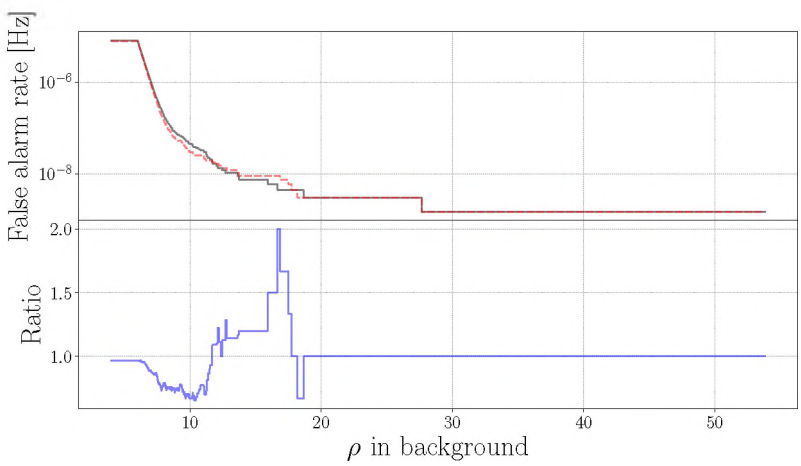

Figure 20. False alarm rates before (gray-solid) and after (red-dashed) glitch subtraction (top) and the ratio of the latter to the former.

Table 3. Percentages ($P^{\rm i}_{\rm ab}/P^{\rm i}_{\rm n}$) of injections (near to or overlapping with glitches/in the absence of glitches) with non-reduced iFAR after glitch subtraction and percentages $P^{\rm i}_{\rm w}$ of injections with iFAR above a month after glitch subtraction out of injections with iFAR below a month before glitch subtraction, and ratios ($\langle R_{\rm ab}\rangle/\langle R_{\rm n}\rangle$) of iFAR after glitch subtraction to iFAR before glitch subtraction averaged over injections (near to or overlapping with glitches/in the absence of glitches).

Glitch class	Testing sample	Injection	Full window			Partial window		
			($P^{\rm i}_{\rm ab}/P^{\rm i}_{\rm n}/P^{\rm i}_{\rm w}$)	$\langle R_{\rm ab}\rangle$	$\langle R_{\rm n}\rangle$	($P^{\rm i}_{\rm ab}/P^{\rm i}_{\rm w}/P^{\rm i}_{\rm n}$)	$\langle R_{\rm ab}\rangle$	$\langle R_{\rm n}\rangle$
Scattered light	Optimal	High frequency	(90/1/91)%	1.3	1.02	(90/3/89)%	3.5	1.02
		Low frequency	(87/46/89)	96	1.01	(90/57/92)%	260	1.04
		BBH	(93/40/90)%	97	1.02	–	–	–
	Median	High frequency	(88/1/91)%	1.9	1.02	(88/4/92)%	1.7	1.03
		Low frequency	(94/42/93)%	6.0	1.03	(98/53/90)%	28	1.02
		BBH	(90/45/90)%	10	1.01	–	–	–
Extremely loud	Optimal	High frequency	(94/31/92)%	800	1.01	(100/30/91)%	1400	1.02
		Low frequency	(94/44/95)%	700	1.02	(98/20/96)%	650	1.03
		BBH	(94/41/96)%	760	1.02	–	–	–
	Median	High frequency	(91/14/94)%	380	1.01	(100/9/92)%	380	1.01
		Low frequency	(91/13/93)%	210	1.01	(99/5/97)%	150	1.02
		BBH	(91/18/95)%	320	1.02	–	–	–

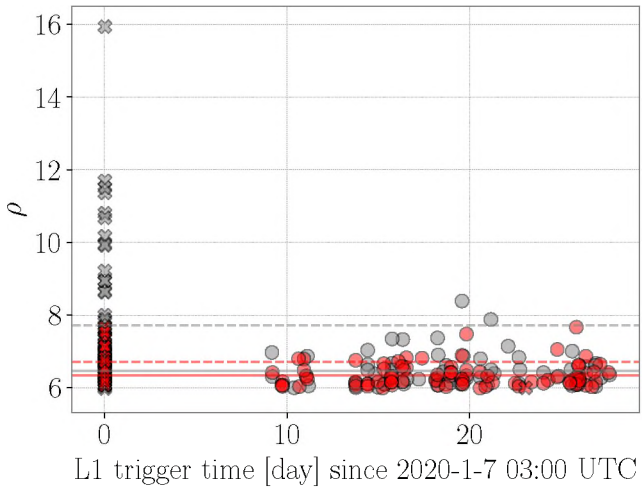

Figure 21. *Background* triggers within the intervals of the subtracted data portions for the data before (gray) and after (red) glitch subtraction for *Scattered light* (cross) and *Extremely loud* (circle) glitches, respectively. The dashed and solid lines denote the average values of ρ for these triggers for *Scattered light* and *Extremely loud* glitches, respectively.

istic of glitches, modeling coupling mechanisms is typically challenging. Without prior knowledge of the physical coupling mechanisms, our algorithm takes the data from the sensors monitoring the instrumental and environmental noise transients and then estimates the glitch waveform in the detector's output, providing the glitch-subtracted data stream. Subtracting glitches improves the quality of the data and will enhance the detectability of astrophysical GW signals.

Using two classes of glitches with distinct noise couplings in the aLIGO data, we find that our algorithm successfully reduces the SNR of the data due to the presence of glitches by $10-70\%$. Subtracting glitches from the data enhances the cWB ranking statistic by a factor of $\sim 1.03 \sim 3.5$ and $\sim 1.2 \sim 2.7$ averaged over Gaussian modulated sinusoidal injections and BBH injections, respectively. We find that the source-direction, central frequency and chirp mass estimated by cWB after glitch subtraction are comparable or more accurate than that before glitch subtraction. The iFAR of injections in the data portion in the absence of glitches is increased by ~ 1.02 by subtracting glitches in $\sim 0.1\%$ of the

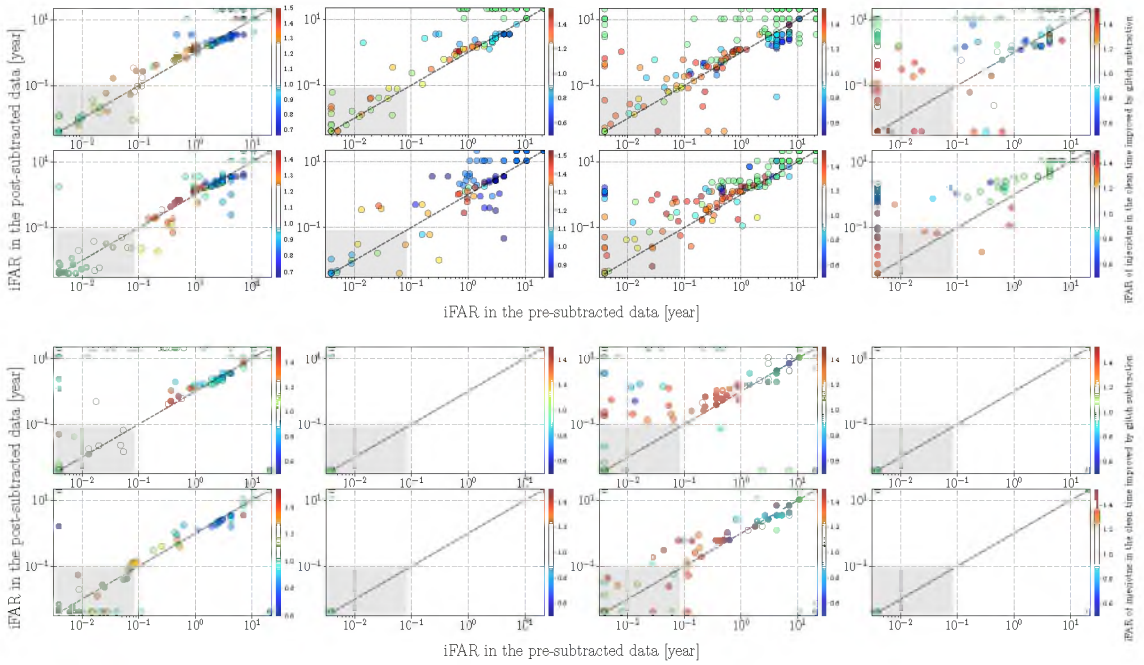

Figure 22. Distributions of the iFAR for Gaussian-modulated sinusoidal injections. The panels show distributions of the iFAR for high-frequency (1-2$^{\text{th}}$ columns) and low-frequency (3-4$^{\text{th}}$ columns) Gaussian-modulated sinusoidal waveforms injected in the full (1,3$^{\text{th}}$ columns) and partial (2,4$^{\text{th}}$ columns) windows of the optimal (1,3$^{\text{th}}$ rows) and median (2,4$^{\text{th}}$ rows) testing samples of *Scattered light* (1-2$^{\text{th}}$ rows) and *Extremely loud* (2-4$^{\text{th}}$ rows) glitches, respectively. The color scale denotes the ratio of the iFAR of injections in the no-glitch data evaluated with the background ρ distribution obtained with the post-subtracted data to that obtained with the pre-subtracted data. The shaded area denotes the iFAR less than 1 month.

20.4-day data from the L1 detector. We find that injections near to or overlapping with glitches typically have significant enhancements with glitch subtraction. The iFAR of those injections is increased by a factor $\sim 1.3 \sim 1400$.

In this paper, we focus on the two classes of glitches and apply the glitch subtraction technique to only $\sim 0.1\%$ of the L1 data so that we find no significant reduction of ρ in the background. Creating the CNN network models for other glitch classes and subtract a higher number of glitches both in the L1 and H1 could provide the statistically robust measure of the effect of the glitch subtraction technique on the data.

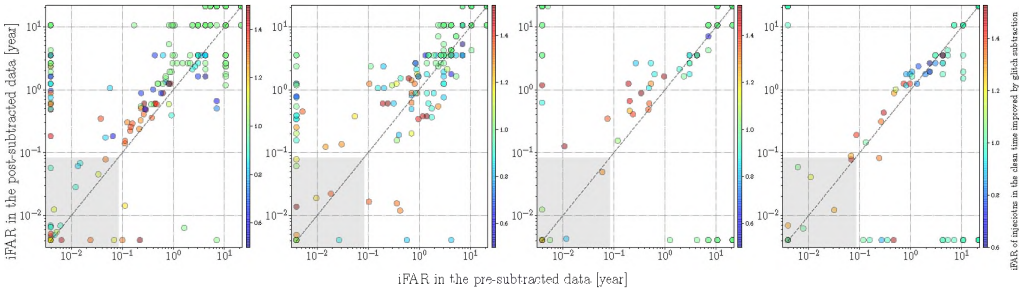

Figure 23. Distributions of iFAR for BBH injections. The panels show distributions of iFAR of BBH injections in the full window of the optimal ($1/3^{th}$ columns) and median ($2/4^{th}$ columns) testing sample of (*Scattered light/Extremely loud*) glitches, respectively. The color scale denotes the ratio of the iFAR of injections in the no-glitch data evaluated with the background ρ distribution obtained with the post-subtracted data to that obtained with the pre-subtracted data. The shaded area denotes the iFAR less than 1 month.

Currently, the LIGO-Virgo collaboration vetoes glitch classes focused on this paper and other glitch classes with witness channels. For example, over the course of the 20.4-day data from the L1 data, $\sim$ 15000 glitches with SNR above 7.5 in the two classes are present and have a total period of $\sim$ 1.8% (so-called *deadtime*), which would be vetoed. By accounting for the deadtime and injections removed by the veto, the comparison of the *volume-time* integrals Davis *et al.* (2019) between the vetoing method and the glitch subtraction technique allows us to find a better approach.

We find that using the spectrograms of the data as the input for the network is more successful than using time series as the input. However, it might improve the glitch subtraction efficiency by using the FGL transformation as well as the amplitude and phase corrections within the loss function to train the network. Improved glitch subtraction would allow us to detect astrophysical signals with higher confidence and brings us a better understanding of the physics in the universe.

ACKNOWLEDGEMENTS

K.M. is supported by the U.S. National Science Foundation grant PHY-1921006. The author would like to thank their LIGO Scientific Collaboration and Virgo Collaboration colleagues for their help and useful comments, in particular Yanyan Zheng, Stuart B. Anderson and Duncan MacLeod. The objective was discussed in the group meeting at the Missouri University of Science and Technology. The author is grateful for computational resources provided by the LIGO Laboratory and supported by the U.S. National Science Foundation Grants PHY-0757058 and PHY-0823459, as well as a service of the LIGO Laboratory, the LIGO Scientific Collaboration and the Virgo Collaboration. LIGO was constructed and is operated by the California Institute of Technology and Massachusetts Institute of Technology with funding from the U.S. National Science Foundation under grant PHY-0757058. Virgo is funded by the French Centre National de la Recherche Scientifique (CNRS), the Italian Istituto Nazionale di Fisica Nucleare (INFN) and the Dutch Nikhef, with contributions by Polish and Hungarian institutes. Our method is made use of python packages including PyTorch (Paszke *et al.*, 2019), Scipy (Virtanen *et al.*, 2020), GWpy (Macleod *et al.*, 2020), Pandas (Reback *et al.*, 2021), Matplotlib (Hunter, 2007), nds2utils (Cahillane, 2020), and scikit-learn (Pedregosa *et al.*, 2011). This manuscript has been assigned LIGO Document Control Center number LIGO-P2100159.

REFERENCES

Aasi, J. *et al.*, 'Advanced ligo,' Class. Quant. Grav., 2015a, **32**(7), p. 074001.

Aasi, J. *et al.*, 'Advanced LIGO,' Class. Quant. Grav., 2015b, **32**, p. 074001, doi: 10.1088/0264-9381/32/7/074001.

Abadie, J. *et al.*, 'Implications For The Origin Of GRB 051103 From LIGO Observations,' Astrophys. J., 2012a, **755**, p. 2, doi: 10.1088/0004-637X/755/1/2.

Abadie, J. *et al.*, 'Search for gravitational waves associated with gamma-ray bursts during LIGO science run 6 and Virgo science runs 2 and 3,' Astrophys. J., 2012b, **760**, p. 12, doi: 10.1088/0004-637X/760/1/12.

Abbott, B. *et al.*, 'Search for gravitational waves associated with 39 gamma-ray bursts using data from the second, third, and fourth LIGO runs,' Phys. Rev. D, 2008, **77**, p. 062004, doi: 10.1103/PhysRevD.77.062004.

Abbott, B. P. *et al.*, 'Search for gravitational-wave bursts associated with gamma-ray bursts using data from LIGO Science Run 5 and Virgo Science Run 1,' Astrophys. J., 2010, **715**, pp. 1438–1452, doi: 10.1088/0004-637X/715/2/1438.

Abbott, B. P. *et al.*, 'Characterization of transient noise in Advanced LIGO relevant to gravitational wave signal GW150914,' Class. Quant. Grav., 2016a, **33**(13), p. 134001, doi: 10.1088/0264-9381/33/13/134001.

Abbott, B. P. *et al.*, 'Observation of Gravitational Waves from a Binary Black Hole Merger,' Phys. Rev. Lett., 2016b, **116**(6), p. 061102, doi: 10.1103/PhysRevLett.116.061102.

Abbott, B. P. *et al.*, 'Gwtc-1: A gravitational-wave transient catalog of compact binary mergers observed by ligo and virgo during the first and second observing runs,' Phys. Rev. X, 2019, **9**, p. 031040, doi: 10.1103/PhysRevX.9.031040.

Abbott, R. *et al.*, 'GW190521: A Binary Black Hole Merger with a Total Mass of 150 $M_{\odot}$,' Phys. Rev. Lett., 2020a, **125**, p. 101102, doi: 10.1103/PhysRevLett.125.101102.

Abbott, R. *et al.*, 'Properties and Astrophysical Implications of the 150 $M_{\odot}$ Binary Black Hole Merger GW190521,' Astrophys. J. Lett., 2020b, **900**(1), p. L13, doi: 10.3847/2041-8213/aba493.

Abbott, R. *et al.*, 'GWTC-2: Compact Binary Coalescences Observed by LIGO and Virgo During the First Half of the Third Observing Run,' Phys. Rev. X, 2021, **11**, p. 021053, doi: 10.1103/PhysRevX.11.021053.

Adrian-Martinez, S. *et al.*, 'A First Search for coincident Gravitational Waves and High Energy Neutrinos using LIGO, Virgo and ANTARES data from 2007,' JCAP, 2013, **06**, p. 008, doi: 10.1088/1475-7516/2013/06/008.

Baldi, P., 'Autoencoders, unsupervised learning, and deep architectures,' in I. Guyon, G. Dror, V. Lemaire, G. Taylor, and D. Silver, editors, 'Proceedings of ICML Workshop on Unsupervised and Transfer Learning,' volume 27 of *Proceedings of Machine Learning Research*, PMLR, Bellevue, Washington, USA, 2012 pp. 37–49.

Bank, D., Koenigstein, N., and Giryes, R., 'Autoencoders,' 2021.

Biswas, R. *et al.*, 'Application of machine learning algorithms to the study of noise artifacts in gravitational-wave data,' Phys. Rev. D, 2013, **88**(6), p. 062003, doi: 10.1103/PhysRevD.88.062003.

Cahillane, C., 'nds2utils,' 2020, https://pypi.org/project/nds2utils/.

Cheuk, K. W., Anderson, H., Agres, K., and Herremans, D., 'nnaudio: An on-the-fly gpu audio to spectrogram conversion toolbox using 1d convolutional neural networks,' IEEE Access, 2020, **8**, pp. 161981–162003, doi: 10.1109/ACCESS.2020.3019084.

Cuoco, E. *et al.*, 'Enhancing Gravitational-Wave Science with Machine Learning,' Mach. Learn. Sci. Tech., 2021, **2**(1), p. 011002, doi: 10.1088/2632-2153/abb93a.

Davis, D., Massinger, T. J., Lundgren, A. P., Driggers, J. C., Urban, A. L., and Nuttall, L. K., 'Improving the Sensitivity of Advanced LIGO Using Noise Subtraction,' Class. Quant. Grav., 2019, **36**(5), p. 055011, doi: 10.1088/1361-6382/ab01c5.

Davis, D. *et al.*, 'LIGO Detector Characterization in the Second and Third Observing Runs,' Class. Quant. Grav., 2021, **38**(13), p. 135014, doi: 10.1088/1361-6382/abfd85.

Driggers, J. *et al.*, 'Improving astrophysical parameter estimation via offline noise subtraction for Advanced LIGO,' Phys. Rev. D, 2019, **99**(4), p. 042001, doi: 10.1103/PhysRevD.99.042001.

Essenwanger, O., *Elements of Statistical Analysis*, General climatology, Elsevier, 1986, ISBN 9780444424266.

Essick, R., Godwin, P., Hanna, C., Blackburn, L., and Katsavounidis, E., 'iDQ: Statistical inference of non-gaussian noise with auxiliary degrees of freedom in gravitational-wave detectors,' Machine Learning: Science and Technology, 2020, **2**(1), p. 015004, doi: 10.1088/2632-2153/abab5f.

Essick, R., Mo, G., and Katsavounidis, E., 'A Coincidence Null Test for Poisson-Distributed Events,' Phys. Rev. D, 2021, **103**(4), p. 042003, doi: 10.1103/PhysRevD.103.042003.

Godwin, P. *et al.*, 'Incorporation of Statistical Data Quality Information into the GstLAL Search Analysis,' 2020.

Griffin, D. and Jae Lim, 'Signal estimation from modified short-time fourier transform,' IEEE Transactions on Acoustics, Speech, and Signal Processing, 1984, **32**(2), pp. 236–243, doi: 10.1109/TASSP.1984.1164317.

Hahnloser, R. H. R., Sarpeshkar, R., Mahowald, M. A., Douglas, R. J., and Seung, H. S., 'Digital selection and analogue amplification coexist in a cortex-inspired silicon circuit,' Nature, 2000, **405**, pp. 947–51, doi: 10.1038/35016072.

Hunter, J. D., 'Matplotlib: A 2d graphics environment,' Computing in Science & Engineering, 2007, **9**(3), pp. 90–95, doi: 10.1109/MCSE.2007.55.

Ioffe, S. and Szegedy, C., 'Batch normalization: Accelerating deep network training by reducing internal covariate shift,' ICML, 2015, **37**, pp. 448–456.

Isogai, T., 'Used percentage veto for LIGO and virgo binary inspiral searches,' J. Phys. Conf. Ser., 2010, **243**, p. 012005, doi: 10.1088/1742-6596/243/1/012005.

Khan, S., Husa, S., Hannam, M., Ohme, F., Pürrer, M., Forteza, X. J., and Bohé, A., 'Frequency-domain gravitational waves from nonprecessing black-hole binaries. ii. a phenomenological model for the advanced detector era,' Phys. Rev. D, 2016, **93**, p. 044007, doi: 10.1103/PhysRevD.93.044007.

Kingma, D. and Ba, J., 'Adam: A method for stochastic optimization,' International Conference on Learning Representations, 2014.

Klimenko, S., Yakushin, I., Mercer, A., and Mitselmakher, G., 'Coherent method for detection of gravitational wave bursts,' Class. Quant. Grav., 2008, **25**, p. 114029, doi: 10.1088/0264-9381/25/11/114029.

Klimenko, S. *et al.*, 'Method for detection and reconstruction of gravitational wave transients with networks of advanced detectors,' Phys. Rev. D, 2016, **93**(4), p. 042004, doi: 10.1103/PhysRevD.93.042004.

Kwee, P., Bogan, C., Danzmann, K., Frede, M., Kim, H., King, P., Pöld, J., Puncken, O., Savage, R. L., Seifert, F., Wessels, P., Winkelmann, L., and Willke, B., 'Stabilized high-power laser system for the gravitational wave detector advanced ligo,' Opt. Express, 2012, **20**(10), pp. 10617–10634, doi: 10.1364/OE.20.010617.

Lemley, J., Bazrafkan, S., and Corcoran, P., 'Smart augmentation learning an optimal data augmentation strategy,' IEEE Access, 2017, **5**, pp. 5858–5869.

Macleod, D., Urban, A. L., Coughlin, S., Massinger, T., Pitkin, M., rngeorge, paulaltin, Areeda, J., Singer, L., Quintero, E., Leinweber, K., and Badger, T. G., 'gwpy/gwpy: 2.0.2,' 2020, doi: 10.5281/zenodo.4301851.

Masci, J., Meier, U., Cireşan, D., and Schmidhuber, J., 'Stacked convolutional auto-encoders for hierarchical feature extraction,' in T. Honkela, W. Duch, M. Girolami, and S. Kaski, editors, 'Artificial Neural Networks and Machine Learning – ICANN 2011,' Springer Berlin Heidelberg, Berlin, Heidelberg, ISBN 978-3-642-21735-7, 2011 pp. 52–59.

Massey, F. J., 'The Kolmogorov-Smirnov test for goodness of fit,' Journal of the American Statistical Association, 1951, **46**(253), pp. 68–78.

Meadors, G. D., Kawabe, K., and Riles, K., 'Increasing LIGO sensitivity by feedforward subtraction of auxiliary length control noise,' Class. Quant. Grav., 2014, **31**, p. 105014, doi: 10.1088/0264-9381/31/10/105014.

Mogushi, K., 'Application of a new transient-noise analysis tool for an unmodeled gravitational-wave search pipeline,' Classical and Quantum Gravity, 2021.

Mogushi, K., Quitzow-James, R., Cavaglia, M., Kulkarni, S., and Hayes, F., 'Nnetfix: An artificial neural network-based denoising engine for gravitational-wave signals,' Machine Learning: Science and Technology, 2021.

Mukund, N., Abraham, S., Kandhasamy, S., Mitra, S., and Philip, N. S., 'Transient Classification in LIGO data using Difference Boosting Neural Network,' Phys. Rev. D, 2017, **95**(10), p. 104059, doi: 10.1103/PhysRevD.95.104059.

Mukund, N. *et al.*, 'Bilinear noise subtraction at the GEO 600 observatory,' Phys. Rev. D, 2020, **101**(10), p. 102006, doi: 10.1103/PhysRevD.101.102006.

Nair, V. and Hinton, G. E., 'Rectified linear units improve restricted boltzmann machines,' in 'Proceedings of the 27th International Conference on International Conference on Machine Learning,' ICML'10, Omnipress, Madison, WI, USA, ISBN 9781605589077, 2010 p. 807–814.

Ormiston, R., Nguyen, T., Coughlin, M., Adhikari, R. X., and Katsavounidis, E., 'Noise Reduction in Gravitational-wave Data via Deep Learning,' Phys. Rev. Res., 2020, **2**(3), p. 033066, doi: 10.1103/PhysRevResearch.2.033066.

Paszke, A. *et al.*, 'Pytorch: An imperative style, high-performance deep learning library,' in H. Wallach, H. Larochelle, A. Beygelzimer, F. d Alché-Buc, E. Fox, and R. Garnett, editors, 'Advances in Neural Information Processing Systems 32,' pp. 8024–8035, Curran Associates, Inc., 2019.

Pedregosa, F., Varoquaux, G., Gramfort, A., Michel, V., Thirion, B., Grisel, O., Blondel, M., Prettenhofer, P., Weiss, R., Dubourg, V., Vanderplas, J., Passos, A., Cournapeau, D., Brucher, M., Perrot, M., and Duchesnay, E., 'Scikit-learn: Machine learning in Python,' Journal of Machine Learning Research, 2011, **12**, pp. 2825–2830.

Perez, L. and Wang, J., 'The effectiveness of data augmentation in image classification using deep learning,' ArXiv, 2017, **abs/1712.04621**.

Perraudin, N., Balazs, P., and Søndergaard, P. L., 'A fast griffin-lim algorithm,' in '2013 IEEE Workshop on Applications of Signal Processing to Audio and Acoustics,' 2013 pp. 1–4, doi: 10.1109/WASPAA.2013.6701851.

Ratnaparkhi, A., 'A maximum entropy model for part-of-speech tagging,' in 'Conference on Empirical Methods in Natural Language Processing,' 1996 .

Reback, J., jbrockmendel, McKinney, W., den Bossche, J. V., Augspurger, T., Cloud, P., Hawkins, S., gfyoung, Sinhrks, Roeschke, M., Klein, A., Petersen, T., Tratner, J., She, C., Ayd, W., Hoefler, P., Naveh, S., Garcia, M., Schendel, J., Hayden, A., Saxton, D., Gorelli, M. E., Shadrach, R., Jancauskas, V., McMaster, A., Battiston, P., Li, F., Seabold, S., Dong, K., and chris b1, 'pandas-dev/pandas: Pandas 1.3.0rc1,' 2021, doi: 10.5281/zenodo.4940217.

Reynar, J. C. and Ratnaparkhi, A., 'A maximum entropy approach to identifying sentence boundaries,' in 'Fifth Conference on Applied Natural Language Processing,' Association for Computational Linguistics, Washington, DC, USA, 1997 pp. 16–19, doi: 10.3115/974557.974561.

Riles, K., 'Gravitational Waves: Sources, Detectors and Searches,' Prog. Part. Nucl. Phys., 2013, **68**, pp. 1–54, doi: 10.1016/j.ppnp.2012.08.001.

Robinet, F., Arnaud, N., Leroy, N., Lundgren, A., Macleod, D., and McIver, J., 'Omicron: A tool to characterize transient noise in gravitational-wave detectors,' SoftwareX, 2020, p. 100620, ISSN 2352-7110, doi: https://doi.org/10.1016/j.softx.2020.100620.

Rumelhart, D., HINTON, G., and WILLIAMS, R., 'Learning internal representations by error propagation,' in A. Collins and E. E. Smith, editors, 'Readings in Cognitive Science,' pp. 399–421, Morgan Kaufmann, ISBN 978-1-4832-1446-7, 1988, doi: https://doi.org/10.1016/B978-1-4832-1446-7.50035-2.

Schofield, R., 'aLIGO LHO Logbook,' 2016.

Shorten, C. and Khoshgoftaar, T. M., 'A survey on image data augmentation for deep learning,' Journal of Big Data, 2019, **6**(1), p. 60, doi: 10.1186/s40537-019-0197-0.

Smith, J. R., Abbott, T., Hirose, E., Leroy, N., Macleod, D., McIver, J., Saulson, P., and Shawhan, P., 'A Hierarchical method for vetoing noise transients in gravitational-wave detectors,' Class. Quant. Grav., 2011, **28**, p. 235005, doi: 10.1088/0264-9381/28/23/235005.

Soni, S. *et al.*, 'Reducing scattered light in LIGO's third observing run,' Class. Quant. Grav., 2020, **38**(2), p. 025016, doi: 10.1088/1361-6382/abc906.

Soni, S. *et al.*, 'Discovering features in gravitational-wave data through detector characterization, citizen science and machine learning,' 2021.

Tiwari, V. *et al.*, 'Regression of Environmental Noise in LIGO Data,' Class. Quant. Grav., 2015, **32**(16), p. 165014, doi: 10.1088/0264-9381/32/16/165014.

Usman, S. A. *et al.*, 'The pycbc search for gravitational waves from compact binary coalescence,' Class. Quant. Grav., 2016, **33**(21), p. 215004, doi: 10.1088/0264-9381/33/21/215004.

Vajente, G., Huang, Y., Isi, M., Driggers, J. C., Kissel, J. S., Szczepanczyk, M. J., and Vitale, S., 'Machine-learning nonstationary noise out of gravitational-wave detectors,' Phys. Rev. D, 2020, **101**(4), p. 042003, doi: 10.1103/PhysRevD.101.042003.

Vincent, P., Larochelle, H., Lajoie, I., Bengio, Y., and Manzagol, P.-A., 'Stacked denoising autoencoders: Learning useful representations in a deep network with a local denoising criterion,' Journal of Machine Learning Research, 2010, **11**(110), pp. 3371–3408.

Virtanen, P. *et al.*, 'SciPy 1.0: Fundamental Algorithms for Scientific Computing in Python,' Nature Methods, 2020, **17**, pp. 261–272, doi: 10.1038/s41592-019-0686-2.

Was, M., Gouaty, R., and Bonnand, R., 'End benches scattered light modelling and subtraction in advanced Virgo,' Class. Quant. Grav., 2021, **38**(7), p. 075020, doi: 10.1088/1361-6382/abe759.

Was, M., Sutton, P. J., Jones, G., and Leonor, I., 'Performance of an externally triggered gravitational-wave burst search,' Phys. Rev. D, 2012, **86**, p. 022003, doi: 10.1103/PhysRevD.86.022003.

Yamaguchi, K., Sakamoto, K., Akabane, T., and Fujimoto, Y., 'A neural network for speaker-independent isolated word recognition,' in 'ICSLP,' 1990 .

Zevin, M. *et al.*, 'Gravity Spy: Integrating Advanced LIGO Detector Characterization, Machine Learning, and Citizen Science,' Class. Quant. Grav., 2017, **34**(6), p. 064003, doi: 10.1088/1361-6382/aa5cea.

SECTION

4. AN ARTIFICIAL NEURAL NETWORK-BASED DENOISING ENGINE FOR GRAVITATIONAL-WAVE SIGNALS FROM COMPACT BINARY COALESCENCE

In the previous chapter, we have discussed a machine learning-based method for subtracting glitches that are witnessed with a set of auxiliary channels which are not coupled with any astrophysical signals. Because only glitches that are coupled with excess power witnessed by those channels can be subtracted, our method presented in the previous chapter can be applied to glitches overlapping with astrophysical GW signals without introducing unintended changes on the observed GW-signal waveform in principle. The above method can be applied to both modeled and unmodeled GW signals. Subtracting glitches can improve the detectability of GW signals as well as provide a better estimate of source parameters. The trade-off of this method is that it is not able to subtract glitches with no witness channels. For example, one class of short-lived glitches called *blip* glitches is adversely affecting GW searches. To remove these glitches, we focus on modeled signals, in particular, produced from CBCs in this chapter. CBC signals are well modeled with theoretical waveforms. Mogushi *et al.* (2021) employ a machine learning-based algorithm to remove glitches coincident with a CBC signal and discuss the efficiency in reconstructing time series and the effect on the sky localization error region of the sources. The content of this chapter is closely based on Mogushi *et al.* (2021). The NNETFIX code can be found in `https://gitlab.com/RQJ/nnetfix`) with the MIT license without restriction about the rights to use, copy, modify, merge, publish and distribute it.

4.1. BACKGROUND

As mentioned in the previous chapter, LIGO-Virgo detected about 50 confident events of GW signals (Abbott *et al.*, 2019d, 2021b). Among these events, the first detection of a GW signal from a BNS merger on August 17th, 2017, GW170817, broadened multi-messenger astronomy by including GW observations Abbott *et al.* (2017c). Approximately 1.7 seconds after the BNS signal ended, a short gamma-ray burst (GRB) was detected (Abbott *et al.*, 2017d). The sky maps of GW170817 and the GRB were used to verify their association with high confidence (Abbott *et al.*, 2017c,d). This association supports the long-thought theory that at least a class of sources of short GRB is BNS mergers (Abbott *et al.*, 2017b).

As mentioned earlier, ground-based GW detectors must be extremely sensitive to detect GW signals. As a trade-off, those detectors are exceedingly susceptible to glitches (Abbott *et al.*, 2019d). The presence of a glitch near a detected GW signal is likely to cause an adverse effect on the analysis of the latter, such as an estimate of the source location in the sky. The most remarkable instance of such an occurrence was GW170817. To mitigate the effect of a glitch on the signal, a low-latency operation that removes the contaminated portion of the data was applied (Abbott *et al.*, 2017c).

One of the easiest choices to remove the effect of the contaminating glitch on the analysis is to use only the data from the non-glitch affected detector. However, this approach tends to significantly increase the size of the sky localization error region for the two-detector observation. When a glitch overlaps with a signal in the single detector observation, non-glitch affected data is not available. Instead of discarding the entire data from a detector, another technique in low-latency is so-called *gating*. One method of gating is to set the data affected by the glitch to zero using a window function and smoothly joint the gated portion and the surrounding part (Usman *et al.*, 2016). In the case of GW170817, gating was applied to provide a better estimate of the source sky location for EM follow-

up observations (Pankow *et al.*, 2018). On larger latencies, glitch mitigation techniques including using BayesWave (Cornish and Littenberg, 2015) to model and subtract the glitch can be applied (Chatziioannou *et al.*, 2021; Cornish, 2021; Pankow *et al.*, 2018).

Figure 4.1 displays an example of the deleterious effect of gating data on the sky localization error region obtained with a simulated BBH merger signal. The sky localization of the gated data significantly alters from the sky localization of the full data. After applying the gate, the 90% sky localization error region no longer includes the true sky position of the injected signal.

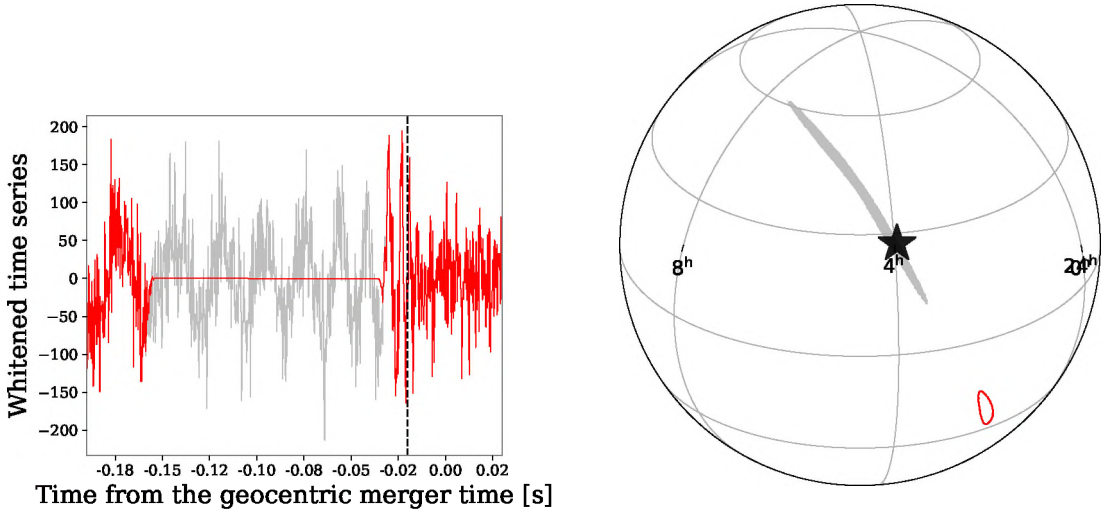

Figure 4.1. Left: Whitened time series of a simulated BBH signal with two-detector network SNR $\rho_{\mathrm{N}} = 42.4$ and component masses $(m_1, m_2) = (35, 29)\ M_{\odot}$ in aLIGO recolored Gaussian noise (gray curve). Right: The 90% sky localization error regions. A 130 millisecond-long gate is applied 30 ms before the geocentric merger time (red curve). The vertical black-dashed line denotes the merger time in H1. The star denotes the true sky position of the simulated signal.

In future observation runs, more sensitive detectors are expected to achieve higher detection rates, possibly making higher chances of observing CBC signals being contaminated by glitches. The inaccurate estimate of the sky localization of CBC signals could lead

to misidentification of potential EM counterparts. Hence, developing and implementing accurate low-latency denoising methods could be highly advantageous to multi-messenger astrophysics.

In the following sections, we present a machine learning-based pipeline to denoise transient GW signals produced from CBC sources called NNETFIX ("A Neural NETwork to 'FIX' GW signals coincident with short-duration glitches in detector data") (Mogushi *et al.*, 2021). The output of NNETFIX can be fed into other algorithms including the rapid sky localization pipeline BAYESTAR (Singer and Price, 2016) and source-parameter estimation pipelines called LALINFERENCE (LIGO Scientific Collaboration, 2018) or BILBY (Ashton *et al.*, 2019). NNETFIX employs artificial neural networks (ANNs) to interpolate the portion of a signal that is lost due to the presence of an overlapping glitch. The ANN can be trained using any types of CBC waveforms including those originated by BBH, BNS, and neutron star and black hole (NSBH) signals. In the following sections, we focus on BBH waveforms. To train the ANN, we use a template bank of simulated BBH waveforms injected into the simulated noise data. To assess the accuracy of our algorithm, we compare the recovered waveforms and the sky maps from the processed data to the corresponding quantities obtained from the data before gating based on a set of statistical metrics.

4.2. ALGORITHM ARCHITECTURE AND TRAINING AND TESTING

As the implementation of the algorithm, we consider a situation where a CBC signal is detected in at least two detectors in the GW detector network, and the part of the data in a detector is gated to remove the presence of glitches overlapping the signal. We may rely on external algorithms such as IDQ (Essick *et al.*, 2020) and OMICRON (Robinet *et al.*, 2020) to identify the presence of glitches.

Without loss of generality, we choose the scenario where a signal is detected with the L1 and H1 detectors and setting the data in the H1 detector to be gated partially for our analysis. We assume the merger time at the geometric center time of Earth is approximately

known from the L1 data. We let $s_f(t)$, $s_g(t)$, and $s_r(t)$ denote the full time series without the glitch, the gated time series, and the NNETFIX reconstructed time series, respectively. We define $s_r(t)$ as the output of the NNETFIX-reconstruction function F which maps $s_g(t)$ to an estimate of $s_f(t)$:

$$s_r(t) := F\left[s_g(t)\right] \ . \tag{4.1}$$

The pipeline employs a type of ANN, Multi-Layered Perceptron (MLP) regressor (Rosenblatt, 1961) in SCIKIT-LEARN (Pedregosa *et al.*, 2011) for the proof of concept. Other types of machine learning algorithms such as CNN (Chatterjee *et al.*, 2019; Ormiston *et al.*, 2020; Wei and Huerta, 2020) and *long short-term memory* recursive neural network (Bengio *et al.*, 1994; Hochreiter and Schmidhuber, 1997) can be used to possibly improve results. In a MLP regressor, the array of the artificial neurons (mathematical functions) are connected to every neuron in the preceding and/or subsequent layers. Each neuron computes a weighted linear combination of the outputs from the preceding layer and passes through a non-linear activation function. During the training, the weights are updated according to the gradient of the difference (so-called *loss*) between the ANN output and the corresponding true values iteratively.

NNETFIX uses ANN of one hidden layer consisting of 200 neurons and the rectified linear unit (*ReLU*) activation function (Hahnloser *et al.*, 2000; Nair and Hinton, 2010). For determining the weights in the ANN, we use the *ADAM* stochastic gradient-based optimizer (Kingma and Ba, 2014) with a learning rate of 10^{-3}. Setting ten percent of the training data samples aside, we validate the training process. To make the ANN map the input and the output for the data not contained in the training data set, we terminate the training iteration if the ANN performance plateaus with a tolerance level of 10^{-4}. The choice of the ANN structure employed in NNETFIX is motivated by our study where we find one hidden layer is more suitable than multiple hidden layers for our chosen objective function which the ANN seeks to optimize through training. As the function optimized by the ANN (so-called

loss function)in this study, we choose MSE which is the average of the squared difference of the input and output of the ANN. The number of neurons seems to not significantly affect the values of the objective function.

As a training data set, we first create template banks of simulated non-spinning IMRPHENOMD BBH merger waveforms (Khan *et al.*, 2016) with varying intrinsic and extrinsic parameters. To reduce the potential overfitting, each template bank also contains a number of (pure) noise time series. We choose the direction of the injected signals to be distributed isotropically in the sky. The waveform coalescence phase, polarization angle, and cosine of the inclination angle are set to be uniformly distributed in the intervals $[0, 2\pi]$, $[0, \pi]$, and $[-1, 1]$, respectively. We choose the network SNR ρ_{N} (Usman *et al.*, 2016) of the simulated signals to be uniformly distributed in the range $[11.3, 42.4]$.

To assess the prediction accuracy of the trained ANNs for different signal lengths, we consider three distinct template banks corresponding to low, medium, and high BBH component masses. The BBH component masses are uniformly sampled in accordance with a Jeffreys prior for the matched-filter detection statistic. As the mass of the BBH merger reduces, the bank contains a larger number of waveforms to properly cover the mass parameter space (Cokelaer, 2007; Harry *et al.*, 2009; Manca and Vallisneri, 2010; Van Den Broeck *et al.*, 2009).

For each of the three distinct template banks, we create 12 training-testing sets. First, we inject each waveform into 50 distinct realizations of recolored Gaussian noise for Advanced LIGO (aLIGO) at design sensitivity (Abbott *et al.*, 2020a). Second, we include the (pure) noise time series in the data set. Third, we shuffle and split the set by 70%–30% for training and testing, where we use 10% of the training set for the internal validation set. Finally, we apply the 12 combinations of gate durations $t_d = \{50, 75, 130\}$ ms and gate end-times before the geocentric merger time $t_e = \{15, 30, 90, 170\}$ ms. The time series are downsampled to 4096 Hz from 16384 Hz, whitened, and then high-passed by choosing a conservative value of 25 Hz for the high-pass filter. As the gate, we choose a reversed Tukey

window function with a taper of 0.1 s and being fixed to geocentric merger time. However, we emphasize that the merger time observed in the H1 detector naturally shifts due to the sky position and the polarization angle of the GW signal. For high (medium, low) mass scenario, the primary mass m_1 ranges in 28-42 (15-25, 10-15) $M_\odot$, and the secondary mass m_2 ranges 23-35 (12-18, 8-12) $M_\odot$, the number of waveforms n_s is 61 (251, 348), the number of pure noise series n_n is 300 (1350, 1900), and the dimension of the set ($n_s \times 50 + n_n$) is 3355, (13900, 19300) (see Table 1 in (Mogushi *et al.*, 2021)).

After building the ANN models, we calculate the coefficient of determination R^2 using the testing sets to quantify the effectiveness of the ANN prediction. For this calculation, we employ a SCIKIT-LEARN library (Pedregosa *et al.*, 2011). The R^2 is defined using the sum of squares of residuals (SSR) and the total sum of squares (TSS) as

$$R^2 = 1 - \frac{\mathrm{SSR}}{\mathrm{TSS}}, \tag{4.2}$$

where

$$\mathrm{SSR} = \sum_{i=1}^{n} \sum_{k=1}^{N} [y_i(t_k) - \hat{y}_i(t_k)]^2 , \tag{4.3a}$$

$$\mathrm{TSS} = \sum_{i=1}^{n} \sum_{k=1}^{N} [y_i(t_k) - \bar{y}(t_k)]^2 , \tag{4.3b}$$

where $y_i(t_k)$ and $\hat{y}_i(t_k)$ are the gated portion of true time series and the predicted time series at the k^{th} timestamp of the i^{th} sample in the testing set, $\bar{y}(t_k) = \sum_{i=1}^{n} y_i(t_k)$ is the mean of y_i over samples, and n and N denote the numbers of samples and the timestamps, respectively. The R^2 ranges from $-\infty$ (inaccurate) to 1 (perfect prediction), with positive values corresponding to some degree of accuracy. The ranges of the R^2 for the testing sets are [0.773, 0.882], [0.750, 0.883], and [0.691, 0.879] for the low-mass, medium-mass, and high-mass scenarios, respectively, and the mean values are 0.833, 0.827, and 0.814 (Mogushi *et al.*, 2021).

Because the R^2 is calculated using the time series in the gated region, we next evaluate the effect of NNETFIX on quantities such as time-series match and sky localization using the reconstructed time series constructed after concatenating the time series inside and outside of the gated portion and being re-colored. The performance of NNETFIX changes for different component masses, network SNR, and gate settings. Therefore, we construct 108 additional independent *exploration* sets with fixed network SNR ρ_{N} = (11.3, 28.3, 42.4) and component masses of (12, 10), (20, 15), (35, 29) $M_{\odot}$, and identical combinations of gate durations and end-times as the training+testing sets. Having each exploration set to consist of 512 independent time series with the remaining parameters distributed as in the training-testing sets, we account for the statistical variation as well.

4.3. PERFORMANCE IN THE TIME-DOMAIN

The effectiveness of the NNETFIX reconstruction can be evaluated using the SNRs of the full, reconstructed, gated time series (see Mogushi *et al.* (2021)).

Because the effectiveness of NNETFIX is characterized by both the amount of SNR gained from the gated time series as well as the amount of residual SNR relative to that of the full time series, we account for these factors. In the SNR calculation, the maximum-likelihood method estimates a waveform by optimizing the phase, the merger time, and the amplitude. Time series with different noise realizations result in different estimated waveforms even for a signal with a fixed injected SNR. As a result, the calculated SNRs for the same signal injected into different noise realizations distribute according to a standard normal distribution because of the uncertainty of the maximum-likelihood method (Vitale *et al.*, 2020). When the NNETFIX reconstructed waveform has peak amplitude in the gated portion, the merger time estimated through the maximum-likelihood method is farther away from the true merger time, causing a too-large SNR gain even for a signal mismatched with the true waveform. To account for these factors, we use a complementary metric called fractional match gain (FMG) which indicates how well the NNETFIX reconstructed data

matches the signal compared to the full and gated data (Mogushi *et al.*, 2021):

$$\mathrm{FMG} = \frac{M_r - M_g}{M_f - M_g}, \tag{4.4}$$

where the match M_i between a time series s_i and the injected waveform h (Nitz *et al.*, 2020) is

$$M_i = \frac{(\tilde{s}_i|\tilde{h})}{\sqrt{(\tilde{s}_i|\tilde{s}_i)(\tilde{h}|\tilde{h})}}, \tag{4.5}$$

where the tilde indicates the Fourier transform, and $(\cdot|\cdot)$ denotes the noise-weighted inner product defined in Equation (1.73) with a slight modification with the lower and higher frequency cutoffs to be high-pass frequency and the Nyquist frequency, respectively.

In Eq. (4.4), we only consider the samples with $M_f - M_g > 0$. M_g becomes larger than M_f in only rare instances (0.5% of all exploration set data samples) when values of single interferometer peak SNR of the full time series are ~ 4.5. These instances are observed when the gated portion of the data is noise-dominant and anti-correlated with the injected waveform. Such low-SNR signals are not expected to be detected in the online GW searches but they could be categorized as *sub-threshold* triggers in the offline searches (Abbott *et al.*, 2019d; Riles, 2013). Because we seek to use NNETFIX in low-latency operations, in the following we remove these samples from the exploration sets.

Positive (negative) values of FMG indicate that the reconstructed time series is more (less) matching with the injected waveform than the gated time series. Values of FMG larger than 1 indicate that the reconstructed time series is more similar to the injected waveform than the full time series. Hence, we consider the reconstructions with $0 < \mathrm{FMG} \leq 1$ to be successful. Figures 4.2 and 4.3 show the distributions of FMG for two exploration sets from the medium-mass scenario. Figure 4.4 shows the comparison of these distributions.

Values of FMG across the exploration sets generally increase with component masses, and gate end-time, and network SNR. The set of component masses is the dominant factor that affects values of FMG. Values of FMG increase with component masses. Median

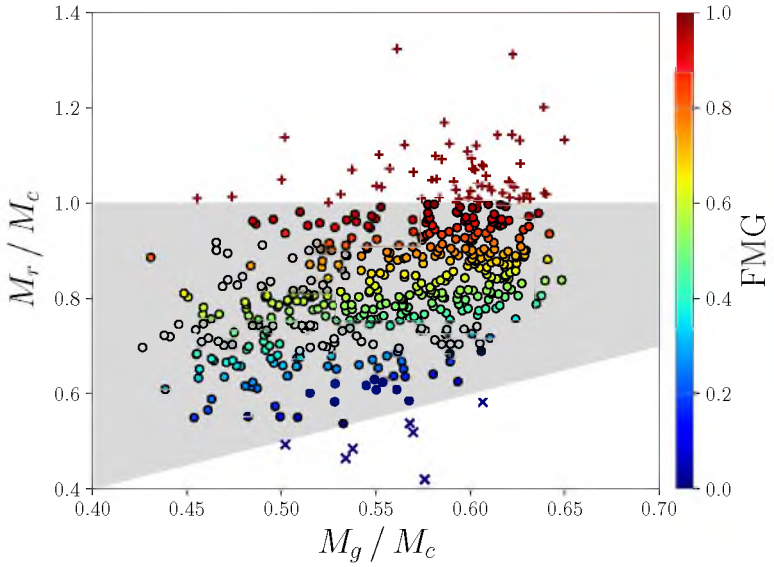

Figure 4.2. Scatterplot of M_r/M_f vs. M_g/M_f for the exploration set with $\rho_N = 42.4$, $(m_1, m_2) = (35, 29)\ M_\odot$, $t_d = 130$ ms and $t_e = 30$ ms. The circles denote samples with $0 < \text{FMG} \leq 1$, the $\times$ markers denote samples with $\text{FMG} \leq 0$ and the + markers denote overfitted samples with $\text{FMG} > 1$. The gray area denotes the region of the parameter space with $0 < \text{FMG} \leq 1$, which contains 86% of the reconstructed time series.

values for the high-mass sets are higher than the corresponding values for the low-mass sets by a factor ranging from ~ 1.3 ($\rho_N = 28,3$ with $t_d = 50$ ms and $t_e = 90$ ms) to ~ 3.3 ($\rho_N = 11.3$ with $t_d = 130$ ms and $t_e = 90$ ms). For signals with higher component masses, NNETFIX's reconstructed time series tends to be more similar to the injected signals than the full time series. The fraction of samples with FMG above 1 for the high-mass sets is larger than the corresponding value for the low-mass sets by a factor of ~ 6 on average.

The second most important factor for values of FMG is the gate end-time. Median FMG values typically increase as values of the gate end-time become larger. A gate farther away from the merger time removes the portion of a signal with smaller energy, corresponding to smaller $M_f - M_g$. Therefore, NNETFIX tends to efficiently recover the energy of the signal lost due to the gate. The median values of FMG for the sets with

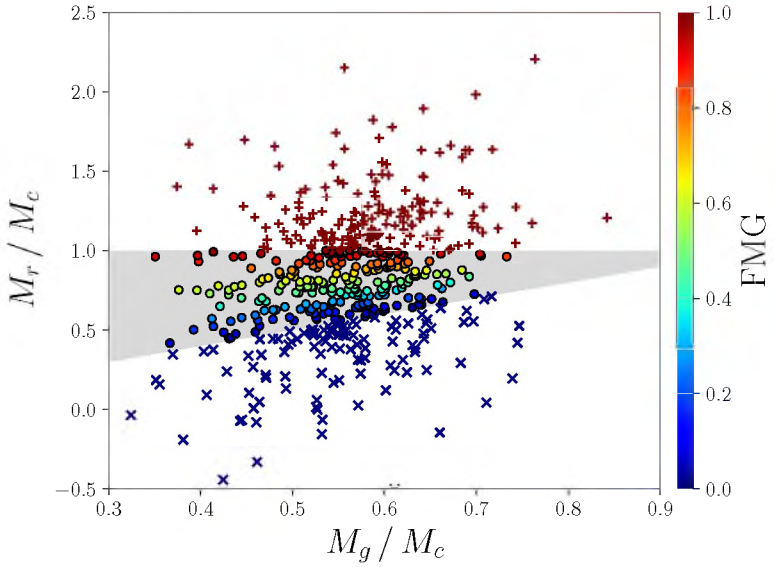

Figure 4.3. Scatterplot of M_r/M_f vs. M_g/M_f for the exploration set with $\rho_N = 11.3$, $(m_1, m_2) = (35, 29)\ M_\odot$, $t_d = 130$ ms and $t_e = 30$ ms. The circles denote samples with $0 < \text{FMG} < 1$, the $\times$ markers denote samples with $\text{FMG} \leq 0$ and the + markers denote overfitted samples with $\text{FMG} > 1$. The gray area denotes the region of the parameter space with $0 < \text{FMG} \leq 1$, which contains 44% of the reconstructed time series.

$t_e = 170$ ms are larger than the corresponding values for the sets with $t_e = 15$ ms by a factor ranging from ~ 1.2 (the high-mass scenario with $\rho_N = 42.4$ and $t_d = 130$ ms) to ~ 2.9 (the medium-mass scenarios with $\rho_N = 11.3$ and $t_d = 130$ ms).

Median FMG values typically increase with network SNR. NNETFIX efficiently reconstructs time series containing signals with larger SNRs. Median values of FMG for the sets with $\rho_N = 42.4$ are greater than the corresponding values for the sets with $\rho_N = 11.3$ by a factor ranging from ~ 1 (the low-mass scenario with $t_d = 75$ ms and $t_e = 30$ ms) to ~ 1.3 (the medium-mass scenario with $t_d = 50$ ms and $t_e = 15$ ms).

FMG values typically increase as values of the gate duration become smaller. Smaller gate durations correspond to smaller signal losses so that NNETFIX efficiently provides a larger recovery of signal energy for smaller gate durations. Median value of FMG for the sets with $t_d = 50$ ms are larger than the corresponding values for the sets with

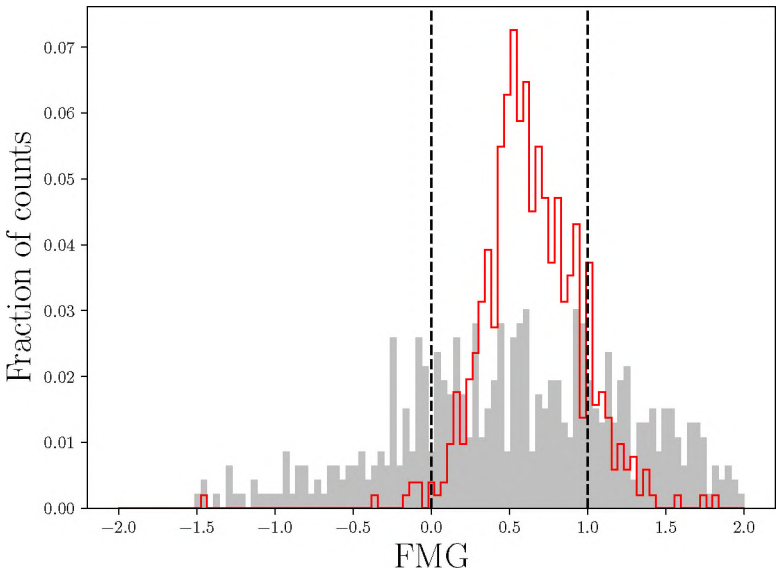

Figure 4.4. Distribution of FMG for the exploration sets with component masses $(m_1, m_2) = (35, 29)\ M_\odot$, gate duration $t_d = 130$ ms, gate end-time $t_e = 30$ ms, and $\rho_N = 11.3$ (gray-filled) and $\rho_N = 42.4$ (red). The vertical dashed lines denote FMG= 0 and FMG= 1. The efficiency of the set with $\rho_N = 11.3$ is 44%. The efficiency of the set with $\rho_N = 42.3$ is 86%.

$t_d = 130$ ms by a factor ranging from ~ 1.01 (the high-mass scenario with $\rho_N = 11.3$ and $t_e = 15$ ms) to ~ 1.9 (the medium-mass scenario with $\rho_N = 28.3$ and $t_e = 30$ ms). As rare exceptional cases for the high-mass sets with $t_e = 90$, median values of FMG for the sets with $t_d = 50$ ms are smaller than the corresponding values for the sets with $t_d = 130$ ms by a factor $\sim 1.3 \sim 1.2$ across values of ρ_N used. These exceptional sets with $t_d = 130$ ms tends to have a higher number of samples with FMG greater than 1 compared with the sets with $t_d = 50$ ms by a factor $\sim 1.3 \sim 2$.

To quantify NNETFIX's performance including the variation of FMG in each exploration set, we define the efficiency to be the fraction of successfully reconstructed samples. More specifically, the efficiency is the fraction of samples with $0 < \text{FMG} \leq 1$. The fractions of samples with $\text{FMG} \leq 0$, $0 < \text{FMG} \leq 1$ and $\text{FMG} > 1$ for all exploration sets can be found in Tables 2-3 of Mogushi *et al.* (2021).

The efficiency across all exploration sets ranges from approximately 0.31 to over 0.95. The component masses mildly affect the efficiency. The median value of the efficiency reduces from 0.77 for the low-mass scenario to 0.61 for the high-mass scenario with the network SNR, gate duration, and gate end-time held fixed. The worst case with 68% of the samples being unsuccessfully reconstructed occurs in the medium-mass scenario with $\rho_N = 11.3$, $t_e = 170$ ms, and $t_d = 130$ ms.

With a chosen mass scenario with fixed gate duration and gate end-time, the efficiency typically increases by a factor $\sim$ 1.5–2 as the network SNR becomes larger. For higher SNRs, the algorithm can use a larger amount of signal energy before and after the gated portion of the data as the input to reconstruct the time series. NNETFIX successfully reconstructs over 66% of the data samples with $\rho_N = 28.3$ or larger for all low-mass and medium-mass exploration sets while over 50% of the data samples are successfully reconstructed for the high-mass sets except for two marginal cases with gate duration $t_d = 75$ ms and gate end-time $t_e = 90$ ms. The exploration sets with $\rho_N = 11.3$ have lower efficiencies in the range from 31% for the high-mass set with $t_d = 75$ ms and $t_e = 90$ ms to 66% for the low-mass set with $t_d = 130$ ms and $t_e = 15$ ms.

Figures 4.5 and 4.6 show the efficiency as a function of the single interferometer peak SNR for the low-mass and high-mass exploration sets, respectively. The efficiency as a function of the single interferometer peak SNR for the medium-mass exploration sets can be found in Figure 7 of Mogushi *et al.* (2021). The percentage of successful reconstructions varies from $\sim$ 33%–66% at low peak SNR to $\gtrsim$ 80% at high peak SNR. The lowest values $\lesssim$ 40% occur for the sets with $t_d \geq 75$ ms and $t_e \geq 30$ ms. More than 70% of the data samples with peak SNR above $\sim$ 20 have successful reconstructions irrespective of gate duration and end-time.

The efficiency seems not to significantly change with varying gate durations at fixed network SNR and gate end-time across all exploration sets. Similarly, the gate end-time before merger time also has a marginal effect on the efficiency for fixed gate duration and

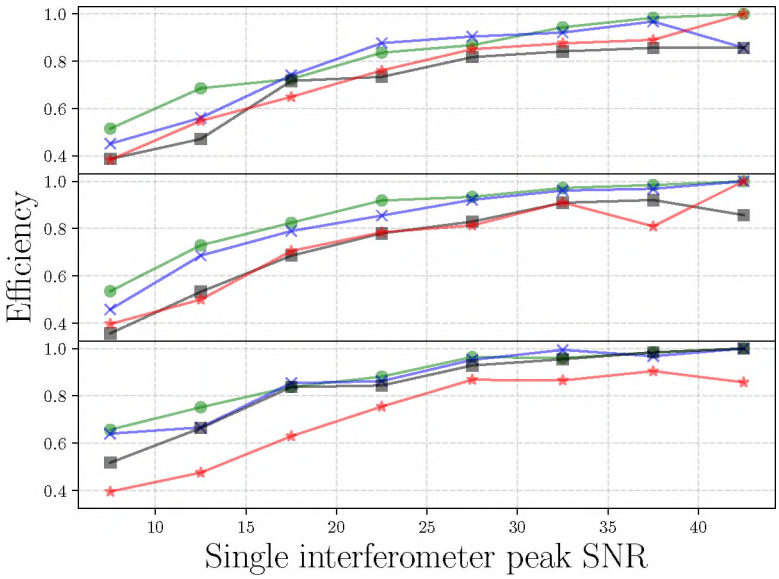

Figure 4.5. Efficiency as a function of the single interferometer peak SNR for the scenario with component masses $(m_1, m_2) = (12, 10)\ M_\odot$. Each line corresponds to a different gate duration and gate end-time combination. The top (middle, bottom) panel shows the efficiency for $t_d = 50\ (75, 130)$ ms. Green circle (blue cross, black square, red star) markers denote gate end-times $t_e = 15\ (30, 90, 170)$ ms. The bin width is 5.

network SNR. However, NNETFIX typically produces better reconstructions for gate end-times closer to the merger time in the cases of the low and medium mass scenarios with longer gate durations.

Figure 4.7 shows the NNETFIX-reconstructed data for the time series of Figure 4.1. As shown in Figure 4.8, the signal energy in the gated portion in the reconstructed time series is larger than the energy in the gated time series. In this case, FMG = 1.02.

As a conclusion in this section, we find that NNETFIX may successfully reconstruct gated data of durations up to a few hundreds of milliseconds and up to a few tens of milliseconds before the merger time for a majority of the data samples with single interferometer peak SNR greater than 20.

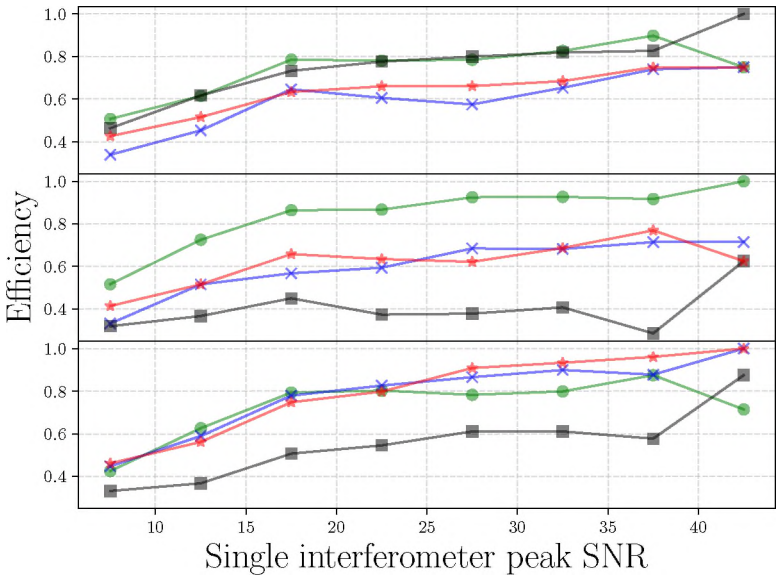

Figure 4.6. Efficiency as a function of the single interferometer peak SNR for the scenario with component masses $(m_1, m_2) = (35, 29)\ M_\odot$. Each line corresponds to a different gate duration and gate end-time combination. The top (middle, bottom) panel shows the efficiency for $t_d = 50$ (75, 130) ms. Green circle (blue cross, black square, red star) markers denote gate end-times $t_e = 15$ (30, 90, 170) ms. The bin width is 5.

4.4. PERFORMANCE OF SKY MAPS

After NNETFIX reconstructs the gated data, the output of NNETFIX can be used as the input for external pipelines to infer the astrophysical properties of the CBC sources such as the sky localization error region. Because NNETFIX typically recovers the signal energy in the gated portion, the sky maps obtained from the reconstructed time series are expected to be better in estimating the accurate sky localization error region than the sky maps of the gated time series.

To evaluate this improvement, Mogushi *et al.* (2021) compare the overlap between the sky map obtained from the gated time series and the sky map obtained from the full time series to the overlap between the sky map obtained from the reconstructed time series and the latter. We create the sky maps using a modified version of a PYCBC (Nitz *et al.*, 2020) script, PYCBC_MAKE_SKYMAP, where the data can be manually gated.

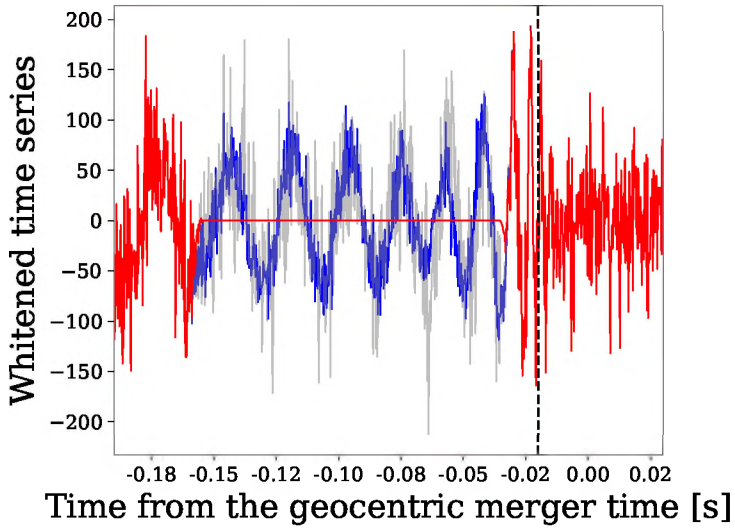

Figure 4.7. The whitened full time series (gray), the gated time series (red), and the reconstructed time series (blue) for the simulated event of Figure 4.1. The vertical black-dashed line denotes the merger time in H1. The value of FMG for this data isFMG = 1.02.

The sky localization error region is provided as a probability density over pixelized solid angles in the sky. Using the sky localization error region, we define a complementary metric, contour level enhancement (contour level enhancement (CLE)) as

$$\mathrm{CLE} = \frac{1 - C_r}{1 - C_g}, \tag{4.6}$$

where C_r and C_g are the sums of probability densities of pixels with their values greater than the value of the pixel containing the sky location of the injected signal (so-called *contour level*) in the sky map obtained from the reconstructed and gated time series, respectively. The contour level ranges in $[0, 1)$. Smaller values of the contour level indicate that the injected sky locations are located in a higher probable region of the sky, i.e., the sky localization algorithm tends to estimate the injected location more accurately. Values of CLE above (below) 1 imply that the sky map obtained from the reconstructed time series is better (worse) than the sky map obtained from the gated time series.

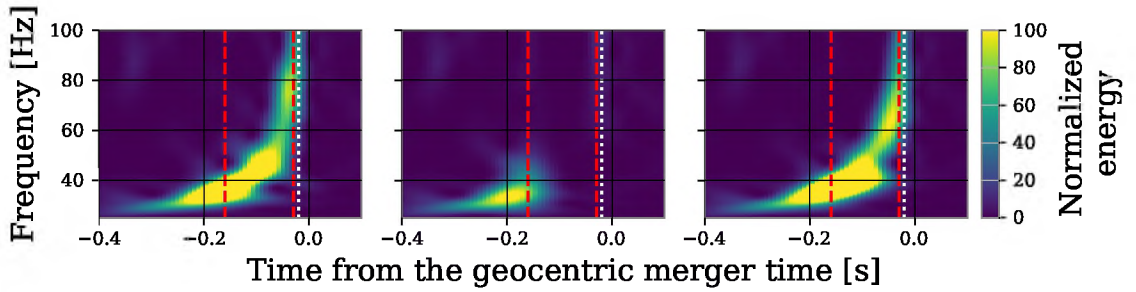

Figure 4.8. Time-frequency representations of the full (left), gated (middle), and reconstructed (right) time series for the simulated event of Figure 4.7 using the Q transform (Chatterji *et al.*, 2004). The vertical red-dashed line denotes the gate and the vertical white-dotted line denotes the merger time in H1.

Figures 4.9 and 4.10 show the distributions of the contour levels and CLE distributions for the exploration sets from the high-mass scenario. Figure 4.11 shows the comparison of these CLE distributions. Figure 4.12 shows the cumulative distribution of the contour level obtained from the full, reconstructed, and the gated time series.

In Appendix B, median values of CLE for all exploration sets are given in Tables 1-3, and the fraction of samples with CLE greater than 1 for all exploration sets are summarized in Tables 4-6.

Values of CLE across the exploration sets generally become higher for larger network SNR, component masses, and gate duration.

Among the four factors, the network SNR of the signal is the dominant factor affecting the value of CLE. Because NNETFIX effectively reconstructs the gated data comprising signals with large SNRs corresponding to higher network SNRs, the sky map of the reconstructed time series estimates the true injected sky location more accurately than the sky map of the gated time series. We find that median values of CLE are positive for most exploration sets with $\rho_N \geq 28.3$, irrespective of mass, gate duration, and end-time. For these sets, median values for the high-SNR sets are larger than the corresponding values for the low-SNR sets by a factor ranging from $\sim$ 1.04 (the medium-mass scenario with $t_d = 50$ ms and $t_e = 170$ ms) to $\sim$ 187 (the high-mass scenario with $t_d = 130$ ms and $t_e = 30$

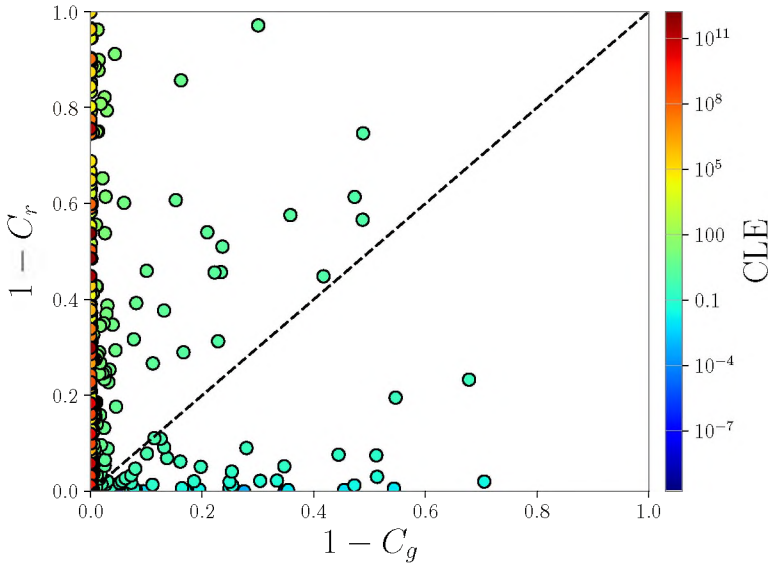

Figure 4.9. Scatterplot of C_r and C_g for the 512 samples from the exploration set with $\rho_N = 42.4$, component masses $(m_1, m_2) = (35, 29)\ M_\odot$, gate end-time $t_e = 30$ ms and gate duration $t_d = 130$ ms. The color denotes CLE. The diagonal dashed line denotes when $C_r = C_g$. 80% of samples have C_r smaller than C_g.

ms). The NNETFIX-reconstruction has a small impact on the sky maps of the time series containing signals with small SNRs. We find that median values of CLE for the sets with $\rho_N = 11.3$ are typically around one, irrespective of the mass scenario, gate duration, and gate end-time.

The second most dominating factor affecting CLE is the set of component masses. Values of CLE typically increase for larger values of the component masses. For the exploration sets with $\rho_N = 28.3$ (42.4), the high-mass sets have greater median values of CLE than the low-mass sets by a factor varying from ~ 1.05 (1.2) for $t_d = 50$ ms and $t_e = 170$ ms ($t_d = 50$ ms and $t_e = 170$ ms) to ~ 3.7 (107) for $t_d = 130$ ms and $t_e = 15$ ms ($t_d = 130$ ms and $t_e = 30$ ms).

Values of CLE typically increase as the gate duration becomes larger. Because the gate with longer durations loses a greater amount of the signal energy, NNETFIX's reconstruction supplies larger SNR recovery, resulting in greater CLE values as the gate

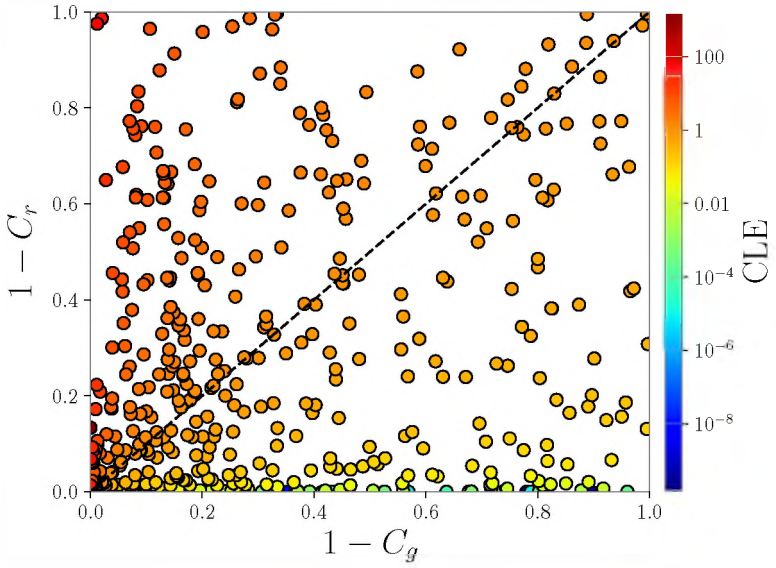

Figure 4.10. Scatterplot of C_r and C_g for the 512 samples from the exploration set with $\rho_N = 11.4$, component masses $(m_1, m_2) = (35, 29)\ M_\odot$, gate end-time $t_e = 30$ ms and gate duration $t_d = 130$ ms. The color denotes CLE. The diagonal dashed line denotes when $C_r = C_g$. 40% of samples have C_r smaller than C_g.

duration becomes larger. For the high-SNR and medium-SNR exploration sets, median values of CLE for the sets with $t_d = 130$ ms are larger than the corresponding values for the set with $t_d = 50$ ms by a factor ranging from ~ 1.01 (medium-mass scenario with $\rho_N = 28.3$ and $t_e = 170$ ms) to ~ 44 (high-mass scenario with $\rho_N = 42.4$ and $t_e = 30$ ms).

The portion of a signal close to the merger time affects more the estimate of the source sky location than the portion of the signal in the early inspiral phase. Hence, the medium-SNR and high-SNR exploration sets with $t_e = 15$ ms have typically higher median values of CLE than the sets with $t_e = 170$ ms by a factor ranging from ~ 1.02 (low-mass scenario with $\rho_N = 42.4$ and $t_d = 50$ ms) to ~ 38 (high-mass scenario with $\rho_N = 42.4$ and $t_d = 130$ ms). Figure **??** shows the 90% probability sky localization error regions obtained with the reconstructed time series shown in Figure 4.1.

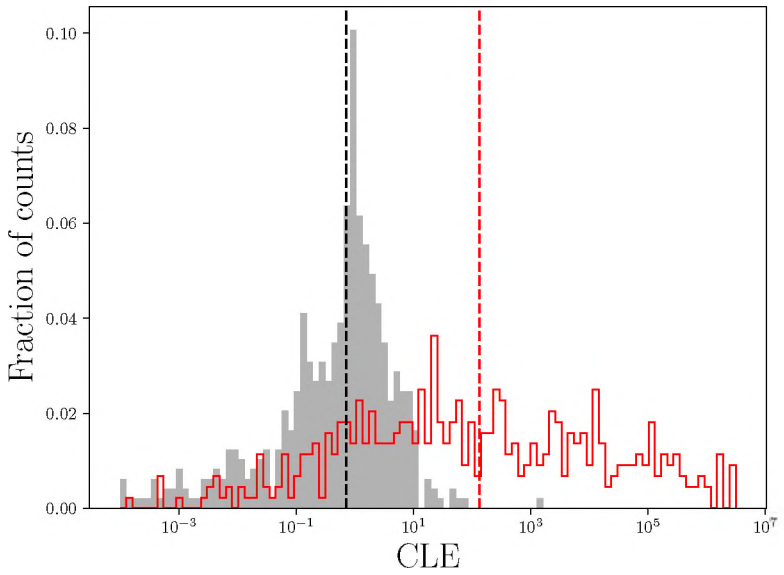

Figure 4.11. Distribution of CLE for the exploration sets with component masses $(m_1, m_2) = (35, 29)\ M_\odot$, gate duration $t_d = 130$ ms, gate end-time $t_e = 30$ ms, and $\rho_N = 11.3$ (gray-filled) and $\rho_N = 42.4$ (red). The vertical dashed black (red) line denote the median value of CLE for the set with $\rho_N = 11.3$ ($\rho_N = 42.4$). 40% (80%) of samples in the set with $\rho_N = 11.3$ ($\rho_N = 42.4$) have CLE above 1.

As a summary of this section, we find that the contour level at the injection location in the sky maps obtained from reconstructed time series with network SNR $\rho_N \geq 28.3$ are greater with the corresponding quantity in the sky maps obtained from the gated series (in some cases by a factor up to ~ 130) for a majority of the cases with gate durations up to a few hundreds of milliseconds and as close as a few tens of milliseconds to the merger time.

4.5. POSTFACE

In this chapter, we have presented a new machine learning-based algorithm called NNETFIX (Mogushi *et al.*, 2021). NNETFIX is designed to interpolate the portion of data containing a CBC signal that is lost due to the presence of glitches in coincidence with the signal. The NNETFIX reconstructed data can be fed into external pipelines that infer astrophysical properties of the sources including the source-parameter estimation and sky

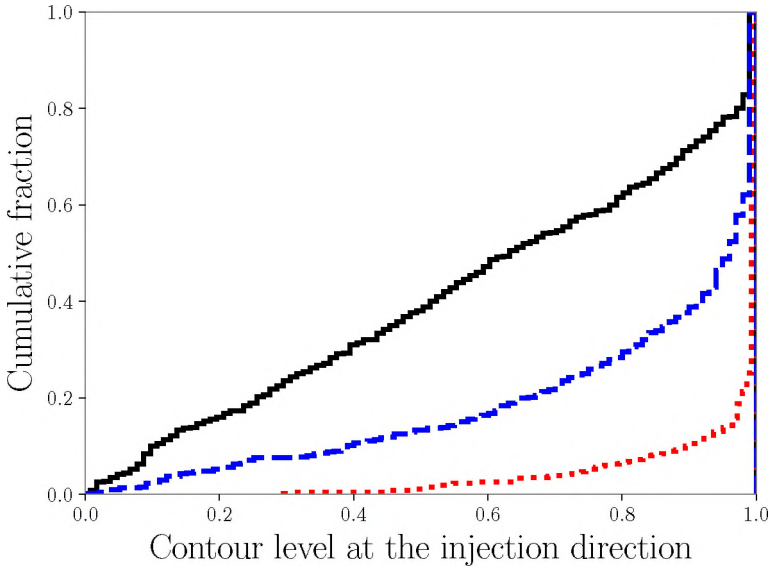

Figure 4.12. Cumulative distributions of the contour levels at the injection location obtained from the full (black), reconstructed (blue), and gated (red) time series in the exploration sets with component masses $(m_1, m_2) = (35, 29)\ M_\odot$, gate duration $t_d = 130$ ms, gate end-time $t_e = 30$ ms, and $\rho_N = 42.3$.

localization. To test the accuracy of the reconstruction, we have used different choices of signal parameters and gate settings and evaluate the reconstruction performance based on several metrics.

We find that NNETFIX may successfully reconstruct a majority of BBH signals with peak single interferometer SNR greater than 20 and gates with durations up to a few hundreds of milliseconds as close as a few tens of milliseconds before their merger time.

Because the NNETFIX reconstructed time series matches more with the injected waveform than the gated time series, the contour level at the injection location in the sky map derived from the reconstructed time series is more accurate than the sky map derived from the gated time series. In the cases of the successful reconstructions, we have found that the contour levels at the injection location in the sky maps from the reconstructed data improve compared with corresponding quantities in the sky maps obtained with the gated data by a factor up to 130.

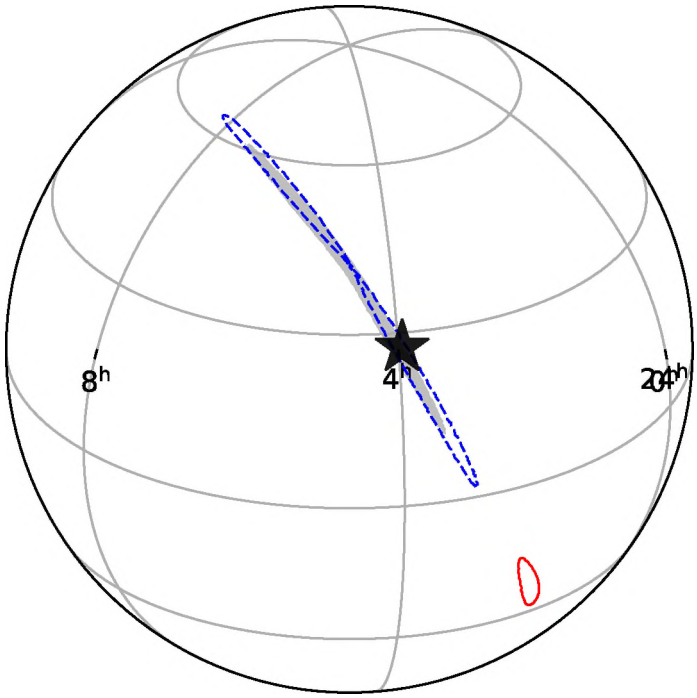

Figure 4.13. The 90% probability sky localization error regions obtained with the reconstructed (dashed-blue), full (gray area) and gated (solid-red) time series for the case of Figure 4.1. The star denotes the injection location. The value of CLE for this case is CLE = 2×10^{11}.

After the algorithm used in Mogushi *et al.* (2021) is trained, reconstructing the gated data takes of the order of a few seconds for the gate durations up to hundreds of milliseconds. Hence, the method could be used in low-latency operations when the data is contaminated by glitches.

Other than signals from BBH mergers tested in our analysis, the method could be applied to other CBC signals including BNS and NSBH mergers. Because of this possible application and the low-latency ability, NNETFIX is potentially beneficial to aid in observing EM counterparts associated with GW signals.

5. CONCLUSION

In 1916, the existence of GWs, small perturbations of spacetime produced by accelerating massive objects was first predicted as solutions of Einstein's Theory of General Relativity (Einstein, 1916). A century after 1915, LIGO-Virgo collaboration detected the first direct GW signal from the collision of a binary system of two black holes. We have seen as GWs in the linearized theory that describes the spacetime with the weak gravitational field. In the linearized theory, we have observed that the accelerating quadrupole moments are the source of GWs. To show how GWs interact with masses, we have followed (Carroll, 2003; Poisson and Will, 2014; Saulson, 1994). We have seen that GWs stretch and squeeze the space perpendicular to the direction of the propagation. We have observed that the relative length of the two arms of the detector changes as GWs are passing by GW detectors, allowing scientists to observe GWs. With GW detectors, scientists are looking for more GW detections and/or new types of GW signals.

To detect GW signals, the detectors must be extremely sensitive, causing them to be susceptible to instrumental and environmental noise artifacts. In particular, transient noise artifacts, or *glitches* adversely affect the detector-data quality. Hence, removing glitches is crucial to improve the confidence of astrophysical signals. LIGO detectors have numerous sensors monitoring the various aspects of the detector controls including optic suspensions and laser-alignment controls as well as the detector's output readout. Some of these sensors can be potential witnesses of glitches. In Chapter 2, We have presented a software package called PyChChoo (Mogushi, 2021a) that statistically identifies witness sensors of glitches. This work was first presented in Mogushi *et al.* (2021).

After identifying the witness sensors, we have presented a new machine learning-based algorithm to subtract glitches by using the data from a set of witness channels. Without knowing the physical coupling mechanisms inside and around the detector, our algorithm learns glitch-couplings from the data and successfully estimates short-lived linear and non-

linear features of glitches. Using two distinct classes of glitches observed in the LIGO detector, we have found that the excess power due to the presence of glitch is reduced by $20 - 70\%$ and the ranking statistics of one of the unmodeled GW detection pipelines called cWB improves after glitch subtraction by a factor of $\sim 1.03 \sim 3.5$ and $\sim 1.2 \sim 2.7$ on average for Gaussian modulated sinusoidal and BBH injections. We also have found that the cWB estimated source-direction, central frequency, and chirp mass after glitch subtraction are comparable or more accurate than that before glitch subtraction. In the current work presented in this dissertation, we have found that the FAR distribution in the background is not reduced significantly after glitch subtraction because we have focused only on the two glitch classes and applied the glitch-subtraction technique to 10% of glitches that would be subtracted. In the future, we shall try to create networks for different glitch classes and subtract all possible glitches and compare the time-volume integrals between the subtracted data and the vetoed data to see which method is preferable. While this algorithm can be used for both modeled or unmodeled GW detection pipelines, glitches with no witnesses can not be mitigated.

To mitigate glitches with no witnesses, we focused on modeled GWs, in particular, signals from binary coalescences. We have presented a method called NNETFIX which employs a machine-learning algorithm to estimate the data containing a CBC signal that is partially removed due to the presence of an overlapping glitch. This work was published in Mogushi *et al.* (2021). Using simulated BBH signals with a high SNR injected in the simulated colored Gaussian data with LIGO's design sensitivity, we have observed that the overlap of the sky localization error region obtained with the NNETFIX reconstructed data and the sky error region of the data in the absence of glitches is better than the overlap of the latter with the sky error region of the partially removed data in the majority of cases. This work employs a fully connected MLP for the proof of concept. To improve the reconstruction performance, different machine learning algorithms such as CNN autoencoder and/or recurrent neural network can be used. Because CBC signals evolve their frequencies

and amplitudes over time towards their merger times, parts of signals in near time are more close to each other than parts in far time. Therefore, the CNN network might be more suitable than a fully connected MLP for reconstructing signals. Longer signal waveforms such as BNS signals have more chance to overlap with glitches. Improvements in the sky localization error region for BNS signals might be more beneficial for identifying EM counterparts. A computational challenge for BNS signals is the latency because of a larger amount of data. Using GPU might be a possible way to overcome the above computational challenge. In the current setting, NNETFIX trains a network using a gate with a fixed position and a fixed duration. This setting might be a limitation to use NNETFIX in the real data because the position and duration of an overlapping glitch are arbitrary. Therefore, it is more useful to train a single network with various gates. Spins of CBCs are crucial factors for the sky localization error region, where small differences in spins make the sky localization error region differ significantly. In the future, BNS signals with non-zero spins with various gates should be used to train a single network in NNETFIX. Another limitation in the current NNETFIX is the loss function. We have observed that a higher number of hidden layers lowers the reconstruction accuracy though it is expected to improve the accuracy. This contradiction is due to the choice of the loss function, MSE. The noise is a random variable so that the network with a higher number of hidden layers tends to find smaller values MSE by reducing the noise in the reconstructed time series. Hence, using MSE as a loss function prevents NNETFIX from improving the reconstruction accuracy. To overcome this limitation, one can use different loss functions such as the entropy loss calculated by Kullback–Leibler divergence (Joyce, 2011). If one of the ultimate goals in the use of NNETFIX is to obtain better sky localization error regions, one can train the network to directly predict the sky-localization probability distribution by choosing the entropy loss between the true distribution and the predicted counterpart.

The O3a vetoed times in the LIGO detectors in O3a are less than one percent of the entire analyzable data (Abbott *et al.*, 2021b). However, future detectors with even higher sensitivities would observe a higher number of GW signal candidates, causing them to overlap with glitches more often. Hence, removing glitches would be crucial in the future. Also, subtracting glitches might help to detect GW signal candidates that are otherwise classified as sub-threshold triggers (Abbott *et al.*, 2019d; Riles, 2013). Improved data quality would allow us to detect astrophysical signals with higher confidence and brings us a better understanding of the physics in the universe.

APPENDIX A.

CONVENTIONS IN SPECIAL AND GENERAL RELATIVITY

1. CONVENTIONS OF METRIC SIGNATURE, UNITS

We write the conventions commonly used in special and general relativity based on Poisson and Will (2014).

1.1. COORDINATES AND SPACETIME INTERVAL

Because space and time are interchangeable, it is convenient to use a unified spacetime coordinate to refer to an event which is labeled with the spatial coordinates (x, y, z) and the time t. Using the speed of light c which is invariant, unified coordinates can be written as $x^\mu = (ct, x, y, z)$ such that each element has a dimension of length. The index μ runs over the values $\{0, 1, 2, 3\}$; we set $x^0 = ct$, $x^1 = x$, $x^2 = y$, and $x^3 = z$. The spacetime interval ds^2 is defined as

$$ds^2 := -(cdt)^2 + dx^2 + dy^2 + dz^2 \,. \tag{A.1}$$

Using the flat-spacetime metric $\eta_{\mu\nu} = diag(-1, 1, 1, 1)$, or the Minkowski tensor, the spacetime interval is simplified as

$$ds^2 = \sum_{\mu=0}^{3} \sum_{\nu=0}^{3} \eta_{\mu\nu} dx^\mu dx^\nu := \eta_{\mu\nu} dx^\mu dx^\nu \,, \tag{A.2}$$

where a pair of the same lower and upper indices denotes summing over all the values $\{0, 1, 2, 3\}$.

1.2. RAISING AND LOWERING OPERATOR

As well as being used in the spacetime interval, the Minkowski metric $\eta_{\mu\nu}$ serves as raising and lowering operators for vectors and tensors. A vector with a lower index (known as a *covariant* vector) is defined as

$$A_\mu = \eta_{\mu\nu} A^\nu \,. \tag{A.3}$$

Similarly for a tensor, the Minkowski metric operates; $B_{\mu\nu} = \eta_{\mu\alpha}\eta_{\nu\beta}B^{\alpha\beta}$. The raising operator is the inverse Minkowski metric $\eta^{\mu\nu}$, which satisfies $\eta^{\mu\rho}\eta_{\rho\nu} = \delta^{\mu}_{\ \nu}$. A vector with the upper index is obtained from its covariant vector as

$$A^{\mu} = \eta^{\mu\nu}A_{\nu}\,. \tag{A.4}$$

Using vectors with upper and lower indices, Equation (A.2) can be rewritten as $ds^2 = dx_{\mu}dx^{\mu}$. Because the index μ runs over values in the entries $\{0, 1, 2, 3\}$, the spacetime interval can be interpreted as the inner product of the spacetime displacements with themselves. The inner product is a scalar quantity. Any scalars such as $A_{\mu}B^{\mu}$ are invariant.

1.3. LORENTZ INVARIANCE

The flat-spacetime interval ds^2 is invariant under Lorentz transformations. Let us define the Lorentz transformation $x^{\mu} \rightarrow x'^{\mu}$ as

$$dx'^{\mu} = \Lambda^{\mu}_{\ \nu}dx^{\nu}\,, \tag{A.5}$$

where $\Lambda^{\mu}_{\ \nu}$ is the Lorentz-transformation operator. The spacetime interval ds'^2 becomes

$$ds'^2 = \eta_{\mu\nu}dx'^{\mu}dx'^{\nu} = \eta_{\mu\nu}\Lambda^{\mu}_{\ \alpha}\Lambda^{\nu}_{\ \beta}dx^{\alpha}dx^{\beta}\,. \tag{A.6}$$

Because $\eta_{\mu\nu}\Lambda^{\mu}_{\ \alpha}\Lambda^{\nu}_{\ \beta} = \eta_{\alpha\beta}$, the previous equation becomes

$$ds'^2 = \eta_{\mu\nu}dx'^{\mu}dx'^{\nu} = \eta_{\alpha\beta}dx^{\alpha}dx^{\beta}\,. \tag{A.7}$$

Indeed, the spacetime interval is invariant under the Lorentz transformation. The interval in curved spacetime is defined using the generalized metric $g_{\mu\nu}$ instead of $\eta_{\mu\nu}$.

1.4. LORENTZ-TRANSFORMATION OPERATORS

Lorentz transformations include *boosts* such that a new inertia frame is moving with a velocity relative to an old inertia frame as well as spatial-coordinate rotations from an old inertial frame to a new inertial frame. The matrix representation of a Lorentz boost $x'^{\mu} = B^{\mu}{}_{\nu}x^{\nu}$ in the case, where the new frame is moving with the velocity $\vec{v}$ relative to the old frame, is given as

$$B(\vec{v}) = \begin{pmatrix} \gamma & -\gamma v_x/c & -\gamma v_y/c & -\gamma v_z/c \\ -\gamma v_x/c & 1+(\gamma-1)v_x^2/v^2 & (\gamma-1)v_x v_y/v^2 & (\gamma-1)v_x v_z/v^2 \\ -\gamma v_y/c & (\gamma-1)v_y v_x/v^2 & 1+(\gamma-1)v_y^2/v^2 & (\gamma-1)v_y v_z/v^2 \\ -\gamma v_z/c & (\gamma-1)v_z v_x/v^2 & (\gamma-1)v_z v_y/v^2 & 1+(\gamma-1)v_z^2/v^2 \end{pmatrix}. \tag{A.8}$$

where v_x, v_y, v_z are the velocities in $x-, y-, z-$-axes, respectively, $v = \sqrt{v_x^2 + v_y^2 + v_z^2}$ is the magnitude of the velocity, and $\gamma = 1/\sqrt{1 - v^2/c^2}$ is the Lorentz factor. For example, if $\vec{v} = v_x \hat{e}_x$, the Lorentz boost is represented as

$$B(\vec{v}) = \begin{pmatrix} \gamma & -\gamma v_x/c & 0 & 0 \\ -\gamma v_x/c & \gamma & 0 & 0 \\ 0 & 0 & 1 & 0 \\ 0 & 0 & 0 & 1 \end{pmatrix}, \tag{A.9}$$

and

$$\begin{aligned} \eta_{\mu\nu} B^{\mu}{}_{\alpha} B^{\nu}{}_{\beta} &= \begin{pmatrix} \gamma & -\gamma v_x/c & 0 & 0 \\ -\gamma v_x/c & \gamma & 0 & 0 \\ 0 & 0 & 0 & 0 \\ 0 & 0 & 0 & 0 \end{pmatrix} \begin{pmatrix} -1 & 0 & 0 & 0 \\ 0 & 1 & 0 & 0 \\ 0 & 0 & 1 & 0 \\ 0 & 0 & 0 & 1 \end{pmatrix} \begin{pmatrix} \gamma & -\gamma v_x/c & 0 & 0 \\ -\gamma v_x/c & \gamma & 0 & 0 \\ 0 & 0 & 0 & 0 \\ 0 & 0 & 0 & 0 \end{pmatrix}, \\ &= \begin{pmatrix} -\gamma^2 + \gamma^2 v_x^2/c^2 & 0 & 0 & 0 \\ 0 & \gamma^2 - \gamma^2 v_x^2/c^2 & 0 & 0 \\ 0 & 0 & 1 & 0 \\ 0 & 0 & 0 & 1 \end{pmatrix}, \\ &= \begin{pmatrix} -1 & 0 & 0 & 0 \\ 0 & 1 & 0 & 0 \\ 0 & 0 & 1 & 0 \\ 0 & 0 & 0 & 1 \end{pmatrix}, \end{aligned} \tag{A.10}$$

by invoking the Lorentz factor $\gamma = 1/\sqrt{1 - v_x^2/c^2}$. Hence, Equation (A.6) is satisfied. The successive Lorentz boosts $B(\vec{w}) = B(\vec{u})B(\vec{v})$ from the un-primed frame to the double-primed frame such that $x''^{\mu} = B(\vec{u})^{\mu}{}_{\nu}x'^{\nu}$ and $x' = B(\vec{v})^{\mu}{}_{\nu}x^{\nu}$, are also included in Lorentz transformations. A spatial ration and successive rations are Lorentz transformations. For example, the rotation along z-axis is represented as

$$R(\phi) = \begin{pmatrix} 1 & 0 & 0 & 0 \\ 0 & \cos\phi & -\sin\phi & 0 \\ 0 & \sin\phi & \cos\phi & 0 \\ 0 & 0 & 0 & 1 \end{pmatrix}, \tag{A.11}$$

and

$$\begin{aligned} \eta_{\mu\nu}R^{\mu}{}_{\alpha}R^{\nu}{}_{\beta} &= \begin{pmatrix} 1 & 0 & 0 & 0 \\ 0 & \cos\phi & \sin\phi & 0 \\ 0 & -\sin\phi & \cos\phi & 0 \\ 0 & 0 & 0 & 1 \end{pmatrix}\begin{pmatrix} -1 & 0 & 0 & 0 \\ 0 & 1 & 0 & 0 \\ 0 & 0 & 1 & 0 \\ 0 & 0 & 0 & 1 \end{pmatrix}\begin{pmatrix} 1 & 0 & 0 & 0 \\ 0 & \cos\phi & -\sin\phi & 0 \\ 0 & \sin\phi & \cos\phi & 0 \\ 0 & 0 & 0 & 1 \end{pmatrix}, \\ &= \begin{pmatrix} -1 & 0 & 0 & 0 \\ 0 & \cos^2\phi + \sin^2\phi & -\cos\phi\sin\phi + \cos\phi\sin\phi & 0 \\ 0 & -\cos\phi\sin\phi + \cos\phi\sin\phi & \cos^2\phi + \sin^2\phi & 0 \\ 0 & 0 & 0 & 1 \end{pmatrix}, \\ &= \begin{pmatrix} -1 & 0 & 0 & 0 \\ 0 & 1 & 0 & 0 \\ 0 & 0 & 1 & 0 \\ 0 & 0 & 0 & 1 \end{pmatrix}. \end{aligned} \tag{A.12}$$

Hence, Equation (A.6) is satisfied in this case as well.

APPENDIX B.

SUMMARY OF CONTOUR LEVEL ENHANCEMENT FOR NNETFIX

1. TABLES OF QUANTITIES WITH CONTOUR LEVELS IMPROVED BY NNETFIX

Table 1. Median values of CLE for the exploration sets with component masses $(m_1, m_2) = (12, 10)\ M_\odot$. Boldface entries denote sets with CLE above 1.

Network SNR		11.3			28.3			42.4		
Gate duration [ms]		50	75	130	50	75	130	50	75	130
tbm [ms]	15	0.95	0.98	0.97	0.997	0.996	**1.07**	**1.05**	**1.12**	**1.22**
	30	0.98	0.96	0.99	**1.003**	**1.02**	**1.05**	**1.05**	**1.1**	**1.26**
	90	0.98	0.98	0.99	**1.01**	**1.01**	**1.07**	**1.04**	**1.05**	**1.14**
	170	0.99	0.99	0.96	**1.01**	**1.002**	**1.03**	**1.03**	**1.04**	**1.08**

Table 2. Median values of CLE for the exploration sets with component masses $(m_1, m_2) = (20, 15)\ M_\odot$. Boldface entries denote sets with CLE above 1.

Network SNR		11.3			28.3			42.4		
Gate duration [ms]		50	75	130	50	75	130	50	75	130
tbm [ms]	15	0.91	0.90	0.94	**1.05**	**1.10**	**1.24**	**1.17**	**1.49**	**2.6**
	30	0.93	0.93	0.94	**1.03**	**1.13**	**1.41**	**1.22**	**1.39**	**2.26**
	90	0.99	0.97	0.85	**1.02**	1.000	**1.13**	**1.08**	**1.16**	**1.48**
	170	0.99	0.99	0.94	**1.003**	**1.006**	**1.01**	**1.06**	**1.13**	**1.21**

Table 3. Median values of CLE for the exploration sets with component masses $(m_1, m_2) = (25, 29)\ M_\odot$. Boldface entries denote sets with CLE above 1.

Network SNR		11.3			28.3			42.4		
Gate duration [ms]		50	75	130	50	75	130	50	75	130
tbm [ms]	15	0.86	0.82	0.35	**1.63**	**2.68**	**3.97**	**3.76**	**12.97**	**58.4**
	30	0.91	0.70	0.72	**1.62**	**2.22**	**4.97**	**3.07**	**9.81**	**134.9**
	90	0.99	0.93	0.76	**1.15**	**1.44**	**1.91**	**1.32**	**2.40**	**7.62**
	170	0.99	0.985	0.97	**1.06**	**1.14**	**1.18**	**1.20**	**1.37**	**1.53**

Table 4. Fraction of samples with CLE above 1 for the exploration sets with component masses $(m_1, m_2) = (12, 10)\ M_\odot$. Boldface entries denote sets where the fraction of samples with CLE ≥ 1 is larger than 50%.

Network SNR		11.3			28.3			42.4		
Gate duration [ms]		50	75	130	50	75	130	50	75	130
tbm [ms]	15	0.40	0.44	0.43	0.50	0.49	**0.60**	**0.56**	**0.60**	**0.65**
	30	0.44	0.43	0.46	**0.51**	**0.54**	**0.56**	**0.55**	**0.58**	**0.67**
	90	0.43	0.42	0.47	**0.51**	**0.52**	**0.58**	**0.56**	**0.56**	**0.60**
	170	0.43	0.46	0.38	**0.53**	**0.51**	**0.54**	**0.57**	**0.55**	**0.57**

Table 5. Fraction of samples with CLE above 1 for the exploration sets with component masses $(m_1, m_2) = (20, 15)\ M_\odot$. Boldface entries denote sets where the fraction of samples with CLE ≥ 1 is larger than 50%.

Network SNR		11.3			28.3			42.4		
Gate duration [ms]		50	75	130	50	75	130	50	75	130
tbm [ms]	15	0.36	0.37	0.41	**0.53**	**0.56**	**0.60**	**0.61**	**0.67**	**0.72**
	30	0.42	0.39	0.42	**0.52**	**0.59**	**0.67**	**0.61**	**0.66**	**0.72**
	90	0.44	0.42	0.35	**0.53**	**0.50**	**0.57**	**0.59**	**0.62**	**0.62**
	170	0.44	0.47	0.40	**0.51**	**0.51**	**0.51**	**0.58**	**0.59**	**0.60**

Table 6. Fraction of samples with CLE above 1 for the exploration sets with component masses $(m_1, m_2) = (35, 29)\ M_\odot$. Boldface entries denote sets where the fraction of samples with CLE ≥ 1 is larger than 50%.

Network SNR		11.3			28.3			42.4		
Gate duration [ms]		50	75	130	50	75	130	50	75	130
tbm [ms]	15	0.42	0.41	0.33	**0.62**	**0.67**	**0.62**	**0.71**	**0.78**	**0.71**
	30	0.44	0.37	0.40	**0.60**	**0.64**	**0.69**	**0.73**	**0.72**	**0.80**
	90	0.47	0.43	0.41	**0.59**	**0.61**	**0.62**	**0.65**	**0.67**	**0.72**
	170	0.48	0.48	0.45	**0.56**	**0.57**	**0.59**	**0.61**	**0.64**	**0.65**

APPENDIX C.

PERCENTAGES OF CONTRIBUTIONS

100% to work presented in Paper I

100% to work presented in Paper II

50% (data creation, code implementation, data analysis, and writing the article) to work presented in Section 2

APPENDIX D.

LIST OF AUTHORED PAPERS

1. LIST OF AUTHORED PAPERS NOT INCLUDED IN THE DISSERTATION

The author of this dissertation became an LSC collaboration co-author since October 13th, 2017, and has been authored for 66 collaboration papers. Here, we briefly describe the list of authored papers, Mogushi *et al.* (2019), Zheng *et al.* (2021), and Davis *et al.* (2021) that are not included in this dissertation.

On August 17th, 2017, the LIGO-Virgo collaboration detected the first GW signal produced by a BNS called GW170817 in coincidence with the EM observation of the short gamma-ray burst (sGRB) called GRB 170817A. This detection verified the long-thought hypothesis that at least some sGRBs are produced by BNS mergers (Abbott *et al.*, 2017b,c; Goldstein *et al.*, 2017). The observed luminosity of GRB 170817A is lower than that of all other sGRBs with known redshift by at least two orders of magnitude. This discrepancy could be explained by GRB 170817A being viewed off-axis, i.e., at a large inclination angle (Abbott *et al.*, 2017b). Based on the Very Long Baseline Interferometric detection of superluminal motion in GRB 170817A, Mooley *et al.* (2018) rule out the "uniform top-hat" model where the sGRB is described by a conical jet with uniform, relativistic emission (Rhoads, 1999) in favor of a "structured jet" model, where a narrower ultrarelativistic jet is surrounded by a mildly relativistic sheath (Kumar and Granot, 2003; Rossi *et al.*, 2002; Zhang and Meszaros, 2002). Mogushi *et al.* (2019) estimate the detection rate of coincident GW and sGRB observations by the network of GW detectors and constrain the physical parameters of the sGRB jet structure, using a catalog of sGRB observations by Neil Gehrels Swift Observatory Burst Alert Telescope and the GW170817/GRB 170817A observational data. The estimated rate of GW detections coincident with sGRB detections by the Fermi Gamma-ray Burst Monitor is between ~ 0.1 and ~ 0.6 yr^{-1} in the O3 of LIGO-Virgo. The typical value of the half-opening angle in a structure jet profile (Pescalli *et al.*, 2015) is estimated between 7° and 22° with the power-law decay exponent varying between 5 and 30 at 1σ confidence level.

Zheng *et al.* (2021) present a review about a FAR as a detection criterion of GW signals in the LIGO-Virgo collaboration by analogizing it with the forecast example. A fewer number of sunny days that were predicted to be rainy corresponds to a higher confident forecast for days predicted to be rain. Similarly, GW signal candidates with smaller FARs are of astrophysical origin with higher confidence.

Davis *et al.* (2021) present a comprehensive overview of detector-characterization methods and results of LIGO and Virgo in O2 and O3 with developments towards the fourth observation run (O4). The overview begins with a summary of the data set including the duty cycle factors and the sensitivity evolution in O2 and O3, and also covers major software tools and infrastructures used in the LIGO and Virgo. This paper also summarizes 1) results about the mitigation of noise due to instrumental disturbances to improve the performance of the LIGO detectors, 2) methods used for transient GW-signal searches and procedures to validate signal candidates based on the data characterization aspects, and 3) the data-quality studies employed for continuous GW searches. This paper concludes with the future prospectus such as automation efforts designated for a higher number of signal candidates due to even higher sensitivities of detectors.

APPENDIX E.

NOISE-WEIGHTED INNER PRODUCT

The noise-weighted inner product is defined (Brown, 2004; Finn, 1992) as

$$(\tilde{a}|\tilde{b}) = \int_{-\infty}^{\infty} df \frac{\tilde{a}^*(f)\tilde{b}(f) + \tilde{a}(f)\tilde{b}^*(f)}{S_n(|f|)}, \tag{E.1}$$

where $\tilde{a}(f)$ and $\tilde{b}(f)$ are the Fourier transforms of the time series $a(t)$ and $b(t)$, respectively, the star denotes the complex conjugate, and $S_n(|f|)$ is the one-sided PSD of the noise. When $a(t)$ is real, i.e. $a^*(t) = a(t)$, its Fourier transform satisfies the following the relation:

$$\begin{aligned} \tilde{a}^*(f) &= \left(\int_{-\infty}^{\infty} a(t) e^{-2\pi i f t} dt \right), \\ &= \int_{-\infty}^{\infty} a(t) e^{-2\pi i (-f) t} dt, \\ &= \tilde{a}(-f). \end{aligned} \tag{E.2}$$

When $a(t)$ and $b(t)$ are real, Equation (E.1) becomes

$$\begin{aligned} (\tilde{a}|\tilde{b}) &= \int_{-\infty}^{\infty} df \frac{\tilde{a}^*(f)\tilde{b}(f)}{S_n(|f|)} + \int_{-\infty}^{\infty} df \frac{\tilde{a}(f)\tilde{b}^*(f)}{S_n(|f|)}, \\ &= \int_{-\infty}^{\infty} df \frac{\tilde{a}^*(f)\tilde{b}(f)}{S_n(|f|)} - \int_{\infty}^{-\infty} df' \frac{\tilde{a}(-f')\tilde{b}^*(-f')}{S_n(|f'|)}, \\ &= \int_{-\infty}^{\infty} df \frac{\tilde{a}^*(f)\tilde{b}(f)}{S_n(|f|)} - \int_{\infty}^{-\infty} df' \frac{\tilde{a}^*(f')\tilde{b}(f')}{S_n(|f'|)}, \\ &= 2 \int_{-\infty}^{\infty} df \frac{\tilde{a}^*(f)\tilde{b}(f)}{S_n(|f|)}. \end{aligned} \tag{E.3}$$

Also, $\tilde{a}(f)\tilde{b}^*(f)$ is the complex conjugate of $\tilde{a}^*(f)\tilde{b}(f)$ so that

$$\tilde{a}^*(f)\tilde{b}(f) + \tilde{a}(f)\tilde{b}^*(f) = 2\Re\left[\tilde{a}^*(f)\tilde{b}(f)\right]. \tag{E.4}$$

Equation (E.1) can be written as

$$
\begin{aligned}
(\tilde{a}|\tilde{b}) &= 2\left[\int_0^\infty df \frac{\tilde{a}^*(f)\tilde{b}(f)}{S_n(f)} + \int_{-\infty}^0 df \frac{\tilde{a}^*(f)\tilde{b}(f)}{S_n(|f|)}\right], \\
&= 2\left[\int_0^\infty df \frac{\tilde{a}^*(f)\tilde{b}(f)}{S_n(|f|)} - \int_\infty^0 df' \frac{\tilde{a}^*(-f')\tilde{b}(-f')}{S_n(f')}\right], \\
&= 2\left[\int_0^\infty df \frac{\tilde{a}^*(f)\tilde{b}(f) + \tilde{a}(f)\tilde{b}^*(f)}{S_n(|f|)}\right], \\
&= 4\Re\int_0^\infty df \frac{\tilde{a}^*(f)\tilde{b}(f)}{S_n(f)}. \qquad \text{(E.5)}
\end{aligned}
$$

APPENDIX F.

VALIDATION OF THE GAUSSIANITY

1. COMPARISON BETWEEN SCATTERED LIGHT GLITCHES AND QUIET TIMES

To show that the frequency region above 100 Hz in time periods containing *Scattered light* glitches in the strain channel has no excess power and are compatible with the corresponding frequency region of the Gaussian noise, we compare 693 spectrograms containing *Scattered light* glitches with 306 spectrograms when the strain channel is quiet, statistically evaluate them using the KS test (Massey, 1951).

To create the data set of *Scattered light* glitches, we whiten the time series of the strain channel with a software called GWPY (Macleod *et al.*, 2020) and then apply a low-pass filter at 512 Hz as used in Sec. 2. We have the *Scattered-light* set with a sample size of 693 by selecting time periods with a duration of 8 seconds that contains *Scattered light* glitches. To have a set of quiet data, we use the observing-mode strain channel data with a duration of 4096 seconds beginning from April 2nd, 2019 at 5:04 UTC, without data quality issues such as the corrupting data, the presence of glitches, and hardware injections of simulated signals. We whiten and apply the high-pass filter to the quiet time series and then cut the edge of the whitened time series to remove artifacts of the Fourier transform. By diving the whitened time series into 8-second segments, we have the quiet-data set with a sample size of 301. We create mSTFTs of the *Scattered-light* set and the *quiet* set. Figure 1 shows the mSTFT of a *Scattered light* glitch and a quiet time.

Figure 2 shows distributions of the mSTFTs in the frequency region above or below 100 Hz in the *Scattered-light* set and the *quiet* set. The *Scattered-light* (*quiet*) set has 1.6% and 9.5% (1.6% and 2.1%) of pixels with values above 10 for the frequency region above and below 100 Hz across the set, respectively. To verify the upper-frequency region of the *Scattered light* set has no excess power above Gaussian fluctuations, we calculate one-sided KS-test statistics for randomly selected 500 pairs of a mSTFT from the *Scattered-light* set and a mSTFT from the *quiet* set by taking the mSTFT variations in both sets into account. As the null hypothesis in the one-sided KS test, we consider mSTFT-pixel values of a

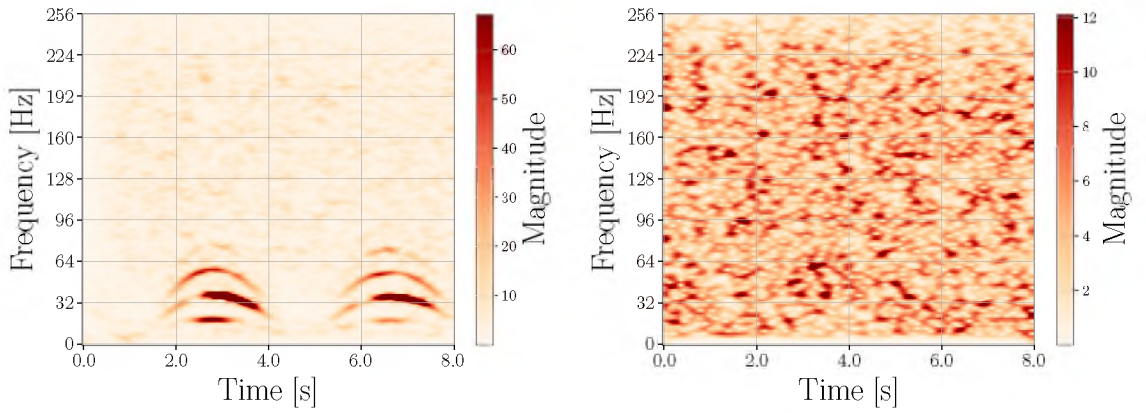

Figure 1. Magnitude of STFTs of *Scattered light* glitch (left) and a quiet time (right).

Scattered-light-glitch data is lower than that of the *quiet* data because we want to verify if the hypothesis that the upper-frequency region of the *Scattered light* set has no excess power above Gaussian fluctuations can be rejected. Because the KS-test statistics calculated above contain the variation of mSTFT in both sets, we also calculate one-sided KS-test statistics for randomly selected 500 pairs of two mSTFTs from the *quiet* set. The right panel in Figure 3 shows distributions of KS-statistics of these pairs.

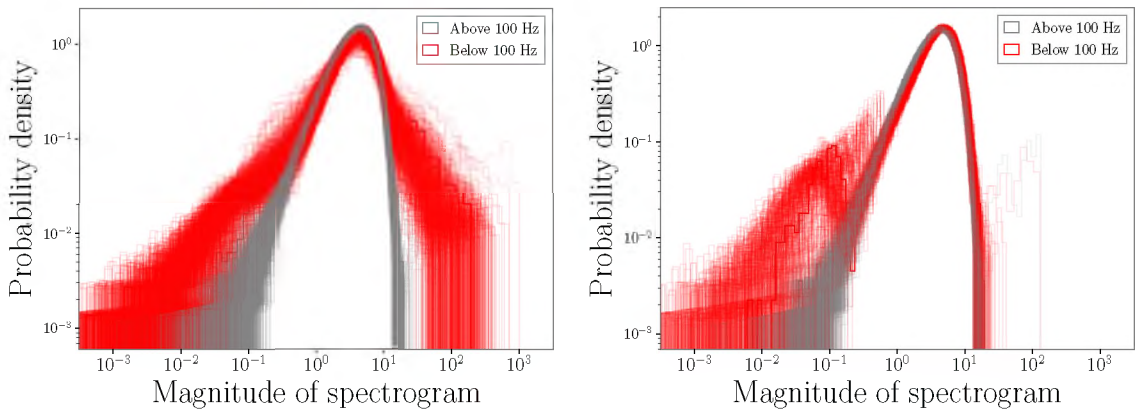

Figure 2. Distributions of mSTFT-pixel values of 693 Scattered light glitches (left) and 306 quiet-time segments (right).

We then perform a one-sided KS test for the above two distributions of KS statistics. We find that the p-value of the test to be 0.099, which is not confident enough to reject the hypothesis that the upper-frequency region of the data containing *Scattered light* glitches has no excess power.

As a supplementary study, we perform the same procedure for the frequency region below 100 Hz. The left panel in Figure 3 shows distributions of KS statistics calculated with mSTFT pairs in the frequency region below 100 Hz. We find the p-value of the test to be 2.4×10^{-141} so that *Scattered light* glitches have excess power below 100 Hz.

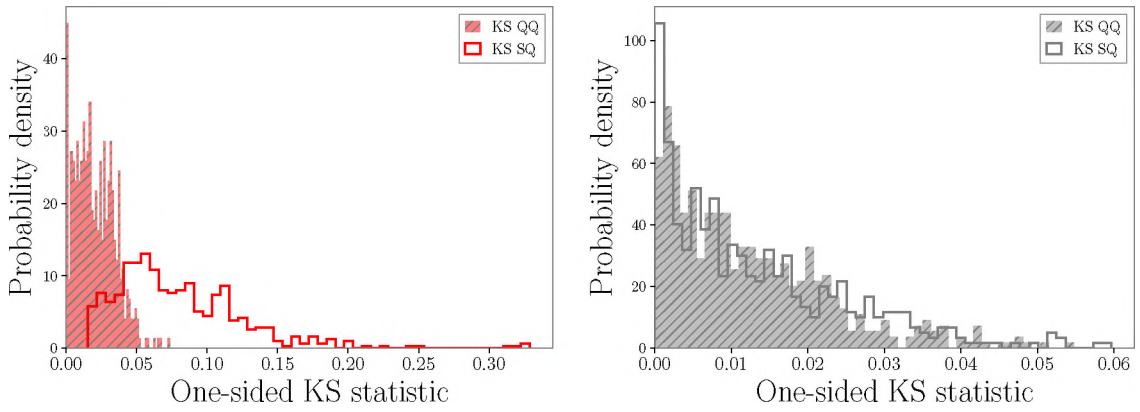

Figure 3. Distributions of KS statistics calculated with 500 random pairs of mSTFTs in the frequency region below (left) and above (right) 100 Hz. QQ and SQ denote pairs of two mSTFTs from the *quiet* set and pairs of a mSTFT from the *Scattered-light* set and a mSTFT from the *quiet* set, respectively.

To robustly verify that the null hypothesis that the mSTFT of the data containing *Scattered light* glitches has no excess power in the frequency region above 100 Hz, can not be rejected, we vary the number of pairs and random pair-selection realizations for p-values.

Similar to the process mentioned above, we randomly select N pairs of a mSTFT from the *Scattered-light* set and a mSTFT from the *quiet* set as well as N pairs of two mSTFTs from the *quiet* set, subsequently calculate one-sided KS statistics for paired mSTFTs in the frequency region above x Hz for both *Scattered-light*-quiet and quiet-quiet pair sets. Then, we perform the one-sided KS test for the two KS-statistic distributions from two pair-sets.

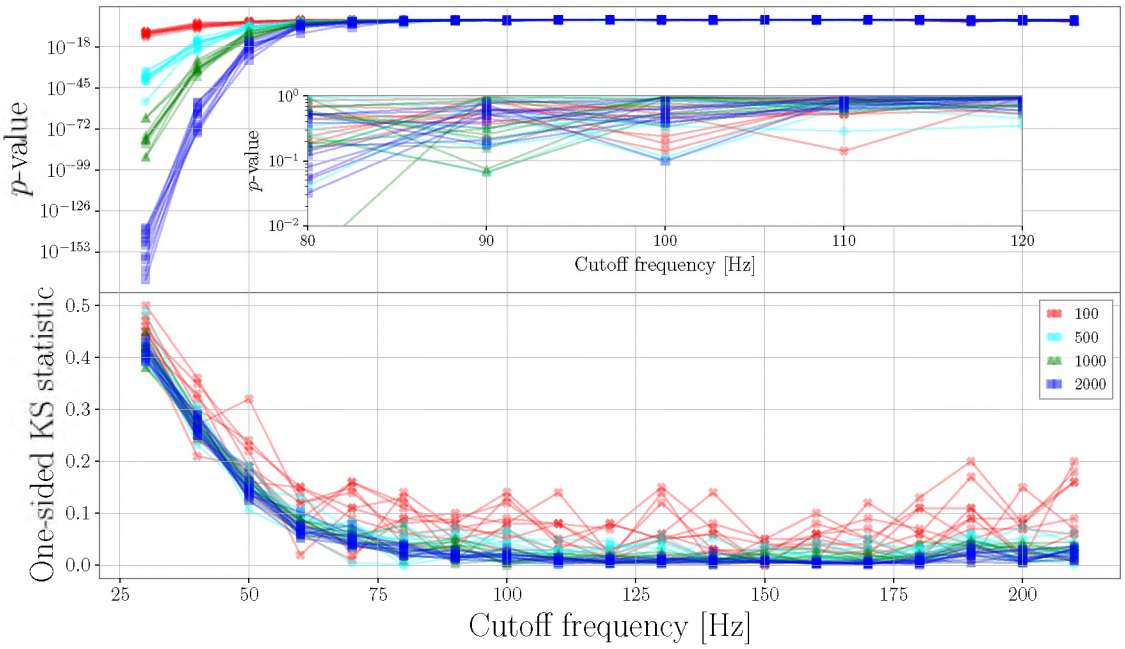

Figure 4. The variations of p-values (top) and one-sided KS statistics (bottom) for the mSTFTs above a given cutoff frequency. The one-sided KS-statistics in this figure are the statistics calculated using the two KS-statistic distributions from the *Scattered-light-quiet* pair and the *quiet-quiet* pair. Note the y-axis in the figure differs from the x-axis in Figure 3. Markers denote N number of pairs to perform the KS-test. Different curves with the same marker denote different realizations in the N-pair selection.

We vary values of N between 100 and 2000 and x between 30 Hz and 210 Hz to show the variation of p-values due to selected numbers of pairs N and cutoff frequencies x. Also, to see the effect of the pair-selection realizations on p-values, we repeat 10 times each test for a given value of N and x. Figure 4 shows the variations of p-values and the corresponding KS statistics. The p-values with cutoff frequencies below 75 Hz significantly smaller, indicating high confidence in rejecting the null hypothesis. For cutoff frequencies below 75 Hz, larger values of N corresponds to smaller p-values because the sample errors are smaller for a set with larger samples even if statistics with larger N are slightly smaller than values with smaller N. The p-values with a cutoff frequency above 100 Hz are comparable, meaning that no excess power is observed in the frequency region above 100 Hz irrespective of values of N and the pair-selection realizations.

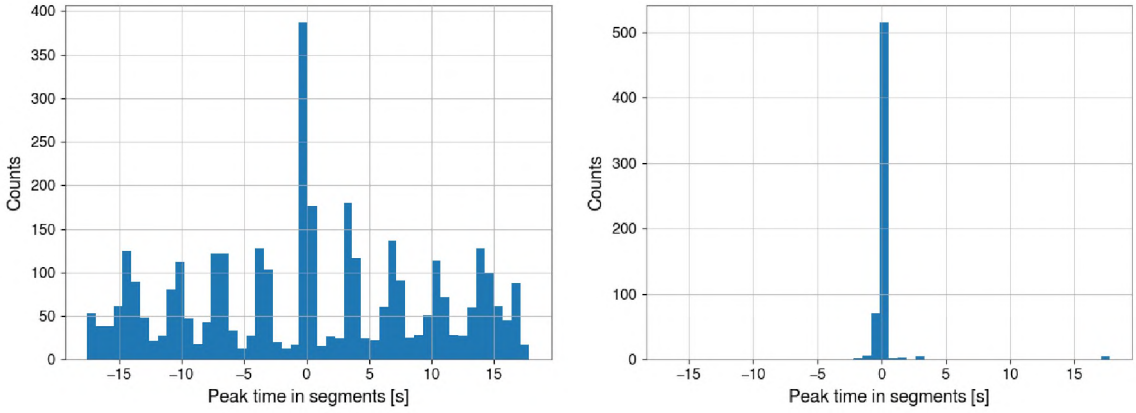

Figure 5. Peak time of *Scattered light* (left) and *Extremely loud* (right) glitches in 36-second time periods.

2. PEAK TIME OF GLITCHES

To determine choices of splitting time-frequency regions in mSTFTs of the data containing glitches, one can use the peak time of glitches to identify if glitches are isolated in the time domain.

Figure 5 shows peak times of *Scattered light* glitches and *Extremely loud* glitches in 36-seconds time periods. *Extremely loud* glitches are isolated in the time domain and their peak times are generally within ±1 around the Omicron-trigger (Robinet *et al.*, 2020) times. *Scattered light* glitches are repeatedly present because this glitch class is generated due to swinging mirror motions caused by seismic activities. Therefore, to estimate the mSTFT of the Gaussian noise, we use the frequency region above 100 Hz for *Scattered light* glitches and the time region outside of ±2.5 seconds around the trigger time for *Extremely loud* glitches.

3. PIXEL THRESHOLD TO EXTRACT GLITCH WAVEFORMS

After determining the time-frequency region of the data to estimate the STFT of the noise, we extract a glitch waveform from the STFT. Because glitches generally can not be modeled, we choose a threshold for pixel values of the STFT to extract glitch waveforms.

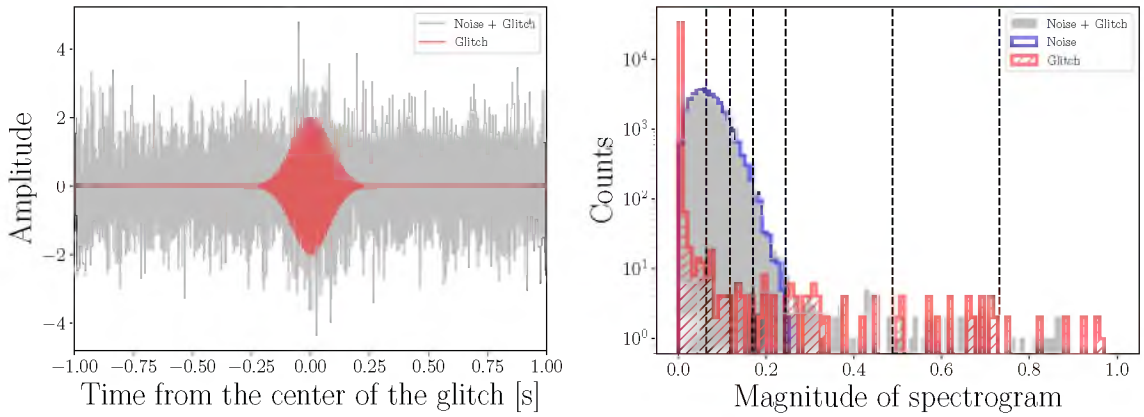

Figure 6. Time series (left) of a hypothetical glitch injected into the simulated Gaussian noise and the histogram of mSTFT-pixel values (right). The dashed vertical lines are 50, 90, 99, 100 percentiles of pixel values of the noise mSTFT, and 100 percentile multiplied by 2 and 3, from left to right in the right panel.

We keep pixels of the STFT (hereafter called excess pixels) with their magnitude values above a threshold estimated from the STFT representing the noise. The left panel of Figure 6 shows a hypothetical glitch injected into the simulated Gaussian data. Its right panel shows the histograms of mSTFTs of the injected data, the noise only, and the glitch only. Smaller thresholds let excess pixels have a larger number of noise and glitch pixels while larger thresholds let excess pixels have a smaller number of the noise pixels but smaller glitch pixels.

To determine the best pixel threshold, we take mSTFT pixels with their magnitude values below a threshold (hereafter called un-excess pixels) and then use the two-sided KS test between the un-excess pixels and mSTFT pixels of quiet times. If un-excess pixels are similar to quiet pixels, excess pixels tend to have the majority of glitch pixels and smaller numbers of noise pixels. To quantitatively determine the best threshold, we randomly select 200 pairs of un-excess-pixel mSTFTs with quiet mSTFTs and calculate two-sided KS statistics for each pair. We use the two-sided KS statistic because we want to see the similarity of two mSTFT in a pair. Likewise, we randomly select 200 pairs of two quiet mSTFTs and calculate two-sided KS statistics. We take the ratio of the KS statistic averaged over the un-excess-quiet pairs to the KS statistic averaged over the quiet-quiet pairs.

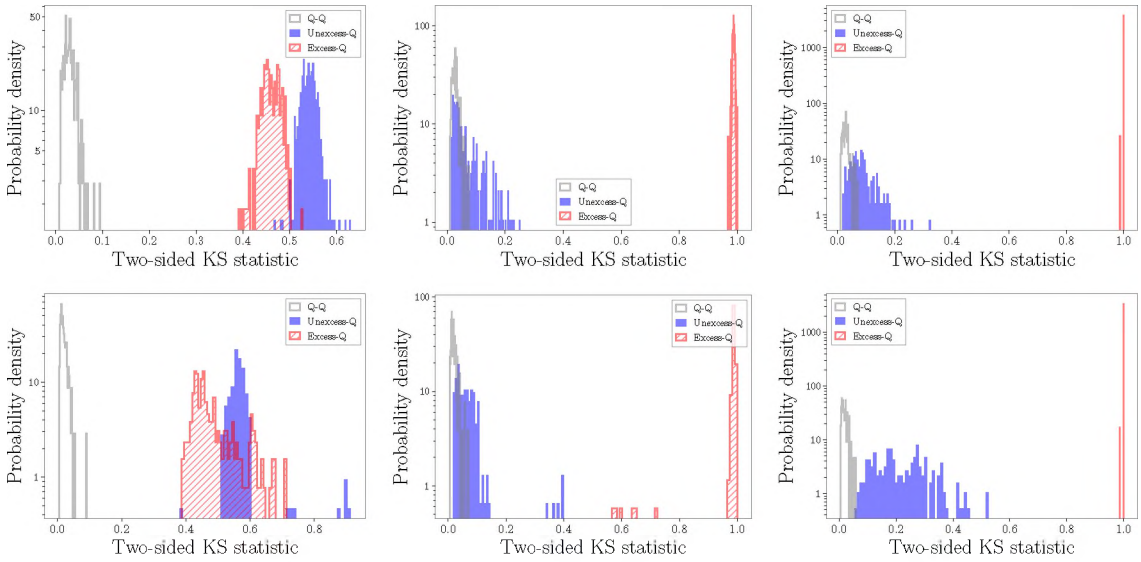

Figure 7. Histograms of two-sided KS statistics of quiet-quiet, un-exess-quiet, excess-quiet pairs with 50 percentile (left), 99 percentile (middle), and 100 percentile multiplied by 5 (right) as pixel thresholds for *Scattered light* (top) and *Extremely loud* (bottom) glitches.

Figure 7 shows histograms of KS statistics of 200 quiet-quiet pairs, 200 un-excess-quiet pairs, and 200 excess-quiet pairs with different pixel thresholds. The ratio is closed to one when the un-excess pixels are similar to the quiet pixels, i.e., excess pixels contain the majority of glitch pixels and fewer noise-pixel. Whereas, larger values of the ratio imply that 1) only smaller amplitude noise pixels are contained in un-excess pixels, i.e., excess pixels contain a larger amount of noise pixels (corresponding smaller pixel thresholds), or 2) un-excess pixels have a higher number of glitch pixels, i.e., excess pixels have only a few glitch pixels (corresponding to larger pixel thresholds). We vary the pixel threshold from 50, 90, 99, 99.9, 100 percentiles of the mSTFT in the time-frequency region that is expected to contain no glitches (see the above sections). Also, we consider values of 100-percentile multiplied by 2, 3 and, 5 as the threshold.

Therefore, minimizing the ratio over pixel thresholds allows us to find the best pixel threshold. Figure 8 shows the ratio of the un-excess-quiet pair KS statistic to the quiet-quiet pair KS statistic. For *Scattered light* glitches, the ratio reaches the lowest values $\sim 2.1 \sim 2.2$ with thresholds of 99, 99.9, and 100 percentiles. For *Extremely loud* glitches, the ratio has

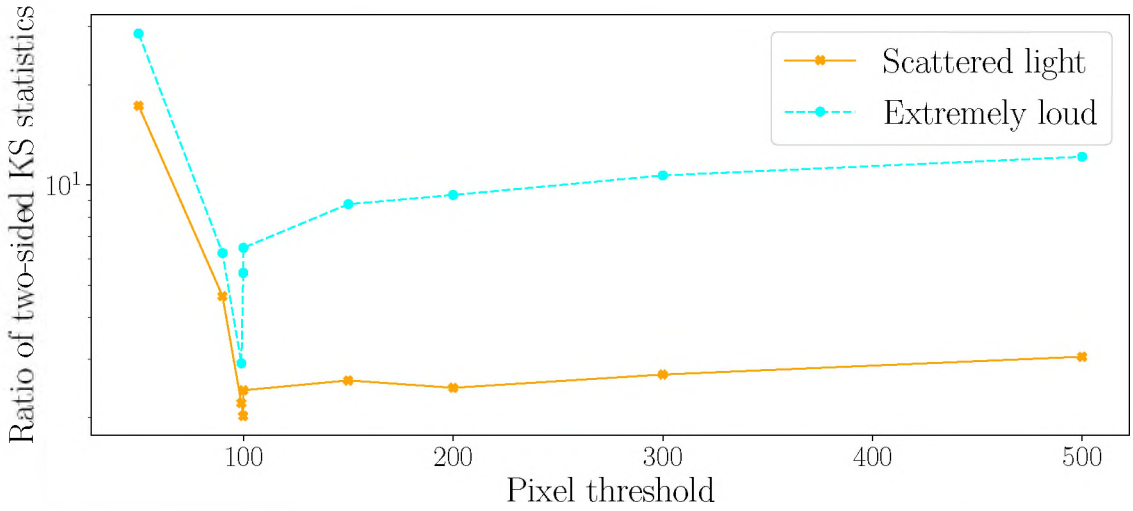

Figure 8. The ratio of the un-excess-quiet pair KS statistic to the quiet-quiet pair KS statistic. Pixels thresholds below 100 denote percentiles of mSTFT in the time-frequency region that is expected to contain no glitches. Pixel thresholds above 100 denote 100 percentile multiplied by 2, 3, or 5.

the minimum value of $\sim$ 3.9 with 99 percentile. *Extremely loud* glitches have extremely high SNR so that the ratio is more sensitive to the pixel threshold. According to the above study, we set the best threshold to be 99 percentile for both classes of glitches.

4. GRIFFIN-LIM TRANSFORM AND FAST GRIFFIN-LIM TRANSFORM

4.1. OVERVIEW OF GRIFFIN-LIM TRANSFORM

We present a brief overview of the Griffin-Lim (GL) transformation (Griffin and Jae Lim, 1984) and the FGL transformation (Perraudin *et al.*, 2013) which is a modified version of the GL transformation to fasten the convergence.

The GL transformation provides a real-value time series from a given mSTFT by estimating the phase. We first show the introduction of the method (Griffin and Jae Lim, 1984) to estimate a time series whose STFT is close to an arbitrary STFT which is not guaranteed to have an exact corresponding time series. Then, we show the GL transformation to estimate a time series for an arbitrary mSTFT.

Let $x(n)$ denote a time series with its time-stamp index n. Using a real non-zero window function $w(n)$ over $0 \leq n \leq L$, where L represents the window length, the STFT of $x(n)$ is written as

$$X_w(mS,\omega) = \sum_{l=-\infty}^{\infty} x_w(mS,l)e^{-i\omega l}\,, \tag{F.1}$$

where the windowed time series is

$$x_w(mS,l) = w(mS-l)x(l)\,, \tag{F.2}$$

where S is a positive integer, which represents the sampling period to calculate the FFT, m runs over (. . . , -1, 0, 1, . . .), ω denote angular frequencies.

For a given STFT $Y_w(mS,\omega)$, the corresponding windowed time series is expressed with the inverse STFT as

$$y_w(mS,l) = \frac{1}{2\pi}\int_{-\pi}^{\pi} Y_w(mS,\omega)e^{i\omega l}d\omega\,. \tag{F.3}$$

An arbitrary $Y_w(mS,\omega)$ is not guaranteed to have its corresponding time series $y_w(mS,l)$. The time series $x(n)$ whose STFT $X_w(mS,\omega)$ closest to $Y_w(mS,\omega)$ is obtained by considering the difference between $X_w(mS,\omega)$ and $Y_w(mS,\omega)$ summed over time and frequency:

$$\mathcal{L}[x(n),Y_w(m),\omega)] = \sum_{m=-\infty}^{\infty}\frac{1}{2\pi}\int^{\pi} -\pi|X_w(mS,\omega)-Y_w(mS,\omega)|^2 d\omega\,. \tag{F.4}$$

According to Parseval's theorem (Hardy and Titchmarsh, 1931), Equation (F.4) can be written as

$$\mathcal{L}[x(n),Y_w(mS,\omega)] = \sum_{m=\infty}^{\infty}\sum_{l=\infty}^{\infty}[x_w(mS,l)-y_w(mS,l)]^2\,, \tag{F.5}$$

if there exists $y_w(mS, l)$ which satisfies Equation (F.3). Because Equation (F.5) is a quadratic from of $x(n)$, a solution $x(n)$ that minimizes Equation (F.5) is obtained by taking derivative of Equation (F.5) with respect to $x(n)$. Using Equation (F.2), the solution is

$$\begin{aligned} x(n) &= \frac{\sum_{m=-\infty}^{\infty} w(mS-n) y_w(mS,n)}{\sum_{m=-\infty}^{\infty} w^2(mS-n)}, \\ &= \frac{\sum_{m=-\infty}^{\infty} w(mS-n) \frac{1}{2\pi} \int_{-\pi}^{\pi} Y_w(mS,\omega) e^{i\omega n} d\omega}{\sum_{m=-\infty}^{\infty} w^2(mS-n)}. \end{aligned} \tag{F.6}$$

Modifying Equation (F.6), Griffin and Jae Lim (1984) presented the method to estimate $x(n)$ from the arbitrary mSTFT iteratively. Suppose x^j is the estimate at the j^{th} iteration, the $(j+1)^{\text{th}}$ estimate x^{j+1} is given as

$$x^{j+1}(n) = \frac{\sum_{m=-\infty}^{\infty} w(mS-n) \frac{1}{2\pi} \int_{-\pi}^{\pi} \hat{X}_w^j(mS,\omega) e^{i\omega n} d\omega}{\sum_{m=-\infty}^{\infty} w^2(mS-n)}, \tag{F.7}$$

where

$$\hat{X}_w^j(mS,\omega) = |Y_w(mS,\omega)| \frac{X_w^j(mS,\omega)}{|X_w^j(mS,\omega)|}, \tag{F.8}$$

where $\hat{X}_w^j(mS,\omega)$ is set to equal to $|Y_w(mS,\omega)|$ with an arbitrary phase if $|X_w^j(mS,\omega)| = 0$. Equation (F.8) constrain the magnitude of the estimated STFT to always be the same as $|Y_w(mS,\omega)|$ and the inverse STFT in Equation (F.7) puts a hard constraint on the estimated time series such that its STFT is $\hat{X}_w^j(mS,\omega)$ so that the phase is implicitly estimated. $X_w^j(mS,\omega)$ is obtained using Equation (F.1). Note that the GL transform converges to a critical point, where the gradient of $\mathcal{L}$ is zero between $(j+1)^{\text{th}}$ and j^{th} iterations. However, a critical point does not necessarily to be the global minimum as pointed in Griffin and Jae Lim (1984).

To fasten the convergence, Griffin and Jae Lim (1984) presented a modified version called the FGL transformation. Let us rewrite the iteration rule in the GL transformation by letting G denote the operator to get the STFT of the time series in Equation (F.1) as

$$X_w^{j+1}(mS,\omega) = G[x^{j+1}(n)] := \sum_{l=-\infty}^{\infty} w(mS-n)x^{j+1}(n)e^{-i\omega n}, \tag{F.9}$$

and G^{-1} denote the operator to get x^{j+1} from $\hat{X}^j$ in Equation (F.7) as

$$x^{j+1}(n) = G^{-1}[\hat{X}^j(mS,\omega)] := \frac{\sum_{m=-\infty}^{\infty} w(mS-n)\frac{1}{2\pi}\int_{-\pi}^{\pi}\hat{X}_w^j(mS,\omega)e^{i\omega n}d\omega}{\sum_{m=-\infty}^{\infty} w^2(mS-n)}. \tag{F.10}$$

The iteration rule for the estimated STFT in the GL transformation can be rewritten as

$$X_w^{j+1}(mS,\omega) = G\left\{G^{-1}\left[|Y_w(mS,\omega)|\frac{X_w^j(mS,\omega)}{|X_w^j(mS,\omega)|}\right]\right\}, \tag{F.11}$$

where X_w^0 is chosen to be the STFT of the Gaussian noise. The FGL transformation adds one extra step after Equation (F.11) per iteration as

$$\begin{aligned} K_w^{j+1}(mS,\omega) &= G\left\{G^{-1}\left[|Y_w(mS,\omega)|\frac{X_w^j(mS,\omega)}{|X_w^j(mS,\omega)|}\right]\right\}, \\ X_w^{j+1}(mS,\omega) &= K_w^{j+1}(mS,\omega) + \alpha[K_w^{j+1}(mS,\omega) - K_w^j(mS,\omega)], \end{aligned} \tag{F.12}$$

where $K_w^0 = G[G^{-1}(|Y_w|\frac{X_w^0}{|X_w^0|})]$. Equation (F.12) updates X_w using the gradient between the estimated STFT in the current and previous iterations by a factor of α to fasten the convergence. However, adding this extra step does not guarantee the theoretical convergence as pointed in (Perraudin *et al.*, 2013).

Figure 9 shows the FNR as a function of FGL iteration with $\alpha = 0.99$ (recommended value in Perraudin *et al.* (2013)). Values FNR are comparable after 20 iterations. We choose 32 iterations (default value in Cheuk *et al.* (2020)) and $\alpha = 0.99$ in Paper II.

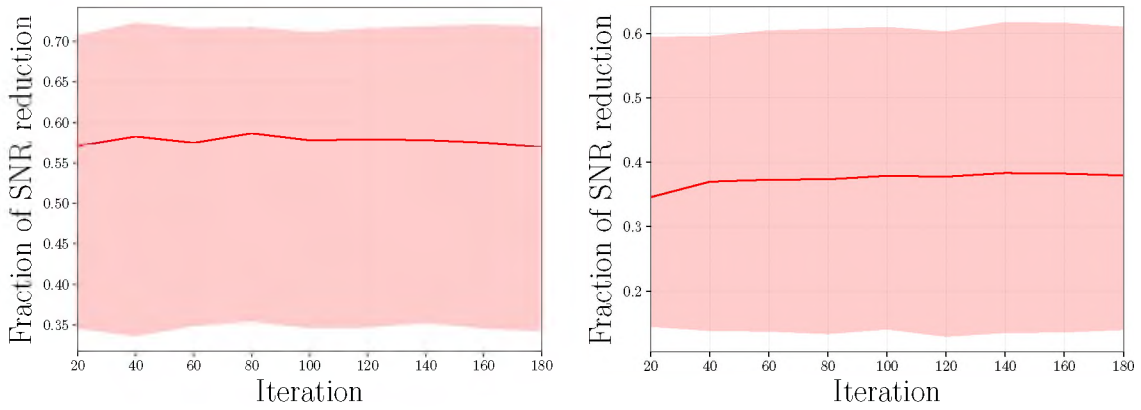

Figure 9. Fraction of SNR reduction versus the number of FGL iterations for *Scattered light* (left) and *Extremely loud* glitches. The solid curves denote the median values and the shaded areas denote 1-σ percentiles.

The data used in Paper II does not guarantee the theoretical convergence inherited from the algorithm of the FGL transformation and the convergent point to be the global minimum inherited from the GL transformation. We address the accuracy of the FGL transformation on the data used in Paper II in the next section.

4.2. ACCURACY OF FAST GRIFFIN-LIM TRANSFORM

To quantify the accuracy of FGL transform, we calculate *match M* (defined in Equation (4.5)) between extracted glitch waveforms and the FGL transformed time series from the mSTFT of the same extracted glitch waveforms. Values of M range from -1 (fully anti-correlated) to 1 (perfect match). The FGL transformed time series has a phase error. Also, we apply the phase correction before subtracting glitches from the data before subtracting glitches. we also calculate the match maximized over phase and time, defined as

$$M_{\max} = \mathrm{argmax}_{t_0} \frac{|(\tilde{a}, \tilde{b}e^{2\pi i f t_0})_{\mathrm{complex}}|}{\sqrt{(\tilde{a}, \tilde{a})(\tilde{b}, \tilde{b})}}, \tag{F.13}$$

where the complex inner product $(\tilde{a}, \tilde{b}e^{2\pi i f t_0})_{\text{complex}}$ is defined as

$$(\tilde{a}, \tilde{b}e^{2\pi i f t_0})_{\text{complex}} = 4 \int_0^\infty df \frac{\tilde{a}^*(f)\tilde{b}(f)e^{2\pi i f t_0}}{S_n(f)} . \tag{F.14}$$

We use extracted glitch waveforms in the testing set of *Scattered light* and *Extremely loud* glitches with sample sizes of 678 and 1233, respectively. Figure 10 shows distributions of the match and maximized match.

Samples with values of $M \sim \pm 1$ and $M_{\text{max}} \sim 1$ indicate that the FGL transformed time series are similar to the original extracted-glitch waveforms with some degree of phase shifts. Samples with values of $M \sim 0$ and $M_{\text{max}} \sim 1$ indicate that the FGL transformed time series have phase shifts such that they mismatch with the extracted glitch waveforms. Samples with values of $M \sim 0$ and $M_{\text{max}} \sim 0$ indicate that the FGL transformed time series mismatch with the original extracted-glitch waveforms with both phases and amplitudes. The median and 90 percentile of absolute values of the time shift t_0 which maximizes the match are ~ 0.02 (~ 0.003) and ~ 0.06 (~ 0.0034) seconds for *Scattered light* (*Extremely loud*) glitches, respectively.

Figure 11 shows the optimal and least accurate FGL transformed time series. The optimal and least values of M_{max} are ~ 0.27 (~ 0.27) and ~ 0.99 (~ 0.97) for *Scattered light* (*Extremely loud*) glitches, respectively. The FGL transform seems to produce no significant deviations on the amplitude in the portion where the extracted glitch waveforms have amplitudes close to zero. Therefore, the amount of the mismatch seems to be due to the amplitude difference in the portion where extracted glitch waveforms have large amplitudes.

To understand the meaning of values of M_{max} between the FGL transformed time series and the extracted glitch waveforms in terms of amplitude uncertainty of the FGL transform, we calculate M_{max} between the extracted waveform and themselves injected into the Gaussian noise with zero mean and a given standard deviation. Assuming the FGL transformation provides the amplitude error following a Gaussian distribution with

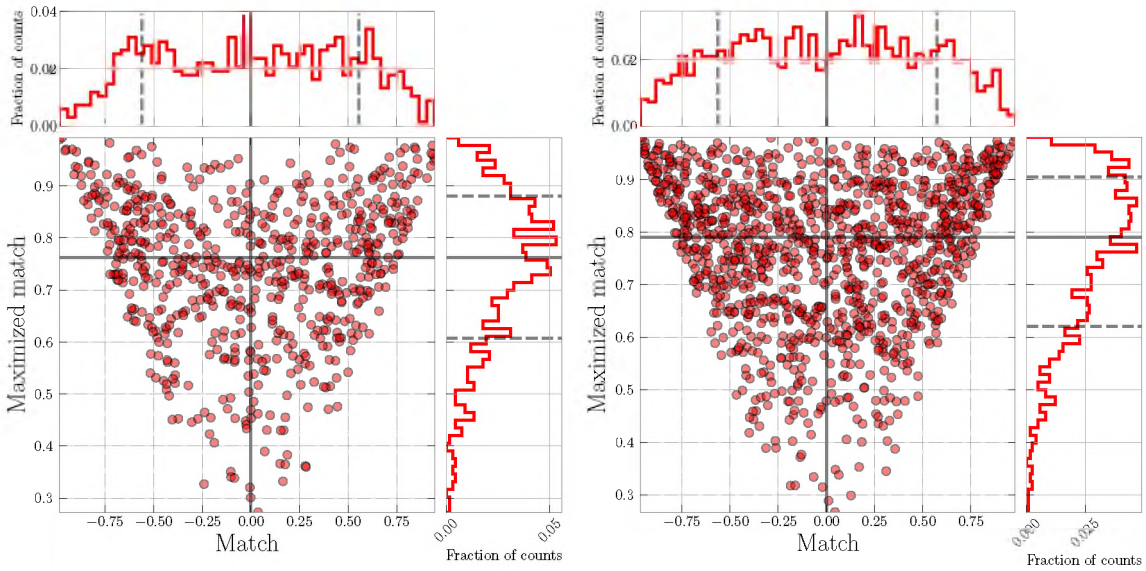

Figure 10. Distributions of the match M and maximized match $M_{\max}$ between extracted waveforms and FGL transformed waveforms for *Scattered light* (left) and *Extremely loud* (right) glitches. Black lines denote the median values and dashed lines denote 1-σ percentiles.

zero mean throughout time series, we can find the standard deviation of the Gaussian noise corresponding to the amplitude uncertainty of the FGL transform. We find that *Scattered light* and *Extremely loud* glitches have the amplitude uncertainties equivalent to the $\sim 0.4\sigma$ and $\sim 8\sigma$ noise, respectively, as shown in Figure 12. As discussed above, the FGL transformation produces no significant amplitude errors in the portion where the extracted glitch waveforms have amplitudes close to zero. Therefore, the above estimates using the noise with a given σ has a bias for waveforms with larger amplitudes in limited time portions such as *Extremely loud* glitches. One of the possible approaches to correct the phase and amplitudes of the FGL transformed time series is to split the time series into small segments and change the phase and amplitude in each segment (see details in Sec. 2.5).

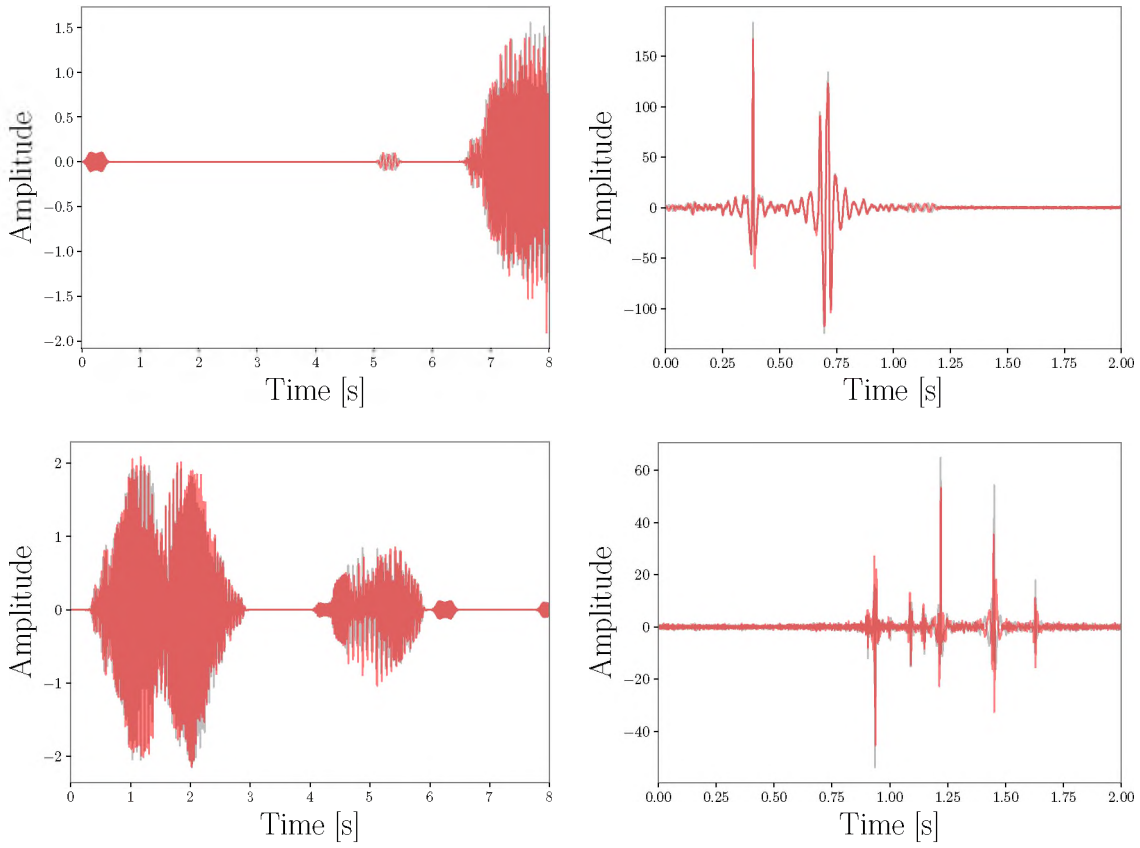

Figure 11. Optimally (top) and least (bottom) accurate FGL transformed time series (red) and extracted glitch waveforms (gray) of *Scattered light* (left) and *Extremely loud* (right) glitches. The optimal and least values of $M_{\max}$ are ~ 0.27 (~ 0.27) and ~ 0.99 (~ 0.97) for *Scattered light* (*Extremely loud*) glitches, respectively.

4.3. TIME WINDOW TO SUBTRACT GLITCHES

Applying the FGL transform to the estimated mSTFT from the trained network, we obtain the estimated glitch waveforms. Using the estimated glitch waveforms, we subtract glitches from the data. In the glitch-subtraction process, we determine portions of the data containing g glitches based on the estimated glitch waveforms. We only subtract the data in portions containing glitches and use the original data in the rest portions without the glitch subtraction. To determine the data portions, we use the estimated glitch waveforms in the testing set with sample sizes of 678 and 1233 for *Scattered light* and *Extremely loud* glitches. We first calculate the absolute values of the estimated glitch waveforms and then smooth

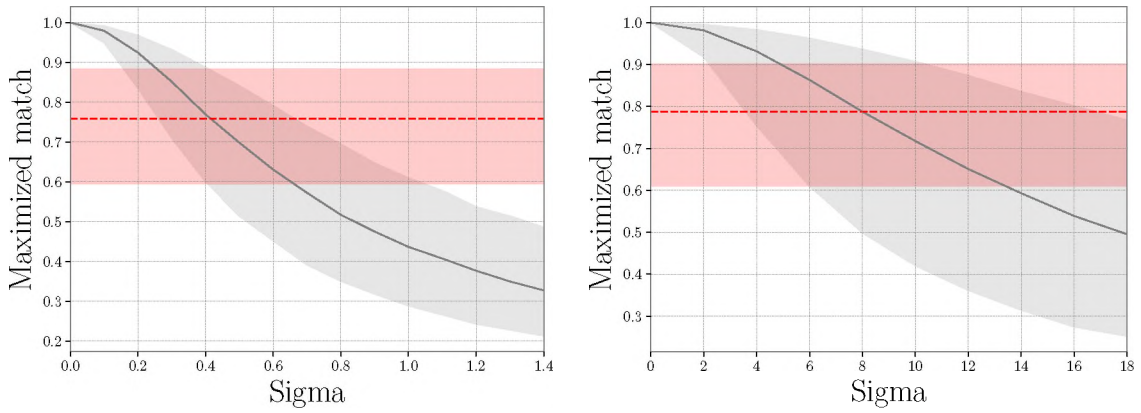

Figure 12. Median of maximized matches (gray solid) between the extracted glitch waveforms and themselves injected into the Gaussian distributed noise with zero mean and a given standard deviation as well as the median of maximized matches (red dashed) between the FGL transformed time series and the extracted glitch waveforms for *Scattered light* (left) *Extremely loud* (right) glitches. The shaded areas denote 1-σ percentiles.

the curve. We consider data portions to be the regions where the smoothed curves are above thresholds. Smaller thresholds make the data portions to be larger so that larger data are used in the subtraction process, where larger fractions of the data portions have no glitches and no need to be subtracted. Larger thresholds make the data portions to be smaller so that only small fractions of glitches are subtracted. We consider various percentiles of the absolute value of the estimated glitch waveforms as thresholds. Figure 13 shows the variation of FNRs due to the choices of percentiles. We find that the peak of median FNRs are obtained with and 60 and 55 percentiles for *Scattered light* and *Extremely loud*, respectively. Below the peak values, values of FNRs are compatible within the 1-σ uncertainty because the regions with the absence of glitches are not similar to the corresponding portions of the estimated glitch waveform other than the Gaussian fluctuations, causing no glitches to be subtracted subtraction in that regions. Larger percentiles corresponding to larger thresholds let only small fractions of glitches be subtracted, causing smaller values of FNR. Threshold values used in Sec. 3.1 and Sec. 3.2 are 70 percentile and 90 percentile for *Scattered light* and *Extremely loud*, respectively, whose values of FNR are smaller than the peak median values by only $\sim 3\%$.

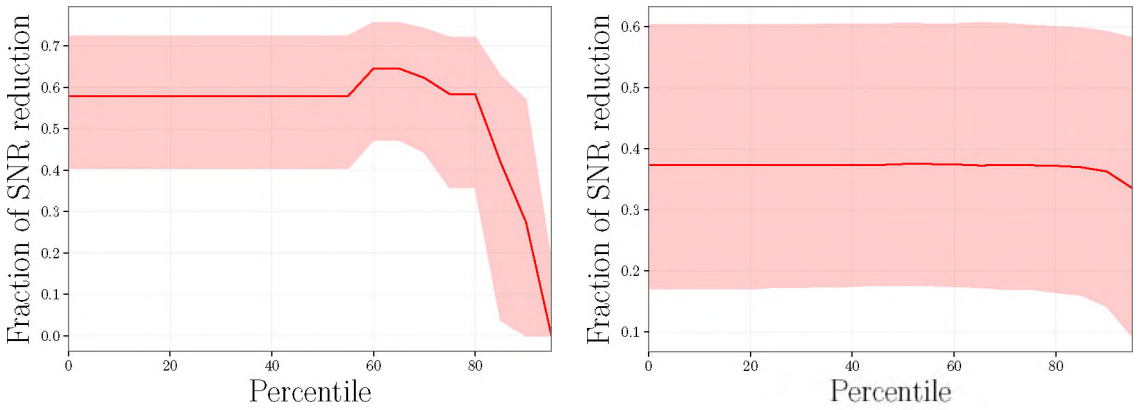

Figure 13. Fraction of SNR reduction as a function of percentile as thresholds for the glitch present portions for *Scattered light* (left) and *Extremely loud* (right) glitches. The solid curves denote the median values and the shaded areas denote 1-σ percentiles.

4.4. COMPARISON OF ACCURACY BETWEEN MODELED AND UNMODELED SEARCHES PIPELINES

Unmodeled GW search pipelines are typically less sensitive than modeled pipelines. The sky localization error regions obtained with the unmodeled search pipelines are also less accurate than those obtained with modeled pipelines. To compare their accuracy, we make 9 sets of injected simulated BBH signals with the network SNR of 42.4, 28.3, 11.3 with the component masses of $(m_1, m_2) = (35, 29), (20, 15), (12, 10)$ $M_\odot$ into simulated colored Gaussian noise with the LIGO design sensitivity in the two-detector network. We choose the waveform coalescence phase, polarization angle, and cosine of the inclination angle to be uniformly distributed in the intervals $[0, 2\pi]$, $[0, \pi]$, and $[-1, 1]$. We use a modified version of a PYCBC (Nitz *et al.*, 2020) script, PYCBC_MAKE_SKYMAP, and cWB (Klimenko *et al.*, 2008, 2016) as modeled and unmodeled sky-map generators, respectively.

Figure 14 shows the comparison of the contour levels at the injection directions. 63-82% of injections have their contour levels below 0.9 for in sky maps obtained by the modeled search irrespective of all used network SNRs. No more than 50% of injections have their contour levels less than 0.9 for the sky maps obtained by cWB. For cWB, larger component masses correspond to more accurate estimates of the source directions because

higher signal energy is concentrated on smaller time periods and the signal reconstructions are more accurate. Sets with the network SNR of 11.3 have less than 53% of injections found by cWB because the ranking statistic $\rho = 6$ is chosen as a typical criterion to report the reconstruction. The network SNR of 11.6 corresponds to $\rho \sim 5.8$, which is lower than this criterion so that the majority of injections are not found for the network SNR of 11.6.

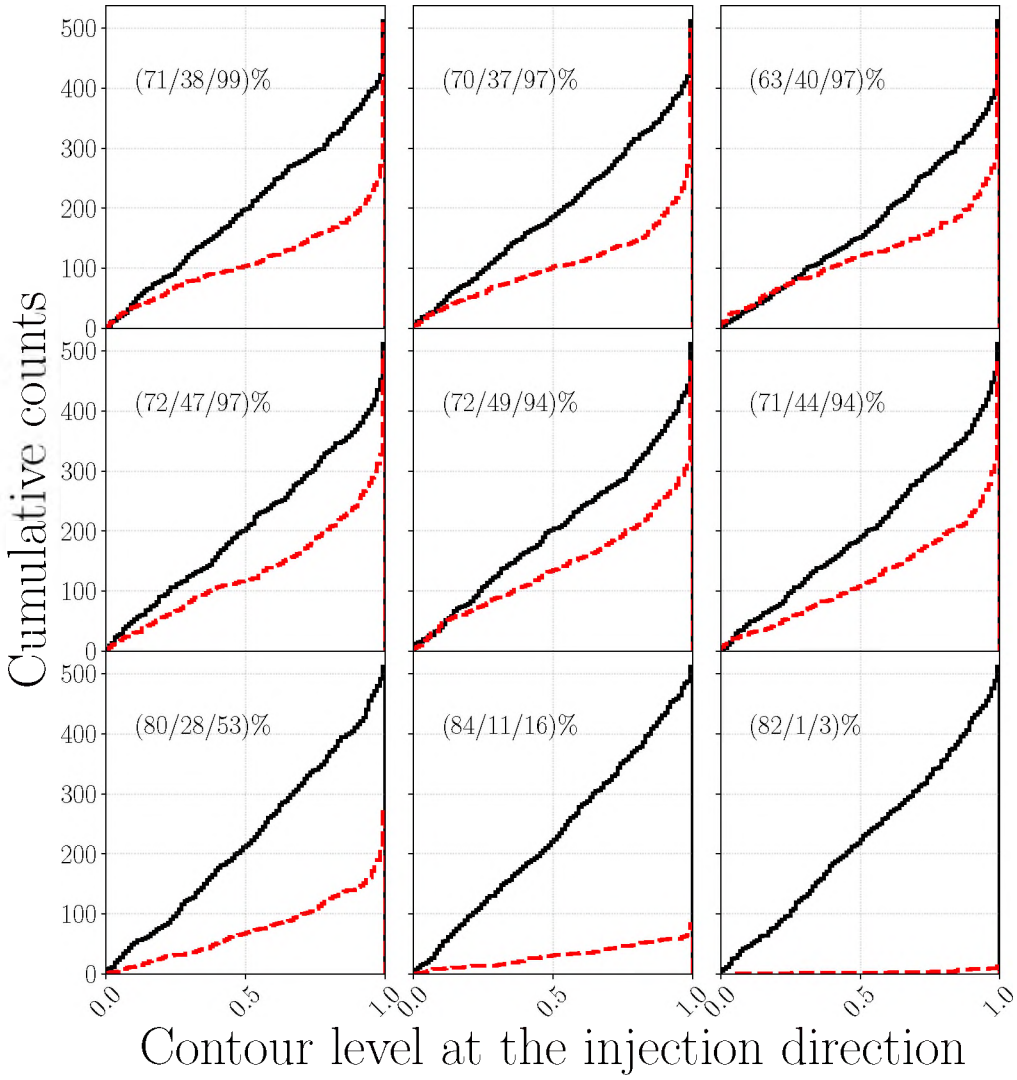

Figure 14. Comparisons of the contour level obtained by Bayestar (solid-black) and cWB (dashed-red) for 512 simulated BBH signals with the network SNR of 42.4 (1^{st} row), 28.3 (2^{nd} row), and 11.3 (3^{rd} row) with the component masses of $(m_1, m_2) = (35, 29)\ M_\odot$ (1^{st} column), $(m_1, m_2) = (20, 15)\ M_\odot$ (2^{nd} column), and $(m_1, m_2) = (12, 10)\ M_\odot$ (3^{rd} column) injected into the simulated colored Gaussian data with LIGO's design sensitivity. The first and second quoted values are the percents of injections with their contour levels below 0.9 in the sky maps obtained by Bayestar and cWB, respectively. The last quoted values are percents of injections found by cWB.

REFERENCES

Aasi, J. *et al.*, 'Advanced LIGO,' Class. Quant. Grav., 2015, **32**, p. 074001, doi: 10.1088/0264-9381/32/7/074001.

Abadie, J. *et al.*, 'A Gravitational wave observatory operating beyond the quantum shot-noise limit: Squeezed light in application,' Nature Phys., 2011, **7**, pp. 962–965, doi: 10.1038/nphys2083.

Abbott, B. *et al.*, 'Search for gravitational waves from galactic and extra-galactic binary neutron stars,' Phys. Rev. D, 2005, **72**, p. 082001, doi: 10.1103/PhysRevD.72.082001.

Abbott, B. *et al.*, 'GW150914: Implications for the stochastic gravitational wave background from binary black holes,' Phys. Rev. Lett., 2016a, **116**(13), p. 131102, doi: 10.1103/PhysRevLett.116.131102.

Abbott, B. *et al.*, 'All-sky search for continuous gravitational waves from isolated neutron stars using Advanced LIGO O2 data,' Phys. Rev. D, 2019a, **100**(2), p. 024004, doi: 10.1103/PhysRevD.100.024004.

Abbott, B. *et al.*, 'All-sky search for long-duration gravitational-wave transients in the second Advanced LIGO observing run,' Phys. Rev. D, 2019b, **99**(10), p. 104033, doi: 10.1103/PhysRevD.99.104033.

Abbott, B. P. *et al.*, 'A First Targeted Search for Gravitational-Wave Bursts from Core-Collapse Supernovae in Data of First-Generation Laser Interferometer Detectors,' Phys. Rev. D, 2016b, **94**(10), p. 102001, doi: 10.1103/PhysRevD.94.102001.

Abbott, B. P. *et al.*, 'All-sky search for long-duration gravitational wave transients with initial LIGO,' Phys. Rev. D, 2016c, **93**(4), p. 042005, doi: 10.1103/PhysRevD.93.042005.

Abbott, B. P. *et al.*, 'GW150914: First results from the search for binary black hole coalescence with Advanced LIGO,' Phys. Rev. D, 2016d, **93**(12), p. 122003, doi: 10.1103/PhysRevD.93.122003.

Abbott, B. P. *et al.*, 'Observation of Gravitational Waves from a Binary Black Hole Merger,' Phys. Rev. Lett., 2016e, **116**(6), p. 061102, doi: 10.1103/PhysRevLett.116.061102.

Abbott, B. P. *et al.*, 'Exploring the Sensitivity of Next Generation Gravitational Wave Detectors,' Class. Quant. Grav., 2017a, **34**(4), p. 044001, doi: 10.1088/1361-6382/aa51f4.

Abbott, B. P. *et al.*, 'Gravitational Waves and Gamma-Rays from a Binary Neutron Star Merger: GW170817 and GRB 170817A,' Astrophys. J., 2017b, **848**(2), p. L13, doi: 10.3847/2041-8213/aa920c.

Abbott, B. P. *et al.*, 'Gw170817: Observation of gravitational waves from a binary neutron star inspiral,' Phys. Rev. Lett., Oct 2017c, **119**, p. 161101, doi: 10.1103/PhysRevLett.119.161101.

Abbott, B. P. *et al.*, 'Multi-messenger Observations of a Binary Neutron Star Merger,' Astrophys. J., 2017d, **848**(2), p. L 12, doi: 10.3847/2041-8213/aa91c9.

Abbott, B. P. *et al.*, 'The basic physics of the binary black hole merger GW150914,' Annalen Phys., 2017e, **529**(1-2), p. 1600209, doi: 10.1002/andp.201600209.

Abbott, B. P. *et al.*, 'All-sky search for long-duration gravitational wave transients in the first Advanced LIGO observing run,' Class. Quant. Grav., 2018, **35**(6), p. 065009, doi: 10.1088/1361-6382/aaab76.

Abbott, B. P. *et al.*, 'All-Sky Search for Short Gravitational-Wave Bursts in the Second Advanced LIGO and Advanced Virgo Run,' Phys. Rev. D, 2019c, **100**(2), p. 024017, doi: 10.1103/PhysRevD.100.024017.

Abbott, B. P. *et al.*, 'Gwtc-1: A gravitational-wave transient catalog of compact binary mergers observed by ligo and virgo during the first and second observing runs,' Phys. Rev. X, Sep 2019d, **9**, p. 031040, doi: 10.1103/PhysRevX.9.031040.

Abbott, B. P. *et al.*, 'Search for gravitational-wave signals associated with gamma-ray bursts during the second observing run of Advanced LIGO and Advanced Virgo,' Astrophys. J., 2019e, **886**, p. 75, doi: 10.3847/1538-4357/ab4b48.

Abbott, B. P. *et al.*, 'Prospects for observing and localizing gravitational-wave transients with Advanced LIGO, Advanced Virgo and KAGRA,' Living Rev. Rel., 2020a, **23**(1), p. 3, doi: 10.1007/s41114-020-00026-9.

Abbott, B. P. *et al.*, 'A Gravitational-wave Measurement of the Hubble Constant Following the Second Observing Run of Advanced LIGO and Virgo,' Astrophys. J., 2021a, **909**(2), p. 218, doi: 10.3847/1538-4357/abdcb7.

Abbott, R. *et al.*, 'Search for Gravitational Waves Associated with Gamma-Ray Bursts Detected by Fermi and Swift During the LIGO-Virgo Run O3a,' 10 2020b.

Abbott, R. *et al.*, 'GWTC-2: Compact Binary Coalescences Observed by LIGO and Virgo During the First Half of the Third Observing Run,' Phys. Rev. X, 2021b, **11**, p. 021053, doi: 10.1103/PhysRevX.11.021053.

Abbott, R. *et al.*, 'Tests of general relativity with binary black holes from the second LIGO-Virgo gravitational-wave transient catalog,' Phys. Rev. D, 2021c, **103**(12), p. 122002, doi: 10.1103/PhysRevD.103.122002.

Acernese, F. *et al.*, 'Advanced Virgo: a second-generation interferometric gravitational wave detector,' Class. Quant. Grav., 2015, **32**(2), p. 024001, doi: 10.1088/0264-9381/32/2/024001.

Akutsu, T. *et al.*, 'Overview of KAGRA: Detector design and construction history,' Progress of Theoretical and Experimental Physics, 08 2020, **2021**(5), ISSN 2050-3911, doi: 10.1093/ptep/ptaa125, 05A101.

Allen, B., 'χ^2 time-frequency discriminator for gravitational wave detection,' Phys. Rev. D, Mar 2005, **71**, p. 062001, doi: 10.1103/PhysRevD.71.062001.

Allen, B., Anderson, W. G., Brady, P. R., Brown, D. A., and Creighton, J. D. E., 'FINDCHIRP: An Algorithm for detection of gravitational waves from inspiraling compact binaries,' Phys. Rev. D, 2012, **85**, p. 122006, doi: 10.1103/PhysRevD.85.122006.

Ashton, G., Hübner, M., Lasky, P. D., Talbot, C., Ackley, K., Biscoveanu, S., Chu, Q., Divakarla, A., Easter, P. J., Goncharov, B., Vivanco, F. H., Harms, J., Lower, M. E., Meadors, G. D., Melchor, D., Payne, E., Pitkin, M. D., Powell, J., Sarin, N., Smith, R. J. E., and Thrane, E., 'Bilby: A user-friendly bayesian inference library for gravitational-wave astronomy,' The Astrophysical Journal Supplement Series, apr 2019, **241**(2), p. 27, doi: 10.3847/1538-4365/ab06fc.

Bengio, Y., Simard, P., and Frasconi, P., 'Learning long-term dependencies with gradient descent is difficult,' IEEE Transactions on Neural Networks, 1994, **5**(2), pp. 157–166, doi: 10.1109/72.279181.

Biswas, R. *et al.*, 'Application of machine learning algorithms to the study of noise artifacts in gravitational-wave data,' Phys. Rev. D, 2013, **88**(6), p. 062003, doi: 10.1103/PhysRevD.88.062003.

Bond, C., Brown, D., Freise, A., and Strain, K., 'Interferometer techniques for gravitational-wave detection,' LIVING REVIEWS IN RELATIVITY, December 2016, **19**, pp. 1–221, ISSN 1433-8351, doi: 10.1007/s41114-016-0002-8.

Brown, D. A., *Searching for gravitational radiation from binary black hole MACHOs in the galactic halo*, Other thesis, 12 2004.

Burrows, A., Hayes, J., and Fryxell, B. A., 'On the nature of core collapse supernova explosions,' Astrophys. J., 1995, **450**, p. 830, doi: 10.1086/176188.

Cannon, K. C., 'Efficient algorithm for computing the time-resolved full-sky cross power in an interferometer with omnidirectional elements,' Phys. Rev. D, Jun 2007, **75**, p. 123003, doi: 10.1103/PhysRevD.75.123003.

Carroll, S., *Spacetime and Geometry: An Introduction to General Relativity*, Benjamin Cummings, 2003, ISBN 0805387323.

Chatterjee, C., Wen, L., Vinsen, K., Kovalam, M., and Datta, A., 'Using Deep Learning to Localize Gravitational Wave Sources,' Phys. Rev. D, 2019, **100**(10), p. 103025, doi: 10.1103/PhysRevD.100.103025.

Chatterji, S., Blackburn, L., Martin, G., and Katsavounidis, E., 'Multiresolution techniques for the detection of gravitational-wave bursts,' Class. Quant. Grav., 2004, **21**, pp. S1809–S1818, doi: 10.1088/0264-9381/21/20/024.

Chatziioannou, K., Cornish, N., Wijngaarden, M., and Littenberg, T. B., 'Modeling compact binary signals and instrumental glitches in gravitational wave data,' Phys. Rev. D, 2021, **103**(4), p. 044013, doi: 10.1103/PhysRevD.103.044013.

Cheuk, K. W., Anderson, H., Agres, K., and Herremans, D., 'nnaudio: An on-the-fly gpu audio to spectrogram conversion toolbox using 1d convolutional neural networks,' IEEE Access, 2020, **8**, pp. 161981–162003, doi: 10.1109/ACCESS.2020.3019084.

Cokelaer, T., 'Gravitational waves from inspiralling compact binaries: Hexagonal template placement and its efficiency in detecting physical signals,' Phys. Rev. D, 2007, **76**, p. 102004, doi: 10.1103/PhysRevD.76.102004.

Cornish, N. J., 'Rapid and Robust Parameter Inference for Binary Mergers,' Phys. Rev. D, 2021, **103**(10), p. 104057, doi: 10.1103/PhysRevD.103.104057.

Cornish, N. J. and Littenberg, T. B., 'Bayeswave: Bayesian inference for gravitational wave bursts and instrument glitches,' Classical and Quantum Gravity, Jun 2015, **32**, p. 135012, doi: 10.1088/0264-9381/32/13/135012.

Couch, S. M. and Ott, C. D., 'The Role of Turbulence in Neutrino-Driven Core-Collapse Supernova Explosions,' Astrophys. J., 2015, **799**(1), p. 5, doi: 10.1088/0004-637X/799/1/5.

Davis, D., Massinger, T. J., Lundgren, A. P., Driggers, J. C., Urban, A. L., and Nuttall, L. K., 'Improving the Sensitivity of Advanced LIGO Using Noise Subtraction,' Class. Quant. Grav., 2019, **36**(5), p. 055011, doi: 10.1088/1361-6382/ab01c5.

Davis, D. *et al.*, 'LIGO Detector Characterization in the Second and Third Observing Runs,' Class. Quant. Grav., 2021, **38**(13), p. 135014, doi: 10.1088/1361-6382/abfd85.

Drago, M., *Search for transient gravitational wave signals with a known waveform in the LIGO Virgo network of interferometric detectors using a fully coherent algorithm*, Ph.D. thesis, Padua U., 2010.

Einstein, A., 'Zur elektrodynamik bewegter körper,' Annalen der Physik, 1905, **322**(10), pp. 891–921, doi: https://doi.org/10.1002/andp.19053221004.

Einstein, A., 'The Field Equations of Gravitation,' Sitzungsber. Preuss. Akad. Wiss. Berlin (Math. Phys.), 1915, **1915**, pp. 844–847.

Einstein, A., 'Näherungsweise Integration der Feldgleichungen der Gravitation,' Sitzungsberichte der Königlich Preußischen Akademie der Wissenschaften (Berlin, January 1916, pp. 688–696.

Essick, R., Godwin, P., Hanna, C., Blackburn, L., and Katsavounidis, E., 'iDQ: Statistical inference of non-gaussian noise with auxiliary degrees of freedom in gravitational-wave detectors,' Machine Learning: Science and Technology, dec 2020, **2**(1), p. 015004, doi: 10.1088/2632-2153/abab5f.

Finn, L. S., 'Detection, measurement, and gravitational radiation,' Phys. Rev. D, Dec 1992, **46**, pp. 5236–5249, doi: 10.1103/PhysRevD.46.5236.

Goldstein, A. *et al.*, 'An Ordinary Short Gamma-Ray Burst with Extraordinary Implications: Fermi-GBM Detection of GRB 170817A,' Astrophys. J. Lett., 2017, **848**(2), p. L14, doi: 10.3847/2041-8213/aa8f41.

Griffin, D. and Jae Lim, 'Signal estimation from modified short-time fourier transform,' IEEE Transactions on Acoustics, Speech, and Signal Processing, 1984, **32**(2), pp. 236–243, doi: 10.1109/TASSP.1984.1164317.

Hahnloser, R. H. R., Sarpeshkar, R., Mahowald, M. A., Douglas, R. J., and Seung, H. S., 'Digital selection and analogue amplification coexist in a cortex-inspired silicon circuit,' Nature, 07 2000, **405**, pp. 947–51, doi: 10.1038/35016072.

Hardy, G. H. and Titchmarsh, E., 'A Note on Parseval's Theorem for Fourier Transforms,' Journal of the London Mathematical Society, 01 1931, **s1-6**(1), pp. 44–48, ISSN 0024-6107, doi: 10.1112/jlms/s1-6.1.44.

Harry, I. W., Allen, B., and Sathyaprakash, B., 'A Stochastic template placement algorithm for gravitational wave data analysis,' Phys. Rev. D, 2009, **80**, p. 104014, doi: 10.1103/PhysRevD.80.104014.

Herant, M., 'The convective engine paradigm for the supernova explosion mechanism and its consequences,' Physics Reports, 1995, **256**(1), pp. 117–133, ISSN 0370-1573, doi: https://doi.org/10.1016/0370-1573(94)00105-C, the Physics of Supernovae.

Hochreiter, S. and Schmidhuber, J., 'Long Short-Term Memory,' Neural Computation, 11 1997, **9**(8), pp. 1735–1780, ISSN 0899-7667, doi: 10.1162/neco.1997.9.8.1735.

Hulse, R. and Taylor, J., 'Discovery of a pulsar in a binary system,' Astrophys. J. Lett., 1975, **195**, pp. L51–L53, doi: 10.1086/181708.

Iyer, B. *et al.*, 'LIGO-India, Proposal of the Consortium for Indian Initiative in Gravitational-wave Observations (IndIGO),' 2011.

Joyce, J. M., *Kullback-Leibler Divergence*, pp. 720–722, Springer Berlin Heidelberg, Berlin, Heidelberg, ISBN 978-3-642-04898-2, 2011, doi: 10.1007/978-3-642-04898-2_327.

Khan, S., Husa, S., Hannam, M., Ohme, F., Pürrer, M., Forteza, X. J., and Bohé, A., 'Frequency-domain gravitational waves from nonprecessing black-hole binaries. ii. a phenomenological model for the advanced detector era,' Phys. Rev. D, Feb 2016, **93**, p. 044007, doi: 10.1103/PhysRevD.93.044007.

Kingma, D. and Ba, J., 'Adam: A method for stochastic optimization,' International Conference on Learning Representations, 12 2014.

Kittel, C., *Elementary Statistical Physics*, Dover Books on Physics Series, Dover Publications, 2004, ISBN 9780486435145.

Klimenko, S., Mohanty, S., Rakhmanov, M., and Mitselmakher, G., 'Constraint likelihood analysis for a network of gravitational wave detectors,' Phys. Rev. D, 2005, **72**, p. 122002, doi: 10.1103/PhysRevD.72.122002.

Klimenko, S., Mohanty, S., Rakhmanov, M., and Mitselmakher, G., 'Constraint likelihood method: generalization for colored noise.' Journal of Physics: Conference Series, mar 2006, **32**, pp. 12–17, doi: 10.1088/1742-6596/32/1/003.

Klimenko, S., Yakushin, I., Mercer, A., and Mitselmakher, G., 'Coherent method for detection of gravitational wave bursts,' Class. Quant. Grav., 2008, **25**, p. 114029, doi: 10.1088/0264-9381/25/11/114029.

Klimenko, S. *et al.*, 'Method for detection and reconstruction of gravitational wave transients with networks of advanced detectors,' Phys. Rev. D, 2016, **93**(4), p. 042004, doi: 10.1103/PhysRevD.93.042004.

Kumar, P. and Granot, J., 'The Evolution of a structured relativistic jet and GRB afterglow light- curves,' Astrophys. J., 2003, **591**, pp. 1075–1085, doi: 10.1086/375186.

LIGO Scientific Collaboration, 'LIGO Algorithm Library - LALSuite,' free software (GPL), 2018, doi: 10.7935/GT1W-FZ16.

Luck, H. *et al.*, 'The upgrade of GEO600,' J. Phys. Conf. Ser., 2010, **228**, p. 012012, doi: 10.1088/1742-6596/228/1/012012.

Lynch, R., Vitale, S., Essick, R., Katsavounidis, E., and Robinet, F., 'Information-theoretic approach to the gravitational-wave burst detection problem,' Phys. Rev. D, 2017, **95**(10), p. 104046, doi: 10.1103/PhysRevD.95.104046.

Macleod, D., Urban, A. L., Coughlin, S., Massinger, T., Pitkin, M., rngeorge, paulaltin, Areeda, J., Singer, L., Quintero, E., Leinweber, K., and Badger, T. G., 'gwpy/gwpy: 2.0.2,' December 2020, doi: 10.5281/zenodo.4301851.

Manca, G. M. and Vallisneri, M., 'Cover art: Issues in the metric-guided and metric-less placement of random and stochastic template banks,' Phys. Rev. D, 2010, **81**, p. 024004, doi: 10.1103/PhysRevD.81.024004.

Massey, F. J., 'The Kolmogorov-Smirnov test for goodness of fit,' Journal of the American Statistical Association, 1951, **46**(253), pp. 68–78.

Meers, B. J., 'Recycling in laser-interferometric gravitational-wave detectors,' Phys. Rev. D, Oct 1988, **38**, pp. 2317–2326, doi: 10.1103/PhysRevD.38.2317.

Michelson, A. A. and Morley, E. W., 'On the Relative Motion of the Earth and the Luminiferous Ether,' Am. J. Sci., 1887, **34**, pp. 333–345, doi: 10.2475/ajs.s3-34.203.333.

Misner, C. W., Thorne, K. S., and Wheeler, J. A., *Gravitation*, W. H. Freeman, San Francisco, 1973, ISBN 978-0-7167-0344-0, 978-0-691-17779-3.

Modjaz, M., 'Stellar Forensics with the Supernova-GRB Connection,' Astron. J., 2011, **332**, p. 434, doi: 10.1002/asna.201111562.

Mogushi, K., 'Application of a new transient-noise analysis tool for an unmodeled gravitational-wave search pipeline,' Classical and Quantum Gravity, 2021a.

Mogushi, K., 'Reduction of transient noise artifacts in gravitational-wave data using deep learning,' 5 2021b.

Mogushi, K., Cavaglià, M., and Siellez, K., 'Jet geometry and rate estimate of coincident gamma-ray burst and gravitational-wave observations,' The Astrophysical Journal, jul 2019, **880**(1), p. 55, doi: 10.3847/1538-4357/ab1f76.

Mogushi, K., Quitzow-James, R., Cavaglia, M., Kulkarni, S., and Hayes, F., 'Nnetfix: An artificial neural network-based denoising engine for gravitational-wave signals,' Machine Learning: Science and Technology, 2021.

Mooley, K. P., Deller, A. T., Gottlieb, O., Nakar, E., Hallinan, G., Bourke, S., Frail, D. A., Horesh, A., Corsi, A., and Hotokezaka, K., 'Superluminal motion of a relativistic jet in the neutron-star merger GW170817,' Nature, 2018, **561**(7723), pp. 355–359, doi: 10.1038/s41586-018-0486-3.

Nair, V. and Hinton, G. E., 'Rectified linear units improve restricted boltzmann machines,' in 'Proceedings of the 27th International Conference on International Conference on Machine Learning,' ICML'10, Omnipress, Madison, WI, USA, ISBN 9781605589077, 2010 p. 807–814.

Necula, V., Klimenko, S., and Mitselmakher, G., 'Transient analysis with fast Wilson-Daubechies time-frequency transform,' J. Phys. Conf. Ser., 2012, **363**, p. 012032, doi: 10.1088/1742-6596/363/1/012032.

Neyman, J. and Pearson, E. S., 'On the Problem of the Most Efficient Tests of Statistical Hypotheses,' Phil. Trans. Roy. Soc. Lond. A, 1933, **231**(694-706), pp. 289–337, doi: 10.1098/rsta.1933.0009.

Nitz, A., Harry, I., Brown, D., Biwer, C. M., Willis, J., Canton, T. D., Capano, C., Pekowsky, L., Dent, T., Williamson, A. R., Davies, G. S., De, S., Cabero, M., Machenschalk, B., Kumar, P., Reyes, S., Macleod, D., Pannarale, F., dfinstad, Massinger, T., Tápai, M., Singer, L., Khan, S., Fairhurst, S., Kumar, S., Nielsen, A., shasvath, Dorrington, I., Lenon, A., and Gabbard, H., 'gwastro/pycbc: Pycbc release 1.16.4,' Jun 2020, doi: 10.5281/zenodo.3904502.

Ormiston, R., Nguyen, T., Coughlin, M., Adhikari, R. X., and Katsavounidis, E., 'Noise Reduction in Gravitational-wave Data via Deep Learning,' Phys. Rev. Res., 2020, **2**(3), p. 033066, doi: 10.1103/PhysRevResearch.2.033066.

Ott, C., 'The Gravitational Wave Signature of Core-Collapse Supernovae,' Class. Quant. Grav., 2009, **26**, p. 063001, doi: 10.1088/0264-9381/26/6/063001.

Pankow, C. *et al.*, 'Mitigation of the instrumental noise transient in gravitational-wave data surrounding gw170817,' Phys. Rev. D, Oct 2018, **98**, p. 084016, doi: 10.1103/PhysRevD.98.084016.

Pedregosa, F., Varoquaux, G., Gramfort, A., Michel, V., Thirion, B., Grisel, O., Blondel, M., Prettenhofer, P., Weiss, R., Dubourg, V., Vanderplas, J., Passos, A., Cournapeau, D., Brucher, M., Perrot, M., and Duchesnay, E., 'Scikit-learn: Machine learning in Python,' Journal of Machine Learning Research, 2011, **12**, pp. 2825–2830.

Perraudin, N., Balazs, P., and Søndergaard, P. L., 'A fast griffin-lim algorithm,' in '2013 IEEE Workshop on Applications of Signal Processing to Audio and Acoustics,' 2013 pp. 1–4, doi: 10.1109/WASPAA.2013.6701851.

Pescalli, A., Ghirlanda, G., Salafia, O. S., Ghisellini, G., Nappo, F., and Salvaterra, R., 'Luminosity function and jet structure of Gamma-Ray Burst,' Mon. Not. Roy. Astron. Soc., 2015, **447**(2), pp. 1911–1921, doi: 10.1093/mnras/stu2482.

Poisson, E. and Will, C. M., *Gravity: Newtonian, Post-Newtonian, Relativistic*, Cambridge University Press, 2014, doi: 10.1017/CBO9781139507486.

Rhoads, J. E., 'The dynamics and light curves of beamed gamma-ray burst afterglows,' Astrophys. J., 1999, **525**, pp. 737–749, doi: 10.1086/307907.

Riles, K., 'Gravitational Waves: Sources, Detectors and Searches,' Prog. Part. Nucl. Phys., 2013, **68**, pp. 1–54, doi: 10.1016/j.ppnp.2012.08.001.

Robinet, F., Arnaud, N., Leroy, N., Lundgren, A., Macleod, D., and McIver, J., 'Omicron: A tool to characterize transient noise in gravitational-wave detectors,' SoftwareX, 2020, p. 100620, ISSN 2352-7110, doi: https://doi.org/10.1016/j.softx.2020.100620.

Rosenblatt, F., 'Principles of neurodynamics. perceptrons and the theory of brain mechanisms,' Technical report, Cornell Aeronautical Lab Inc Buffalo NY, 1961.

Rossi, E., Lazzati, D., and Rees, M. J., 'Afterglow lightcurves, viewing angle and the jet structure of gamma-ray bursts,' Mon. Not. Roy. Astron. Soc., 2002, **332**, p. 945, doi: 10.1046/j.1365-8711.2002.05363.x.

Saulson, P., *Fundamentals of Interferometric Gravitational Wave Detectors*, World Scientific, 1994, ISBN 9789810218201.

Schnabel, R., Mavalvala, N., Mcclelland, D. E., and Lam, P. K., 'Quantum metrology for gravitational wave astronomy,' Nature Commun., 2010, **1**(8), p. 121, doi: 10.1038/ncomms1122.

Singer, L. P. and Price, L. R., 'Rapid bayesian position reconstruction for gravitational-wave transients,' Phys. Rev. D, Jan 2016, **93**, p. 024013, doi: 10.1103/PhysRevD.93.024013.

Sutton, P. J. *et al.*, 'X-Pipeline: An Analysis package for autonomous gravitational-wave burst searches,' New J. Phys., 2010, **12**, p. 053034, doi: 10.1088/1367-2630/12/5/053034.

Tse, M. *et al.*, 'Quantum-enhanced advanced ligo detectors in the era of gravitational-wave astronomy,' Phys. Rev. Lett., Dec 2019, **123**, p. 231107, doi: 10.1103/PhysRevLett.123.231107.

Usman, S. A. *et al.*, 'The pycbc search for gravitational waves from compact binary coalescence,' Class. Quant. Grav., 2016, **33**(21), p. 215004, doi: 10.1088/0264-9381/33/21/215004.

Van Den Broeck, C., Brown, D. A., Cokelaer, T., Harry, I., Jones, G., Sathyaprakash, B., Tagoshi, H., and Takahashi, H., 'Template banks to search for compact binaries with spinning components in gravitational wave data,' Phys. Rev. D, 2009, **80**, p. 024009, doi: 10.1103/PhysRevD.80.024009.

Vitale, S., Gerosa, D., Farr, W. M., and Taylor, S. R., 'Inferring the properties of a population of compact binaries in presence of selection effects,' 7 2020.

Wei, W. and Huerta, E. A., 'Gravitational Wave Denoising of Binary Black Hole Mergers with Deep Learning,' Phys. Lett. B, 2020, **800**, p. 135081, doi: 10.1016/j.physletb.2019.135081.

Yu, H. *et al.*, 'Quantum correlations between light and the kilogram-mass mirrors of LIGO,' Nature, 2020, **583**(7814), pp. 43–47, doi: 10.1038/s41586-020-2420-8.

Zevin, M. *et al.*, 'Gravity Spy: Integrating Advanced LIGO Detector Characterization, Machine Learning, and Citizen Science,' Class. Quant. Grav., 2017, **34**(6), p. 064003, doi: 10.1088/1361-6382/aa5cea.

Zhang, B. and Meszaros, P., 'Gamma-ray burst beaming: a universal configuration with a standard energy reservoir?' Astrophys. J., 2002, **571**, pp. 876–879, doi: 10.1086/339981.

Zheng, Y., Cavaglià, M., Quitzow-James, R., and Mogushi, K., 'A needle in (many) haystacks: Using the false alarm rate to sift gravitational waves from noise,' Significance, 02 2021, **18**, pp. 26–31, doi: 10.1111/1740-9713.01488.

VITA

Kentaro Mogushi was born in BangKog, Thailand. He received his bachelor of science in the physics department at the Saitama University in 2015 with the award of an excellent student. He moved to the University of Mississippi and received a master's degree in the Physics department in May 2019. In June 2019, he began studying at the Missouri University of Science and Technology and was awarded first prize at the 26th annual Schearer Prize Competition in the physics department. In July 2021, he received his Ph.D. degree in the Physics from Missouri University of Science and Technology, Rolla, MO. His research interests included probability theories, data analysis techniques such as machine learning algorithms, and astrophysics along with general relativity. He published his studies related to the above interests.